MORPHOLOGY-PRESERVING CHEMICAL CONVERSION OF BIOORGANIC AND INORGANIC TEMPLATES

A Dissertation
Presented to
The Academic Faculty

by

Jonathan Paul Vernon

In Partial Fulfillment
Of the Requirements for the Degree
Doctor of Philosophy in Materials Science and Engineering

Georgia Institute of Technology

May, 2012

MORPHOLOGY-PRESERVING CHEMICAL CONVERSION OF BIOORGANIC TEMPLATES

Approved by:

Dr. Kenneth H. Sandhage, Advisor
School of Materials Science
and Engineering
Georgia Institute of Technology

Dr. Peter Vukusic
School of Physics
University of Exeter

Dr. Meilin Liu
School of Materials Science
and Engineering
Georgia Institute of Technology

Dr. Joseph Perry
School of Chemistry & Biochemistry
Georgia Institute of Technology

Dr. Valeria Milam
School of Materials Science
and Engineering
Georgia Institute of Technology

Date Approved: January 10th 2012

Acknowledgements

As I wrap up the 22nd grade, thankfully my final school year, I think it would be impossible to name all of those who have guided me to this point in my life. However, I will do my best to acknowledge all of those responsible for making this document possible.

You were right Prof. Sandhage. A dissertation with a research topic that works from the start is not worth as much to the development of a student as a graduate career that requires overcoming significant obstacles. I am most thankful for your passion for research, your consistency, your patience, and your ethics. Prof. Liu, Prof. Milam, Prof. Perry, and Prof. Vukusic thank you for serving on my dissertation reading committee—your time spent, your guidance, and your approval will not be forgotten.

The hard and soft laboratory skills imparted to me by my professional mentors Dr. Tim Bunning, Dr. Rajesh Naik, Sharon Jones, Angela Petroski, Prof. Ken Sandhage, and Prof. Rod Trice have been invaluable. Thank you to all of the phenomenal collaborators with whom I have had the pleasure to work with including: Dr. Ye Cai, Craig Cameron, Dr. Dimitri Deheyn, Dr. Yunnan Fang, Brandon Goodwin, Dr. Mathias Kolle, Alfie Lethbridge, Andrew Shaw, Dr. Milana Vasudev, Dr. Pete Vukusic, and Dr. Yunshu Zhang. Dr. Cai, without your contributions this dissertation would not have been possible. Vicki Cline and Susan Bowman—you are the heart and soul of the MSE departments from which I have graduated—I cannot give enough thanks to either of you.

Thank you to all of my past and present peers in the Sandhage group and co-workers in the Naik group for providing helpful conversations, patient instruction, and such enjoyable work environments. I would especially like to thank Eric Ernst, Dr. Mike Weatherspoon, Dan Berrigan, Phil Graham, Dr. Matt Dickerson, and Dr. Dave Lipke for their friendship, problem solving skills, and guidance. Nick Haase and Dr. Vonda Sheppard-Smith thanks for making me laugh and giving me perspective. Nicholas Hobbs, it was a pleasure to be your mentor and I thank you for all that you have taught me.

Steven Ludwig and Prof. Kevin Trumble, thank you for your instruction, mentorship, and teaching styles, all of which sparked my interest in chemistry and molded my decision to become a life-long student of Materials Science and Engineering. Writing this thesis would have been impossible without the English teacher who taught me everything I know about writing in a single year—Beth Chaddon, you are truly one of a kind.

From Hilltop to Willowbrook to 123 Andrew's Place and on to Atlanta: thank you Stroh, Janik, Uhler, Brichouse, Greg, and Nathan for putting up with me as a roommate throughout my college years and constituting a group of the most trustworthy men I know. In addition to my roommates, Anna, Fleck, Glenda, Petorak, Graham, Chase, Mitchell, Amber, Snaves, Lindsey, Kyle, Rolando, Kim, Seth, Reggie, and Jackie, your friendships have provided me much needed work/life balance and have created some of my fondest and most memorable experiences.

Most importantly, I acknowledge my Mom and Dad. The two of you have inspired me, taught me, and supported me in ways I still cannot appreciate. I know, as

I grow older, my understanding of what you have done for me will only continue to grow. Andrea, thank you for your support, love and being an older sister I can count on—at least since you stopped asking Mom and Dad to take me back to the hospital to be exchanged for a sister.

Table of Contents

List of Tables

List of Figures

List of Symbols and Abbreviations

a	Nucleation portion of Avrami exponent
b	Growth rate portion of Avrami exponent
3D	Three-Dimensional
BT	$BaTiO_3$
DI	Deionized
EDS	Energy Dispersive X-ray Spectroscopy
hr	hour(s)
HRTEM	High Resolution Transmission Electron Microscopy
HTXRD	High Temperature X-Ray Diffraction
IPA	Anhydrous Isopropyl Alcohol
LA-ICP	Laser Ablation Inductively Coupled Plasma
LA-ICP-MS	Laser Ablation Inductively Coupled Plasma Mass Spectrometry
λ	Wavelength (nm)
LbL	Layer-by-Layer
m	Avrami exponent
μm	Micrometer
MSP	Microspectrophotometry
MWHT	Microwave Hydrothermal
n	Index of Refraction
nm	nanometer(s)
PPC	Photonic Polycrystal
QCM	Quartz Crystal Microbalance
RT	Room Temperature
SE	Secondary Electron
SEM	Scanning Electron Microscopy
SSG	Surface Sol Gel
TEM	Transmission Electron Microscopy
XPS	X-ray photoelectron spectroscopy
X_{SA}	Surface Area Fraction Transformed

Summary

The generation of nanostructured assemblies with complex (three-dimensional, 3D) self-assembled morphologies and with complex (multicomponent) tailorable inorganic compositions is of considerable technological and scientific interest. This dissertation demonstrates self-assembled 3D organic templates of biogenic origin can be converted into replicas comprised of numerous other functional nanocrystalline inorganic materials. Nature provides a spectacular variety of biologically-assembled 3D organic structures with intricate, hierarchical (macro-to-micro-to-nanoscale) morphologies. Such processing on readily-available structurally complex templates provides a framework for chemical conversion of synthetic organic templates and, potentially, production of organic/inorganic composites.

Four specific research thrusts are detailed in this document. First, chemical conversion of a nanostructured bioorganic template into a multicomponent oxide compound (tetragonal $BaTiO_3$) via SSG coating and subsequent morphology-preserving microwave hydrothermal processing is demonstrated. Second, morphology-preserving chemical conversion of bioorganic templates into hierarchical photoluminescent microparticles is demonstrated to reveal both the dramatic change in properties such processing can provide, and the potential utility of chemically transformed templates in anti-counterfeiting / authentication applications. Third, determination of the reaction mechanism(s) for morphology-preserving microwave hydrothermal conversion of TiO_2 to $BaTiO_3$, through Au inert markers on single crystal rutile titania, is detailed. Finally, utilization of constructive coating techniques (SSG) and moderate temperature (< 500°C) heat treatments to modify and replicate

structural color is coupled with deconstructive focused ion beam microsurgery to prepare samples for microscale structure interrogation. Specifically, the effects of coating thickness and composition on reflection spectra of structurally colored templates are examined. Also, the effects of the replacement of natural material with higher index of refraction inorganic materials on optical properties are discussed. The three processing research thrusts constituting chapters 1, 2 and 4 take advantage of moderate temperature processing to ensure nanocrystalline materials, either for shape preservation or to prevent scattering in optical applications. The research thrust detailed in chapter 3 examines hydrothermal conversion of TiO_2 to $BaTiO_3$, not only to identify the reaction mechanism(s) involved in hydrothermal conversion under morphology-preserving conditions, but also to introduce inert marker experiments to the field of microwave hydrothermal processing.

CHAPTER 1: Morphology-Preserving Chemical Conversion of a 3D Bioorganic Template (*Morpho helenor* butterfly scales) into a Multicomponent Oxide Compound ($BaTiO_3$)

Discussions in this chapter are distinct from and expand upon the research presented in: J.P. Vernon, Y. Fang, Y. Cai, and K.H. Sandhage, "Morphology-Preserving Conversion of a 3D Bioorganic Template into a Multicomponent Oxide Compound," *Angew. Chem. Int. Ed.*, vol. **49**, pp. 7765-7768, 2010.

1.1. *Summary*

This work reveals, for the first time, how a 3D organic template may be converted into a positive replica of a nanocrystalline multicomponent oxide compound through a three step process generally consisting of the following steps: (i) application of a thin continuous and conformal 3D inorganic coating through a wet-chemical surface-limited reaction process on an organic template with a hydroxylated surface, (ii) organic pyrolysis of the underlying template material and crystallization of the applied oxide coating, and (iii) low-temperature hydrothermal conversion of resulting inorganic material into a nanocrystalline multicomponent oxide compound replica. This process was demonstrated by converting 3D chitinous *Morpho helenor* butterfly scales into $BaTiO_3$ replicas. Determination of the processing steps and the corresponding conditions within each step of the morphology-preserving chemical conversion process are discussed. Evaluation of the chemistry, phase content, and dimensional changes throughout the chemical conversion process, as well as the interaction between coating precursor and template, are detailed. Such an approach may be readily applied to organic templates produced through biological, or synthetic, means in order to prepare inorganic replicas with a wide variety of compositions, complex structures, and properties.

1.2. *Introduction*

Research focusing on the formation of oxide nanostructures in both planar and three-dimensional (3D) geometries is spurred by anticipated importance for a number of emerging applications including fuel cells[1], batteries[2], photocatalysts[3], solar arrays[4]., sensors[5], photonic bandgap materials[6], ultracapacitors[7], and high-frequency imaging transducers[8]. For example, when reduced to the micrometer and nanometer scale, piezoelectric energy harvesting devices may eliminate the need for replaceable power supplies and expensive battery recharging procedures, reducing the waste generated by batteries used in small portable electronic devices (e.g., cell phones and music players), implantable medical devices, and remote structural health monitoring sensors in aircrafts and ships[9]. Additionally, ultrasonic imaging transducers with submicron piezoelectric elements would increase the imaging frequency, providing increased lateral resolution for small penetration depths[10]. Also, nanostructured photonic crystals could readily form photonic band gaps at desired wavelengths in the visible spectrum by tailoring periodic repeat distance of the structure, the refractive index of the material, or both[11]. Unfortunately, there are considerable scientific and engineering challenges involved in creating devices with nanoscale control of composition and structure. The proposed work aims to expand the currently limited processing repertoire (which becomes increasingly deficient at the nanometer length scale) for the manufacturing of, and tailoring composition within, complex-shaped ceramics.

Obtaining chemically diverse, functional, 3D structures on the nanoscale comprised of multicomponent oxides proves difficult because the high temperatures (generally > 800°C) required to efficiently solid-state react, and/or sinter such ceramic

compounds, typically accompany significant microstructural changes (e.g., grain growth, shrinkage). In addition to structural limitations, the ability to carefully control the local stoichiometry of such ceramics (i.e., composition gradients, layering at the nanoscale) remains a non-trivial challenge. Both the length scale of controlled chemistry and temperature required for crystallization have been reduced by the advent of layer-by-layer (LbL) deposition methods, such as those involving wet-chemical based systems. However, wet-chemical techniques have largely focused on simple geometries (e.g., spin coating, dip coating, spray coating, and precipitating powders) [12,13]. Recently, conformal nanostructured coatings on complex inorganic and inorganic 3D geometries have been demonstrated using a readily-scalable, wet–chemical LbL coating method referred to as surface sol-gel deposition[14,15]. To address the limited material systems and processing methods for generating nanostructured multicomponent oxides, the proposed research aims to develop broadly applicable processes for low temperature synthesis of such materials through the combination of SSG deposition and moderate thermal (< 500°C) processing. SSG-applied coatings were evaluated through oxide deposition on 3D nanostructured bioorganic templates. Microwave hydrothermal (MWHT) processing of such coatings was examined for chemical conversion / phase transformation / crystallization of complex multicomponent oxide structures.

SSG deposition may be used to coat a variety of natural or synthetic templates (e.g., any surface inherently, or functionalized to be, hydroxy- or carboxy- rich), via LbL hydrolysis of alkoxide-based precursors retaining feature sizes of ~1 nm [16,17]. Microwave hydrothermal processing and its analogs (i.e., conventional hydrothermal and solvothermal processing) can produce multicomponent functional ceramic powders and

films at low temperatures (i.e., < 240 °C) into desired polymorphs in reaction times unequalled by conventional ceramic processing [18,19]. Combining SSG with MWHT reactions allows for (i) any surface rich with hydroxyl/carboxyl groups to have monolithic or multicomponent oxide coatings applied, and (ii) subsequent morphology-preserving chemical reaction / crystallization / phase transformation of coatings. The novelty of this work is the integration of the precise chemical and structural control offered by surface-limited reaction SSG coatings with low temperature morphology-preserving processing to yield nanocrystalline functional materials.

Wet-chemical techniques are commonly used to co-precipitate stoichiometric oxide powders, or form films. The advantage of such processing is that firing temperatures required to provide crystalline product formation are considerably less than typical temperatures used for solid-state reaction processing. SSG, a wet-chemical analog to atomic layer deposition, was introduced by Ichinose *et al.* in 1996[16]. The SSG process involves hydrolysis of chemisorbed metal alkoxide precursors on surface hydroxyl or carboxyl groups. Once an alkoxide layer is formed, the surface is rinsed with anhydrous organic solvent to remove unbound alkoxide molecules. The chemisorbed surface is then hydrolyzed by incubating with water to regenerate hydroxy groups on the surface[16]. A schematic of the surface sol-gel process comprises **Figure 1**.

Through the use of a gold-coated quartz crystal microbalance (QCM) resonator (modified with 2-mercaptoethanol to functionalize the surface with hydroxyl groups), the film thicknesses of different metal alkoxides deposited via SSG were determined as a function of incubation time, and number of cycles[16,17]. A consistent, and stable (i.e., frequency shift of QCM does not change after ~2 min of metal alkoxide incubation),

deposition of ~8 Å per layer of alkoxide formed upon exposure of the functionalized QCM crystal to titanium tetrabutoxide[17]. Such experimentation confirmed the linear frequency shift (i.e., repeatable layer thickness) of metal alkoxides on hydroxylated surfaces. Because the SSG process is surface-limited, the total film thickness can be controlled by the number of SSG cycles applied.

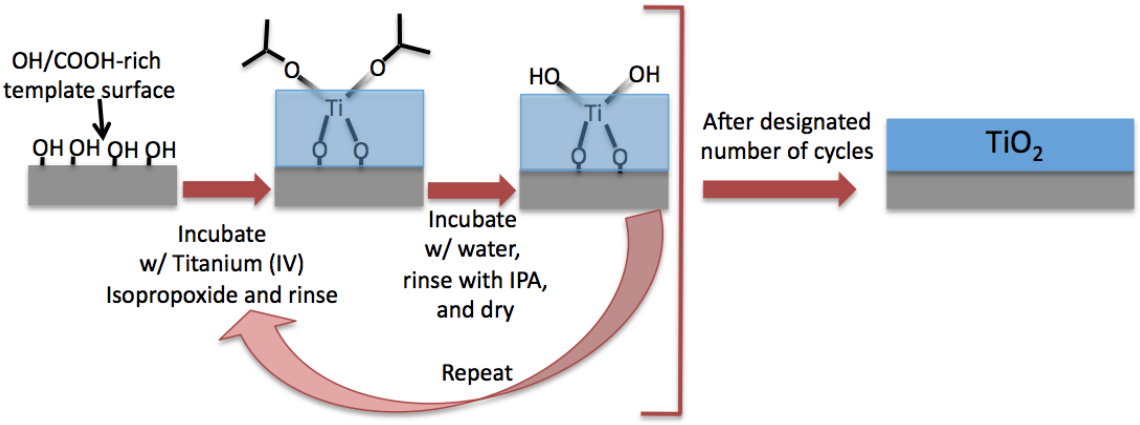

Figure 1: A schematic representation of the surface sol-gel process utilizing titanium(IV) isopropoxide as model metal alkoxide.

Bioorganic templates with hydroxylated surfaces were chosen as model templates to avoid cumbersome top-down and bottom-up processing methods for obtaining micro-to-nano scale features within a large number of synthetically produced 3D templates. *Morpho helenor* butterfly wing scales were the initial templates chosen to evaluate the influences of various processing conditions on nanostructural retention. The *Morpho helenor* butterfly wing template has a regular and well-characterized morphology and is comprised of a robust natural polysaccharide, chitin, that contains an abundance of surface hydroxy groups[20,21]. An intrinsically hydroxylated template surface may eliminate the need for surface modification before SSG deposition to ensure continuous and conformal coatings. Photographs of the two sides of a *Morpho helenor* butterfly wing, SE images of the corresponding microstructures within individual butterfly scales

tiled on the wing surface, and a schematic of the molecular building block (i.e., chitin) of butterfly cuticle are shown in **Figure 2**.

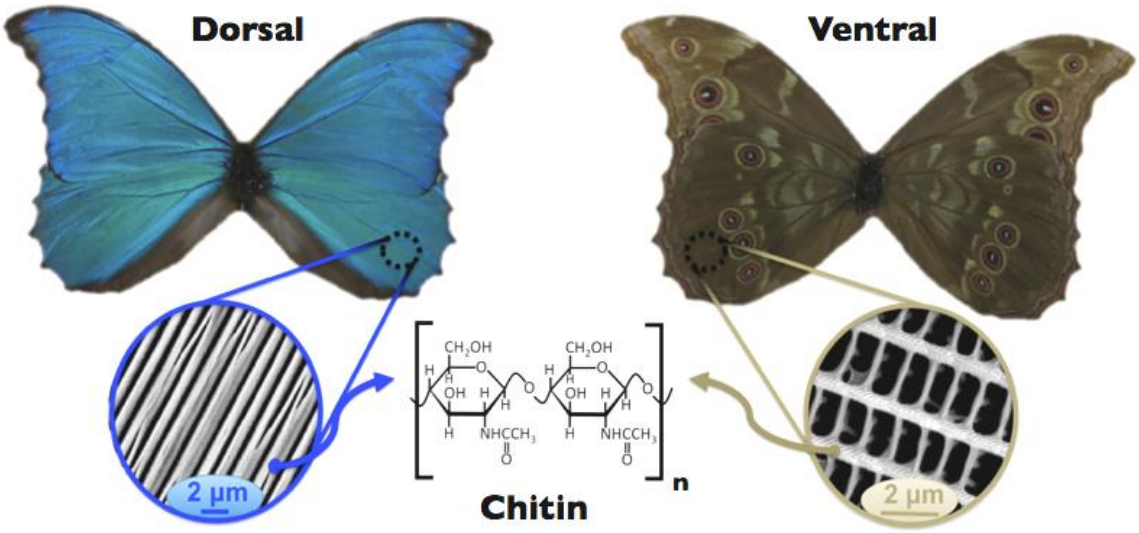

Figure 2: Photographs of both the dorsal and ventral sides of a *Morpho helenor* butterfly, SE images of the corresponding microstructures within single cover scales from both the dorsal and ventral sides of the butterfly wing, and a schematic of chitin, one of the prominent biopolymers present in butterfly cuticle.

Hydrothermal synthesis to geoscientists is a process taking place in the presence of supercritical water (above 374°C) [18]. Hydrothermal synthesis is now often used, although less accurately, to describe aqueous-based synthesis above 100 °C and at a pressure greater than 1 atm[18]. A sealed vessel is used to contain the vapor of the solvent, which is aqueous in hydrothermal processing, or non-aqueous in solvothermal processing. Through hydrothermal processing a desired product may be formed directly from precursor solutions at low temperatures. Other advantages include the control of particle morphology and agglomeration[18,19]. In 1993, Komarneni *et al.* used hydrothermal synthesis in combination with a microwave field to produce single, binary, and multicomponent oxides[18]. In their work with electroceramics, Komarneni *et al.* demonstrated that microwave hydrothermal processing increased reaction kinetics by one

to two orders of magnitude over conventional hydrothermal processing[18]. Some propose microwave radiation couples with, and is absorbed by, a material and the absorbed radiation is converted into thermal energy. The advantage of such internal heating, rather than conventional heating through convection or conduction, is believed to be a contributing mechanism for the reduction in reaction time[19]. Others propose kinetic enhancement results from the increased transport of ions due to the decrease in viscosity of water under hydrothermal conditions[22]. With conventional hydrothermal reactions, tetragonal $BaTiO_3$ has been formed at 240°C in 24 hrs[19]. Microwave hydrothermal syntheses conducted at the same temperature (and with the same reactants) produced tetragonal BT in 10 hrs with a tetragonal character equivalent to BT produced by conventional hydrothermal in 48 hrs[19].

Barium titanate ($BaTiO_3$ or BT) was selected as the representative ceramic material because it is widely used in a number of engineering applications (e.g., multilayer ceramic capacitors (MLCCs), electro-optic devices, and pyroelectric elements)[18,19,22,23,24]. In the aforementioned applications, the ferroelectric properties of BT are exploited. BT is a perovskite (ABO_3) material which transforms from centrosymmetric to noncentrosymmetric crystal symmetries at the Curie temperature. The change in the perovskite-based structure at the Curie temperature for BT is illustrated in **Figure 3**. In the case of BT, displacement of the central Ti^{4+} ion causes a dipole moment in the crystal. Above the Curie temperature a ferroelectric material will lose its polarizability because the thermal energy is great enough to restore the random orientation of domain polarization vectors[25]. Perovskites are referred to as "garbage can" ceramics for the ability to host a broad range of cations on the A and/or B sites. This

chemical flexibility is attractive, especially when processing methods provide precise stoichiometric control, because various properties such as photoluminescence and dielectric response can be tuned via chemical composition. For example, a red-emitting phosphor, Eu^{3+} can be doped up to 8 mol% in a $BaTiO_3$ host lattice without exhibiting concentration quenching[26]. Also, Sr^{2+} is often incorporated within $BaTiO_3$ (i.e., as a solid solution through substitution at Ba^{2+} sites) to produce tunable dielectrics, (e.g., reducing the Curie temperature from ~120°C for BT to ~6.3 °C for $Ba_{0.6}Sr_{0.4}TiO_3$ (BST)[27].

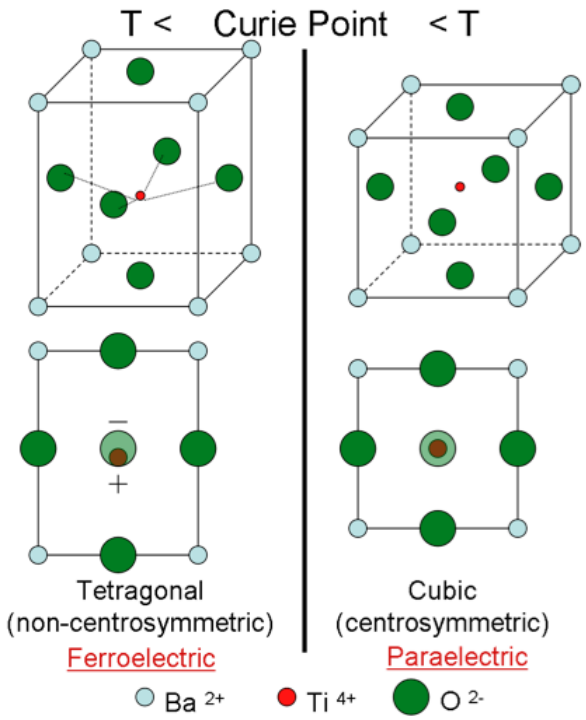

Figure 3: A schematic representation of the perovskite unit cell of barium titanate upon cooling (right to left) through its Curie transition temperature, which is accompanied by the spontaneous polarization of dipoles leading to ferroelectric behavior (left).

The proposed morphology-preserving chemical conversion process for converting chitinous butterfly scales into nanocrystalline multicomponent oxide compound replicas is illustrated in **Figure 4**. Indeed this is a robust process for generating hierarchical assemblies which possess 3D morphologies with both microscale and nanoscale patterns/features. The strategy for such a conversion process relies upon decoupling the

template formation and chemical tailoring processes. By using biological templates with micro-to-nanoscale patterns, one may optimize the conversion processes for application to synthetic templates. The variety of commercially available metal alkoxides available for surface sol-gel deposition in combination with hydrothermal reaction processing provides promise that this methodology may be used to convert synthetic or biogenic organic templates into functional ceramic materials with numerous 3D morphologies, compositions, and properties.

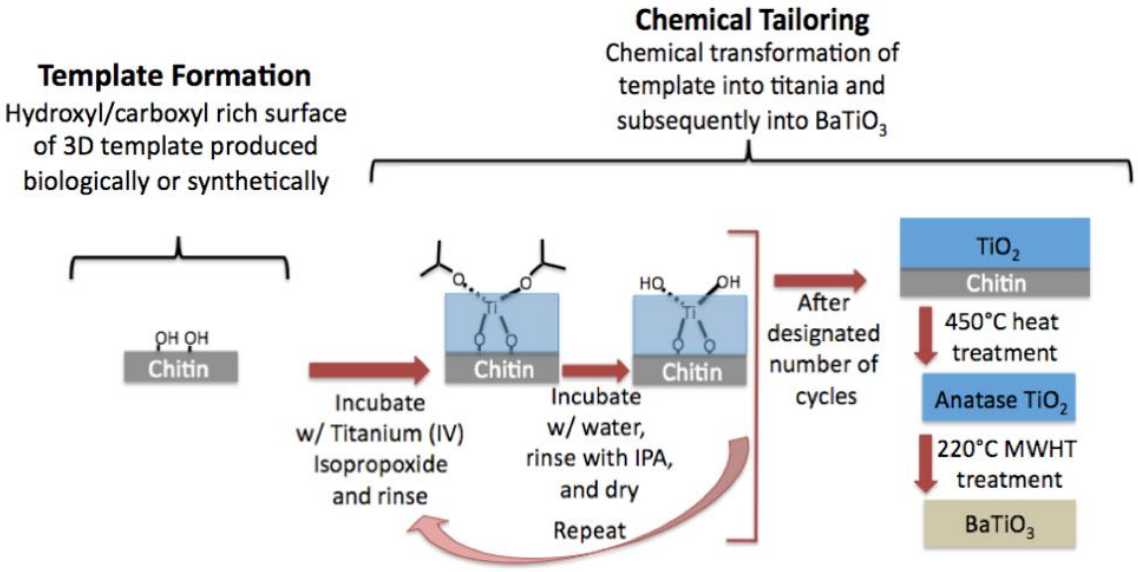

Figure 4: A schematic illustration of the morphology-preserving chemical conversion process which separates template formation and chemical tailoring processing. Once a template is formed the chemical tailoring process entails three steps: (i) applying thin conformal oxide coating, (ii) organic pyrolysis and crystallization of oxide coating, and (iii) hydrothermal conversion of resulting inorganic material into a multicomponent oxide compound.

1.3. *Experimental Procedures*

Morpho helenor butterfly scales (purchased deceased and dehydrated from insect-sale.com, Chia-yi City, Taiwan) were chemically transformed into BT replicas via a three-step process: i) application of a thin Ti-O-bearing coating through a layer-by-layer

surface sol-gel (SSG) process, ii) pyrolysis of the underlying chitinous template and crystallization of the Ti-O coating into anatase TiO_2, and iii) conversion of the resulting titania structure into barium titanate by microwave hydrothermal reaction with a barium acetate- and NaOH- bearing solution. Determination of precursor and processing conditions were studied through the use of hydrolyzed powders of monolithic, mixed alkoxide, and molecular precursors.

1.3.1. Hydrolysis of TiO_2 powder for MWHT Treatment

The generation of Ti-O precipitates entailed adding 6 mL of water to 20 mL of a 0.635 mM solution of Titanium(IV) isopropoxide (99.999% metals basis, Sigma Aldrich, MO, USA) in anhydrous isopropanol (IPA) (Acros Organics, Geel, Belgium). After washing (i.e., with 20 mL of water and then 20 mL IPA) and drying (i.e. 30 min - 1hr at 80 °C in air) the precipitate was loaded into a Teflon™-lined microwave hydrothermal vessel (XP1500 Plus, CEM Corp., Matthews, NC, USA) in a nitrogen atmosphere glove box (to prevent barium carbonate ($BaCO_3$) formation) with 20 mL solution of 1M NaOH (diluted from 50% w/w aq. soln., Alfa Aesar, MA, USA) and 125 mM barium acetate (99% Alfa Aesar, MA, USA) in previously boiled DI water. Samples were treated at 140°C, 170°C, and 220°C for 10 hr in a microwave reaction system (2.45 GHz MARS 230/60, CEM, NC, USA). After reaction, the powders were washed twice with 25 mL of 1 M acetic acid (diluted from glacial acetic acid, 17.4N, 99.9%, Fisher-Scientific, PA, USA) in 50 mL centrifuge tubes rotated at 30 rpm on a RKVSD rotator (Appropriate Technical Resources, MD, USA) for 30 min to remove any potential $BaCO_3$ that may have formed upon opening the vessels in ambient atmosphere. The specimens were then washed twice with 20 mL of previously boiled DI water, and then twice with 20 mL of

IPA, followed by drying in air at 80°C for 1 hr. Each wash, or rinse, step was carried out via 5 min centrifugation of solutions in 50 mL centrifuge tubes (Corning, MA, USA) at 4500 rpm in a centrifuge equipped with a swinging bucket rotor (5408R centrifuge with #A-4-44 rotor, Eppendorf, Hamburg, Germany). Following centrifugation the supernatant was removed by pipette before adding subsequent solution or drying. After drying samples were then ready for XRD analyses.

1.3.2. Hydrolysis of mixed alkoxide and stoichiometric precursors

Precipitation (i.e., via hydrolysis) of Ba and Ti –bearing powders required 6 mL of water to be added to 20 mL of a 0.635 mM barium titanate alkoxide precursor solution. Alkoxide solutions were either a stoichiometric mixture of barium(II) isopropoxide (20% (w/v) in isopropanol, Alfa Aesar, MA, USA) and titanium(IV) isopropoxide, or a molecular precursor, barium titanium ethylhexano isopropoxide (5 wt% $BaTiO_3$, 99% by metals basis, Chemat, CA, USA). After washing twice with 20 mL of DI water and then twice with 20 mL of IPA, the precipitates were dried for 30 minutes in a vacuum centrifuge and then loaded (in a nitrogen atmosphere glove box) into a microwave hydrothermal vessel with 20 mL of a boiled DI water-based solution containing either 0.5 M barium acetate or 100 mM phosphate/citrate buffer (pH 7). Note: some of the precipitate specimens were saved for HTXRD analysis. Precipitate specimens were treated at 240°C and 140 °C for 10 hrs and 2 hrs respectively in the microwave reaction system. The hydrothermally treated powders were washed with 25 mL of 1 M acetic acid for 30 minutes two times to remove any possible $BaCO_3$ that may have formed upon exposure to the ambient atmosphere. The MWHT reaction products were then washed

twice with water, washed twice with IPA, and then dried at 80° C for 1 hr before XRD analysis.

1.3.3. SSG coating of butterfly scales

Each automated cycle (in a N_2 atmosphere glovebox) of the SSG process was conducted by (i) immersing wing sections clipped to a 1.5 x 1.5 cm silicon wafer substrate in a 0.050 M titanium (IV) isopropoxide solution in IPA for 10 min, (ii) washing three times with 4 mL of IPA, (iii) immersing in 4 mL of 40 vol% IPA in DI water for 3 min, (iv) washing again three times with ~4 mL of IPA, and then (v) drying with a stream of flowing air for 5 min at RT. This process was repeated for a total of 51 cycles. The coated wing sections were then placed between two polished (2.54 x 2.54 x 0.159 cm) fused quartz plates (Technical Glass Products, OH, USA) by wetting with ethanol and were allowed to dry for at least1 hr.

1.3.4. Organic pyrolysis and MWHT conversion

The SSG-coated butterfly wing sections were sandwiched between two quartz plates then heated in an MgO crucible in a tube furnace (Lindberg / Blue M, NC, USA,) at 0.5°C/min to 450°C (AutoFire® Controller, Orton Ceramic Foundation, OH, USA outfitted with a k-type thermocouple, OMEGA Engineering, Inc., CT, USA) and held at this temperature for 4 hr in air to allow for pyrolysis of the chitin and crystallization of the titania. The specimens were then furnace-cooled to RT. The pyrolyzed specimens were sealed within MWHT vessels containing a 20 mL solution of 0.125 M barium acetate and 1 M NaOH both dissolved within previously-boiled DI water. The specimens were then heated within 7 min to 220°C in microwave reaction system at a maximum

power output of 1600 W and held at this temperature for 10 hr to allow for complete microwave hydrothermal (MWHT) conversion into BT. After removal from the MWHT vessels, the reacted scales were washed twice for 30 min with 25 mL of 1 M acetic acid in 50 mL centrifuge tubes rotated at 30 rpm on a rotator to remove any potential $BaCO_3$ that may have formed upon opening the vessels in ambient atmosphere. The specimens were then rinsed twice with 20 mL of water, and then twice with 20 mL of IPA, followed by drying in air at 80°C for 1 hr.

1.3.5. Morphology, Phase, and Chemical Analyses

The morphologies of the native *M. helenor* butterfly scales, the SSG-coated scales, the pyrolyzed scales, and the hydrothermally-reacted scales were evaluated with a field emission scanning electron microscope (1530 FEG SEM, LEO / Zeiss Electron Microscopy Thornwood, NY) equipped with energy dispersive X-ray spectrometer (EDS) (INCA Model 7426, Oxford Instruments, Bucks, UK) capability. If indicated that samples were sputtered with gold, a Quorum Q150T ES (Energy Beam Sciences, INC., CT, USA) sputter coater had been utilized to sputter Au for 60 seconds at 20 mA. The phase identification of the MWHT converted powders were evaluated at room temperature using X-ray diffraction (XRD) analyses. XRD analyses were conducted on an X'Pert Pro Alpha-1 diffractometer (PANalytical B.V., ALMELO, Netherlands) with monochromatic $Cu_{K\alpha 1}$(1.5405980 Å) radiation emanating from a 1.8 kW ceramic X-ray tube with a copper anode (45 kV, 40 mA) through a symmetrical Johannson monochromator and detected by an X'Celerator detector. Diffraction specimens were dispersed on quartz cut 6° from (0001) low background specimen support (GEM dugout, PA, USA) via pipetting an aliquot of IPA/powder slurry onto specimen support and

allowing the IPA to evaporate. Some powder diffraction specimens were mounted from IPA/powder slurries with powder that had an internal 10 wt% NIST SRM 640c standard incorporated in order to confirm the line position of the scans. High temperature X-ray diffraction (HTXRD) analyses were performed on an X'pert Pro MPD diffractometer (PANalytical Corp., ALMELO, Netherlands) equipped with an Anton-Parr HTK 1200 furnace with no gas flow. For HTXRD, specimens were also loaded via pipetting of precipitate/isopropyl alcohol slurry, but this time the specimen supports were single crystal MgO plates ((100) oriented single crystal MgO, 10 mm x 10 mm x 1 mm with two-sided polish, MTI corporation, CA, USA). After the IPA evaporated, the first scan was performed at 25°C, and all subsequent scans at 70 °C. Between the scans at 70°C the following procedure was used for heat treatment temperatures ranging from 100°C to 700°C in 100°C increments: heated furnace at 60°C/min to desired heat treatment temperature, held at temperature for 2 hr then cooled at 60°C/ min to 70°C for scan to be taken below Curie temperature.

All transmission electron microscopy (TEM) bright field imaging and selected area electron diffraction (SAED) and high resolution TEM imaging (HRTEM) was performed by Dr. Ye Cai (Georgia Institute of Technology). The analyses were conducted using a JEOL 4000 EX instrument (Japan Electron Optics Laboratory, Tachikawa, Tokyo). Cross-sectional images of specimens were also obtained by Dr. Ye Cai via focused ion beam (FIB) milling (Nova Nanolab 200 FIB/SEM, FEI, Hillsboro, OR, USA). Cross-sectional SE images of the internal structure of *M. helenor* butterfly wings were generated by cutting(via FIB milling) an initial trench ~2 μm x 1μm and then milling sequential 200 nm thick slices ("cleaning cross-sections") away from the face of

the trench being imaged. FIB cross-sections for TEM interrogation were cut from a ridge, bonded to micromanipulator needle via Pt deposition, and then thinned via FIB milling before being placed on a TEM specimen support grid. Oxygen plasma treatment for removal of the as-coated chitin template was conducted (Model PDC-001 Plasma Cleaner, Harrick, Inc., Ossining, NY) with ultra high purity oxygen at a pressure of 300 millitorr for 18 h at a power setting of 29.6 W. Raman spectra were obtained at RT using a confocal Raman microscope (Alpha 300R, WITec, Ulm, Germany) with a 1 mW Ar^+ ion laser (λ=514.5 nm) as the excitation source. A 20x objective lens was used to focus the laser onto each specimen.

1.4. *Results & Discussion*

1.4.1. Converting SSG coatings on complex biotemplate into $BaTiO_3$

In an effort to obtain 3D nanocrystalline structures of tetragonal BT, *Morpho helenor* butterfly wing scales were conformally coated with Ti-O via SSG, pyrolyzed at 450°C, and converted into $BaTiO_3$ with a 220°C MWHT treatment. Reaction conditions were determined by performing MWHT reactions on powders generated by hydrolyzing titanium(IV) isopropoxide precursor as outlined in **Section 1.3.1**. **Figure 5** contains the XRD data generated from TiO_2 powders after being converted via MWHT under caustic conditions in the presence of barium acetate at various temperatures. The key result illustrated in **Figure 5** is the significant peak splitting of (002) from (200)/(020) interplanar spacings of the unit cell (at ~45° 2θ) after treatment at 220°C, which indicated a significant amount of tetragonal polymorph was formed.

The chemical conversion process utilized to convert *Morpho helenor* butterfly scales into tetragonal $BaTiO_3$ replicas is depicted in **Figure 1**. Lepidopteran wings are imbricated with chitinous scales. *M. helenor* butterfly wings have both cover and ground scales as defined in **Figure 6a**. Each individual ventral cover scale (~200-250 µm long by ~100 µm wide) of the female *M. helenor* is rectangular in shape, furcated (typically into 3-5 points) on the exposed end, and tapered to a single stem that attaches the scale to the wing membrane. Such scales also contain ridges running parallel to the long dimension of the scale spaced ~ 2 µm apart as shown in **Figure 6b,c**. Each ridge is striated with ~60 nm thick parallel ribs spaced ~150 nm apart as shown in **Figure 6b,c**. The ridges are connected by horizontal struts as shown in **Figure 6b,c**, and supported by vertical struts (or trabeculae). The vertical struts connect the ridge/horizontal strut structure to the base of the scale as depicted in a SE image of a FIB-milled cross-section of a native ventral cover scale (**Figure 6d)**.

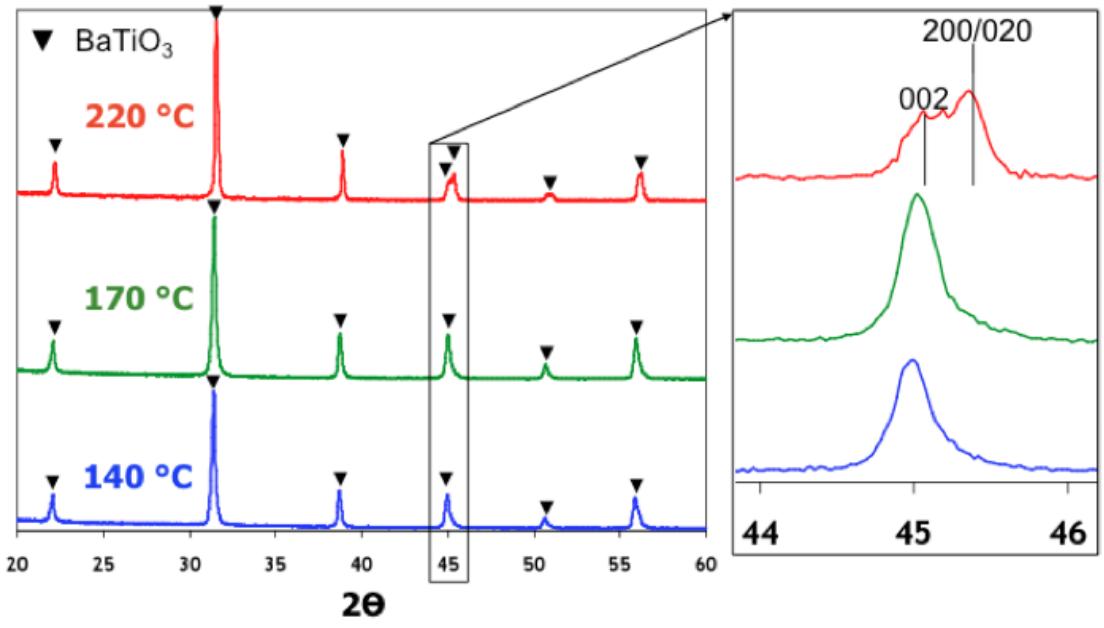

Figure 5: X-ray diffraction patterns of TiO_2 powder (0.635 mM) precipitated via hydrolysis of Titanium(IV) isopropoxide after MWHT treatments at 140, 170, and 220 °C in solution containing

0.125 M barium acetate and 1M sodium hydroxide for 10 hr (left). Close inspection of the peaks near 45 degrees two-theta (right) revealed peak-splitting indicative of the tetragonal phase is evident in the 220 °C specimen.

Thin, conformal and continuous titania-bearing coatings were applied to these nanostructured biotemplates through a computer-controlled SSG process for a total of 51 cycles. Coated scales then underwent organic pyrolysis (450°C, 4hr, in air) to remove the chitinous template. The resulting oxide structures were hydrothermally treated at 220°C for 10 hours in a 0.125 M barium acetate / 1 M NaOH solution. Each step of the transformation process from chitinous butterfly scales to nanocrystalline $BaTiO_3$ structures is illustrated through top view SE micrographs shown in **Figure 7**, which demonstrate the $BaTiO_3$ inorganic replicas retained the overall scale morphology, parallel ridges and perpendicular struts.

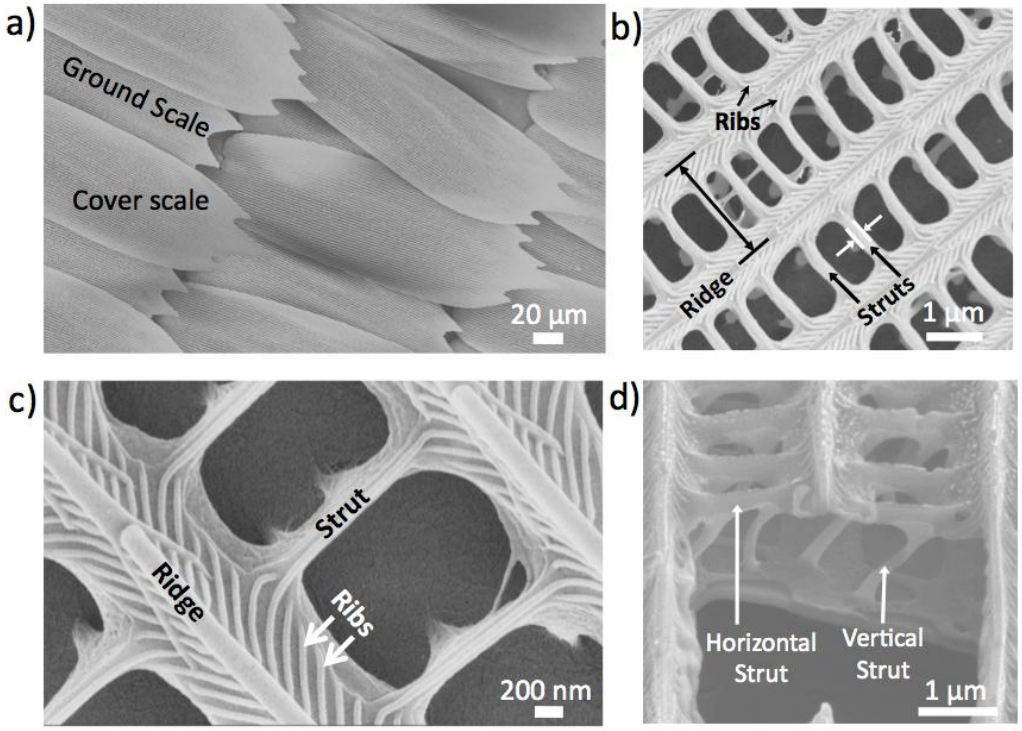

Figure 6: SE images of (a) tiled ventral scales of a female *Morpho helenor* butterfly labeled with cover and ground scales, (b,c) microstructure of individual scales with ridges, struts, and ribs indicated, and (d) FIB cross-section cut through thickness of scale showing vertical struts supporting horizontal struts and ridges.

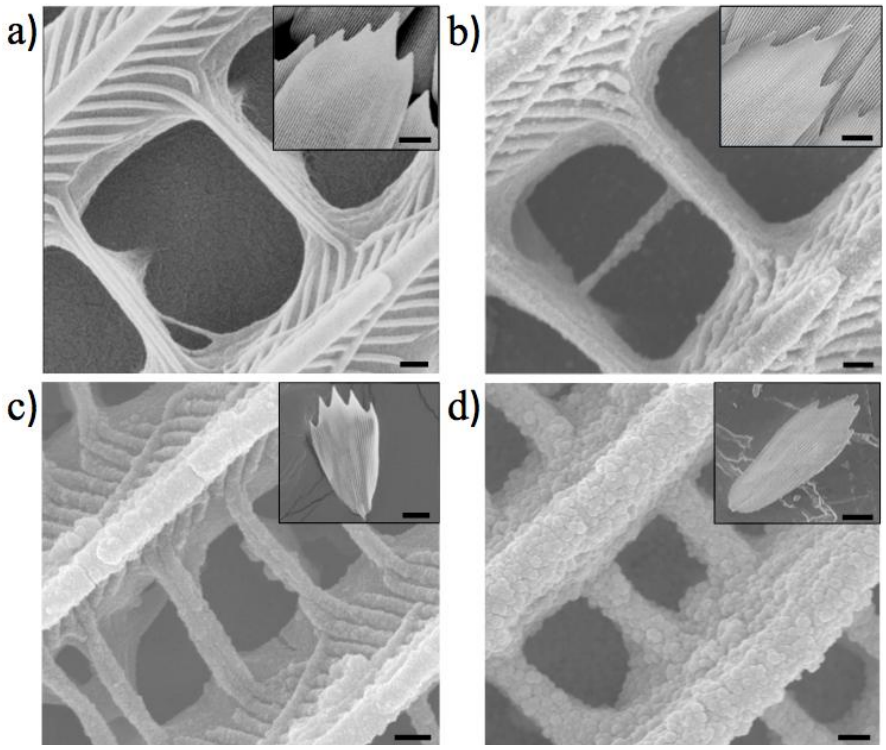

Figure 7: SE images of ventral female *Morpho helenor* wing scales (a) in native state, (b) after 51 SSG deposition cycles, (c) after organic pyrolysis of coated scales, and (d) a SSG coated and pyrolyzed scale after MWHT conversion into $BaTiO_3$. Insets are lower magnification images of the same scales. Scale bars represent 1 µm in primary images and 20 µm in insets.

In order to identify the elements present at each step of the chemical conversion process, EDS spectra (**Figure 8**) were taken on native, coated, pyrolyzed, and hydrothermally converted scales revealing a Ti peak after coating, a decreased N peak after pyrolysis (loss of 2-(acetylamino)-2-deoxy-D-glucose, the building block of chitin), and the presence of Ba and Ti after MWHT. It should be noted C, O, Au were present in all scans. Gold peaks were detected due to sputter coating with gold before determining conditions for SEM able to image uncoated samples. Samples were mounted on carbon tape and may have contained carbon (e.g., native scales). All samples were expected to contain oxygen.

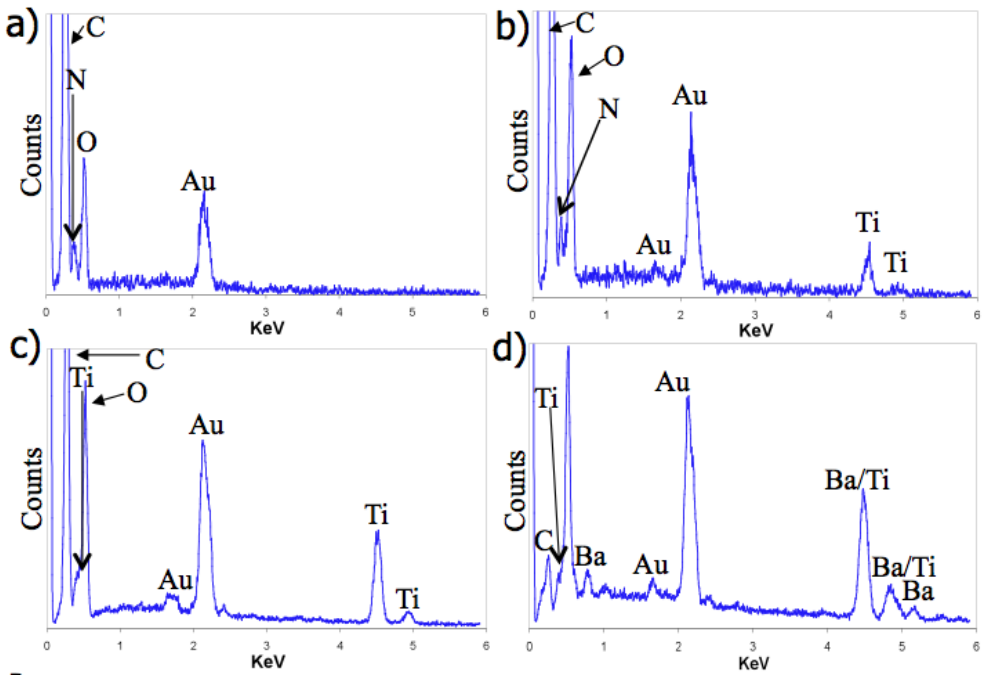

Figure 8: EDS of (a) a native scale, (b) a native scale after 51 SSG Ti-O bearing coating cycles, (c) a SSG-coated scale after organic pyrolysis, and (d) an inorganic scale replica after MWHT conversion into $BaTiO_3$. Note: all samples sputtered with Au for 60 sec.

After coating scales with 51 SSG deposition cycles TEM/SAED of FIB cross-sections (**Figure 9a,b**) revealed the coating and underlying chitinous material was amorphous. All TEM analyses were conducted on FIB cross-sections cut from a single ridge of a butterfly scale. Trenches were milled on either side of a ridge and sputtered platinum was used to attach a micromanipulator to the exposed ridge cross-section which was then thinned via ion milling and transported to a TEM grid with the micromanipulator. SE images of a representative FIB-milled trench and resulting cross-section are shown in **Figure 10a,b**. The corresponding bright field TEM image of and SAED pattern from the coated scale are shown in **Figure 10c,d**. The SAED diffraction pattern (**Figure 9d**) of a FIB cross-section cut from a coated and pyrolyzed scale was consistent with anatase titania[28]. A bright field TEM image (**Figure 9c**) and HRTEM lattice fringe image (**Figure 11a**) indicated the pyrolyzed material was nanocrystalline

with atomic plane spacings of 0.352 nm and 0.243 nm consistent with the (101) and (103) interplanar spacings of anatase titania, respectively. After organic pyrolysis the Raman spectrum peaks shown in **Figure 12** were also consistent with that of anatase titania. After MWHT reaction, high resolution SEM imaging (**Figure 13b**), TEM/SAED analyses (**Figure 9e,f**) as well as lattice fringe images obtained from FIB cross-sections of an individual ridge (**Figure 11b**) indicated the titania had been converted into nanocrystalline $BaTiO_3$. The bright field TEM image shown in **Figure 9e** revealed crystallite sizes between 30 nm and 100 nm which are similar to the particle sizes observed in SEM images (**Figure 7d**, **Figure 13b**). SAED diffraction patterns were consistent with $BaTiO_3$ (**Figure 9f**) and HRTEM (**Figure 11b**) revealed an interplanar spacing of 0.283 nm consistent with the (110) spacing of $BaTiO_3$. All peaks in Raman spectrum of $BaTiO_3$ butterfly scales (**Figure 12**) are consistent with $BaTiO_3$[29]. The tetragonal nature of the $BaTiO_3$ is identified by the presence of two Raman active modes, i.e., peaks centered at about 304 and 720 cm^{-1} (**Figure 12**) that have been reported to be lost upon heating above the $BaTiO_3$ curie temperature (i.e., transform from tetragonal to cubic $BaTiO_3$)[29].

To interrogate the internal structure of the specimens at each stage in the conversion process, FIB milling was used to cut trenches within individual scales. The 3D morphologies of native, coated, pyrolyzed, and hydrothermally converted scales are shown in **Figure 14**. Each stage in the chemical conversion process reveals similar internal morphologies with vertical struts supporting ridge and horizontal strut structure. To ensure such 3D replication was uniform, sequential FIB cuts were made. **Figure 15** contains SE images of sequential FIB cuts after each step in the chemical conversion.

Each row is a distinct conversion step and each column represents a sequential cut into the structure. Such sequential cuts (**Figure 15**) revealed a relatively consistent internal 3D morphology throughout each scale. Another goal of such cuts was to determine the internal structure within a single strut or ridge. Determination of the internal structure within a particular strut or ridge was not possible either due to specimen-beam interactions or the resolution obtainable with samples not sputtered with Au or carbon.

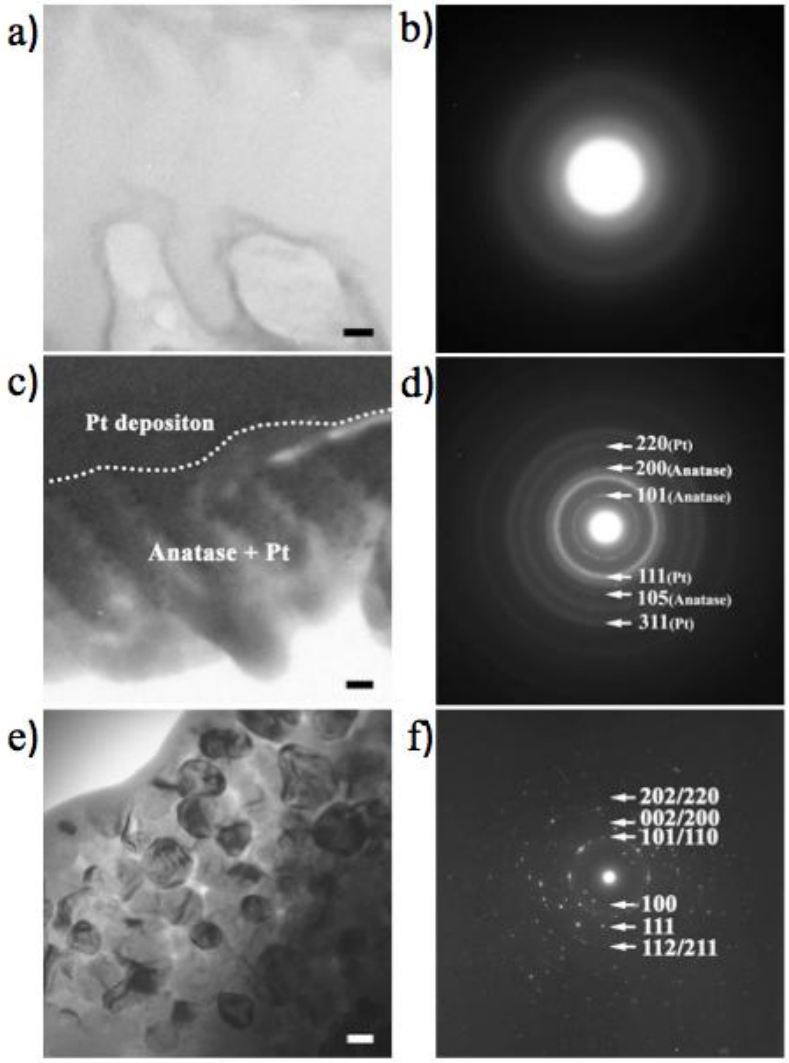

Figure 9: Bright field TEM micrographs (left column) and corresponding SAED patterns (right column) showing (a,b) amorphous chitin coated with 51 layers of amorphous Ti-O containing SSG layers, (c,d) nanocrystalline anatase titania after organic pyrolysis, and (e,f) larger nanocrystalline $BaTiO_3$ after MWHT conversion of coated and pyrolyzed replica. All micrograph scale bars represent 50 nm.

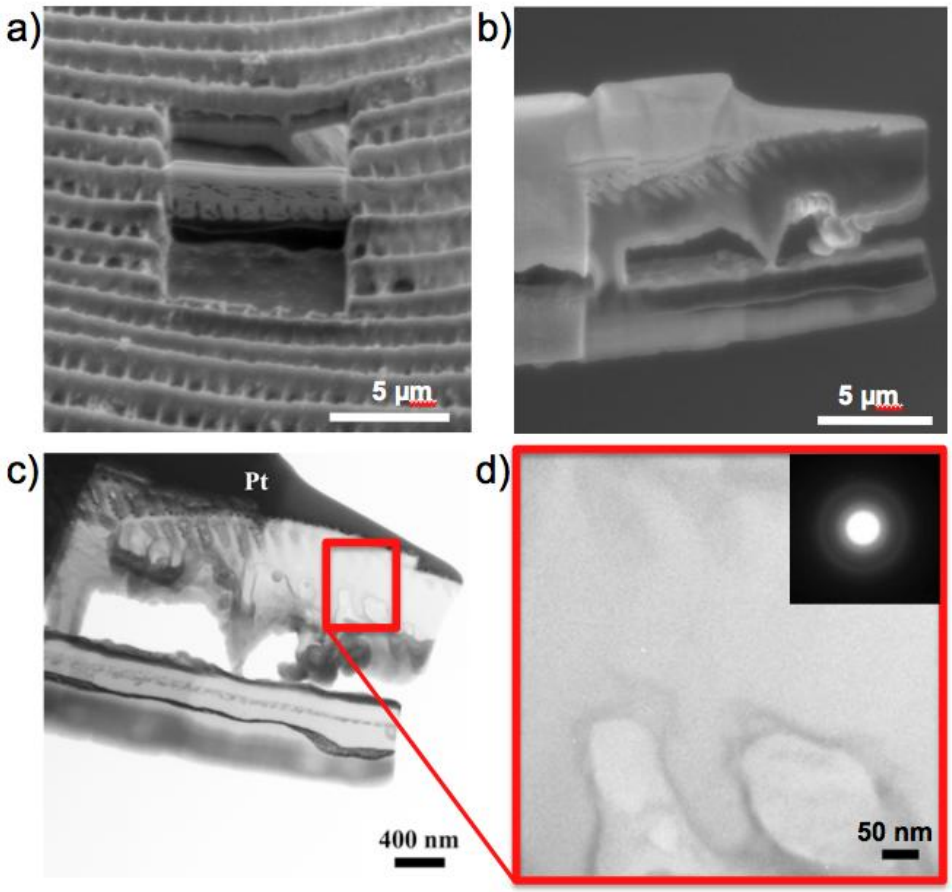

Figure 10: (a) A SE image of milled section (b) a SE image of sample Pt welded to micromanipulator needle on way to TEM grid, (c) low magnification TEM image after Pt deposition, mounting to micromanipulator needle and placing on TEM grid, (d) higher magnification TEM image, and corresponding SAED diffraction pattern (inset) from a Ti-O SSG coating.

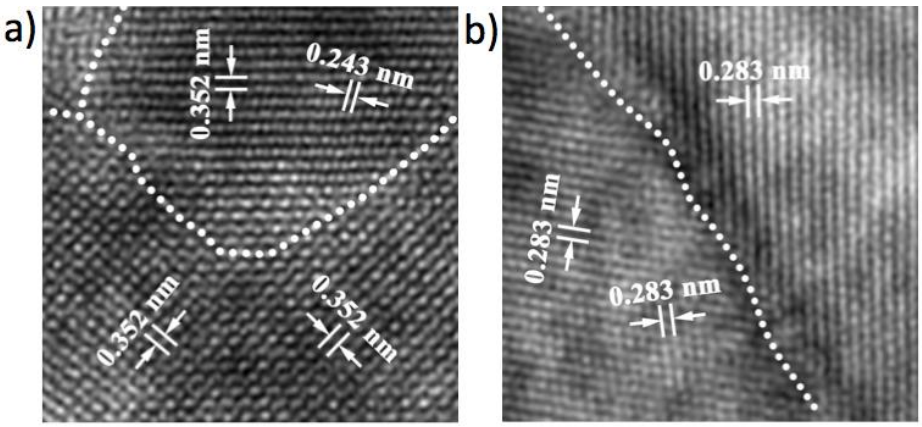

Figure 11: High resolution TEM images of FIB-milled cross-sections of (a) nanocrystalline anatase titania after coating with 51 SSG deposition cycles and being pyrolyzed at 450°C for 4 hr in air, and (b) $BaTiO_3$ grains after MWHT conversion of anatase titania scale replicas.

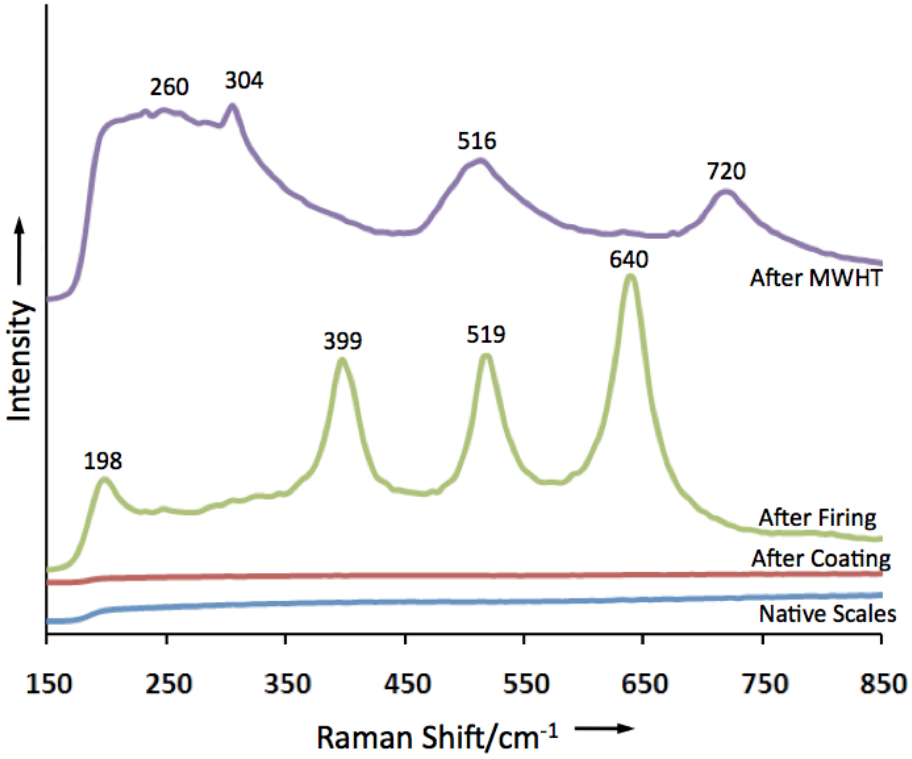

Figure 12: Raman spectra obtained at each step in chemical conversion process of female *Morpho helenor* wing scales (i.e., spectrum from a native scale, after coating scales with 51 Ti-O SSG deposition cycles, after organic pyrolysis of coated scales, and a SSG-coated and pyrolyzed scale after MWHT conversion into $BaTiO_3$. The wavenumber value labeling each peak was determined by measured local maximum peak intensity.

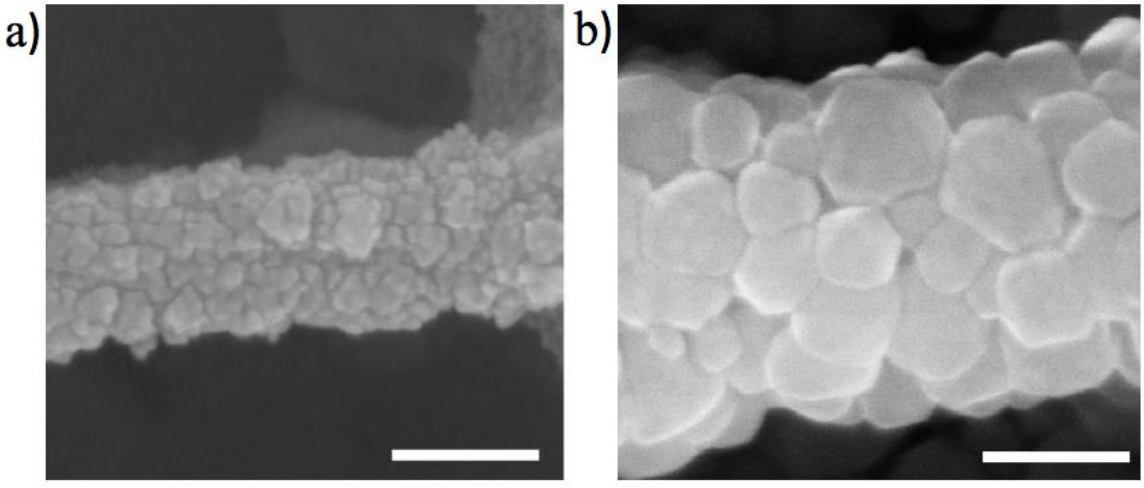

Figure 13: High magnification SE images of horizontal struts within a *M. helenor* butterfly scale after: (a) the conversion into nanocrystalline TiO_2 via exposure to 51 SSG deposition cycles and organic pyrolysis, and (b) after conversion via MWHT reaction of the TiO_2-converted scales into $BaTiO_3$. Both scale bars represent 100 nm.

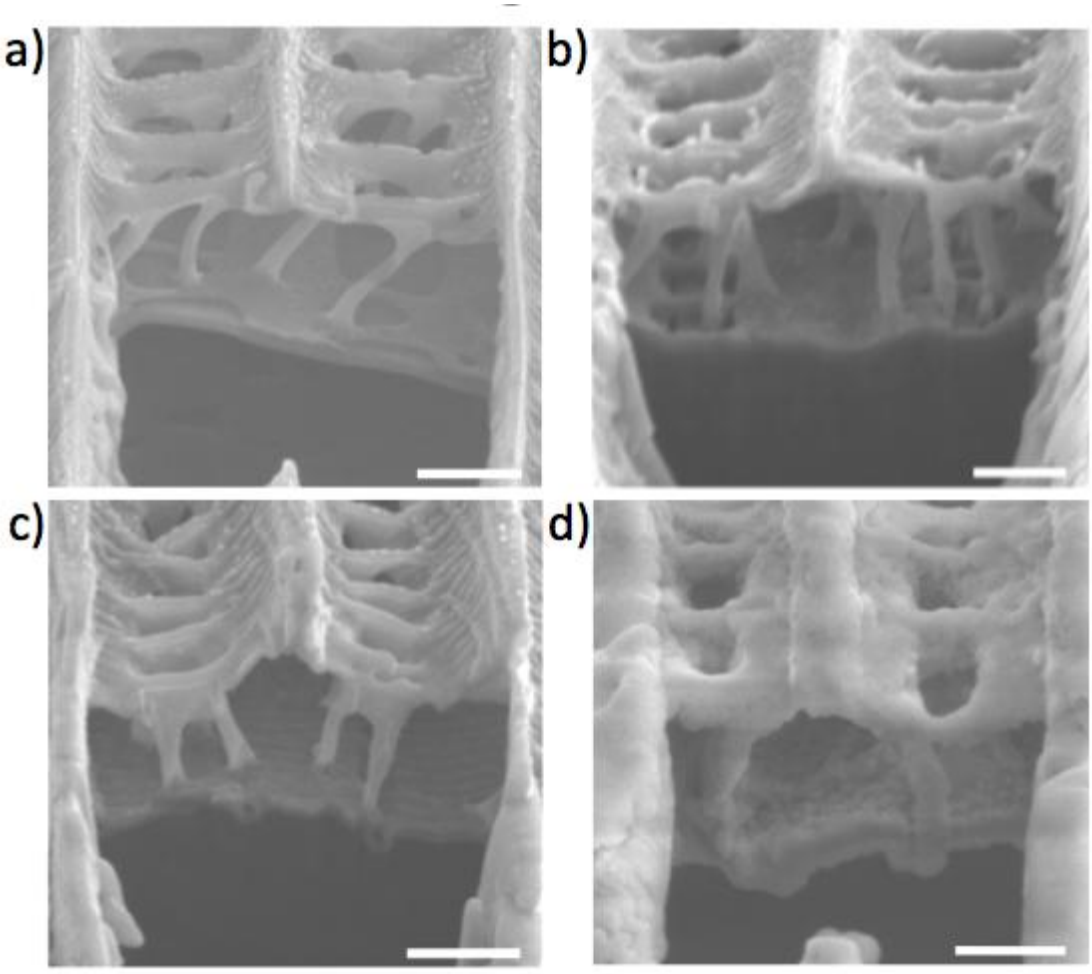

Figure 14: SE images of cross-sections of *M. helenor* ventral cover scales, after FIB milling of trenches, at various stages of conversion: a) a chitinous native scale, b) a native scale after 51 Ti-O SSG deposition cycles, c) a SSG coated scale after organic pyrolysis, and d) a SSG coated and pyrolyzed scale after MWHT conversion into $BaTiO_3$. All scale bars represent 1 µm.

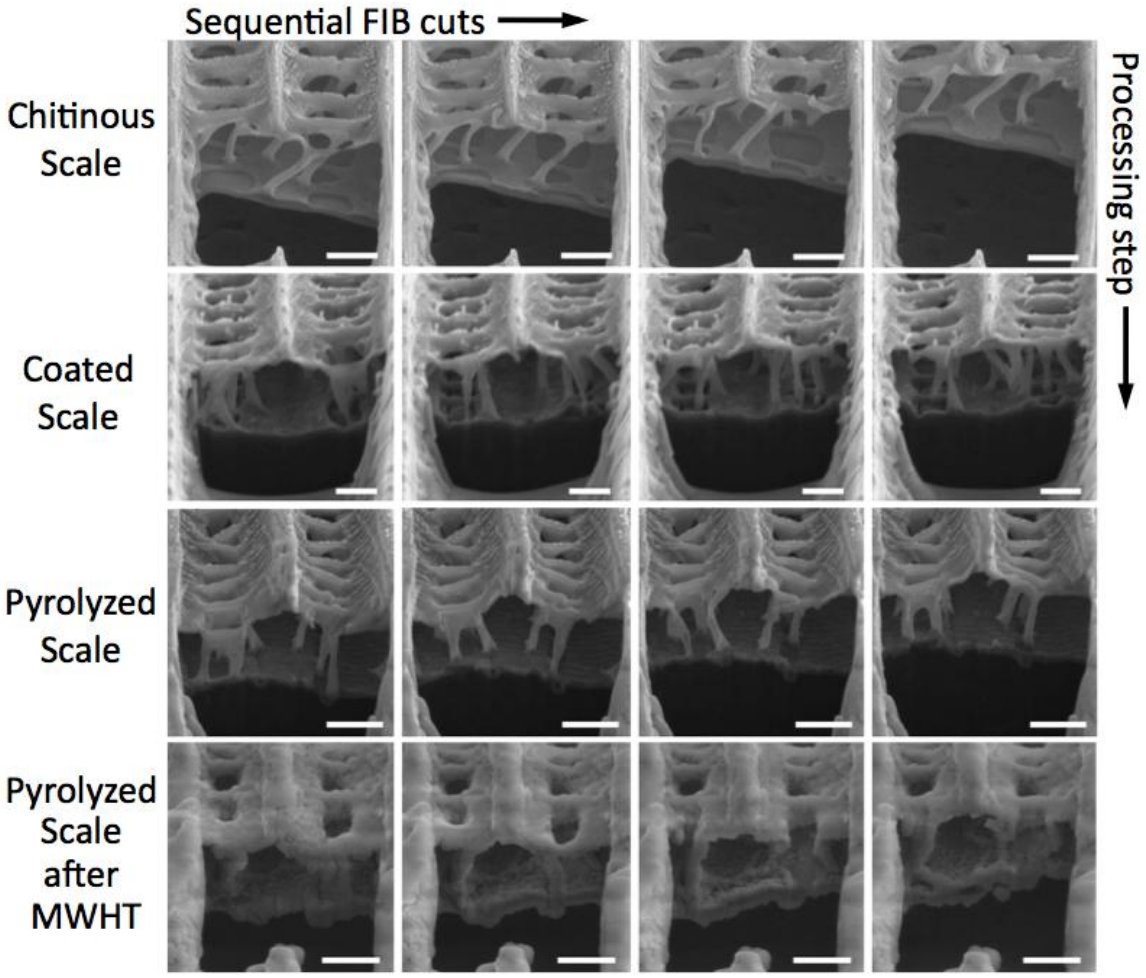

Figure 15: SE images of sequential FIB cuts at each step in the chemical conversion process from native scale (top row) to $BaTiO_3$ scale replica (bottom row). All scale bars represent 1 µm.

1.4.2. Dimensional change analyses and SSG/cuticle interaction

Despite the remarkable morphology retention throughout the chemical conversion process, certain dimensional changes seemed apparent at various stages which led to a quantitative investigation of the dimensional changes. Two dimensions were evaluated through measurements on SE images by performing 5 direct measurements on 15 different micrographs for a total of 75 independent values that were assumed to be normally distributed. The dimensions measured were strut width and ridge spacing and

are defined in **Figure 6b**. The calculated mean and the calculated standard deviation of each dimension throughout the conversion process are tabulated in **Table 1**.

Table 1: Dimensional Measurements at Each Stage of Conversion[a]

Process Step → Feature ↓	Chitinous Scales	After SSG Coating	After organic pyrolysis	After MWHT Treatment
Ridge Spacing (nm) [b]	2230 ± 140	2240 ± 120	1690 ± 120	1880 ± 200
Strut Width (nm)[b]	205 ± 30	270 ± 50	180 ± 30	360 ± 60

[a] Mean and standard deviation reported is based upon average of 75 independent measurements
[b] See Figure 6b for illustration of ridge spacing and strut width.

While the ridge spacing remained essentially unchanged upon application of SSG deposited coatings the average strut width increased by 65 nm. Such a thickness increase is indicative of a sub-nanometer per layer coating process (i.e.,32.5 nm/ 51 cycles or ~0.6nm/cycle). To determine whether or not the chitinous material was infiltrated like a porous material or if it acted as an impermeable solid, the chitinous template was removed through oxygen plasma etching after application of the 51 SSG cycles. SE images of fracture sections of a ridge and a vertical strut are shown in **Figure 16a,b**. The coated, chitin-free ridges and struts exhibited hollow cores. A hollow structure indicated the titanium(IV) isopropoxide did not penetrate considerably into the biotemplate during the coating process. Organic pyrolysis was used in the chemical conversion process to remove the chitinous template and crystallize the inorganic coating. **Figure 16c** also revealed hollow cores in the pyrolyzed state. The retention of the 3D scale morphology in template free inorganic structures, i.e., after removal of chitinous material through

thermal pyrolysis or oxygen plasma treatment, indicated the thin SSG coatings are continuous, highly interconnected, and rigid. After pyrolysis of the coated scales there was a noticeable decrease in the total scale thickness (**Figure 14c vs. b** and **Figure 15 row 2 vs. row 3**). Dimensional measurements (**Table 1**) indicated a significant decrease in strut width and ridge spacing depicted in **Figure 7c vs. b**. However, the shrinkage did not result in complete collapse of the hollow cores to form inorganic positive replicas after organic pyrolysis (**Figure 16c)**. After MWHT conversion of hollow titania structures there was noticeable increase in ridge spacing (**Table 1**; **Figure 7d vs. c**) and strut width **(Table 1; Figure 7d vs. c; Figure 13b vs. a; Figure 14d vs. c; Figure 15 row 4 vs. row 3**). Most interestingly, the hollow cores of the titania struts became largely filled in by $BaTiO_3$ (**Figure 16d vs. c**).

In hindsight, compensation for porosity, increased spacing and increased width dimensions upon conversion of anatase structures into $BaTiO_3$ should not be surprising after consideration of the molar volumes of the two phases. The molar volume of anatase titania and barium titanate are 20.5 and 38.8 cm^3/mol respectively as calculated utilizing International Center on Diffraction Data database Powder Diffraction File Card No. 00-021-1272 for anatase TiO_2 and Card No. 00-005-0626 for tetragonal $BaTiO_3$. Thus, titania coatings swelled when converted to $BaTiO_3$, which led to an increase in the minimum feature size retained through the MWHT conversion method. However, encouragingly, such expansion may reduce porosity of resulting perovskites. The retainment of such complex morphologies was clearly aided by the fluid reaction medium and was consistent with barium titanate formation largely on the surfaces of the titania reactant through either an “In-situ Transformation” or “dissolution-heterogeneous

precipitation" hydrothermal reaction mechanism reported by several authors[30,31,32]. Further investigation into the identification of the reaction mechanism(s) will be reported in **Chapter 3** of this document.

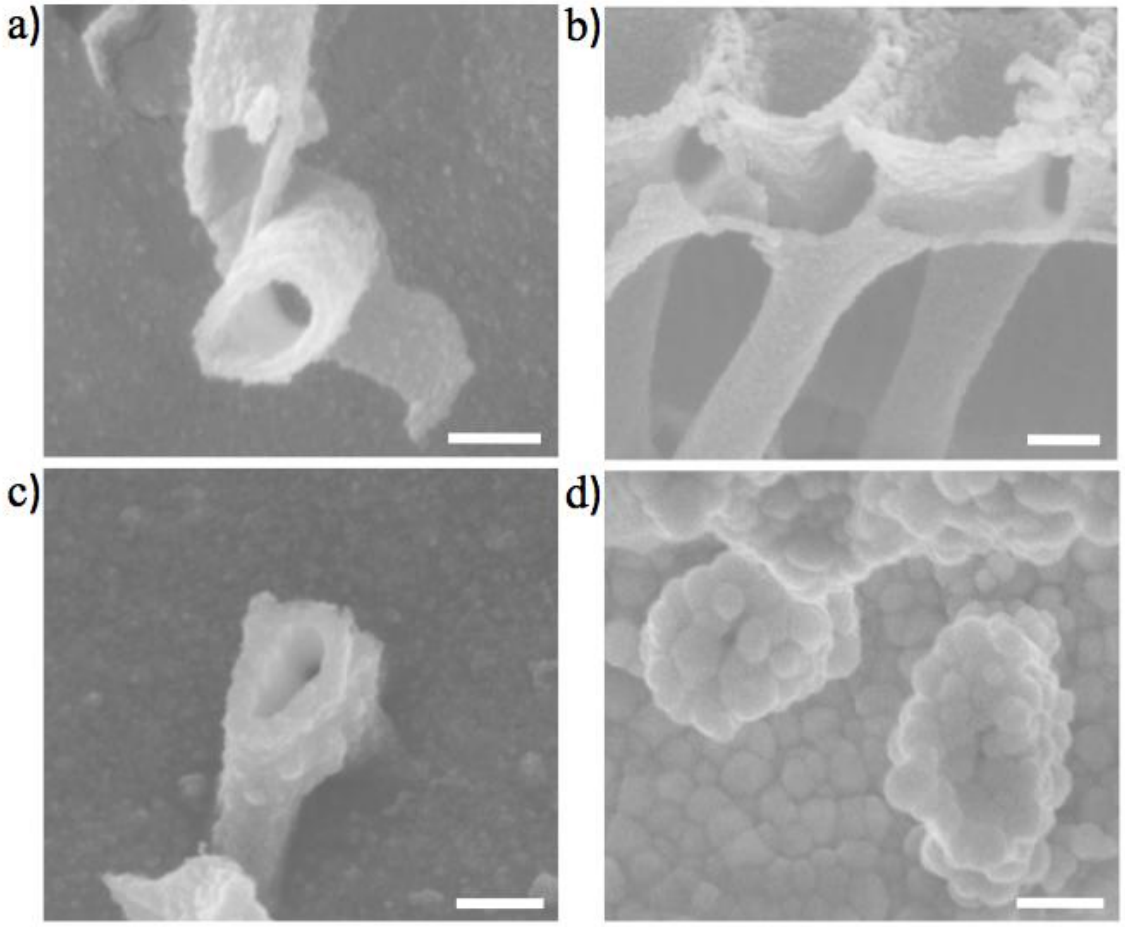

Figure 16: High magnification SE images of fracture sections of ridges and struts at various stages of the conversion process including: (a) a vertical strut and (b) a ridge after 51 cycles of SSG coating and then removal of the chitin by oxygen plasma treatment, (c) a nanocrystalline anatase TiO_2 vertical strut after SSG coating and organic pyrolysis. and (d) a nanocrystalline $BaTiO_3$ vertical strut after SSG coating, organic pyrolysis, and MWHT treatment. All scale bars represent 200 nm.

As expected from macroscopic observation of coated and pyrolyzed wing sections, micrograph measurements indicated statistically significant dimensional changes throughout the chemical conversion process (i.e., shrinkage occurred upon firing due to densification of the amorphous coatings and loss of the chitin template and

swelling attributed to molar volume expansion and particle growth.) Two-sample t-tests with unknown variance were used to compare the average strut widths. Although calculated degrees of freedom (ν) always exceeded 85, ν = 60 was used (biased test against calculating statistical differences). A 99% confidence level was used, which required a test statistic of $t_{\alpha/2,\nu = 60} = 2.606$ [33]. With a 99% confidence level it may be reported the coated strut width was at least 45 nm larger than the native strut width. The pyrolyzed strut width was at least 70 nm narrower than in the coated state, and after MWHT processing, the strut width was at least 160 nm larger than after pyrolysis. Phase ID through Raman spectroscopy and TEM analyses, along with energy dispersive spectroscopy, confirmed the identity, purity, and chemical composition of the phases on the micro and nanoscale. It should be noted without acetic acid washing of reacted barium titanate acicular barium carbonate $BaCO_3$ particles were present. Barium carbonate was formed upon exposure of the excess barium-bearing hydrothermal solution to ambient atmosphere. Although, similar MWHT conditions were used previously to convert titania powders into tetragonal barium titanate powders[34], such processing in combination with SSG has now produced nanocrystalline 3D structural retainment with precise understanding of the dimensional changes associated with the chemical conversion process.

1.4.3. Evaluating other potential combinations of SSG and MWHT

In order to eliminate or reduce molar volume expansion in converting titania replicas to $BaTiO_3$, two solutions were explored. The first solution was the application of coatings containing both barium and titanium oxides. The second solution was the application of fewer layers of titania. For solution one, microwave and conventional

heating was applied to powders formed by hydrolyzing either a stoichiometric mixture of barium/titanium isopropoxide or a molecular precursor, barium titanium ethylhexano isopropoxide. Within the MWHT crystallization/phase transformation experiments, reaction solutions containing combinations of passivating agents (e.g., oxalic acid, phosphate, citrate), buffer (phosphate-citrate, pH 7), and excess concentrations of Ba^{+2} were utilized to formulate alternative crystallization conditions, targeting the formation of tetragonal BT. Solution design was based upon the desire for a moderate pH range (i.e., 6-11) where a chitin template would not be damaged by hydrothermal synthesis conditions.

XRD patterns (**Figure 17a**) generated from both a stoichiometric mixture of isopropoxides (upper pattern) and a molecular precursor (lower pattern) after MWHT treatment at near neutral pH solution conditions were used to evaluate the alkoxide precursors. XRD analyses revealed mixed isopropoxide precipitates crystallized into cubic barium titanate readily whereas the molecular precursor did not. XRD data in **Figure 17b** revealed near-neutral treatment at 240°C, a temperature greater than what is required for tetragonal polymorph formation in caustic solutions, did not crystallize significant BT from the molecular precursor (lower pattern), and did not form tetragonal BT from a stoichiometric isopropoxide mixture (upper pattern). Upon hydrolysis of the molecular precursor, the water-insoluble alkane chain may also be incorporated into the precipitate. The alkane chain could then serve as an in-situ carbon source for the formation of $BaCO_3$. This explanation appeared plausible based upon data in **Figure 17b** which showed an increase in $BaCO_3$ content in the unwashed molecular precursor MWHT product (lower pattern) over that of the stoichiometric mixture MWHT product

(upper pattern). Such high levels of contamination and lack of $BaTiO_3$ formation led to elimination of the molecular precursor as a potential candidate for use in the SSG deposition of Ba-Ti-O- containing coatings.

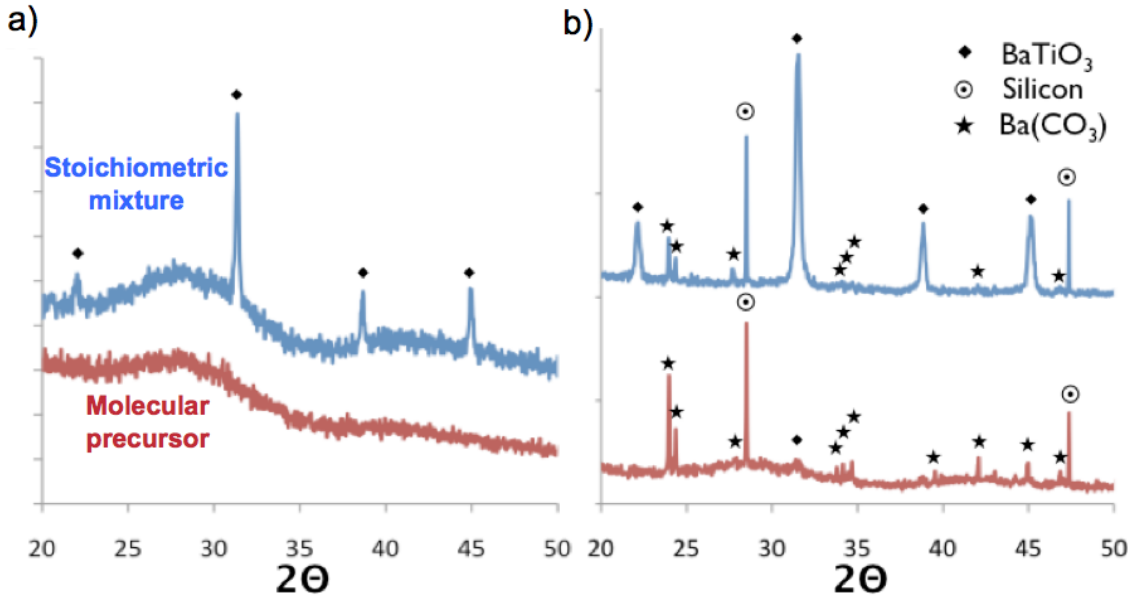

Figure 17: X-ray diffraction patterns of powder precipitated via hydrolysis of stoichiometric mixture of barium and titanium isopropoxide (top) and molecular precursor for $BaTiO_3$, barium titanium ethylhexano isopropoxide (bottom) after having undergone (a) MWHT treatments at 140°C for 2 hrs with 0.100 M phosphate/citrate buffer and (b) MWHT treatment at 240°C for 10 hrs with 0.5 M barium acetate. Silicon peaks in (b) are due to the use of internal NIST SRM 640c standard.

Although near-neutral conditions for the MWHT crystallization of cubic $BaTiO_3$ were found, even a treatment at 240°C for 10 hrs was unable to produce significant tetragonality. However, 220°C MWHT synthesis of Ba-Ti-O- containing precipitates with 1 M NaOH produced tetragonal $BaTiO_3$ from both molecular and stoichiometric precursors within 8 hr. **Figure 18** contains XRD data from the caustically treated stoichiometric mixture precipitates, including an inset showing the significant peak splitting indicative of tetragonal $BaTiO_3$. Precipitates from stoichiometric mixture precursors were also subjected to HTXRD to examine conventional heat treatment temperatures required to form the tetragonal polymorph. The resulting HTXRD data

(shown **Figure 19**) revealed a considerable amount of cubic barium titanate was formed at room temperature. Additionally, heating to 700°C for 2 hr did not produce significant (detectable by XRD) tetragonal content in the $BaTiO_3$. Alternatively, the tetragonality may not detectable by XRD due the peak broadening inherent in nanocrystalline powders.

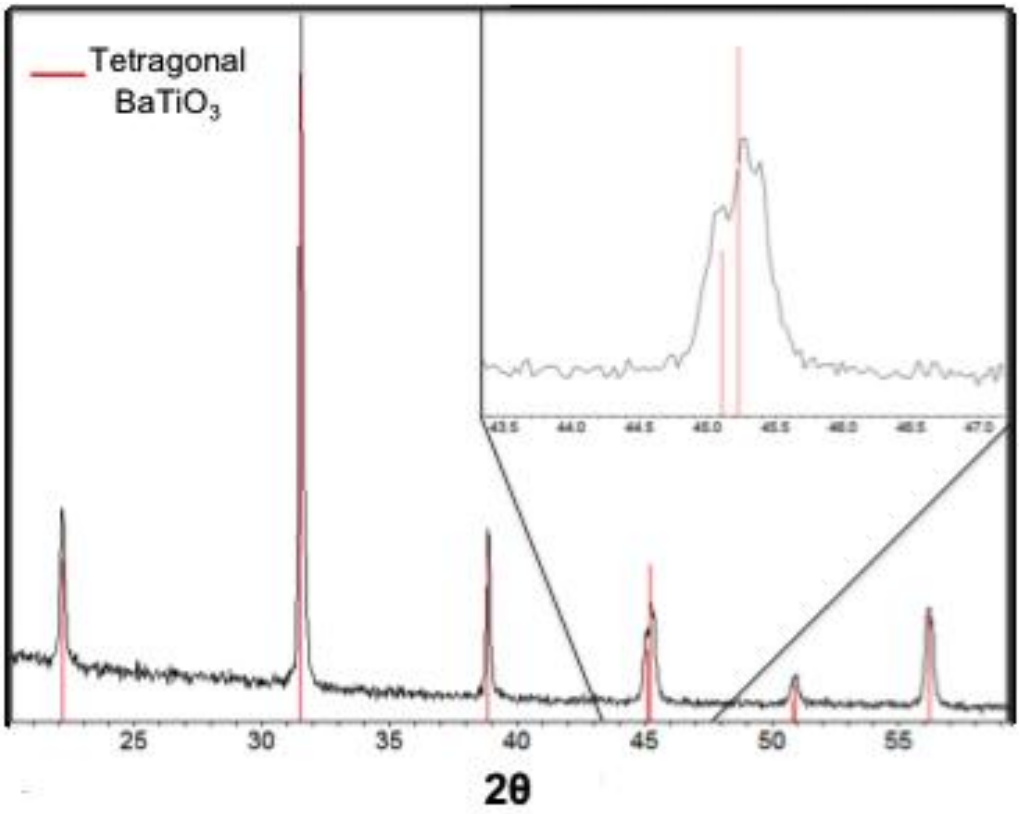

Figure 18: X-ray diffraction patterns of powder precipitated via hydrolysis of stoichiometric mixture of barium and titanium isopropoxide after having undergone MWHT treatment at 220°C for 8 hrs in 20 mL of 1 M barium hydroxide. The inset reveals the emergence of peak splitting at the (200)/(002) peak, which is indicative of the tetragonal polymorph of BT.

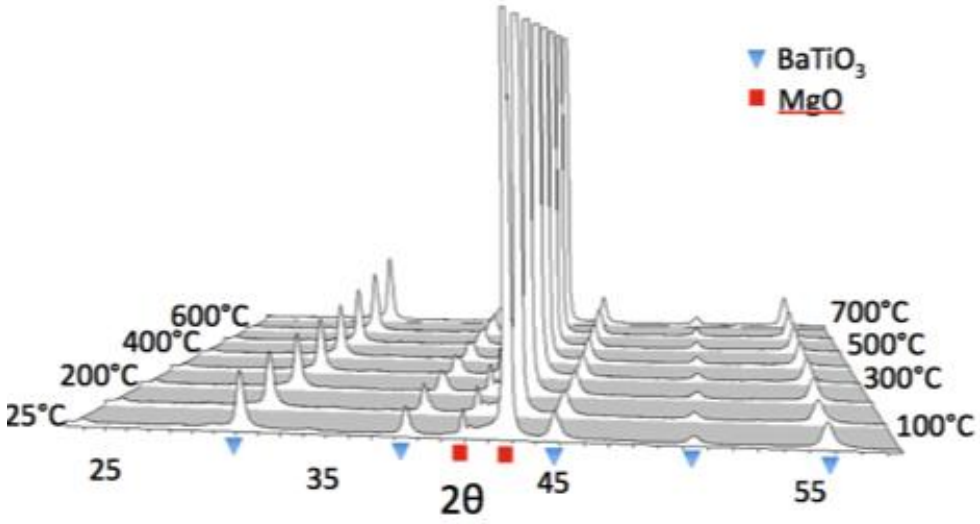

Figure 19: HTXRD data obtained at room temperature (first scan) and then 70 °C (rest of scans), after increasing heat treatments temperatures (2 hrs at each 100 °C increment) of stoichiometric mixture precipitates.

The first attempt to apply coatings containing both Ba and Ti was performed by applying 50 SSG layers of a stoichiometric mixture alkoxide solution containing barium(II) isopropoxide and titanium(IV) isopropoxide rather than just Ti(IV) isopropoxide (see **Section 1.3.3**). Coatings were applied to butterfly scales as illustrated schematically in **Figure 20**. Initial XRD and SEM characterization (**Figure 21**) revealed significant barium carbonate formation from one of the following sources: carbon dioxide in the water used to hydrolyze the coatings, carbon dioxide in the glove box atmosphere, or exposure to ambient atmosphere before characterization. **Figure 21** also shows the effectiveness of acetic acid washings in removing barium carbonate, and confirms $BaCO_3$ adopts an acicular morphology. However, use of acetic acid washes before firing or MWHT processing would require excess Ba^{2+} in MWHT solution as a result of the depletion of barium in the coating caused by removal of barium carbonate. Heat treatment of the Ba-Ti-O- coated scales without acetic acid washing was expected to

form $BaTiO_3$ because typical synthesis of $BaTiO_3$ entails comminution of barium carbonate and titania powders followed by solid-state reaction above 800°C. Treatment at 900°C for 1 hr (after typical slow ramp (0.5°C/min) and hold for 4 hr at 450°C for template removal) resulted in little overall structural retention and grain growth in the few areas exhibiting structural retainment as shown in **Figure 22**..

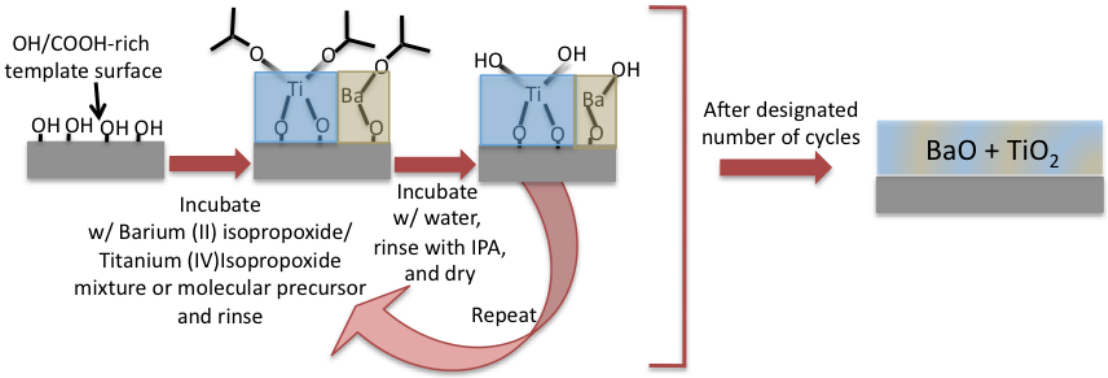

Figure 20: A schematic of the mixed alkoxide SSG deposition technique used to apply Ba-Ti-O-bearing coatings.

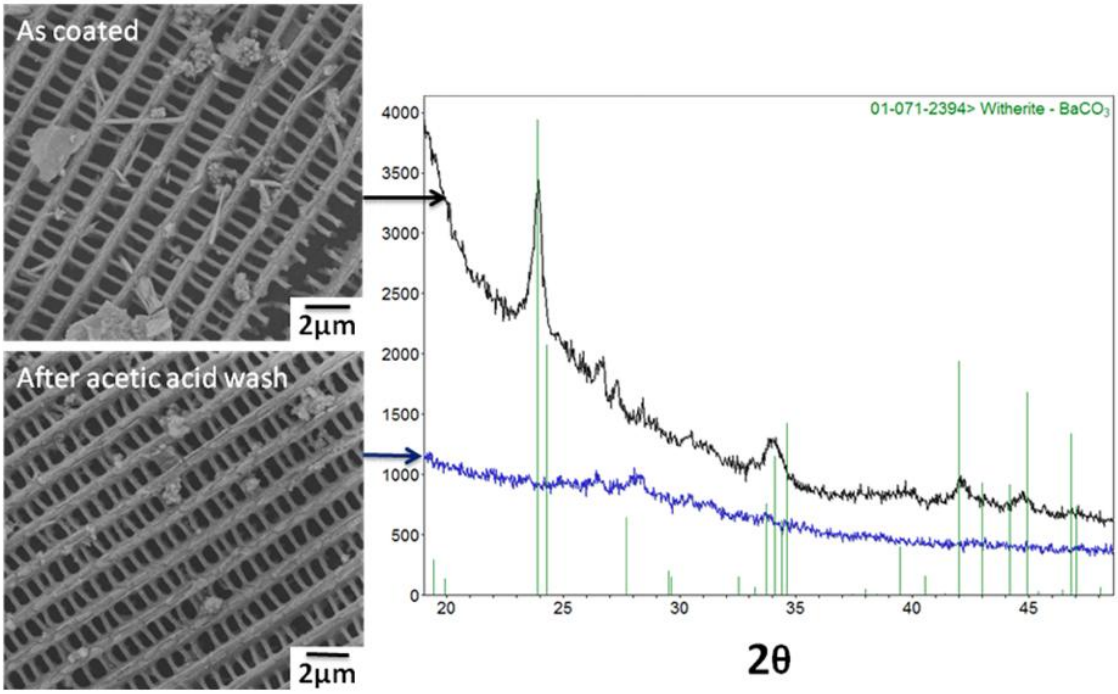

Figure 21: SEM micrographs (left) of *M. helenor* ventral cover scales coated with 50 layers of 10 mM stoichiometric mixture of barium and titanium isopropoxides showing conformal coating and

acicular barium carbonate before (top) and conformal coating after acetic acid washing (bottom). XRD (right) confirms the removal of barium carbonate (stick plot overlay) via acetic acid wash.

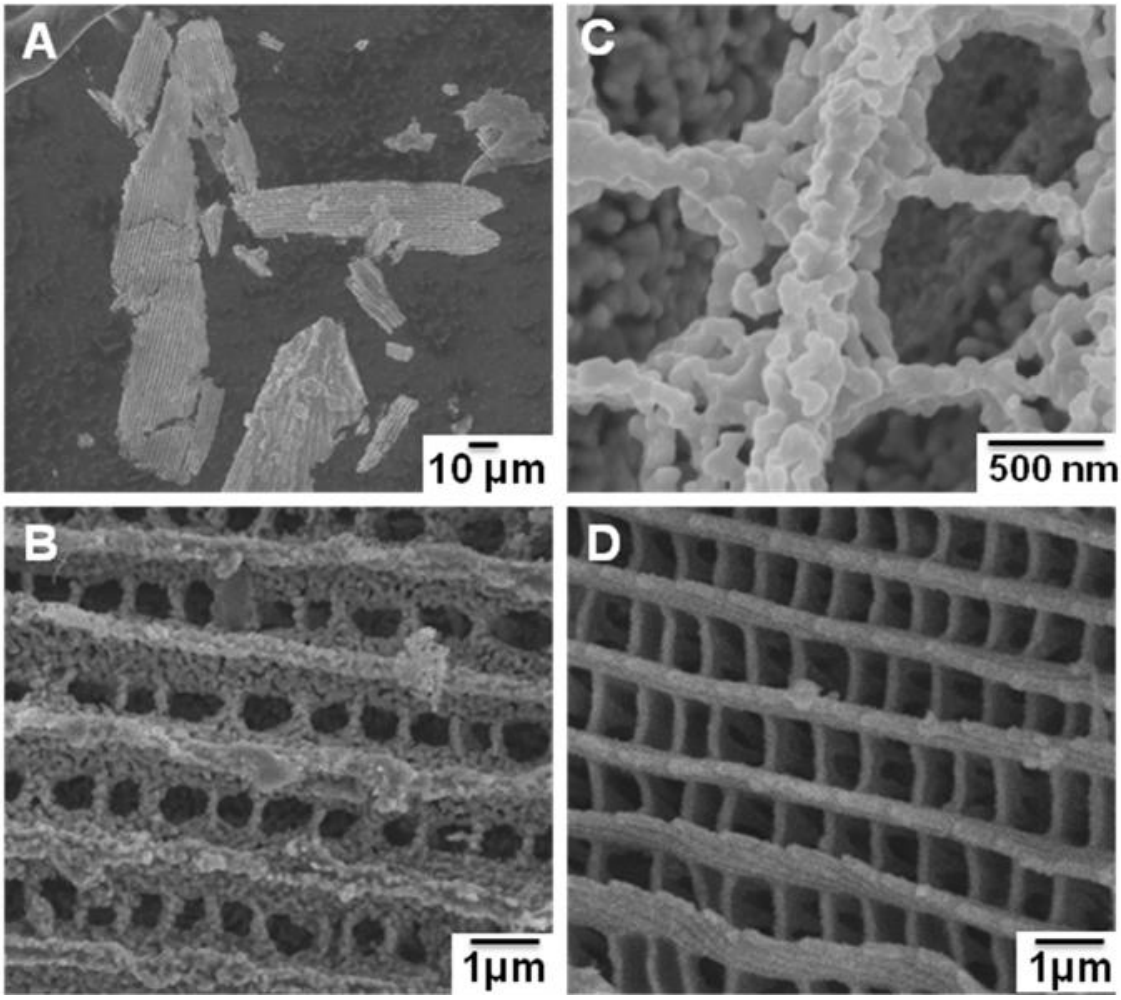

Figure 22: SE images of *M. helenor* ventral cover scales butterfly scales coated with 50 layers of 10 mM barium titanium isopropoxide and fired at 900°C for 1 hr (A,B,C) and 450°C for 4 hr (D). Direct comparison of B and D demonstrates the Ostwald ripening that occurs upon exposure to higher temperature.

XRD analyses of the resulting structures after 1 hr at 900°C did not reveal phase pure barium titanate. XRD also revealed no barium carbonate or barium sulfate phases were present (EDS analyses confirmed the presence of Ba, Sr, Ti, O, C, and S). Most of the peaks not associated with $BaTiO_3$ appeared to correspond to one of two different titanium rich, barium titanium oxide stoichiometries: $Ba_4Ti_{13}O_{30}$ or $Ba_2Ti_9O_{20}$. Thus, either the coating composition was not the same as the solution composition, or the

intermediate formation of barium carbonate caused irreparable composition damage. In addition to $BaCO_3$ complications, only fired samples showed any hint of microstructural retainment after MWHT treatment, meaning that preloading the coatings with barium to decrease the effects of molar volume expansion may also decrease the overall robustness during and after MWHT processing. A decrease in final replica wall thickness is the most likely cause for the yield of replicas to be substantially reduced from that of converting titania coatings. Clearly some processing adjustments need to be made to avoid formation of barium carbonate, and thicker coatings need to be applied if coatings contain all of the elements required to synthesize the desired product.

To fully capitalize on the benefits of SSG, another way to control stoichiometry would be through application of individual oxide layers as illustrated in **Figure 23**. Controlling stoichiometry through stoichiometric layering would also allow the use an outer TiO_2 layer to potentially protect barium layers from the atmosphere in preparation for firing or transporting for characterization. Removing any potential CO_2 in the glovebox could be achieved by adding CO_2 getters on the source N_2 and at the exhaust of the automated surface sol-gel pump system as well as boiling water used in the hydrolysis solution. Although other piezoelectric materials have constituents that do not have the difficulties associated with barium, understanding the best way to apply multicomponent oxides (i.e., layer-by-layer of individual alkoxides, or through mixed alkoxide precursors) through SSG is an interesting future avenue of research.

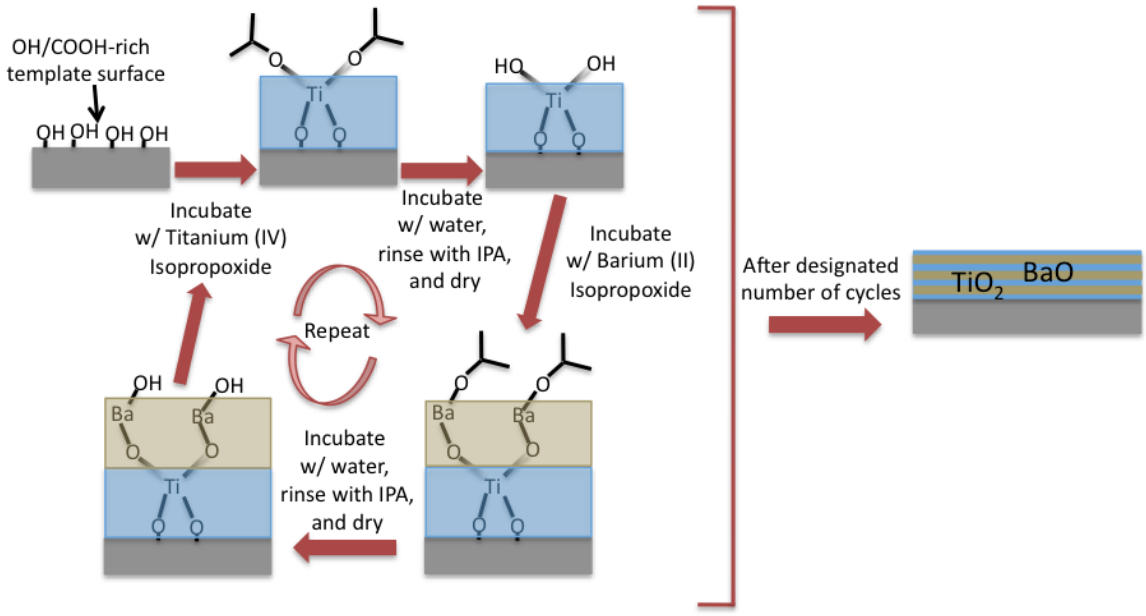

Figure 23: A schematic of a layered alkoxide approach to SSG deposition in which the stoichiometry is controlled by the number of Ti-O and Ba-O bearing layers.

To address the second solution for reducing effects of volume expansion in conversion of titania coatings, 25 layers of SSG titania were applied to *Morpho helenor* butterfly scales. The procedure was identical to that of the SSG procedure used for 51 layers of titania detailed in **Section 1.3.3**. Although successful in coating with titania, and retaining structure after firing, these thin coatings produced no $BaTiO_3$ scale replicas after microwave hydrothermal treatment. It appeared that 25 SSG layers was below the lower limit of the possible coating thickness to produce self-supporting replicas after undergoing MWHT processing.

1.5. *Concluding Remarks*

Multicomponent oxide compound (tetragonal $BaTiO_3$) structures formed from 3D bioorganic templates were produced through the combined use of a conformal coating (SSG) process and a modest temperature microwave hydrothermal reaction process.

Such an approach may be applied to other bioorganic templates, or to synthetic organic templates, provided such templates possess (or can be functionalized to possess) a high surface coverage of hydroxy groups for SSG processing. Self-supporting replicas after oxygen plasma treatment and after organic pyrolysis demonstrated highly-interconnected inorganic coatings were applied. Also, the interaction of SSG processing with a chitinous biotemplate was investigated which revealed the cuticle of Lepidopterans generally (confirmed with multiple species, see **Chapter 4**) acts as a solid template rather than a permeable solid. Additionally, dimensional changes throughout the chemical conversion process were quantified, revealing shrinkage occurred upon organic pyrolysis and swelling occurred during MWHT reaction. Titania coatings swelled when converted to $BaTiO_3$, which led to an increase in the minimum feature size retained through the MWHT conversion method. Although the dimensional changes may not be surprising, the ability to preserve 3D morphology throughout the entire process was remarkable to the author.

Alternative coating methodologies were explored to enhance structural retainment and directly apply multicomponent coatings. The two proposed solutions for minimizing retained feature size were evaluated, and revealed that (i) only reaction systems where templates can be retained or have a more mechanically robust structure would readily allow for thinner coatings to be applied and converted, and (ii) paraelectric BT may readily be obtained from stoichiometric alkoxide mixtures at room temperature, which will transition into ferroelectric BT under similar MWHT conditions used for conversion of titania to ferroelectric barium titanate, and (iii) initial attempts to utilize mixed alkoxide and molecular precursor SSG coating methodologies **(Figure 20**) were

ineffective for applying stoichiometric $BaTiO_3$ coatings. Future research should focus on individual oxide layering through SSG deposition of coatings for the formation of multicomponent oxide coatings. Material systems like PZT, which only require near-neutral pH MWHT processing conditions for transformation/crystallization[35], should become the focus for forming inorganic/organic composites. Given the ubiquitous number of elements available in commercial alkoxides that may be used for sol–gel processing and the capability for low-temperature hydrothermal reaction to transform monolithic and multicomponent coatings into numerous crystalline ceramic compounds[18], this morphology-preserving process may be used to convert a variety of (bio)organic templates into functional multicomponent ceramic materials (and potentially inorganic/organic composites) with a wide variety of 3D morphologies, compositions, and properties.

1.6. *References*

[1] B. Steele and A. Heinzel, "Materials for fuel-cell technologies," *Nature*, vol. 414, pp. 345-352, 2001.

[2] B. T. Holland, "Synthesis of Macroporous Minerals with Highly Ordered Three-Dimensional Arrays of Spheroidal Voids," *Science*, vol. 281, pp. 538-540, 1998.

[3] A. Linsebigler, G. Lu, and J. Yates, "Photocatalysis on TiO_2 Surfaces: Principles, Mechanisms, and Selected Results," *Chemical Reviews*, vol. 95, pp. 735-758, 1995.

[4] M. Gratzel, "Photoelectrochemical cells," *Nature*, vol. 414, pp. 338-344, 2001.

[5] I.-D. Kim, A. Rothschild, B. Lee, D. Kim, S. Jo, and H. Tuller, "Ultrasensitive Chemiresistors Based on Electrospun TiO_2 Nanofibers," *Nano Letters*, vol. 6, pp. 2009-2013, 2006.

[6] C. López, "Materials Aspects of Photonic Crystals," *Advanced Materials*, vol. 15, pp. 1679-1704, 2003.

[7] P. Banerjee, I. Perez, L. Henn-Lecordier, S. Lee, and G. Rubloff, "Nanotubular metal–insulator–metal capacitor arrays for energy storage," *Nature Nanotech*, pp. 1-6, Mar 15 (2009)

[8] M. J. Zipparo, K. K. Shung, and T. R. Shrout, "Piezoceramics for high-frequency (20 to 100 MHz) single-element imaging transducers," *Ultrasonics, Ferroelectrics and Frequency Control, IEEE Transactions on*, vol. 44, pp. 1038-1048, (1997).

[9] S. Priya, "Advances in energy harvesting using low profile piezoelectric transducers," *Journal of Electroceramics*, vol. 19, pp. 167-184, (2007).

[10] G. R. Lockwood, D. H. Turnball, D. A. Christopher, and F. S. Foster, "Beyond 30 MHz [applications of high-frequency ultrasound imaging]," *Engineering in Medicine and Biology Magazine, IEEE*, vol. 15, pp. 60-71, (1996).

[11] J. Silver, R. Withnall, T. G. Ireland, and G. R. Fern, "Novel nano-structured phosphor materials cast from natural Morpho butterfly scales," *Journal of Modern Optics*, vol. 52, pp. 999-1007, 2005.

[12] R. Schwartz, T. Schneller, and R. Waser, "Chemical solution deposition of electronic oxide films," *Comptes Rendus Chimie*, vol. 7, pp. 433-461, 2004

[13] S. Komarneni, I. Abothu, and A. Rao, "Sol-Gel Processing of Some Electroceramic Powders," *Journal of Sol-Gel Science and Technology*, vol. 15, pp. 263-270, 1999.

[14] Michael R. Weatherspoon, Y. Cai, M. Crne, M. Srinivasarao, and K.H. Sandhage, "3D Rutile Titania-Based Structures with Morpho Butterfly Wing Scale Morphologies," *Angewandte Chemie*, vol. 120, pp. 8039-8041, 2008.

[15] M. R. Weatherspoon, M. B. Dickerson, G. Wang, Y. Cai, S. Shian, S. C. Jones, S. R. Marder, and K. H. Sandhage, "Thin, Conformal, and Continuous SnO2 Coatings on Three-Dimensional Biosilica Templates through Hydroxy-Group Amplification and Layer-By-Layer Alkoxide Deposition," *Angewandte Chemie International Edition*, vol. 46, pp. 5724-5727, 2007.

[16] I. Ichinose, H. Senzu, and T. Kunitake, "Stepwise Adsorption of Metal Alkoxides on Hydrolyzed Surfaces: A Surface Sol-Gel Process," *Chemistry Letters*, pp. 831-832, 1996.

[17] I. Ichinose, H. Senzu, and T. Kunitake, "A Surface Sol-Gel Process of TiO2 and Other Metal Oxide Films with Molecular Precision," *Chemistry of Materials*, vol. 9, pp. 1296-1298, 1997.

[18] S. Komarneni, Q. Li, K. Stefansson, and R. Roy, "Microwave-hydrothermal processing for synthesis of electroceramic powders," *Journal of Materials Research*, vol. 8, pp. 3176-3183, 1993.

[19] Y. Ma, E. Vileno, S. Suib, and P. Dutta, "Synthesis of Tetragonal $BaTiO_3$ by Microwave Heating and Conventional Heating," *Chemistry of Materials*, vol. 9, pp. 3023-3031, 1997.

[20] M. Srinivasarao, Nano-optics in the Biological World: Beetles, Butterflies, Birds and Moths," *Chemical Reviews*, vol. 99, pp. 1935-1962, 1999.

[21] P. Vukusic, and R. Sambles, "Photonic Structures in Biology," *Nature*, vol. 424, pp. 852-855, 2002.

[22] A. Testino, V. Buscaglia, M. Buscaglia, M. Viviani, and P. Nanni, "Kinetic Modeling of Aqueous and Hydrothermal Synthesis of Barium Titanate ($BaTiO_3$)," *Chemistry of Materials*, vol. 17, pp. 5346-5356, 2005.

[23] B. Newalkar, "Microwave-hydrothermal synthesis and characterization of barium titanate powders," *Materials Research Bulletin*, vol. 36, pp. 2347-2355, 2001.

[24] D. Hennings, "Barium titanate based ceramic materials for dielectric use," *International Journal of High Technology Ceramics*, vol. 3, pp. 91-111, 1987.

[25] G. Haertling, "Ferroelectric Ceramics: History and Technology," *Journal of the American Ceramic Society*, vol. 82, pp. 797-818, 1999.

[26] J. Li, and M. Kuwabara. Preparation and luminescent properties Eu-doped $BaTiO_3$ Thin Films by sol-gel process," *Science and Technology of Advanced Materials*, vol. 4, pp. 143 – 148, 2003.

[27] H. Abdelkefi, H. Khemakhem, G. Velu, J. Carru, and R. Vondermuhll, "Dielectric properties and ferroelectric phase transitions in $Ba_xSr_{(1-x)}TiO_3$ solid solution," *Journal of Alloys and Compounds*, vol. 399, pp. 1-6, 2005.

[28]U. Balachandran, and N.G. Eror, " Raman Spectra of Titanium Dioxide," *Journal of Solid State Chemistry*, vol 42., pp. 276-282, 1982.

[29] C.H. Perry, and D.B. Hall, "Temperature Dependence of the Raman Spectrum of $BaTiO_3$," *Physical Review Letters*, vol. 1,. pp. 700-702, 1965.

[30] W. Hertl, "Kinetics of Barium Titanate Synthesis," *Journal of the American Ceramic Society*, vol. 71, pp. 879-883, 1988.

[31] J. Eckert, C. Hung-Houston, B. Gersten, M. Lencka, and R. Riman, "Kinetics and Mechanisms of Hydrothermal Synthesis of Barium Titanate," *Journal of the American Ceramic Society*, vol. 79, pp. 2929-2939, 1996.

[32] B. Gersten, "Growth of multicomponent perovskite oxide crystals: Synthesis conditions for the hydrothermal growth of ferroelectric powders," in *Crystal Growth Technology*: Springer-Verlag, 2003, pp. 299-333.

[33] J.L. Devore, *Probability and Statistics for Engineering and the Sciences*, Brooks/Cole—Thomson Learning, Toronto, Ontario, 6th edition, 2004, pp. 372-376 and 743.

[34] W. Sun, W. Liu, and J. Li, "Effects of chloride ions on hydrothermal synthesis of tetragonal $BaTiO_3$ by microwave heating and conventional heating," *Powder Technology*, vol. 166, pp. 55-59, 2006.

[35] M. Lencka, A. Anderko, and R. Riman, "Hydrothermal Precipitation of Lead Zirconate Titanate Solid Solutions: Thermodynamic Modeling and Experimental Synthesis," *Journal of the American Ceramic Society*, vol. 78, pp. 2609-2618, 1995.

CHAPTER 2: Conversion of Complex Bioorganic Morphologies (*Papilio blumei* butterfly scales) into Lanthanoid-doped $BaTiO_3$ Inorganic Phosphor Particles

2.1. *Summary*

For the first time, morphology-preserving wet-chemical hydrothermal reactions have been combined with SSG coatings to completely convert complex-shaped 3D bioorganic templates into freestanding, photoluminescent multicomponent oxide microparticle replicas. The conversion process consisted of three general steps: (i) wet-chemical layer-by-layer surface sol-gel (SSG) deposition (to apply a thin, continuous, conformal single component oxide coating), (ii) organic pyrolysis (to selectively remove the bioorganic template), and (iii) hydrothermal reaction (to generate the desired nanocrystalline functional multicomponent oxide compound). This process was demonstrated by converting 3D macro/micro/nanostructured chitinous *Papilio blumei* butterfly scales into a red-emitting phosphor, europium-doped barium titanate (Eu-doped BT), by incorporating a lanthanoid element within the hydrothermal reaction step. Chitinous templates were also converted into erbium-doped barium titanate (Er-doped $BaTiO_3$), a green emitting phosphor, by incorporating erbium in the SSG deposition process. The hydrothermal reaction process was similar to that described in **Chapter 1**, but the hydrothermal reaction temperature was lower, as there was no need to create tetragonal $BaTiO_3$. Lanthanoid elements were included to impart photoluminescent properties (i.e., emission in the visible portion of the electromagnetic spectrum).

Development of coating methodologies, reaction conditions, and demonstration of anti-counterfeiting capability are detailed. The phase content and chemical composition

at each stage in the conversion process were tracked via XRD and qualitative energy dispersive elemental analyses, respectively. The fidelity of morphology conversion was evaluated through SE imaging of top view and FIB-milled cross-sections. The qualitative fluorescent intensity after each step of the conversion process proved the lanthanoid-modified replicas exhibited significantly enhanced photoluminescent intensity with respect to native, coated, coated and pyrolyzed, and $BaTiO_3$ scales. Incorporation of the resulting phosphor microparticles into/onto paper and subsequent bright field optical, dark field optical, and confocal fluorescent microscopy demonstrated a covert anti-counterfeiting capability.

2.2. *Introduction*

2.2.1. Motivation for Transforming 3D Bioorganic Templates into Inorganic Phosphor Replicas

The generation of nanostructured assemblies with i) complex 3D self-assembled morphologies and ii) tailorable multicomponent inorganic compositions is of considerable technological and scientific interest. Self-assembled 3D inorganic templates, of biogenic origin have been converted into replicas comprised of numerous other functional muticomponent oxide materials (e.g., $BaTiO_3$, Eu-doped $BaTiO_3$, Mn-doped Zn_2SiO_4) by shape-preserving reaction-based and/or coating-based approaches[36,37,38]. Biologically-assembled 3D organic structures with intricate, hierarchical (macro-to-micro-to-nanoscale) morphologies are ubiquitous in nature (e.g., butterfly scales, beetle scales, fish scales, bird wings, plants, and pollen)[39,40,41]. Thus a shape-preserving LbL conformal coating and low-temperature (energy efficient) reaction

process for transforming bioorganic templates into freestanding 3D doped functional multicomponent oxide structures could expand the range of chemistries and structures for potential new functions and applications. Such processing would also be attractive for the chemical conversion of synthetic organic templates. In this work, incorporation of the resulting 3D inorganic phosphor microparticle replicas into/onto paper has revealed how such particles could be used to combat counterfeiting, which is a problem estimated to bring about losses of as much as $575 billion per year (tangible goods only— does not include digitally pirated goods unprotected by proposed technology) to global businesses in 2008[42]. With proper attention to each step, this shape-preserving coat-then-react process may be used to generate macro-to-micro-to-nanoscale structured inorganic assemblies with a wide range of complex 3D morphologies and multicomponent functional oxide chemistries from both synthetic and natural (sustainable) templates.

2.2.2. Choice of Inorganic Material and Bioorganic Template

$BaTiO_3$ (BT) is a perovskite (ABO_3), which is a class of materials with numerous functionalities. BT can also host/contain a wide variety/concentration of dopants or substitutional elements that affect functional properties[43,44]. BT has a band gap of 3.2 eV, allowing for dopant-induced emission of visible light greater than ~400 nm[44]. The incorporation of rare earth cation dopants has been shown to generate photoluminescent properties in BT[44]. It should be noted that the cationic radii of all trivalent rare earth cations are smaller than A-site Ba^{2+} and larger than B-site Ti^{4+}. Eu^{2+} cations have been reported to occupy the A-site of $BaTiO_3$[45]. Instability of europium cations has made identification of Eu^{3+} site occupancy difficult[44,45]. Some rare earth cations (e.g., Er^{3+}) have been shown to be amphoteric (i.e., cations can occupy both A- and B-sites), and

some rare earth cations, if small enough (e.g., Lu^{3+}), have been shown to exclusively occupy B-sites[45].

BT has been reported to incorporate up to 8 mol% Eu as a solid solution dopant before exhibiting concentration quenching[44]. The low temperature processing of $BaTiO_3$ (< 500°C) via a LbL coating methodology, organic pyrolysis, and microwave hydrothermal (MWHT) processing allows for the retention of the Eu^{3+} valence state, meaning that narrow red emission transitions can be seen rather than the green-blue emission (~440 nm) characteristic of the Eu^{2+} valence state[37,44]. Once a morphology-preserving reaction process for converting bioorganic materials to BT was established (**Chapter 1**),[46] the possibility of incorporating rare earth dopants to make phosphors via morphology-preserving reactions was thought to be feasible.

The natural abundance of surface hydroxy groups on chitinous butterfly scales eliminated the need for surface functionalization/functional group amplification for the SSG process[47,48]. The entire scale, as well as subscale (readily resolvable in optical microscope) morphology, of *P. blumei* made it an attractive candidate for potential anti-counterfeiting applications. **Figure 24** shows (**a**) a photograph of a *P. blumei* butterfly, (**b**) a fine-depth composition bright field optical micrograph and secondary electron images of (**c**) an individual color-mixing native scale, and (**d**) the microstructure of an individual scale. Elongated teardrop-shaped individual scales (approximately 100 micrometers in width (at the widest portion of the scale) and approximately 200 micrometers in length) as shown in **Figure 24b,c** imbricate the green stripes on the dorsal side of the forewings and hindwings of the *P. blumei* butterfly. Each individual scale is composed of ridges (**Figure 24d**) running parallel to the length of the scale. Lying

between, and perpendicular to, the ridges are shallow partitions forming concavities (**Figure 24d**) 5-10 micrometers wide, which have been shown to result in a unique property termed color-mixing [49,50,51].

Like many Lepidopterans, *P. blumei* possesses scales with different morphologies. To demonstrate this scale diversity, as well as the ability of the SSG deposition process to coat subsurface scales, the ground scales beneath the color-mixing scales on the dorsal side of the wing were imaged for Er-doped specimens.

An estimated 10^4 - 10^6 scales may imbricate the wings of a given butterfly. Assuming that both the dorsal and ventral sides of the *P. blumei* wing are covered by a single cover and ground scale layer (i.e., 4 total layers of scales), and the exposed area of a single *P. blumei* cover scale (1.8×10^{-4} cm^2 / scale) is representative of the area per each type of scale, then there would be ~2.2×10^4 scales/cm^2 of butterfly wing. The total wing area of a male *P. blumei* butterfly was estimated to be ~50 cm^2 and approximately 16 cm^2 of the wing area was tiled with a cover scale layer of color-mixing scales. Approximately 9×10^4 (16 cm^2 *1 color mixing scale/1.8×10^{-4} cm^2) of the 1.1×10^6 (50 cm^2 * 2.2×10^4 total scales/cm^2) scales on this particular *P. blumei* butterfly were determined to be color-mixing scales.

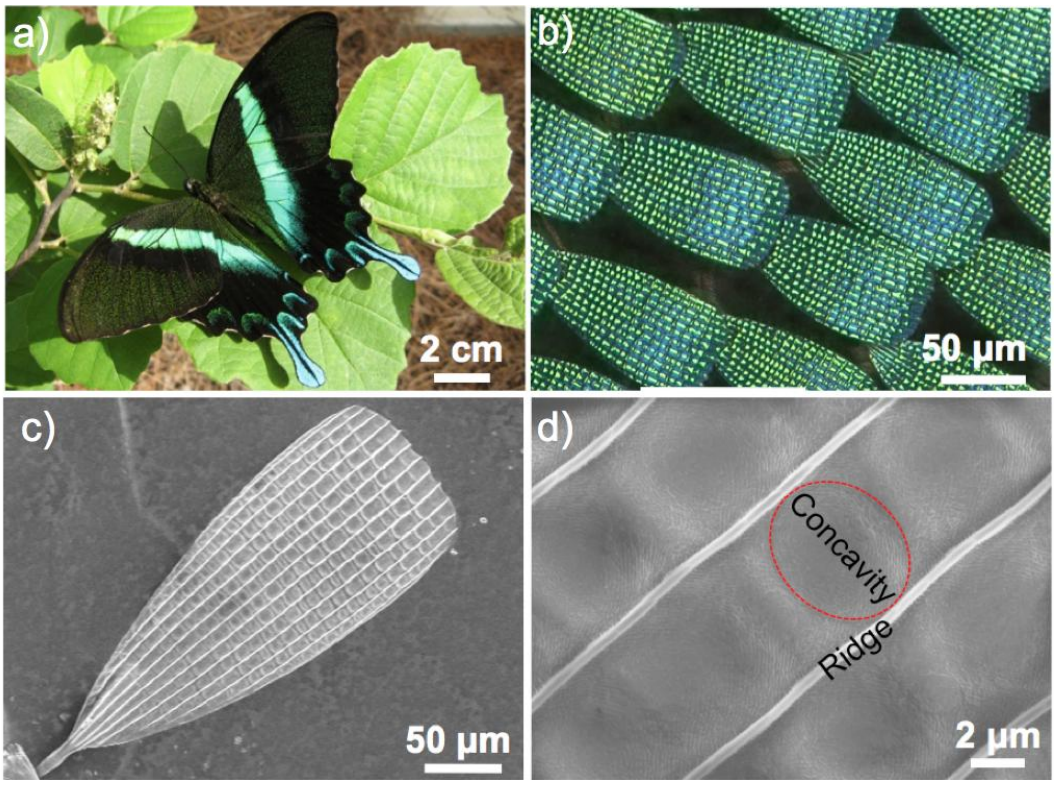

Figure 24: (a) A photograph of a *P. blumei* butterfly composed of color-mixing scales shown in (b) a bright field optical micrograph and SE images of (c) an entire single scale and (d) the intrascale microstructure.

2.3. *Experimental Procedures*

2.3.1. Conversion *P. blumei* Scales into Eu-doped and Pure $BaTiO_3$

Papilio blumei butterfly scales (insect-sale.com, Chia-yi City, Taiwan) were chemically transformed into barium titanate ($BaTiO_3$, BT) and Eu-doped $BaTiO_3$ (Eu-doped BT) replicas via a three-step process: i) application of a thin Ti-O-bearing coating through a layer-by-layer surface sol-gel (SSG) process, ii) pyrolysis of the underlying chitinous template and crystallization of the titania coating, and iii) conversion of the resulting titania structure into barium titanate by microwave hydrothermal reaction with a barium acetate (or barium and europium acetate)-bearing solution.

Each cycle of the SSG process was conducted by (i) immersion wing sections clipped to a 1.5 x 1.5 cm silicon wafer substrate in a 0.025 M titanium(IV) isopropoxide (99.999% metals basis, Sigma Aldrich, MO, USA) solution in anhydrous isopropanol (IPA) (99% purity, Acros Organics, Geel, Belgium) for 2 min, (ii) washing three times with 4 mL of IPA, (iii) immersing in 4 mL of 40 vol% IPA in DI water for 2 min, (iv) washing again three times with 4 mL of IPA, and then (v) drying with a stream of flowing air for 5 min at RT. This process was repeated for a total of 50 cycles. The coated wing sections were then clipped (Staples® black metal mini binder clips, MA, USA) between two ground and polished (2.54 x 2.54 x 0.159 cm) fused quartz plates (Technical Glass Products, OH, USA) and then heated in a tube furnace (Lindberg / Blue M, NC, USA,) at 0.5°C/min to 450°C (AutoFire® Controller, Orton Ceramic Foundation, OH, USA outfitted with a K-type thermocouple, OMEGA Engineering, Inc., CT, USA) and held at this temperature for 4 hr in air to allow for pyrolysis of the chitin and crystallization of the titania. The specimens were then furnace-cooled to RT. The pyrolyzed specimens were sealed within 100 mL Teflon^{TM} vessels (XP1500 Plus, CEM Corp., Matthews, NC, USA) containing a 20 mL solution of 0.125 M barium acetate, or 5 mol% europium(III) acetate hydrate (99.9%, Sigma Aldrich, MO, USA) / 95 mol% barium acetate (99%, Alfa Aesar, MA, USA) and 1 M NaOH (50% w/w aq. Soln., Alfa Aesar, MA, USA) dissolved in previously-boiled water. The sealed specimens were then heated within 5 min to 140°C in a microwave reaction system (MARS 230/60, 2.45 GHz, CEM Corp., Matthews, NC, USA) at a maximum power output of 800W and held at this temperature for 10 hr to allow for microwave hydrothermal (MWHT) conversion into BT / Eu-doped BT. After removal from the Teflon^{TM} vessels, the reacted scales were washed

for 24 hr with 25 mL of 5 M acetic acid (diluted from glacial acetic acid (17.4N, 99.9%, Fisher-Scientific, PA, USA)) in 50 mL centrifuge tubes rotated at 30 rpm on a RKVSD rotator (Appropriate Technical Resources, MD, USA) to remove any potential $BaCO_3$ that may have formed upon opening the vessels in ambient atmosphere and any $Eu(OH)_3$ formed during the hydrothermal reaction. The specimens were then rinsed twice with 20 mL of water, and then twice with 20 mL of IPA, followed by drying in air at 70°C for 1 hr. Each wash/rinse step was carried out via 5 min centrifugation of solutions in 50 mL centrifuge tubes (Corning, MA, USA) at 4500 rpm in a 5408R centrifuge equipped with a swinging bucket rotor (#A-4-44, Eppendorf, Hamburg, Germany), followed by removal of supernatant before adding subsequent solution or drying. (Note: relatively phase pure $Eu(OH)_3$ was separated for SEM and XRD analyses from the top of a pellet of reaction product formed after centrifugation (4500 rpm, 5 min) following the same MWHT treatment and subsequent wash methodology described above. However, in this case, the acetic acid wash step consisted of two 30 min 1M acetic acid washes rather than the 24 hr 5 M acetic acid wash.)

Incorporation of photoluminescent scales into paper for an anti-counterfeiting proof-of-concept demonstration was conducted by placing 0.1 mL of 1 mg/mL butterfly scales dispersed in an IPA solution into a 2.0 mL Spin-x® centrifuge tube filter (Corning, Inc., NY, USA) lined with filter paper (Qualitative P5 medium porosity, slow flow rate filter paper, Fisher Scientific, PA, USA). The solution was filtered via centrifugation (Centrifuge 5415D, Eppendorf, Hamburg, Germany) at 13,200 rpm for 1 min and then dried at 80°C for 1 hr.

2.3.2. Incorporation of Er into SSG coatings

The chemical conversion process was identical to that for the $BaTiO_3$ butterfly scales outlined in **Section 2.3.1** except that erbium(III) isopropoxide (99.9% metals basis, Alfa Aesar, MD, USA) was incorporated in the SSG process. A 25 mM erbium (Er) solution was made by dissolving erbium(III) isopropoxide into 50 mL of anhydrous 1-methoxy-2-propanol (M.IPA, 99%, Sigma Aldrich, MO, USA) in a sealed glass bottle on a hot plate for 12 hr at 100°C. The M.IPA was considered anhydrous after incubating with molecular sieves. Molecular sieves were heated at 300°C for 18 hr in air to eliminate moisture and then removed from the furnace at 200°C and cooled in a Pyrex® #3140 glass desiccator (Corning Incorporated, NY, USA) containing 200 g of 80 wt% DRIERITE (W.A. Hammond DRIERITE Co. LTD, OH, USA) / 20 wt% indicating DRIERITE (i.e., impregnated with cobalt chloride to indicate moisture by turning from blue when dry to pink when hydrated) for 2 hr. Such cooling was utilized to prevent moisture from returning to the sieves. Fifty grams of molecular sieves were added to 1 L of M.IPA in a nitrogen atmosphere glove box. The solution containing molecular sieves was incubated for 12 hr to allow for complete moisture sequestration. The incorporation of Er was attempted through a mixed alkoxide method (illustrated in **Figure 35**) as well as a layered alkoxide approach (depicted in **Figure 36**). In the mixed alkoxide approach, 40 mL of a 25 mM erbium(III) isopropoxide solution was mixed with 160 mL of a 25 mM titanium(IV) isopropoxide in IPA to produce a 20 mol% Er / 80 mol% Ti 25 mM alkoxide solution. In the layered approach, the 25 mM erbium(III) isopropoxide solution was used separately for alkoxide incubation in layers 4, 13, 22, 31, and 42, with the rest of the 50 total SSG deposition SSG cycles using 25 mM Ti(IV) isopropoxide as the metal

alkoxide. Hence 10% of the SSG cycles were Er-O- bearing and 90% were Ti-O-bearing.

2.3.3. Morphology, Phase, Chemical, and Optical Analyses

Photographs of a native butterfly (a dead insect specimen placed on leaves) were taken with a 7.1 mega pixel PowerShot A710 IS digital camera (Canon U.S.A., Inc., NY, USA) with the macro feature enabled and using the image stabilizer with no flash. The morphologies of the starting *P. blumei* wing scales, the SSG coated scales, the pyrolyzed scales, and the hydrothermally reacted scales were evaluated with a field emission scanning electron microscope (1530 FEG-SEM, LEO/Zeiss Electron Microscopy NY, USA) after mounting the scales directly on aluminum stubs (Ted Pella, CA, USA). EDS spectra were collected on the LEO 1530 outfitted with an INCA EDS system (Model 7426, Oxford Instruments, Bucks, UK). Cross-sectional images of specimens were also obtained by Dr. Ye Cai, Georgia Institute of Technology, via focused ion beam (FIB) milling (Nova Nanolab 200 FIB/SEM, FEI, Hillsboro, OR, USA). SE images of FIB cross-sections were generated after cutting an initial trench (~8 μm long x 5 μm wide x 5 μm deep) and then cleaning the face of the trench to be imaged with a final FIB cut (8 μm long x 200 nm wide x 5 μm deep) . Transmission and fluorescence optical images were obtained with a LSM 510 UV confocal microscope (Carl Zeiss MicroImaging, LLC., NY, USA). Scale-only specimens dispersed in IPA were deposited with a 1 mL pipette on pre-cleaned (2.54 x 7.62 x 0.1 cm) microscope slides (Gold Seal® Products, N.H, USA). Filter paper specimens were simply placed on glass slides. Both scale-only and dried filter paper specimens on microscope slides were covered with a square (22 x 22 mm) No. 1.5 cover glass (slip) (VWR International, LLC., PA, USA). The cover slips

were secured to the glass slides with the aid of nail polish (Continuous Treatment Strength, Sally Hansen®, NY, USA). Transmission images of Eu-doped specimens and corresponding controls were generated using a 543 nm (1 mW helium-neon) laser focused through a 10X objective (Plan-neofluor, NA=0.3). Fluorescence images of these specimens were taken using a 488 nm (30 mW Argon Ion) excitation laser and a long pass 585 nm emission filter. Er-doped BT scale transmission images were taken using a 488 nm (30 mW Argon Ion) laser. Fluorescence images of these specimens were generated using a 488 nm excitation laser and a long pass 505 nm filter. Images taken for qualitative brightness comparisons were generated in the same microscopy session using the "Re-Use" function in the ZEN 2009LE software so as to ensure an identical optical path and imaging settings (e.g., same user input settings for laser intensity, brightness, contrast, gain, pinhole, and scan speed). Bright field and dark field images were taken with a Keyence VHX-600 digital microscope (Keyence Corporation, Osaka, Japan) outfitted with a 250x - 2,500x objective. Before taking images the white-balance was set using a Teflon^{TM} block in bright field mode at 1000x magnification. All images were generated with a fine depth composition using at least 5 frames taken at increasing z-heights (i.e., the bottom to top focal planes of object are sequentially brought into focus, imaged, and then stacked so that the entire image was in focus despite different focal depths). Diffraction specimens were dispersed on a quartz (cut 6° from (0001)) low background specimen support (GEM dugout, PA, USA) via pipetting an aliquot of IPA/powder slurry onto the holder and allowing the IPA to evaporate. XRD analyses were conducted on an X'Pert Pro Alpha-1 diffractometer (PANalytical B.V., ALMELO, Netherlands) with monochromatic $Cu_{K\alpha 1}$(1.5405980 Å) radiation emanating from a 1.8

kW ceramic diffraction X-ray tube with copper anode (45 kV, 40 mA) through a symmetrical Johannson monochromator. The incident beam optics were outfitted with 0.04 rad soller slits, a 1° fixed anti-scatter slit, a ½° programmable divergence slit, and a 10 mm mask. The diffracted beam optics were outfitted with a 5.5 mm anti-scatter slit and 0.04 rad soller slits placed before the X'Celerator detector. Each pattern was produced with a summation of 4 identical 30 minute scans conducted with Bragg-Brentano geometry and a step size of 0.01671° 2θ ranging from 20° to 60° 2θ.

Prof. John Olesik of the Trace Element Research Lab at The Ohio State University conducted LA-ICP-MS analyses on single scale specimens. A 193 nm ArF excimer laser (UP193HE, New Wave Research, CA, USA) with beam homogenizing optics was used to ablate each sample using a single laser pulse (20 ns, 100 μm diameter beam at the sample, approximately 0.3 mJ laser pulse energy). The samples were mounted on carbon tape. A 1.0 L/min He gas flow through the ablation cell carried the ablation products out of the cell. After mixing with 1.0 L/min Ar the product(s) were introduced into the 1300 W inductively coupled plasma. An Inductively Coupled Plasma Sector Field Mass Spectrometer (ThermoFinnigan Element 2, Bremen, Germany) was used to measure signals for to ^{47}Ti, ^{138}Ba and ^{153}Eu with a mass spectral resolution ($m/\Delta m$) of approximately 300. ICP-MS signals were integrated over the approximately 10 s that signal was observed following a single laser pulse. The $^{138}Ba^{+}/^{47}Ti^{+}$ and $^{153}Eu^{+}/^{47}Ti^{+}$ ICP-MS signal ratio were calculated from the time integrated $^{47}Ti^{+}$, $^{138}Ba^{+}$ and $^{153}Eu^{+}$ signals. NIST 610 was used as a standard (ablated using a line scan while the laser was fired at 10 Hz) to determine the correlation between the ratio of $^{138}Ba+/^{47}Ti+$ ICP-MS signals and the ratio of Ba/Ti concentration, as well as the correlation between

the ratio of $^{153}Eu^{+}/^{47}Ti^{+}$ ICP-MS signals and the ratio of Eu/Ti concentration[52]. The NIST 610 standard glass was comprised of 434 ppm Ti, 424 ppm Ba, and 461 ppm Eu.

Photoluminescence spectra for BT and Eu-doped BT scales were collected by Jeremy Lerner of Lightform, Inc. Photoluminescence spectra were collected with a Hyperspectral Imaging system (PARISS PHSI Model, LightForm, Inc., NC, USA, www.lightforminc.com). The system incorporated a prism-based spectrograph using a monochrome Retiga 2000R, CCD camera (QImaging, BC, Canada) to collect spectral information along rows of pixels. The system was mounted on a Nikon E800 microscope (Nikon Instruments Inc., NY, USA). Wavelength calibration was performed with a MIDL Hg^{+}/Ar^{+} emission lamp (LightForm, Inc, NC, USA). Wavelength accuracy was recorded and verified to be better than 0.3 nm. The specimen was immersed in IPA between a glass slide and cover-glass. Each spectrum presented is representative* of the major class of spectra presented in 200 acquisitions across a single specimen. Each of the 200 acquisitions was background subtracted, and each acquisition lasted 2 seconds, with no signal averaging. *For example the Eu-doped BT specimen was characterized by 200, 2 second acquisitions that delivered a total of 48,000 spectra. The individual reported spectrum was an average of the 12,314 spectra emanating from the specimen.

2.4. *Results & Discussion*

2.4.1. Chemical conversion of *P. blumei* scales into Eu-doped $BaTiO_3$

The generation of Eu-doped BT butterfly scales began with the coating of a green section (i.e., containing color-mixing cover scales) of the dorsal side of a *P. blumei* forewing with 50 SSG layers of Ti-O. After 50 SSG deposition cycles, wing sections

were pyrolyzed at 450°C for 4 hr in air to remove the organic material. The resulting hollow-core, crystallized anatase titania structures were then subjected to microwave hydrothermal treatment in a 1 M NaOH solution with either a 125 mM barium acetate solution or a 125 mM 5 mol% europium acetate hydrate / 95 mol% barium acetate solution. Each MWHT reaction was conducted in a sealed Teflon^{TM}-lined vessel for 10 hr at 140°C in a microwave assisted reaction system (CEM MARS 230/60). The converted scales were separated from the reaction solution via centrifugation. After removal of supernatant, the samples were washed with 25 mL of 5 M acetic acid for 24 hr to remove any potential $BaCO_3$ (formed due to exposure to CO_2 in the ambient atmosphere) as well as $Eu(OH)_3$ (formed during the reaction). Both the washing and separation via centrifugation were repeated twice with water and then twice with IPA. Single scale specimens generated after each step in the chemical conversion process (including the $BaTiO_3$ control replica) are shown in **Figure 25**. Single scale specimens shown in **Figure 25** include the following: (**a**) a chitinous scale coated with 50 cycles of SSG, (**b**) a scale after 50 SSG coating cycles and organic pyrolysis, (**c**) a scale after 50 SSG coating cycles, pyrolysis, and MWHT conversion to BT or (**d**) Eu-doped BT. Such images show the remarkable fidelity of the reaction process on the 100's of micrometers length scale (with entire scales shown in the insets clearly intact), as well as on the single micron length scale (with the parallel ridges and concavities retained). One should note that considerable shrinkage occurs during the firing step. An in-depth examination of the chitin/sol-gel precursor interaction and dimensional analyses as a function of processing step is available elsewhere in **Chapter 1**. In addition to structural retention, **Figure 26** reveals EDS spectra exhibiting peaks from the expected elements at each step in the

process (i.e., peaks for Ti after SSG deposition and after pyrolysis, peaks for Ba and Ti after conversion to $BaTiO_3$, and peaks for Ba, Ti and Eu after conversion to Eu-doped $BaTiO_3$).

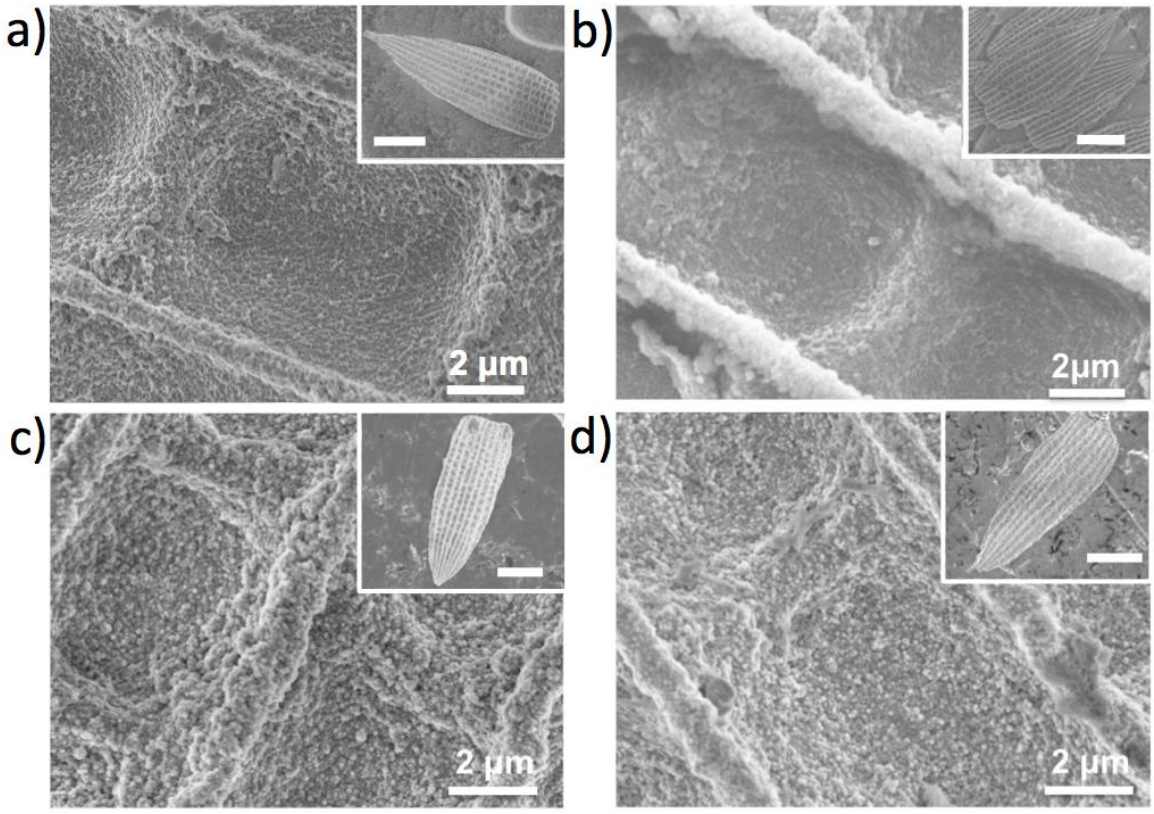

Figure 25: SE images of individual concavities and entire scale morphologies (insets) of *P. blumei* color-mixing scales (a) after 50 SSG cycles, (b) after organic pyrolysis, c) after MWHT treatment to form $BaTiO_3$, d) after MWHT to form Eu-doped $BaTiO_3$. Inset scale bars all represent 40 µm.

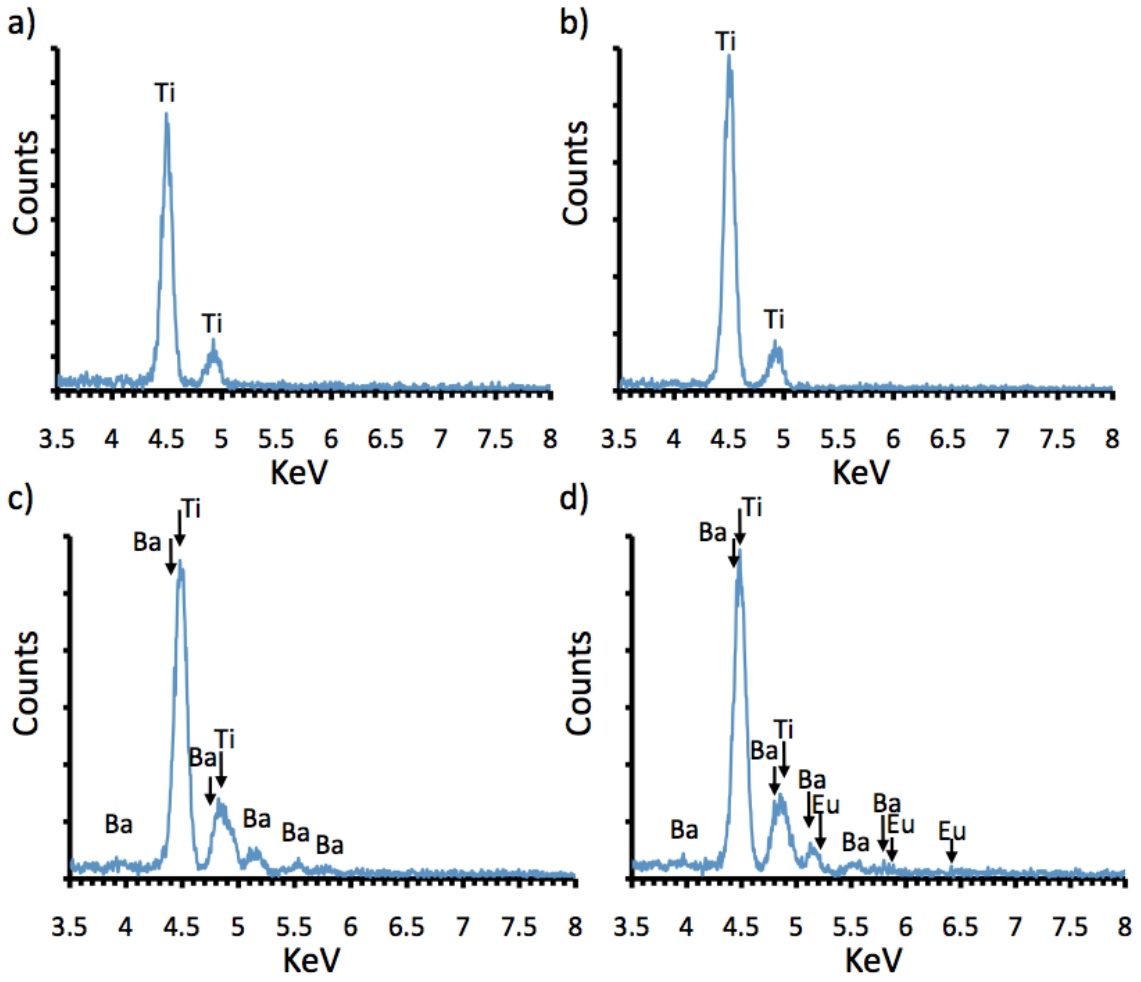

Figure 26: EDS spectra of *P. blumei* scales after (a) coating with 50 SSG cycles of Ti-O, (b) after coating and organic pyrolysis, and after coating, organic pyrolysis, and MWHT conversion into (c) $BaTiO_3$ and (d) Eu-doped $BaTiO_3$. Note that the Eu and Ba peaks overlap thereby making quantitative EDS impossible without a standard.

The focus of this chapter is the formation of structures with unique 3D morphology on different length scales coupled with a unique and tailorable optical signature to potentially provide (i) simple point-of-purchase anti-counterfeiting capability, (ii) in–depth authentication with the aid of high-powered optical microscopes, and/or (iii) automated detection methods to evaluate the emission spectra of the photoluminescent 3D structure.

To evaluate the effectiveness of imparting photoluminescent properties to *P. blumei* scales, confocal fluorescent microscopy was utilized. **Figure 27** qualitatively

reveals the considerable difference in red fluorescent intensity (long pass 585 nm filter with 488 nm excitation) exhibited by the Eu-doped BT scales over that of the native scales, pyrolyzed scales, and pure $BaTiO_3$ scales. Adjacent to such fluorescence images are transmission optical micrographs created utilizing 543 nm light. Both fluorescent and transmission images of each specimen were taken with identical settings within the same microscopy session to ensure that the relative intensities were comparable. It should be noted that, while broad green photoluminescence has been reported for hydrothermally prepared BT particles[53], the relative intensity of fluorescence under the present excitation and emission interrogation conditions was considerably less for the BT specimen than for the Eu-doped BT specimen (**Figure 27 row 3 of column 1 vs. row 4 of column 1)**. Also of interest was the relative translucency of the titania replicas with respect to the BT and Eu-doped BT scale replicas (**Figure 27 row 2 of column 2 vs. rows 3 and 4 of column 2).** Enhanced photoluminescent intensity (488 nm excitation, > 585 nm emission) of scales undergoing MWHT reactions with Eu present corroborated chemical analysis. That is, EDS (**Figure 26**) of the photoluminescent Eu-doped BT scale replicas revealed the presence of Eu, Ba, and Ti. Due to peak overlaps and the relatively small signal-to-noise ratio of the Eu-only peak in EDS spectra, another technique was needed to quantify the Eu concentration in Eu-doped BT scale replicas.

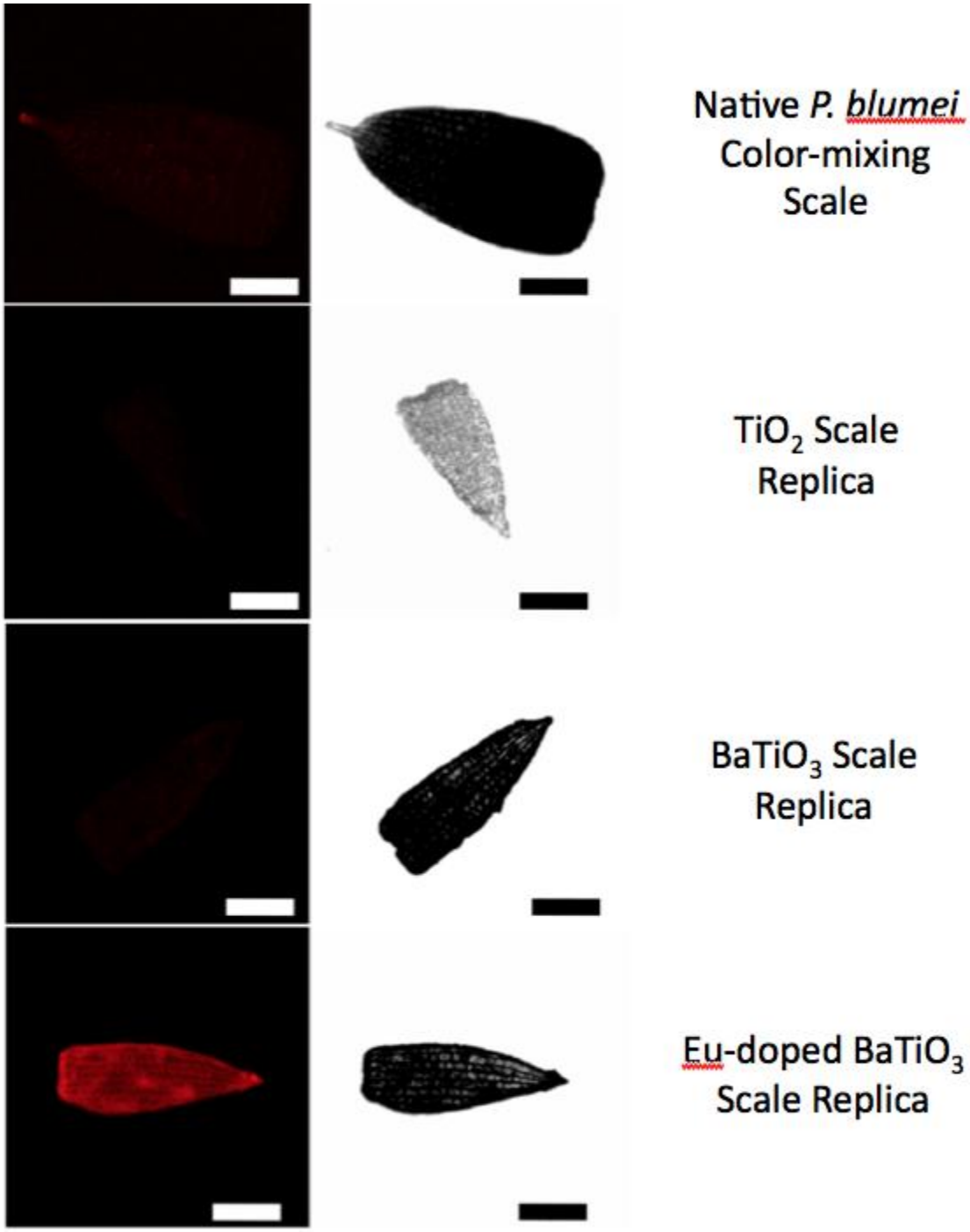

Figure 27: Confocal fluorescence (488 nm excitation, long pass 585 filter) images (left) and transmission (543 nm) micrographs (right) of native (top row), SSG coated and pyrolyzed scales (second row), coated and pyrolyzed scales after hydrothermal conversion into $BaTiO_3$ (third row), and Eu-doped $BaTiO_3$ (bottom row). All images were taken under identical conditions. All scale bars represent 50 micrometers.

LA-ICP-MS analysis, conducted by ablation of individual inorganic scale replicas with a single laser pulse, yielded a europium dopant concentration on the order of 1 mol%. (Note: an SRM 610 NIST glass standard was used for quantitative analysis.) Considerable variation (20%) was obtained in the Ba:Ti ratio from ablating particles with a single laser pulse. Such variation was not detected within the standard. The Ba:Ti ratio was .55:1 rather than 1:1 for commercial $BaTiO_3$ powder that had been determined to be phase pure (via XRD analysis). Including the entire range of measurements (with each type of sample analyzed in quadruplicate) and with/without correction of Ba concentration using commercial $BaTiO_3$ powder, the (Eu / (Eu + Ba)) doping mol% varied from 0.5-3.7 mol%. The europium acetate concentration relative to the barium acetate in the MWHT reaction solution was 5 mol%. The formation of $Eu(OH)_3$ makes the reported values (< 5 mol%) seem reasonable as some of the europium was consumed in the formation of $Eu(OH)_3$ in the hydrothermal reaction. Although apparently not quantitative or reproducible, LA-ICP-MS confirmed the presence of Eu in only the Eu-doped specimens at a concentration level commonly reported for photoluminescence in Eu-doped $BaTiO_3$ (0.1 - 8 mol%) [44,54].

One concern was the possible presence of residual $Eu(OH)_3$ after acid washing, which could be undetectable by XRD due to the low concentration of this phase. However, trace amounts of $Eu(OH)_3$ may be detected by SEM due to the distinct nanorod morphology of $Eu(OH)_3$ observed after MWHT aging. SE images and an XRD pattern of $Eu(OH)_3$ nanorods formed during MWHT treatment at 220°C for 10 hrs are shown in **Figure 28.** Nitric acid was initially used to remove this phase, but such washing drastically reduced the yield of $BaTiO_3$ scales. A 24 hr - 48 hr RT treatment in 5 M

acetic acid was found to be capable of removing all of the $Eu(OH)_3$ nanorods without a noticeable reduction in the yield of $BaTiO_3$ scales. Higher MWHT reaction temperatures and longer reaction times required longer $Eu(OH)_3$ etch times. All morphology, chemical, phase content, and optical characterizations were conducted on samples washed with 5 M acetic acid, which revealed no $Eu(OH)_3$ by XRD analyses (**Figure 29**) or SE analyses (i.e., no detection of nanorod morphology) (**Figure 30b,d**).

Due to a low Eu dopant concentration and the nanocrystalline nature of the coatings, both Eu-doped and pure BT replicas exhibited broadened peaks for phase pure cubic $BaTiO_3$ in X-ray diffraction patterns as shown in **Figure 29**. Peak positions and intensities were matched to Powder Diffraction File Card No. 04-007-6869, which has the highest quality mark (Indexed) in the International Center for Diffraction Data database for cubic ($Pm\bar{3}m$) $BaTiO_3$. Both the pure BT and Eu-doped BT specimens were nanocrystalline. Scherrer analyses (of FWHM of the (111) and (110) peaks) yielded average crystallite sizes for BT and Eu-doped BT of 34 - 38 nm and 38 - 42 nm, respectively. A geometric factor of 0.9 was used in Scherrer's formula because SE images (**Figure 30**) revealed that the smallest particles were roughly spherical. The crystallite size was corroborated by direct particle observation via high magnification SE micrographs of cover scales (**Figure 30a,b**) and ground scales (**Figure 30c,d**) from green dorsal region of the *P. blumei* butterfly. Particles ranging from ~10 – 100 nm in diameter were observed in both pure BT (**Figure 30a,c**) and Eu-doped BT (**Figure 30b,d**) replicas.

Despite nanoscale crystallite sizes and a low temperature of formation, the Eu-doped BT scales exhibited photoluminescence. Although there should be a loss in

mechanical robustness in going from biopolymer template to ceramic replicas, the thin-walled inorganic scales survived organic pyrolysis, hydrothermal reaction, multiple centrifugation steps, washing in a rotator, and pipetting.

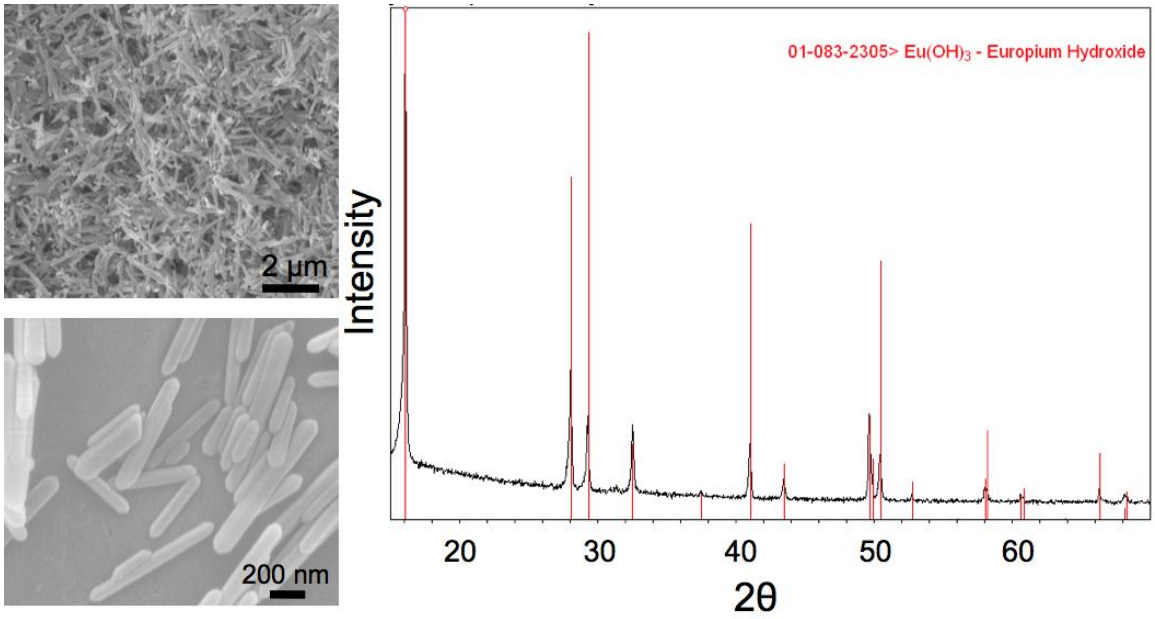

Figure 28: Low (top left) and high (bottom left) magnification SE images of $Eu(OH)_3$-bearing powder after 220°C, 10 hr MWHT treatment of anatase titania *P. blumei* scales in Ba- / Eu- bearing caustic solution. Peak positions were matched to Powder Diffraction File Card No. 01-083-2305, which has the highest quality mark (Indexed) in the International Center for Diffraction Data database for ($P6\frac{3}{m}$) $Eu(OH)_3$. SE images and XRD pattern were obtained from powder drawn off the top of the MWHT product pellet with a pipette after two thirty minute 1 M acetic acid washes rather than a 24 hr 5 M acetic acid wash.

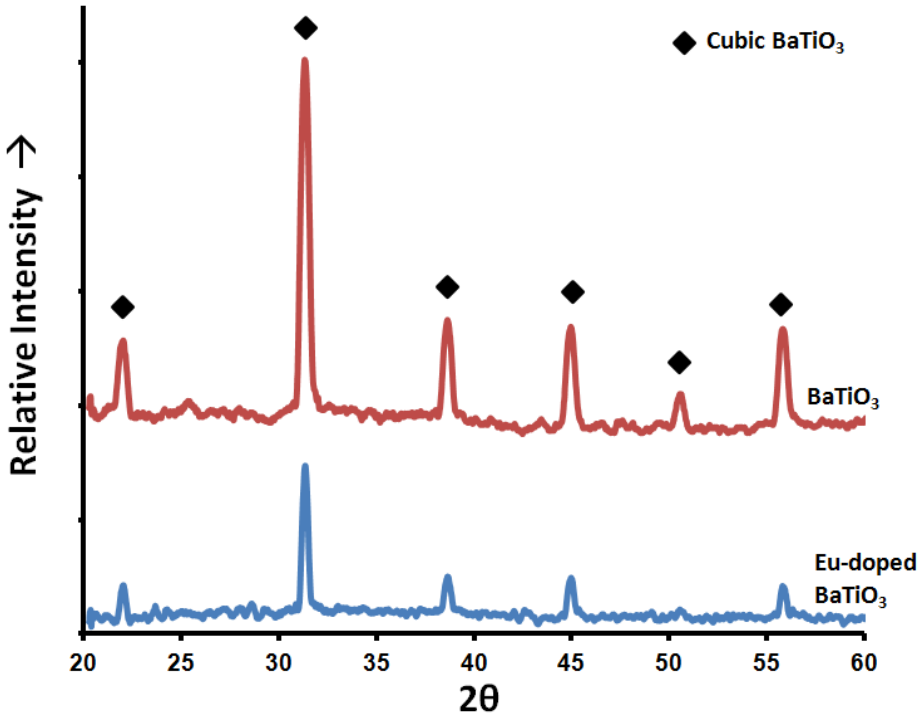

Figure 29: X-ray diffraction patterns of both BT and Eu-doped BT scale replicas after MWHT treatment and 24 hr 5 M acetic acid wash revealing diffraction peaks consistent with cubic $BaTiO_3$. The difference in peak-to-background ratio resulted from differences in sample volumes.

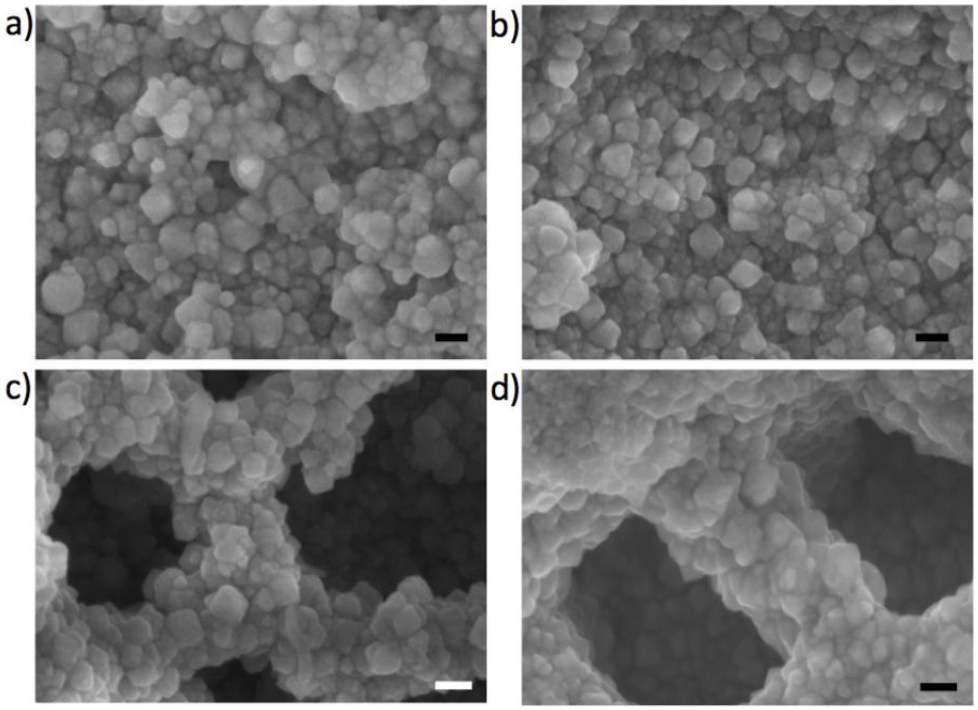

Figure 30: SE images of (a,c) BT and (b,d) Eu-doped BT replica specimens. Top row images were obtained from dorsal cover (i.e., color-mixing) scales, and the bottom row images were obtained from dorsal ground scales. All scale bars represent 100 nm.

The ability of such materials to be used for anti-counterfeiting purposes was tested by incorporating the Eu-doped BT scale replicas into cellulose filter paper. A 1 mg/mL slurry of the scale replicas in IPA was passed through filter paper lining a 2 mL spin-x® centrifuge tube via centrifugation. Such particles could, in principle, also be applied to surfaces by several other means (e.g., electrostatically if of significant tetragonal $BaTiO_3$ content and with poling) or incorporated into polymer films, paints, and adhesives. The covert nature of the scales was apparent when viewed after incorporation into paper via bright field optical microscopy (**Figure 31a**). Higher magnification characterization (**Figure 31a** insets) revealed the whiteness of an individual scale when viewed upon a glass slide. While the utility for incorporating, manipulating, or replicating the native structural color is an interesting avenue to explore,[51] the covert nature of the particles is an asset in this particular application. However, the location of such scales can be identified via dark field optical microscopy as shown in **Figure 31b**. With low magnification (< 100x) dark field imaging, one can readily detect the morphology of individual scales or groups of scales. With a higher power (≥ 500x) objective (**Figure 31 insets**), one can distinguish the parallel ridges and cavities within each scale. Fluorescent confocal microscopy clearly revealed the location of the scales within paper (**Figure 31c)**. Finally, the conformality and spatial location of the scales with respect to cellulose fibers when incorporated into/onto cellulose paper was revealed in **Figure 32**, (a topographical color map). Each individual scale conformed to the surface of the cellulose paper, indicating the mechanical robustness of the thin-walled photoluminescent inorganic replicas. Photoluminescence spectra were generated from pure BT and Eu-doped BT scales (**Figure 33**). The BT spectrum revealed broad

green/yellow luminescence as reported elsewhere[53]. The Eu-doped BT spectrum revealed 6 peaks that were consistent with the positions of Eu-doped BT $^5D_i \rightarrow {}^7F_j$ transitions reported elsewhere[37,44]. Although there were sharp and distinct photoluminescent peaks in the Eu-doped BT sample, the $^5D_0 \rightarrow {}^7F_0$ transition was of considerably higher intensity relative to the $^5D_0 \rightarrow {}^7F_2$ transition than has been reported previously[37,44,54]. Each spectrum was generated with 436 nm excitation and a 510 nm long pass emission filter with a PARISS hyperspectral imaging system.

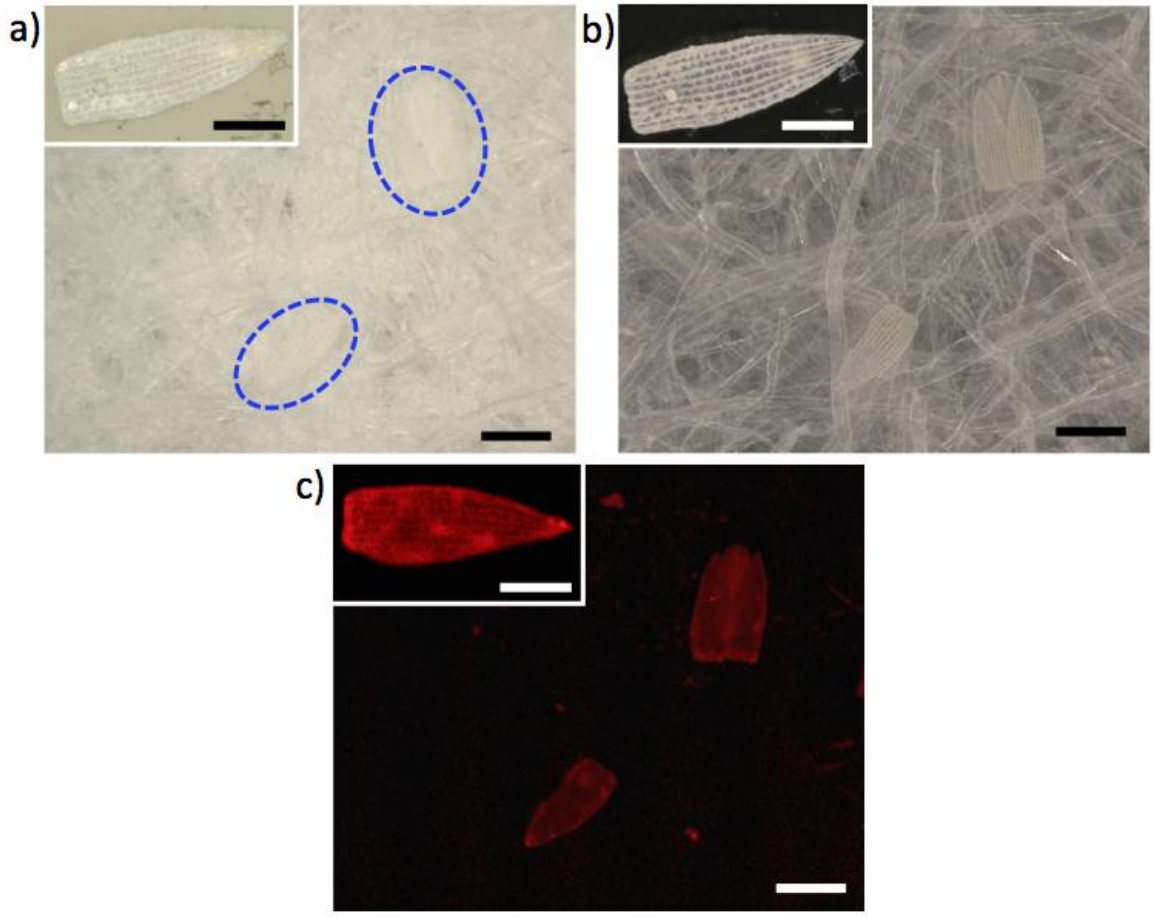

Figure 31: Incorporation of photoluminescent Eu-doped $BaTiO_3$ scales into paper (primary images a,b,c) and on glass slides (inset images a,b,c.) imaged with (a) bright field, (b) dark field, and (c) fluorescence microscopy. Primary image scale bars all represent 100 micrometers; inset scale bars represent 50 µm.

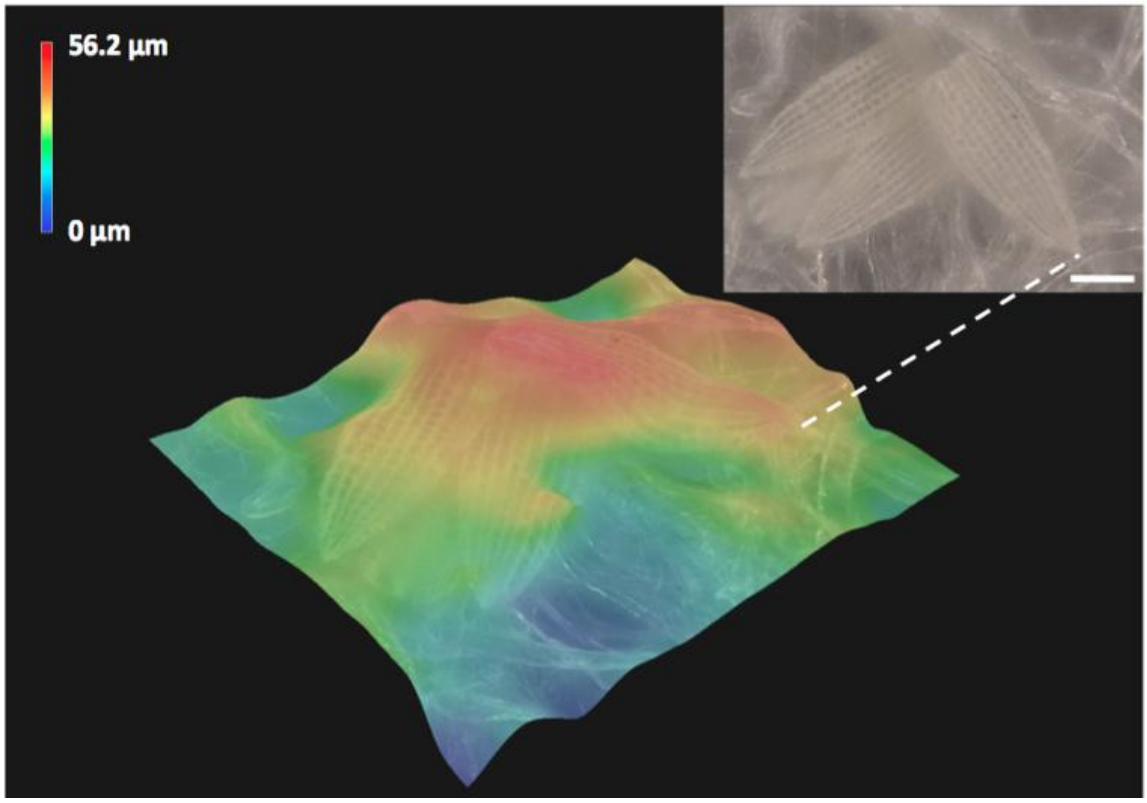

Figure 32: A topographical color map generated through fine depth composition of 50 dark field images with inset of corresponding top view fine depth composition dark field micrograph. Inset scale bar represents 50 µm.

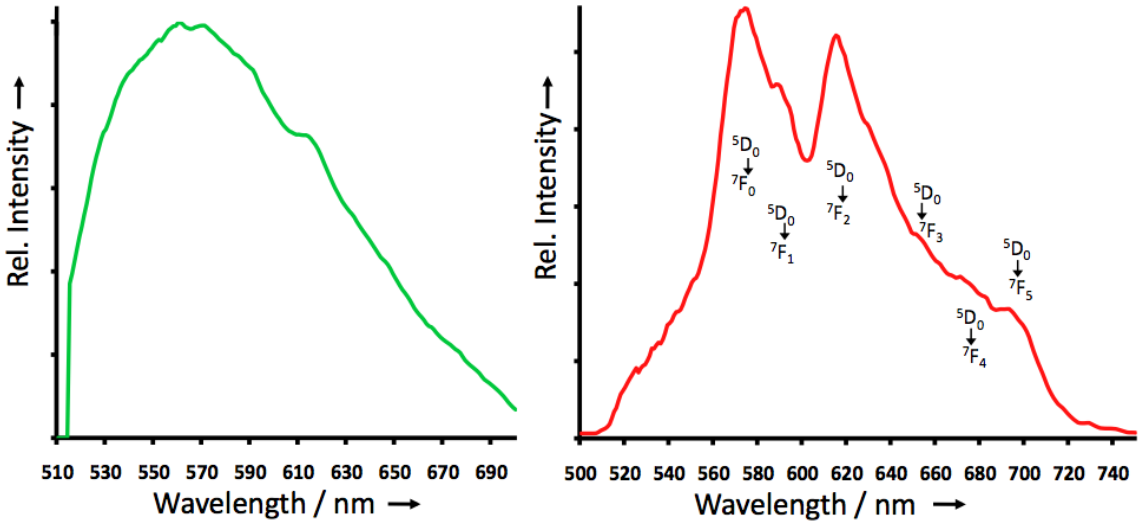

Figure 33: Photoluminescence spectra collected with 434 nm excitation of a single $BaTiO_3$ scale replica (left) and a single Eu-doped $BaTiO_3$ scale replica via PARISS hyperspectral imaging system. Spectra courtesy of Dimitri Deheyn, Scripps Institution of Oceanography, UCSD, and Jeremy Lerner, Lightform, Inc.

The conversion of *P. blumei* scales into BT or Eu-doped BT resulted in a loss of structural color. The crystallite size of the pure and doped $BaTiO_3$ (~30 nm - 40 nm) may have resulted in significant scattering. Additionally, the organic pyrolysis step caused considerable shrinkage. The lack of structural color in the inorganic replica was also likely to have been affected by the lack of precise structural retention of the multilayer structure within each scale. **Figure 34** contains SE images of FIB-milled cross-sections of coated *P. blumei* scales, coated and pyrolyzed scales, and coated/pyrolyzed scales after MWHT conversion to $BaTiO_3$. The starting internal scale structure was comprised of an interconnected cuticle/air multilayer **(Figure 34a,b)**, which was only partially reproduced after organic pyrolysis **(Figure 34c**). After MWHT treatment, the internal structure had been converted into $BaTiO_3$ with a noticeably larger particle size (**Figure 34d**). The inability of the SSG process to penetrate and completely coat the internal multilayer structure was not surprising as ALD deposition of titania on the same species of butterfly also failed to penetrate the internal multilayer structure of the *P. blumei* scales[55].

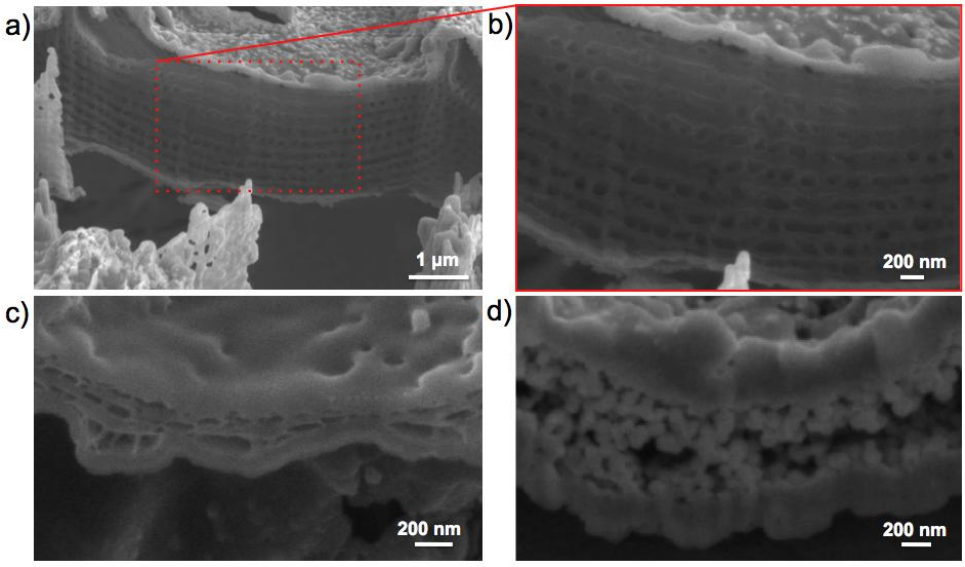

Figure 34: SE images of FIB-milled cross-sections within a single concavity of *P. blumei* dorsal cover scales after (a,b) coating with 50 SSG cycles of TiO_2, (c) organic pyrolysis of coated scales, and (d) MWHT conversion of coated/pyrolyzed scales into $BaTiO_3$.

2.4.2. Chemical conversion of *P. blumei* scales into Er-doped $BaTiO_3$

The production of Eu-doped BT butterfly scale replicas via incorporation of a lanthanoid in the SSG process was also examined. When the europium alkoxide solution was mixed with DI water, little to no hydrolysis occurred, making layered alkoxide (i.e., separate Eu-O and Ti-O SSG deposition cycles) deposition impossible. Also, addition of dissolved europium(III) alkoxide to titanium(IV) isopropoxide stabilized the entire alkoxide solution, such that the mixed solution would not hydrolyze upon the addition of DI water, thereby rendering mixed alkoxide SSG deposition impossible. Thus, different lanthanoid elements were considered. Er(III) isopropoxide was found to be soluble in M.IPA and could be readily hydrolyzed. A 25 mM solution of erbium(III) isopropoxide allowed could be mixed with a 25 mM titanium(IV) isopropoxide for mixed alkoxide SSG deposition (the mixed alkoxide solution also readily hydrolyzed), or kept pure for layered (Er then Ti) alkoxide SSG deposition. SSG deposition processes are depicted in **Figure 35** and **Figure 36** for the mixed alkoxide method and the layered alkoxide deposition method, respectively.

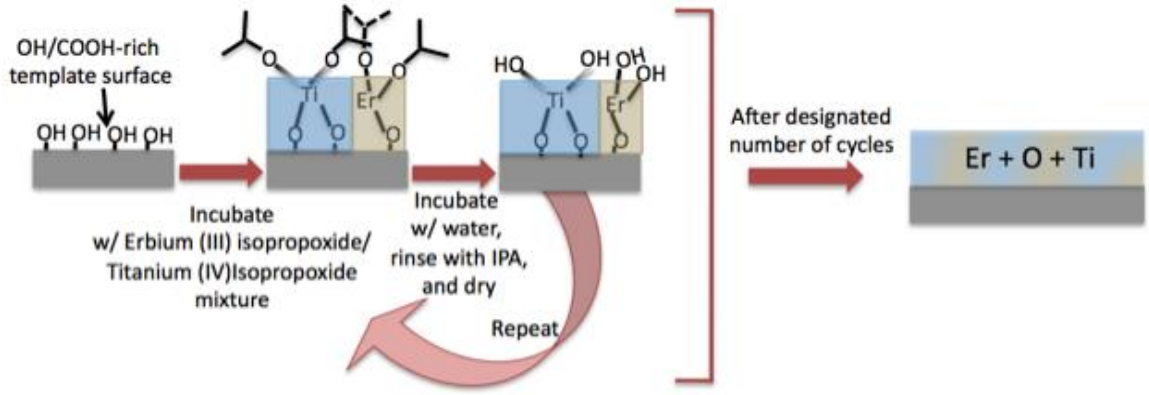

Figure 35: The mixed alkoxide SSG deposition technique used to apply Er-Ti-O- bearing coatings.

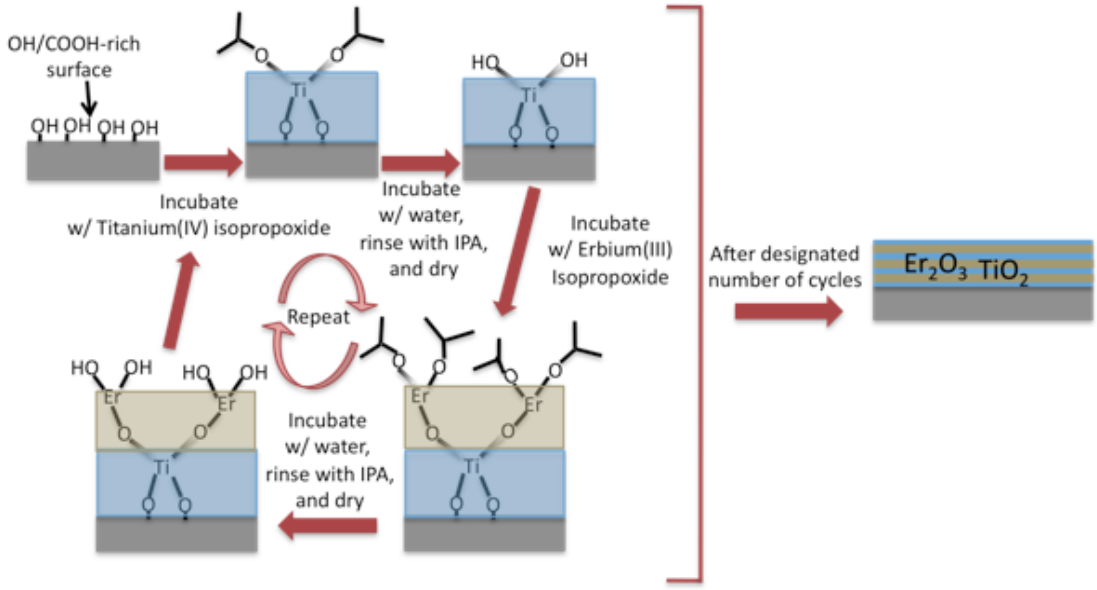

Figure 36: The layered alkoxide approach to SSG deposition in which the stoichiometry is potentially controlled by the number of Ti-O- and Er-O- bearing layers.

Er-Ti-O- containing coatings were applied to *P. blumei* wing sections via fifty layers of SSG deposition, either by the mixed alkoxide or the layered alkoxide method. It was found that the mixed alkoxide method provided the best surface morphology retention in the as-coated state, and thus, was used for the chemical conversion process. **Figure 37** shows the morphology of single concavities within native *P. blumei* scales, Ti-O- coated scales, and Er-Ti-O- coated scales (with both layered and mixed alkoxide coating methods). Clearly, the conventional Ti-O SSG deposition and the mixed alkoxide method for SSG deposition of Er-Ti-O –bearing coatings provided the best surface morphology retention. The open atmosphere coating conditions may have caused some hydrolysis of the pure Er(III) isopropoxide solution, which in turn caused debris to be deposited on the butterfly cover scale surfaces. Ambient atmosphere hydrolysis may also explain why 25 mM Ti(IV) isopropoxide solutions provided better surface morphology coatings of Ti-O bearing SSG than those applied with 50 mM Ti(IV)

isopropoxide concentrations (**Figure 38**). It should be noted that the layered alkoxide deposition of Er-Ti-O coatings may provide excellent morphology retention if applied in a dry nitrogen atmosphere glovebox, or with lower concentrations of Er(III) isopropoxide.

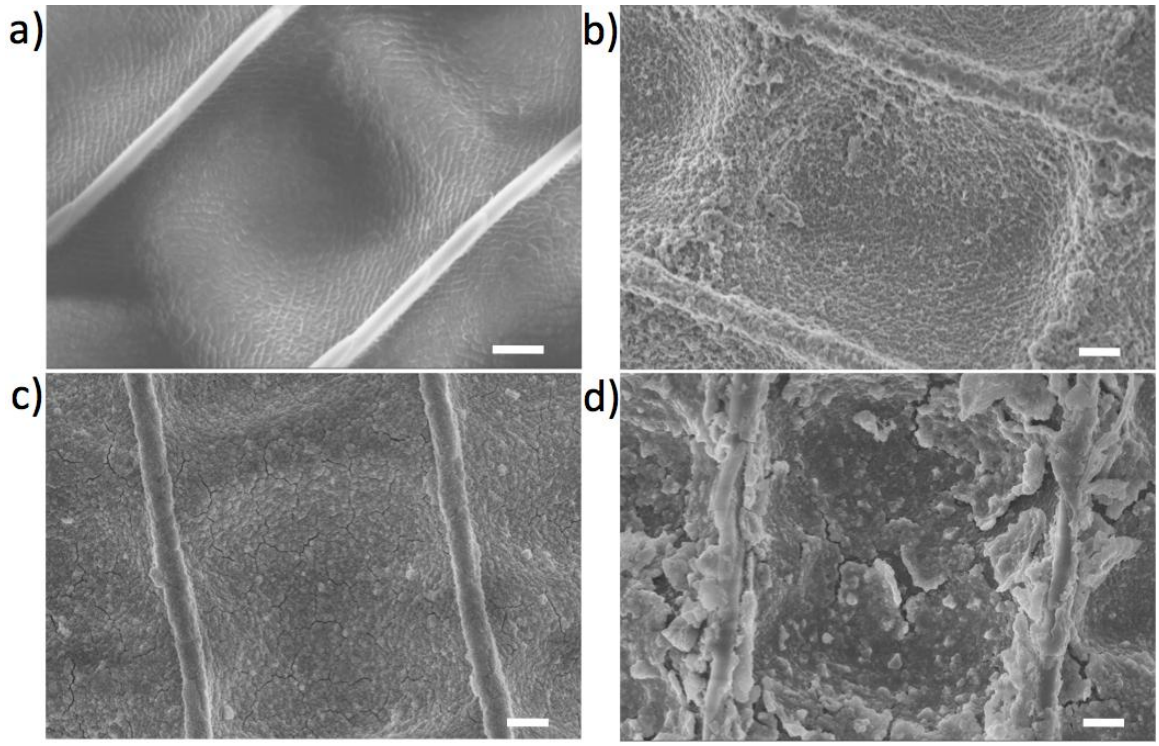

Figure 37: SE images of *P. blumei* cover scales in (a) the native state, (b) after coating with 50 SSG layers of Ti-O, (c) after coating with 50 SSG layers of 20 mol% Er / 80 mol% Ti mixed alkoxide solution, and (d) after coating with SSG using individual Er (5 cycles) and Ti (45 cycles) alkoxide solutions. All scale bars represent 1 µm.

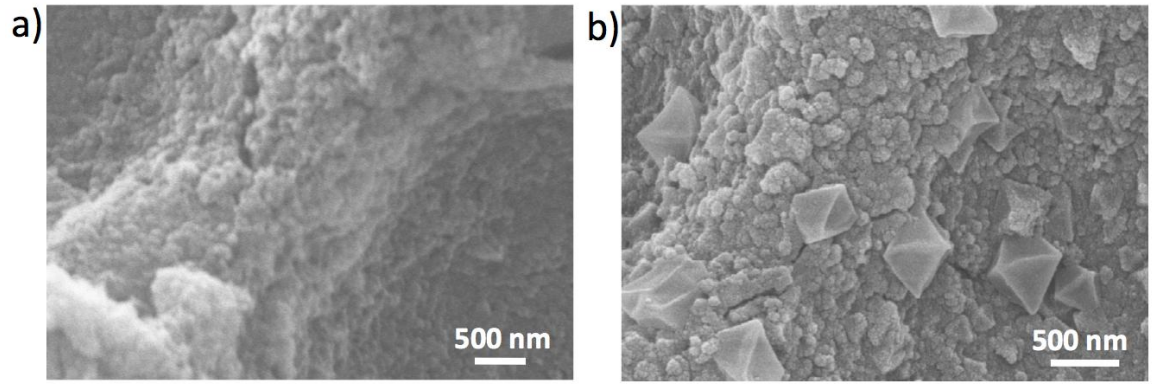

Figure 38: SE images of *P. blumei* cover scales after coating with 50 layers of SSG deposition using (a) 25 mM and (b) 50 mM Ti(IV) isopropoxide.

Samples of *P. blumei* ground scales, located beneath the color-mixing scales on the dorsal side of the wing, were examined for Er-doped BT experimentation. **Figure 39a** shows an entire *P. blumei* ground scale and **Figure 39b** reveals the intrascale microstructure. Like *Morpho helenor* butterflies, the ground scales of *P. blumei* are generally rectangular in shape and are furcated on the end opposite the stem (which attaches the scale to the wing membrane). Such ground scales also contain ridges running parallel to the long dimension of the scale that are separated by an intricate web-like structure rather than perpendicular struts. The Er-doped titania, and Er-doped BT microstructures of such scales are revealed in **Figure 39c** and **Figure 39d,** respectively. **Figure 40** reveals the elemental content of the scales at various stages of the chemical conversion process. Er and Ti are present after coating (**Figure 40a)**, after organic pyrolysis (**Figure 40b)**, and after MWHT conversion into Er-doped $BaTiO_3$ (**Figure 40d)**. There was no Er peak in the EDS spectra obtained from Ti-O-only coated scales after organic pyrolysis and MWHT conversion into $BaTiO_3$ (**Figure 40c**).

Much like the Eu-doped scales, the Er-doped BT scales exhibited considerably more fluorescence than the native, titania, or pure BT counterparts (**Figure 41**). To generate **Figure 41**, a 488 nm excitation source was used for both fluorescence microscopy images (using long pass 505 filter) and transmission images. Also of interest was the relative translucency of the Er-doped titania replicas with respect to the multicomponent scales (**Figure 41 (row 2, column 2)).** The decrease in transparency upon MWHT treatment was likely caused by an increase in particle size. The particle size change from sub 10 nm to 20-100 nm was readily apparent in SE images shown in **Figure 42.**

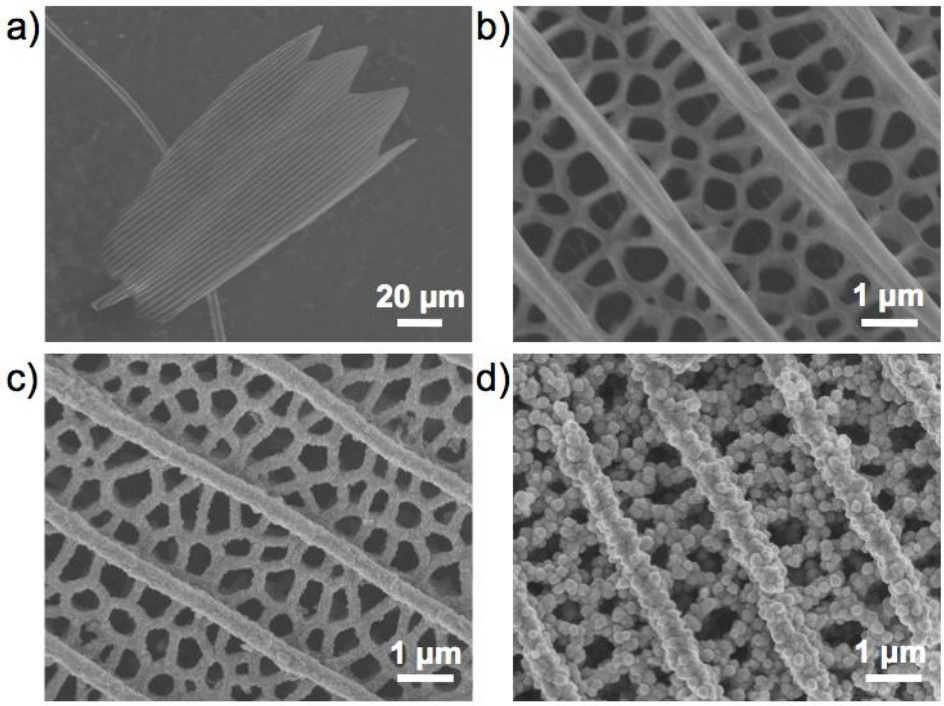

Figure 39: SE images of (a) an entire *P. blumei* native ground scale, and the microstructure within the ground scale in (b) a native state, (c) after coating with Er-Ti-O via the mixed alkoxide SSG process followed by organic pyrolysis, and (d) after hydrothermal conversion into Er-doped BT.

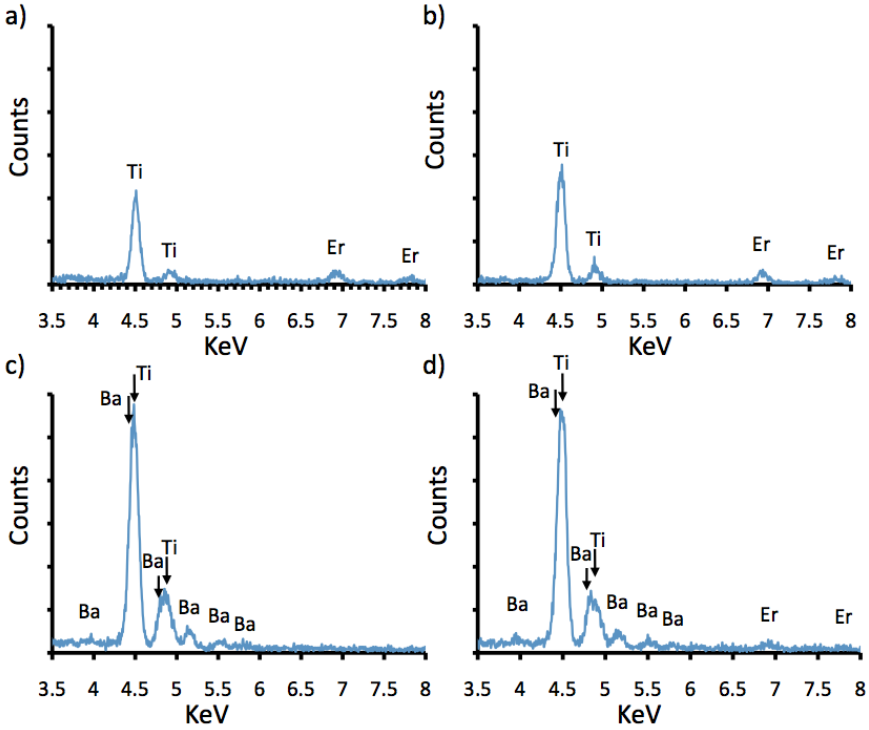

Figure 40: EDS spectra after (a) SSG coating with use of a 25mM solution of 20 mol% Er(III) isopropoxide / 80 mol% Ti(IV) isopropoxide, (b) after coating and organic pyrolysis, and after coating, organic pyrolysis, and MWHT conversion into (c) $BaTiO_3$ and d) Er-doped $BaTiO_3$.

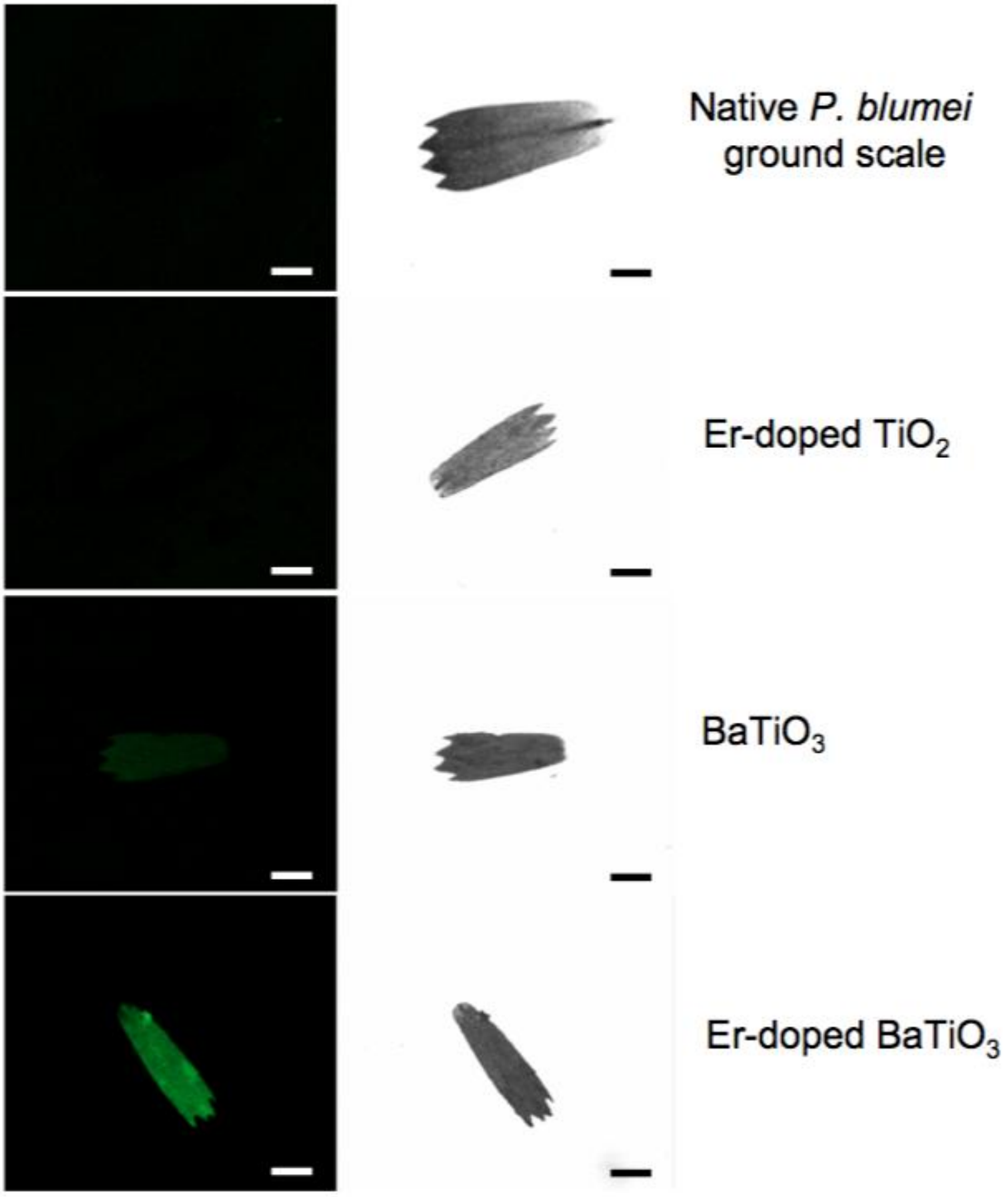

Figure 41: Confocal fluorescence (488 nm excitation, long pass 505 filter) (left) and transmission (488 nm) micrographs of native (top row), SSG coated and pyrolyzed scales (second row), coated and pyrolyzed pure titania scales after hydrothermal conversion into $BaTiO_3$ (third row) , and Er-doped $BaTiO_3$ (bottom row). All scale bars represent 50 micrometers.

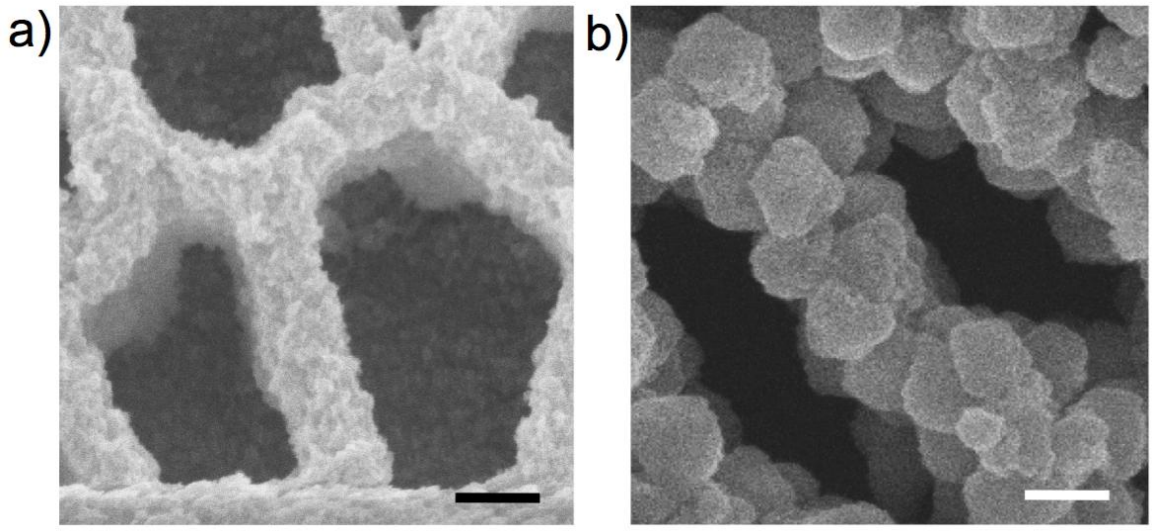

Figure 42: SE images of Er-Ti-O mixed alkoxide SSG coated and pyrolyzed scales (a) before, and (b) after MWHT conversion into nanocrystalline Er-doped $BaTiO_3$. Both scale bars represent 100 nm.

2.5. *Concluding Remarks*

Bioorganic templates were chosen to demonstrate the feasibility of creating functional inorganic materials with unique morphologies on multiple length scales. In fact, the length scales spanned by a single *P. blumei* color-mixing scales spanned over 4 orders of magnitude (0.1 – 100 μm). Eu-doped BT was chosen as the initial product material for the following three reasons (i) for the utility of low–temperature syntheses with respect to preserving the Eu^{3+} valence state, (ii) for imparting photoluminescent properties to demonstrate the uniformity of the chemical conversion process, and (iii) for demonstration of the anti-counterfeiting capability of hierarchical phosphor microparticles. Both the incorporation of Eu in the MWHT process and Er in the SSG process revealed the adaptability of the chemical conversion process developed in **Chapter 1**. Both methods successfully produced photoluminescent inorganic 3D butterfly scale replicas. Such processing versatility is crucial for scalability and cost-effective processing -- not simply proof-of-concept experimentation. Future work should

entail (i) reduction of the Er dopant concentration and subsequent optical interrogation, and (ii) the application of phosphor materials along with retention of a structurally colored template to investigate the effect of emitting materials on the reflectance peaks of templates that exhibit structural color.

2.6. *References*

[36] E. Ernst, B.C. Church, C.S. Gaddis, R.L. Snyder, and K..H. Sandhage, "Enhanced hydrothermal conversion of surfactant-modified diatom microshells into $BaTiO_3$ replicas," *Journal of Materials Research*, vol. 22, pp. 1121-1127, 2007.

[37] M.R. Weatherspoon, M.S. Haluska, Y. Cai, J.S. King, C.J. Summers, R.L. Snyder, and K.H. Sandhage, "Phosphor Microparticles of Controlled Three-Dimensional Shape from Phytoplankton," *Journal of the Electrochemical Society*, vol. 153. pp. H34-H37, 2006.

[38] Y. Cai, M.B. Dickerson, M.S. Haluska, Z. Kang, C.J. Summers, and K.H. Sandhage, "Manganese-doped Zinc Orthosilicate-bearing Phosphor Microparticles with Controlled Three-Dimensional Shapes Derived from Diatom Frustules," *Journal of the American Ceramic Society*, vol. 90, pp. 1304-1308, 2007.

[39] S. Kinoshita and S. Yoshioka, "Structural Colors in Nature: The Role of Regularity and Irregularity in the Structure," *ChemPhysChem*, vol. 6, pp. 1442-1459, 2005.

[40] S. Kinoshita. *Structural Colors in the Realm of Nature*. Toh Tuck Link, Singapore., World Scientific Publishing Co. Pte. Ltd., 2008.

[41] G. Erdtman. *Handbook of palynology: morphology, taxonomy, ecology; an introduction to the study of pollen grains and spores*. New York, Hafner, 1969.

[42] Estimating the global economic and social impacts of counterfeiting and piracy. London, Frontier Economics Ltd, 2011.

[43] G. Haertling, "Ferroelectric Ceramics: History and Technology," *Journal of the American Ceramic Society*, vol. 82, pp. 797-818, 1999.

[44] J. Li; M. Kuwabara. Preparation and luminescent properties Eu-doped $BaTiO_3$ Thin Films by sol-gel process," *Science and Technology of Advanced. Materials*, vol. 4, pp. 143 – 148, 2003.

[45] Y. Tsur, T.D. Dunbar, and C.A. Randall, "Crystal and Defect Chemistry of Rare Earth Cations in $BaTiO_3$," *Journal of Electroceramics*, vol. 7, pp. 25 – 34, 2001.

[46] J. Vernon, Y. Fang, Y. Cai, K.H. Sandhage, "Morphology-Preserving Conversion of a 3D Bioorganic Template into a Nanocrystalline Multicomponent Oxide Compound," *Angewandte Chemie International Ed.*, vol. 49, pp. 7765 -7768, 2010.

[47] M. R. Weatherspoon, M. B. Dickerson, G. Wang, Y. Cai, S. Shian, S. C. Jones, S. R. Marder, and K. H. Sandhage, "Thin, Conformal, and Continuous SnO2 Coatings on Three-Dimensional Biosilica Templates through Hydroxy-Group Amplification and Layer-By-Layer Alkoxide Deposition," *Angewandte Chemie International Edition*, vol. 46, pp. 5724-5727, 2007.

[48] G. Wang, Y. Fang, P. Kim, A. Hayek, M.R. Weatherspoon, J. W. Perry, K.H. Sandhage, S.R. Marder, S.C. Jones, "Layer-By-Layer Dendritic Growth of Hyperbranched Thin Films for Surface Sol-Gel Syntheses of Conformal, Functional, Nanocrystalline Oxide Coatings on Complex 3D (Bio)silica Templates," *Advanced Functional Materials*, vol. 19, pp. 2768-2776, 2009.

[49] P. Vukusic, R.J. Sambles, C.R. Lawrence, "Structural colour: Colour mixing in wing scales of a butterfly," *Nature*, vol. 404, pp. 457, 2000.

[50] P. Vukusic, R.J. Sambles, C.R. Lawrence, G. Wakely, "Sculpted-multilayer optical effects in two species of Papilio Butterfly," *Applied Optics*, vol. 40, pp. 1116-1125, 2001.

[51] Kolle, M.; Salgard-Cunha, P. M.; Scherer, M. R. J.; Huang, F.; Vukusic, P.; Mahajan, S.; Baumberg, J. J.; Steiner, U. ,"Mimicking the colourful wing scale structure of the *Papilio blumei* butterfly," *Nature Nanotechnology*, vol. 5, pp. 511 – 515, 2010.

[52] N.J.G. Pearce, W. T. Perkins, J.A. Westgate, Michael P. Gorton, Simon E. Jackson, Clive R. Neal, and S. P. Chenery, "A compilation of new and published major and trace element data for NIST SRM 610 and NIST SRM 612 glass reference materials," *Geostandards Newsletter: The Journal of Geostandards and Geoanalysis*, vol. 21, pp. 115-144, 1997.

[53] M.L. Moreira, G.P. Mambrini, D.P. Volanti, E.R. Leite, M.O. Orlandi, P.S. Pizani, V.R. Mastelaro, C.O. Paiva-Santos, E. Longo, J.A. Varela, "Hydrothermal Microwave: A New Route to Obtain Photoluminescent Crystalline $BaTiO_3$ Nanoparticles," *Chemistry of Materials*, vol. 20, pp. 5381 – 5387, 2008.

[54] R. Pazik, R.J. Wiglusz, W. Strek, "Luminescence properties of $BaTiO_3$:Eu^{3+} obtained via microwave stimulated hydrothermal method," *Materials Research Bulletin*, vol. 44, pp. 1328 – 1333, 2009.

[55] D.P. Galliot, O. Deparis, V. Welch, B.K. Wagner, J.P. Vigneron, and C.J. Summers, "Composite organic-inorganic butterfly scales: Production of photonic structures with atomic layer deposition," *Physical Review E*, vol. 78, pp. 031922-1 – 031922-6, 2008.

CHAPTER 3: Determination of Microwave Hydrothermal Reaction Mechanism(s) in Converting Titanium Dioxide into Barium Titanate Through Inert Marker Experiments

3.1. *Summary*

The reaction mechanism for the formation of $BaTiO_3$ through hydrothermal reaction of titanium dioxide solid with a Ba^{2+} -bearing fluid has been primarily presented with two models justified with indirect kinetic analysis. An inert marker approach was developed to evaluate the hydrothermal reaction mechanism on the surfaces of (100), (001), and (110) oriented single crystal rutile titanium dioxide plates. Such experimentation provides the first demonstration of the use of an inert marker experiment to aid in the determination of the mechanism of a microwave hydrothermal reaction process. TEM imaging was used to evaluate the position of the inert markers with respect to the product phase formed after exposure to a sodium hydroxide- and barium acetate- bearing solution in a microwave hydrothermal reaction at 220°C (known morphology-preserving reaction conditions for 3D anatase titania hierarchical microparticles). HRTEM imaging was used to characterize the phases present at the reactant/product interface. Through such experimentation, a better understanding of the kinetic mechanism controlling the microwave hydrothermal conversion of titanium dioxide to $BaTiO_3$ was obtained.

3.2. *Introduction*

Prior work on the morphology-preserving reaction of nanocrystalline anatase 3D hierarchical assemblies into $BaTiO_3$ replicas (**Figure 43**) clearly demonstrated the ability

for hydrothermal reactions to preserve morphology[56]. Such hydrothermal reactions used barium acetate to avoid incorporation of unwanted small anions (e.g., Cl^-) into the lattice of the product phase[57]. The reaction conditions also utilized temperatures proven to form barium titanate of significant tetragonality (i.e., can be evaluated via peak splitting within XRD pattern)[58].

Although the morphology-preservation of complex 3D templates is clear, the exact kinetic mechanism by which such a reaction occurs is not. For a rather comprehensive discussion of the experimental methods and indirect analyses used to evaluate hydrothermal reaction mechanisms one should reference the review by Gersten[59]. In short, two mechanisms have been proposed for structural evolution during hydrothermal reaction of solid TiO_2 with a fluid reactant to from solid $BaTiO_3$: i) Dissolution-Precipitation (**Figure 44**) and ii) In-situ Transformation (**Figure 45**)[60]. Dissolution-Precipitation involves, most generally, the dissolution of an anhydrous oxide (e.g., titania) in a highly alkaline (pH >11) barium-bearing solvent and subsequent precipitation of ABO_3 (e.g., $BaTiO_3$). In-situ Transformation involves the reaction of the anhydrous oxide with the solvent at the oxide/solvent interface and subsequent diffusion of cations through the solid reaction layer[60].

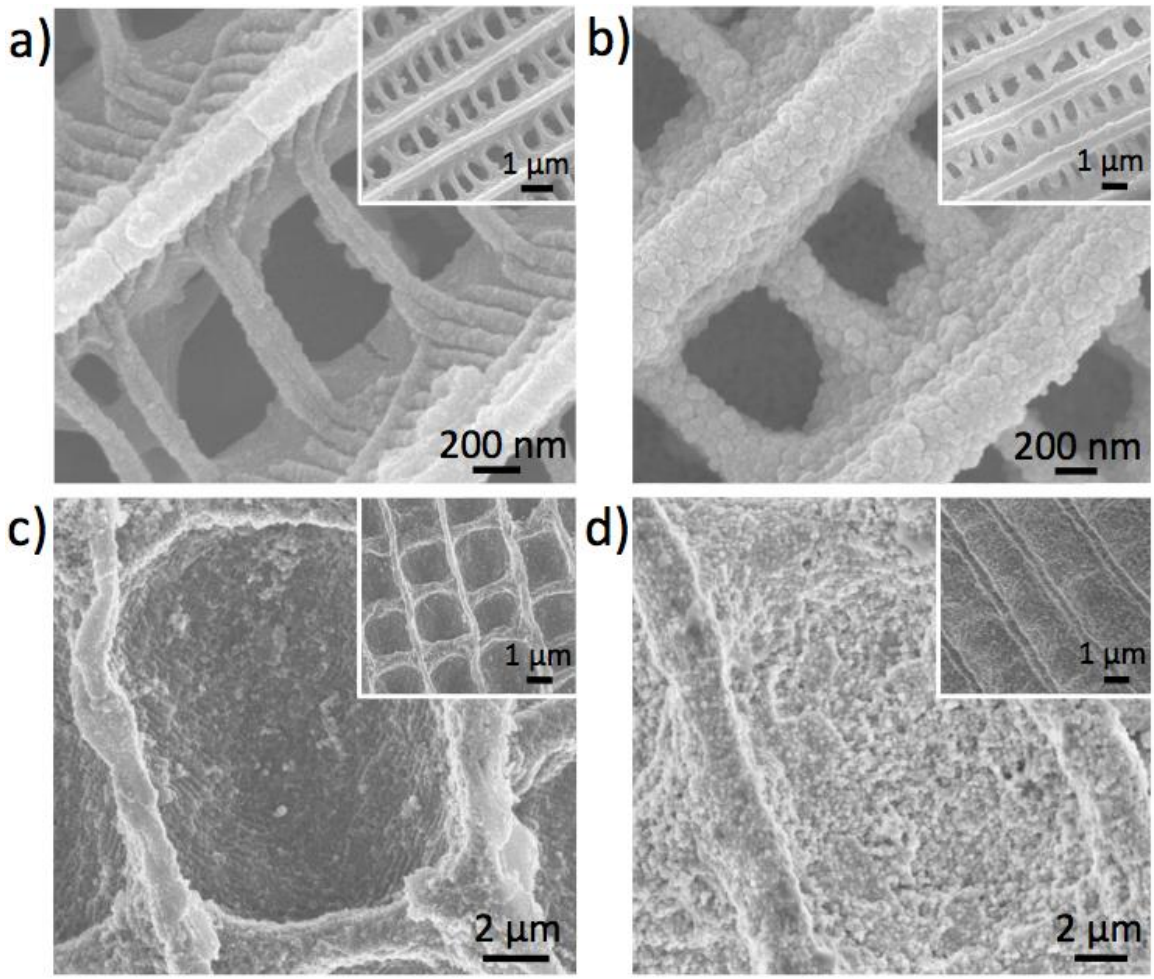

Figure 43: SE images of complex, 3D anatase titania microparticles derived from (a) *Morpho helenor* butterfly wing scales and (c) *Papilio blumei* butterfly wing scales, that were chemically transformed into barium titanate (b, and d respectively) via a morphology-preserving microwave hydrothermal reaction (220°C, 10 hr with 1 M NaOH and 0.125 M barium acetate). Insets are simply lower magnification SE images of each microstructure.

The rate controlling process(es) within the Dissolution-Precipitation mechanism could be chemical reaction at the TiO_2/liquid interface (e.g., via hydrolytic attack to form titanium hydroxide species ($TiOH_x^{4-x}$), liquid phase diffusion of the barium species to the titania species, chemical reaction of barium species with solubilized titania species to form the product $BaTiO_3$, and/or diffusion of barium/titanium cations through the solid product layer (if heterogeneous nucleation on TiO_2). Diffusion of reactant cations to the surface, diffusion of reactant cations through the product layer, and the chemical reaction

between solid and aqueous reactants are possible rate controlling processes for In-situ Transformation[61]. Note that there are two product interfaces either of which could be rate limiting (TiO_2/$BaTiO_3$ and $BaTiO_3$/liquid). Because the Dissolution-Precipitation method involves precipitation after "dissolving" a reactant species, the subsequent product nucleation events can be homogeneous or heterogeneous. As a result, both In-situ Transformation and Dissolution-Precipitation with heterogeneous nucleation could result in conformal $BaTiO_3$ product formation on TiO_2.

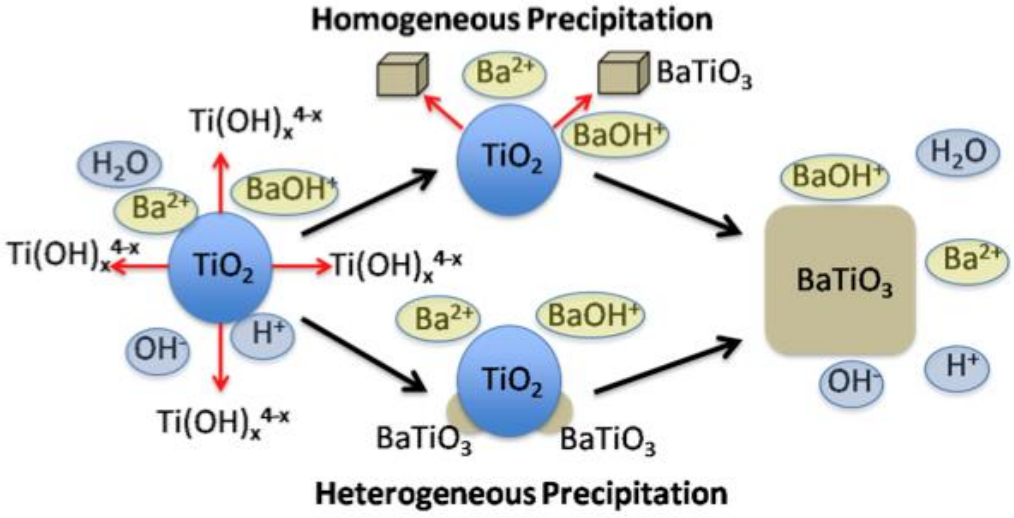

Figure 44: Schematic representation of Dissolution-Precipitation mechanisms showing the precipitation of the product $BaTiO_3$ occurring homogeneously in solution or heterogeneously on a TiO_2 surface.

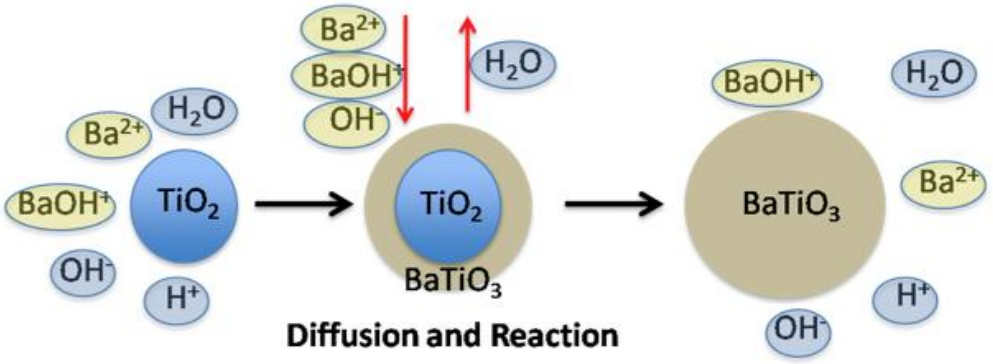

Figure 45: Schematic representation of In-situ Transformation mechanism in which the product $BaTiO_3$ forms on the titania surface and reaction proceeds via solid-state diffusion through the product layer to form $BaTiO_3$.

Experimental observations used to identify reaction mechanism(s) include microstructural analyses. For instance, if the product has the expected same average size (allowing for molar volume expansion upon conversion of anatase titania to cubic or tetragonal $BaTiO_3$) and/or shape as the reactant solid then typically the In-situ Transformation mechanism is cited[59]. If a considerably different particle size distribution than expected (accounting for molar volume change) or different morphology is observed, then a Dissolution-Precipitation mechanism is most often identified[59]. Unfortunately, such evidence is not definitive. One example is when heterogeneous nucleation occurs in the Dissolution-Precipitation process and the product conforms to the surface of the reacting substrate[62,63].

In order to optimize shape preservation, reaction mechanisms may need to be understood and perhaps controlled. Hydrothermal synthesis conditions can be varied to affect the rates of nucleation and growth[64]. Some of the variables likely to affect nucleation and growth mechanisms include the concentrations of reacting species, heating rate, reaction temperature and reaction time[64]. One cannot ignore the effects of the reacting titania polymorph, mineralizer concentration, mineralizer type, barium salt source, barium concentration, mineralizer/TiO_2 ratio, or Ba/Ti ratio[59].

Experimental data demonstrating the effects of mineralizer concentration (KOH) and hydrothermal treatment temperature on the morphology of $BaTiO_3$ formed from anodized titania has been reported[65]. The mineralizer concentration within the hydrothermal solution and the temperature of transformation were used as ordinate and abscissa, respectively, for mapping the resulting $BaTiO_3$ product morphology. Drastic morphological changes were effected by simply changing one variable (temperature or

pH) under thermodynamically favorable conditions for BT formation[66]. Wei, *et al.* proposed that, by increasing mineralizer (KOH) concentration, the nucleation rate could be reduced, producing a "flower" structure rather than a conformal shape-preserved product[66]. However, McCormick and Slamovich produced results that disagree with the conclusions of Wei, *et al.* regarding mineralizer concentration[67]. McCormick and Slamovich hydrothermally treated an amorphous titania film and found that increasing temperature, barium ion concentration, and increasing pH (mineralizer concentration) all led to a reduction in $BaTiO_3$ product grain size, which indicated an increase in the nucleation rate[67]. The discrepancy regarding hydroxyl concentration between the findings in the aforementioned studies can be explained. Wei, *et al.* used barium hydroxide as the barium cation source. By increasing the mineralizer (KOH) concentration, the solubility of barium hydroxide may be reduced (i.e., according to LeChatelier's principle). Additionally, the dissolution rate of the titania may be increased in solutions with increased alkalinity. A reduction of barium cations in solution could be a cause for the reduction in nucleation rate. Also, the enhanced rate of titania dissolution may lead to morphological changes. Based upon the findings of McCormick and Slamovich, who independently analyzed the effects of the barium concentration (i.e., $BaCl_2$) and mineralizer (NaOH) concentration, the "flower" morphology observed by Wei, *et al.* may be due to a slower nucleation rate caused by a reduced Ba:Ti reactant ratio rather than due to an increase in the mineralizer concentration.

To the author's knowledge, there are three reports in which single crystal TiO_2 substrates underwent hydrothermal reaction to form $BaTiO_3$ films[68,69,70]. The current research differs from such prior work for the following reasons: i) in this case *microwave*

hydrothermal processing was utilized, ii) the temperature of conversion was greater than 200°C, iii) such experiments independently varied the Ba and OH concentrations, iv) in this work, cross-sections of more than one crystallographic orientation of TiO_2 were interrogated via SEM and TEM, and v) inert markers were utilized for identification of the interface at which $BaTiO_3$ predominantly formed.

Inert marker experiments (like that used by Smigelskas and Kirkendall[71] to discover the Kirkendall Effect) have often involved the use of radioactive particles, inert oxides, noble metals, or refractory metals to mark the initial interface between two reactants in solid-solid and gas-solid reactions. For example, Pt nanoparticles were used as an inert marker for the reaction between (100), (001), (101), and (110) oriented rutile titania single crystals and "BaO" vapour (i.e., vapor generated by decomposition of $BaCO_3$ through electron beam evaporation under high vacuum and exposed to titania substrate in $1x10^{-1}$ Pa oxygen atmosphere) at temperatures ranging from 700°C to 950°C[72]. In the Pt nanoparticle inert marker study, the morphologies of the single crystal surfaces changed with temperature, and, the apparent diffusing species changed with temperature[72]. Interestingly the phase formation also depended upon temperature with $BaTiO_3$ being the sole product phase at 700°C - 800°C and Ti-rich phases (with respect to $BaTiO_3$, e.g., $Ba_4Ti_{13}O_{30}$) formed between the $BaTiO_3$ product layer and reactant TiO_2. Such experimentation revealed that the location of the inert markers with respect to the final $BaTiO_3/TiO_2$ interface could be used to identify the location of the formation of product material and thereby suggest rate-limiting diffusing species. One should note that the 800°C treatment of single crystal titania with "BaO" vapour and electrochemical hydrothermal treatment of a Ti metal substrate with a radioactive tracer, have both

indicated barium cations as the rate-limiting diffusing species through the $BaTiO_3$ product layer[72,73].

Even with the initial titania/solution interface marked with inert particles, the reaction mechanism may not be readily identified. Possible cross-sections after MWHT treatment of single crystal rutile titania templates with inert markers are identified and depicted schematically in **Figure 46**. Because oxygen is prevalent in the reaction solution and in the titania reactant, cases where oxygen anions act as the rate limiting diffusing species have not been considered. It should also be noted In-situ Transformations in which there are several rate limiting species (e.g., barium cations inward and titanium cations outward) are not shown. In such a case, the inert particles would be suspended within the $BaTiO_3$ product layer closer to the source of the faster diffusing species or directly in the center of the product layer if competing diffusion rates are commensurate. For a dissolution-precipitation mechanism (**case 3** or **4** in **Figure 46**), Au particles are either lost upon dissolution of TiO_2 (**Figure 46**: **case 3b** and **case 4b**) or will mark the TiO_2/liquid interface (**Figure 46**: **case 3a** and **case 4a**). Additionally, the microstructural appearance of **case 1** and **case 4a** may be indistinguishable.

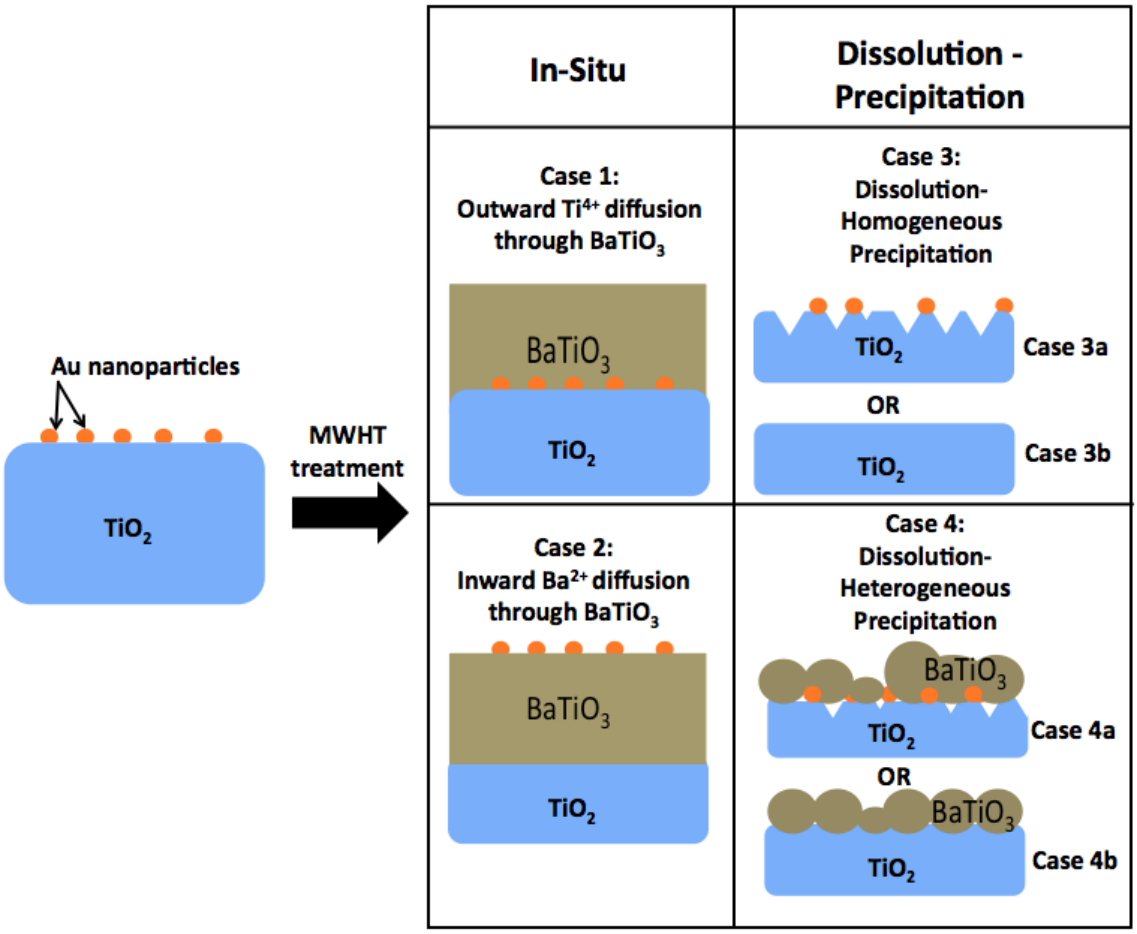

Figure 46: Schematic representations of possible cross-section morphologies resulting from MWHT treatment of single crystal rutile templates decorated with Au nanoparticle inert markers. Note: Au particles may be lost upon dissolution of TiO_2 (case 3b, case 4b).

3.3. *Experimental Procedures*

3.3.1. Preparation of Single Crystal Rutile TiO_2 for MWHT Au-Marker Experiment

Two-side polished (EPI polished to 0.5 -1.0 nm roughness with 1/10 wave flatness) single crystal plates (10 mm x 10 mm x 0.5mm) of rutile titania [(100), (001), and (110) orientations] were purchased from a commercial source (>99.99% purity, MTI Corporation, CA, USA). Such plates were scribed and fractured into four 5 mm x 5 mm x 0.5 mm specimens. The resulting sections were interrogated with grazing incidence

angle XRD and SEM analyses. Some sections were sputter coated with Au for 20 sec at 20 mA. After SEM imaging, sputter coated samples were placed onto a glass slide and then heated in air on a level Cimarec SP131325 stir plate (Barnstead International, IA, USA) to 450°C (temperature confirmed with handheld infrared digital thermometer (MiniTEMP MT6, Raytek Corporation, CA, USA). The samples were held at 450°C for 2 hr, after which time the heater was turned off and the samples were moved to the edge of the hot plate to air cool. Au nanoparticle inert markers were formed by de-wetting of the thin sputter-coated Au films on single crystal rutile titania. An extremely short sputter time and a heat treatment temperature less than 500°C was chosen to create sub 50 nm Au nanoparticles decorated on single crystal rutile titania specimen surfaces[74,75]. The samples were then weighed with an analytical balance (AE240, Mettler-Toledo Inc., OH, USA), interrogated with SEM, and then subjected to MWHT treatment. For corrosion rate data the single crystal specimen weights before MWHT and after MWHT treatment (with no Au markers) were reported from average of 3 measurements. The uncertainty of the weight measurements was represented by sample mean ± calculated standard uncertainty (i.e., represented by estimated standard deviation from 3 independent weight measurements). The difference between the before and after MWHT treatment mean weights were taken, and the total uncertainty was calculated by propagation of error (i.e., taking the positive square root of the added variances). It was assumed that the estimated mean values of the weight losses were approximately normally distributed. For this reason the mean weight loss (m_{wl}) ± combined uncertainties (u_{wl}) reveals that the unknown true value of the weight loss for each single crystal titania specimen is believed to lie in the interval $m_{wl} \pm u_{wl}$ with a 68% confidence

level[76].

3.3.2. MWHT Treatment

The single crystal rutile titania specimens were sealed within 100 mL Teflon™ XP1500 Plus vessels (CEM Corp., Matthews, NC, USA) containing a 20 mL solution of 0.125 M barium acetate (99% purity, Alfa Aesar, MA, USA) / 1 M NaOH (diluted from 50% w/w aq. soln., Alfa Aesar, MA, USA) in previously-boiled water. The sealed specimens were then heated within 7 min to 220°C in a microwave reaction system (MARS 230/60, 2.45 GHz, CEM Corp., Matthews, NC, USA) with a maximum power setting of 1600 W and held at this temperature for 10 hr. Although the ramp times and treatment temperatures were kept constant, some specimens (with and without Au inert markers) were treated with various concentrations of sodium hydroxide and barium acetate and were treated for various times ranging from 1-100 hr.

After removal from the Teflon™ vessels, the rutile titania single crystal sections were placed in 20 mL of 1 M acetic acid (diluted from glacial acetic acid, 17.4N, 99.9% purity, Fisher-Scientific, PA, USA) in a petri dish for 20 min. Reacted sections were then moved into a Petri dish containing 20 mL of boiled DI water for 5 min. After rinsing with water, the single crystal sections were placed in 20 mL of IPA (99% purity, Acros Organics, Geel, Belgium) in a Petri dish for 5 min. Each single crystal was rinsed with 5 mL of flowing IPA (applied via 1 mL pipette) and then dried with warm flowing air for 1 min. Dried single crystal specimens were then weighed with an analytical balance.

3.3.3. Morphology, Phase, and Chemical Characterization

The surfaces and some fracture sections of the single crystals specimens (after each step in the marking and conversion process) were imaged with a field emission scanning electron microscope (1530 SEM, LEO/Zeiss Electron Microscopy NY, USA) after mounting directly on aluminum stubs (Ted Pella, CA, USA) with double-sided carbon tape ((Ted Pella, CA, USA). XRD analyses were conducted on single crystal sections mounted with clay on a sample holder using an X'Pert Pro Alpha-1 diffractometer (PANalytical B.V., ALMELO, Netherlands) with monochromatic $Cu_{K\alpha 1}$(1.5405980 Å) radiation emanating from a 1.8 kW ceramic X-ray tube with a copper anode (45 kV, 40 mA) through a symmetrical Johannson monochromator. The source was outfitted with a 1° fixed anti-scatter slit, a ½° programmable divergence slit, and a 5 mm mask. The diffracted beam optics were outfitted with a 5.5 mm anti-scatter slit before the X'Celerator detector. Each pattern was produced with a summation of 16 identical 40 minute scans conducted with a fixed incident angle of 2° and a step size of 0.01671° 2θ. All transmission electron microscopy (TEM) sample preparation, bright field imaging, selected area electron diffraction (SAED) and high resolution TEM imaging (HRTEM) were performed by Dr. Ye Cai (Georgia Institute of Technology). The TEM analyses were conducted using a JEOL 4000 EX instrument (Japan Electron Optics Laboratory, Tachikawa, Tokyo).

3.3.4. Measuring Transformation and Nucleation Rate

SE micrographs of (110) oriented rutile titania after 1, 2, 4, 6, 8, 10, 40, and 100 hr of MWHT reaction (220C, 0.125 M barium acetate, 1 M sodium hydroxide) taken at 25,000x magnification were used to measure surface area fraction transformed into

$BaTiO_3$ (X_{SA}) and number of nuclei as a function of reaction time. An example micrograph is shown in **Figure 47**. The number of nuclei were counted on five independent micrographs and the calculated mean value of nuclei at each reaction time ± calculated standard uncertainty (i.e., represented by estimated standard deviation of number of nuclei counted on 5 independent micrographs). Note: any nuclei truncated by an edge of the micrograph were counted as ½ and the total was always rounded up to the nearest integral value. For X_{SA}, a 15 x 9 grid with 1 micrometer line spacing (i.e., 135 total intersections as shown in **Figure 47**) was overlaid on SE micrographs and the number of intersections covering $BaTiO_3$ were counted. The number of intersections on $BaTiO_3$ divided by the total number of intersections provided the surface area fraction transformed into $BaTiO_3$ for a particular micrograph. Once again five independent micrographs were interrogated for each reaction time and condition considered. The mean X_{SA} ± calculated standard uncertainty (i.e., represented by estimated standard deviation of X_{SA} measured from 5 independent micrographs). The X_{SA} for 4 hr reaction times were also evaluated with MWHT reaction solutions that contained i) quintuple the sodium hydroxide concentration and ii) quintuple the barium acetate concentration.

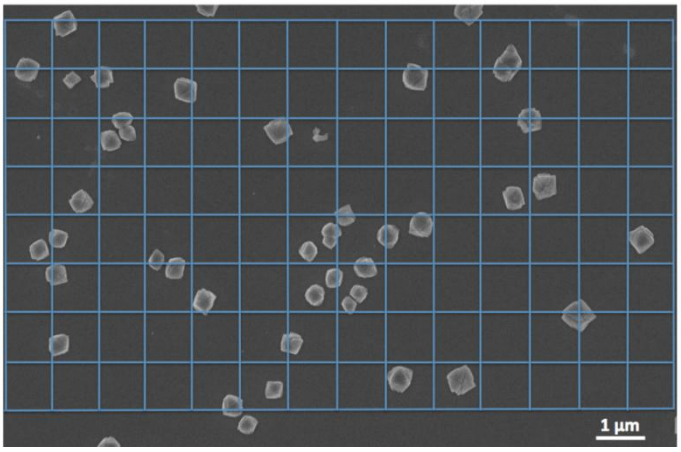

Figure 47: SE electron micrograph of (110) oriented rutile titania single crystal after MWHT reaction with 0.12 5M barium acetate and 1 M NaOH for 2 hr at 220°C. Blue grid overlay used to

determine average surface area fraction transformed into $BaTiO_3$ after a given reaction time. Such micrographs also used to count the number of nuclei formed as a function of time.

3.4. *Results & Discussion*

In order to analyze the morphology-preserving reaction of TiO_2 into $BaTiO_3$ rutile titania single crystals of three different orientations [(100), (001) and (110)] were purchased. These 10 mm x 10 mm x 0.5 mm plates (representative image shown in the inset of **Figure 48**) were confirmed to be single crystal rutile TiO_2, and of the manufacturer's indicated orientation, via XRD analysis shown in **Figure 48.** Such samples were sectioned into 5 mm x 5 mm x 0.5 mm specimens and then sputter coated with Au for 20 sec. Sputter coated sections were then heat treated for 2 hr at 450°C in order to form a surface decorated with Au nanoparticles through de-wetting of the thin Au film. Once Au nanoparticle inert markers were formed, MWHT treatment was conducted using similar conditions as for the morphology-preserving reaction of anatase titania butterfly scale replicas into barium titanate. Top view SE images of (100) oriented rutile TiO_2 single crystals are shown in **Figure 49** in the starting state, after sputter coating, after Au nanoparticle formation, and after MWHT reaction of Au decorated titania with 1M NaOH and 0.125 M barium acetate solution for 10 hr at 220°C. Such images revealed the creation of Au nanoparticles (bright particles) on single crystal titania and the retention of such particles after MWHT reaction. Because the inert markers remained adhered to the substrate after MWHT processing, it appeared that this inert marker method for interrogating the reaction of TiO_2 to $BaTiO_3$ was feasible. The morphologies of all three crystallographic planes marked with Au nanoparticles (bright particles) after MWHT treatment with 1 M NaOH and 0.125 M barium acetate at 220 °C after 1, 10, and 100 hr are shown in **Figure 50**. Note: some of the inert markers were still

visible after all reaction times in the (100) and (001) single crystal TiO_2 specimens. Additionally, the (100) and (001) oriented TiO_2 specimens exhibited the same surface morphology with no exposed TiO_2 for reaction times of 1 -100 hr. In contrast, the (110) surface morphology appeared to noticeably change with an increase in reaction time. On the (110) oriented surface the nucleation and growth of isolated particles that eventually impinged upon one another (after 10-100 hr) was evident. No Au nanoparticles were apparent in the top view micrograph of the (110) oriented specimen after 100 hr of MWHT (**Figure 50 row 3, column 3**).

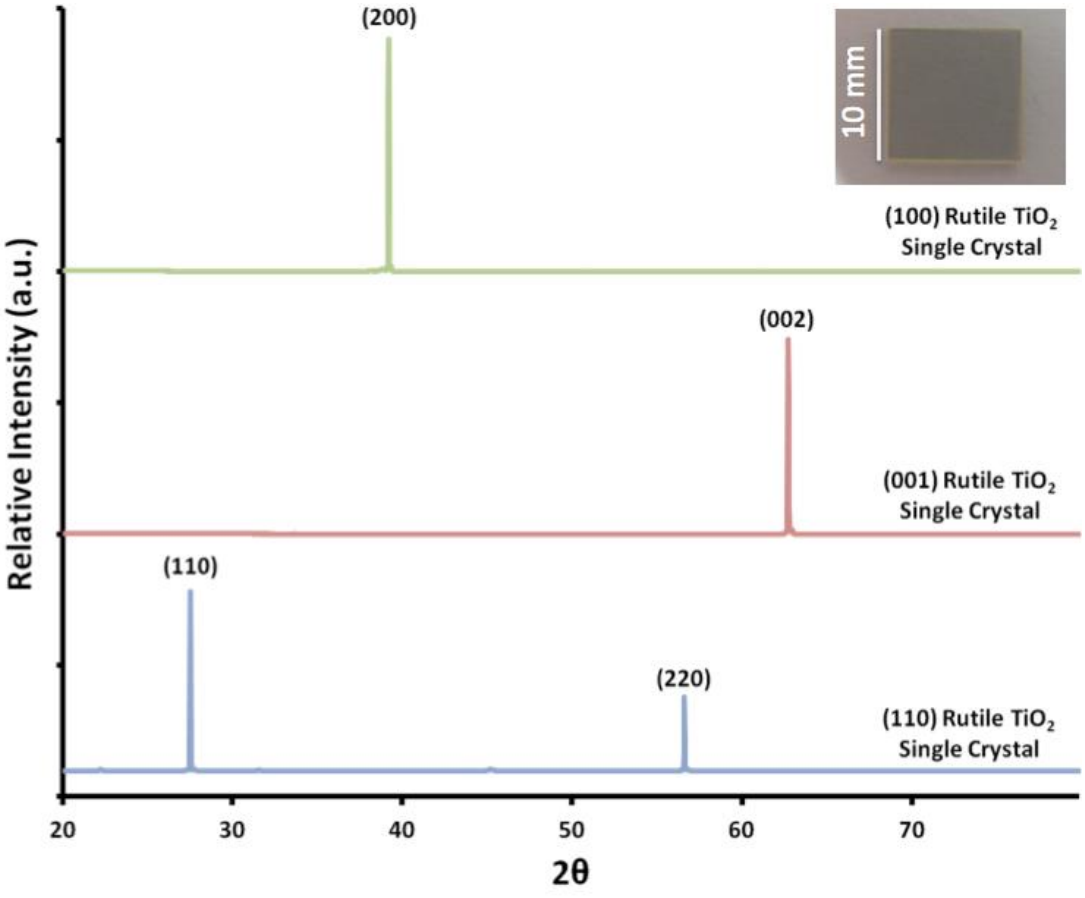

Figure 48: XRD patterns obtained from (100), (001), and (110) oriented single crystal rutile plates. A photograph of a (100) rutile titania plate is shown in the inset and is representative of the two-side polished 10 mm x 10 mm x 0.5 mm samples of each orientation as received from MTI corporation.

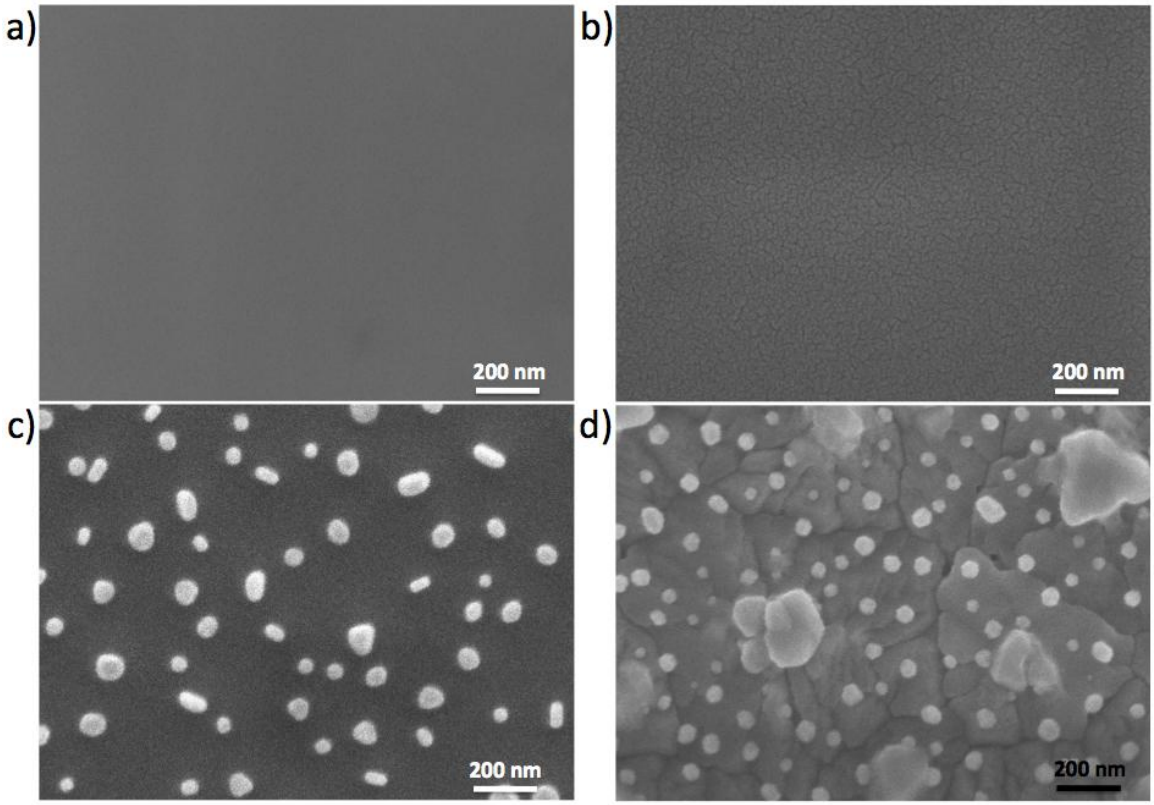

Figure 49: Top view SE images of (100) oriented single crystal rutile TiO_2 plates (a) as received, (b) after sputter coating with gold for 20 sec, (c) after 2 hr of 450°C heat treatment of a sputter coated specimen to create Au nanoparticle markers, and (d) after Au marker formation and 10 hr of MWHT treatment at 220 °C with 1M NaOH and 0.125 M barium acetate.

Elemental analyses of the (110) specimen after 10 hr of MWHT reaction (Representative SE micrograph shown in **Figure 50 bottom row, middle column**), using EDS point analyses, confirmed the presence of Au in the brightest particles, Ba, Ti, and O in the gray regions, and Ti and O in the dark gray regions. To confirm the phases present, as well as the location of the inert markers, TEM cross-sections were prepared. TEM images are projections of a cross-sectioned (ion-milled to a thickness often < 20 nm) sample which may prove difficult to analyze. As an example, consider a case where Au particles are in contact with the titania surface and are encased in $BaTiO_3$. Depending on where the Au-particle/TiO_2 point of contact is located with respect to the ion milled cross-section, one may, or may not, see a gap between the titania and the gold. **Figure 51**

schematically illustrates differences in TEM micrographs due solely to location of ion milled cross-section. Low magnification TEM shots, taking a number of images (i.e., simply increasing sampling) and viewing a reaction layer much thicker than the size of the inert markers can be used to more confidently evaluate the position of inert markers.

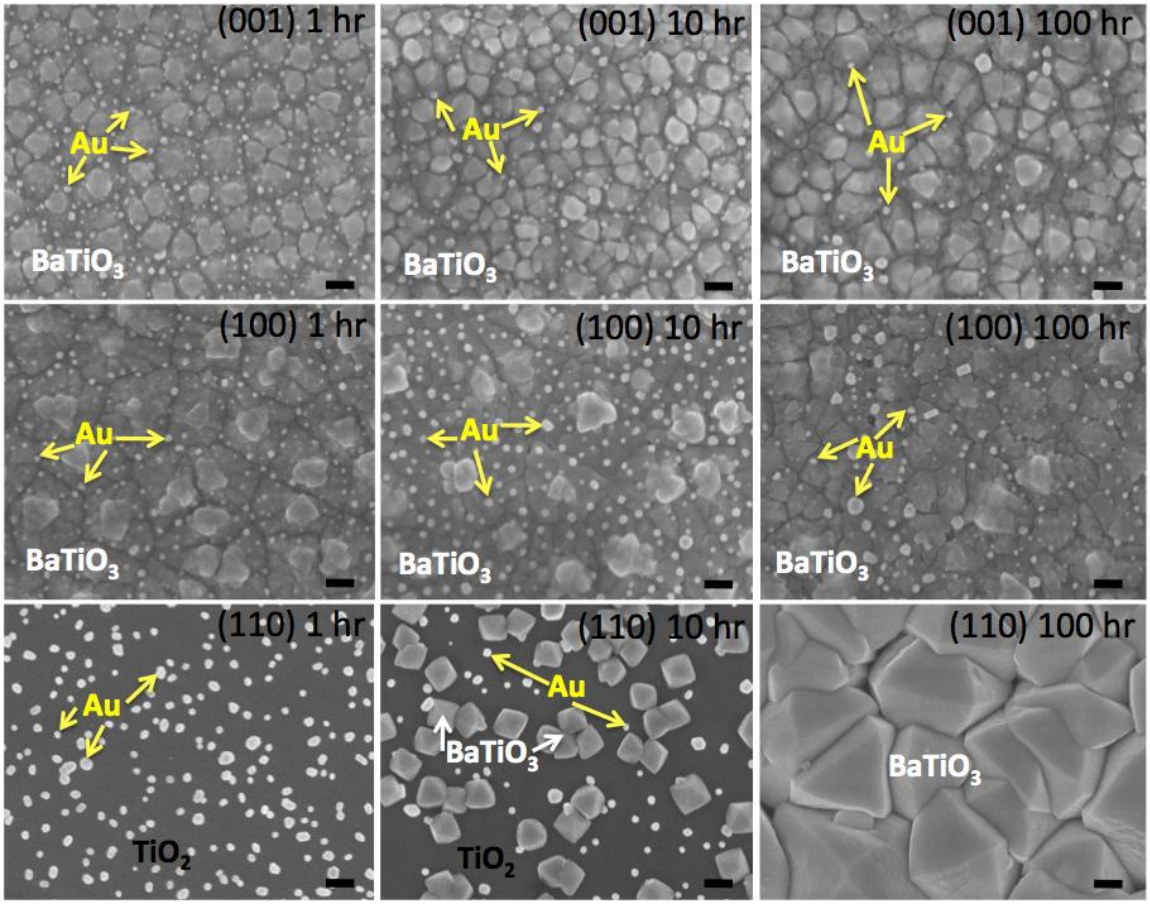

Figure 50: Top view SE images of Au-marked single crystal specimens {(001)-top, (100)-middle, (110)-bottom row} after 220°C MWHT treatment with 1 M NaOH and 0.125 M barium acetate for 1, 10, and 100 hr (increasing reaction time from left column to right column). All scale bars represent 200 nm. Au particles are brightest, followed by $BaTiO_3$ films/particles, and then TiO_2

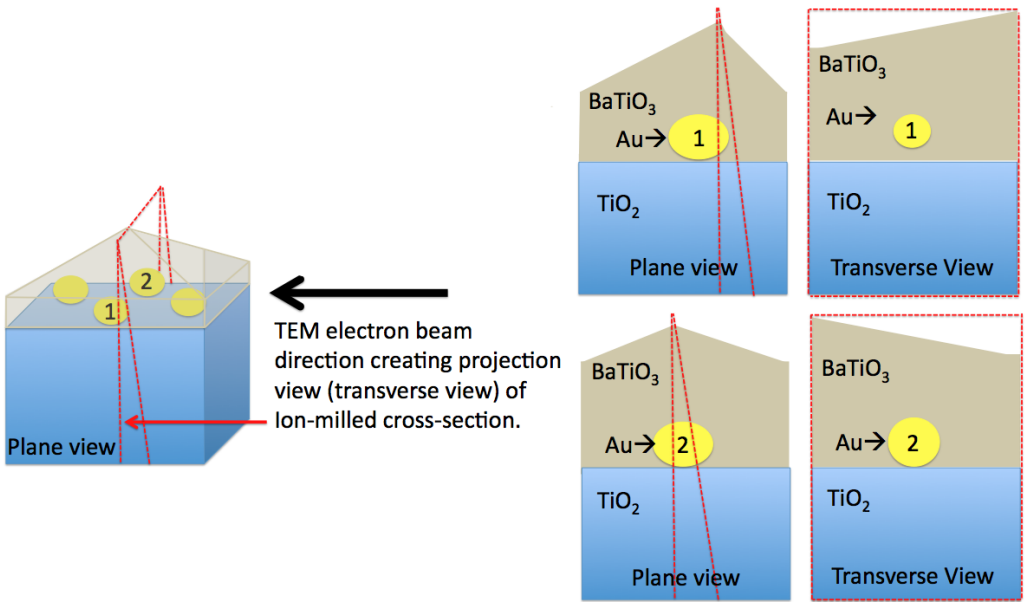

Figure 51: Schematic illustration as to how an ion-milled cross-section location may affect the perceived location of particles within a TEM projection view.

The need for TEM cross-sections was elucidated after evaluating SE images taken of a fracture section from a (110) oriented single crystal treated for 100 hr (**Figure 52 (bottom)**). The $BaTiO_3$ and TiO_2 phases show contrast differences in the SEM image and the uneven TiO_2 surface after reaction is indicated, but the location of the Au nanoparticles cannot be identified. An ion milled TEM cross-section taken at similar magnification clearly revealed the location of the inert marker layer (**Figure 52 (top)**). Such correlation between SE imaging of fracture section and TEM imaging of ion milled cross-section also revealed there were no adverse affects to the surface in the mounting, polishing, and ion milling used for TEM sample preparation (e.g., the $BaTiO_3$ film thickness is equivalent in both characterization methods). The manufacturer-reported sub-nanometer surface roughness of the single crystal templates before MWHT reaction is shown locally with bright field TEM images of (110) oriented single crystal TiO_2 cross-sections after Au sputtering and heat treatment (**Figure 53**).

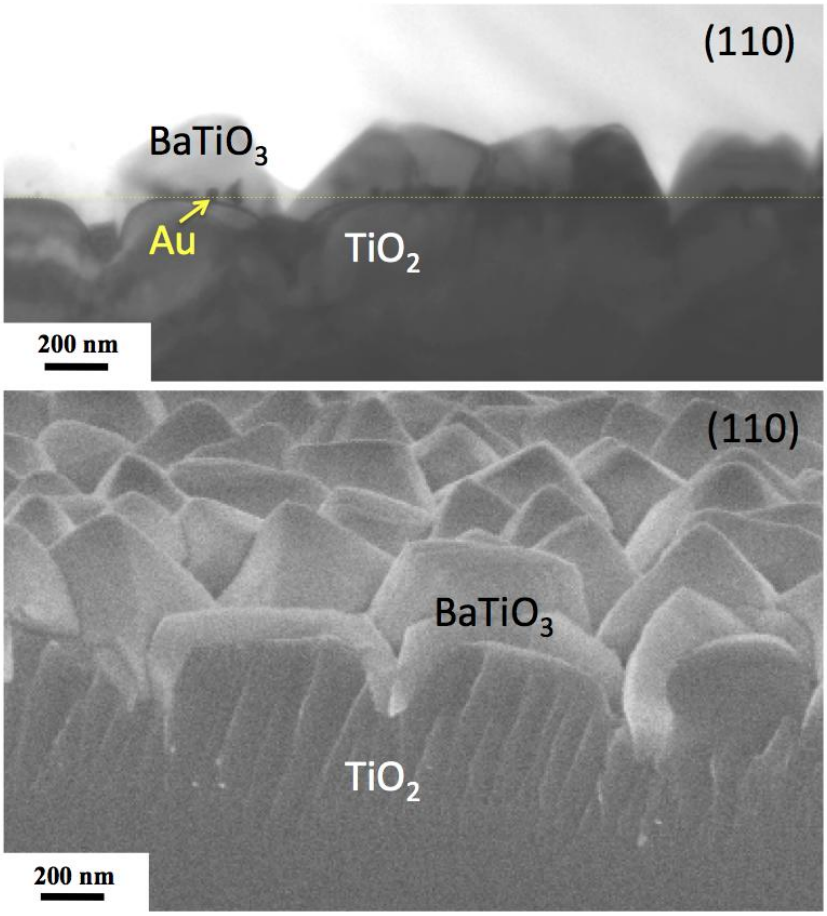

Figure 52: Bright field TEM cross-sectional micrograph (top) and SE micrograph of fracture section mounted vertically and stage tilted 15° (bottom) of (110) rutile titania single crystal after 100 hr 220°C MWHT treatment with 0.125 M barium acetate and 1 M NaOH solution. The magnifications of the images are nearly identical.

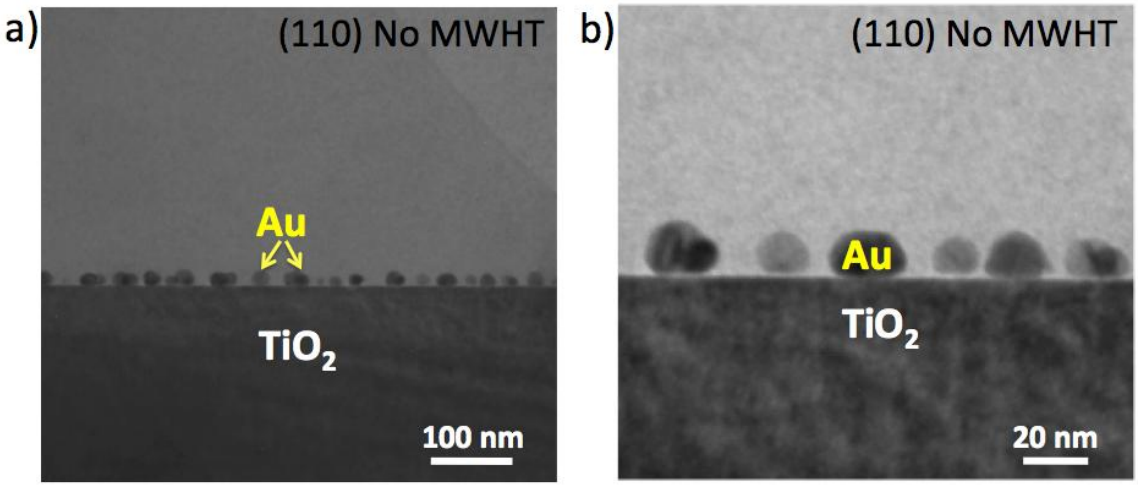

Figure 53: (a) Low magnification and (b) high magnification bright field TEM micrographs of cross-section from Au sputtered and heat treated (110) rutile titania with no MWHT reaction.

A bright-field TEM micrograph of a cross-section from the (001) oriented specimen after MWHT reaction for 10 hr (**Figure 54a**) indicated the location of Au particles (dark particles within a light $BaTiO_3$ product phase) near the TiO_2 surface. In **Figure 54b** a HRTEM lattice fringe image shows that the interface between $BaTiO_3$ and TiO_2 is free of other product phases. Within **Figure 54b,** the identity of the phases present are marked adjacent to the corresponding interplanar spacings of (111) Au, (111) $BaTiO_3$, and (101) rutile TiO_2.

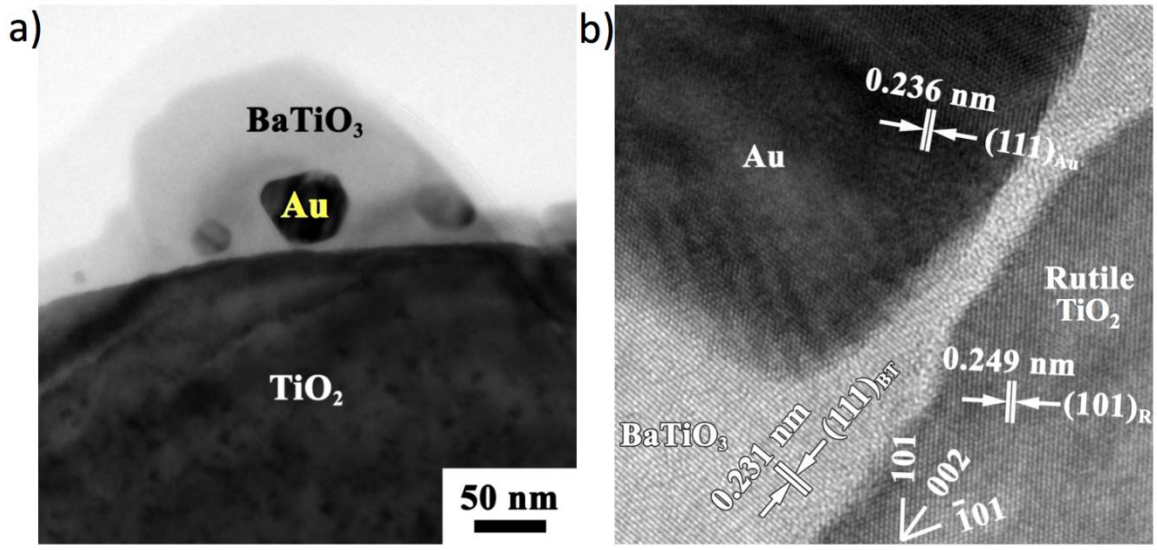

Figure 54: (a) Bright field TEM micrograph and (b) HRTEM lattice fringe image from cross-section of surface of (001) oriented single crystal titania with Au inert markers after MWHT reaction for 10 hrs at 220°C with 0.125 M barium acetate and 1 M NaOH solution. HRTEM image revealed a clean $BaTiO_3/TiO_2$ interface with no product phases other than $BaTiO_3$.

Varied MWHT reaction times were utilized to potentially measure an increase in the $BaTiO_3$ product layer thickness with reaction time. Top view SE micrographs and TEM cross-sections of (001) single crystal titania specimens after 10 hr and 100 hr reaction times are shown in **Figure 55**. Both bright Au particles and $BaTiO_3$ are apparent in the top view SEM images. Low magnification TEM shows a continuous $BaTiO_3$/Au layer over the single crystal titania. Arrows mark the Au markers within lower

magnification TEM images (**Figure 55c,d)** that would be visible in top view SE images (like those shown in **Figure 55a,b**). Although the majority of the Au markers are near the $BaTiO_3$ interface (**Figure 55e,f**) the inert marker experiments on the (001) oriented single crystal titania specimens are inconclusive because the inert markers are not considerably smaller than the entire $BaTiO_3$ product layer. In fact some of the particles span the entire $BaTiO_3$ product layer as shown in **Figure 55c,d**. Interestingly, the product layer did not appear to change in thickness after an order of magnitude increase in reaction time. Top view SE images of (001) and (100) oriented titania single crystals revealed Au particles, similar reaction rates, and similar surface morphologies (**Figure 50 middle** vs. **top row**),. Based upon such SE images, it has been hypothesized the inert marker/ product layer thickness problem also exists with (100) oriented single crystal titania specimens. Difficulty in preparing TEM cross-sections from (100) oriented specimens due to the especially fragile nature of this particular orientation of single crystal rutile titania has prevented TEM, HRTEM, and SAED analyses.

The evolution of the $BaTiO_3$ particle density and size for MWHT-reacted (110) oriented TiO_2 specimens is demonstrated with top view SE images in **Figure 56**. **Figure 57a** is a bright field TEM micrograph taken at the (110) oriented TiO_2 surface after a 10 hr MWHT treatment. Gold particles (dark particles within a light $BaTiO_3$ product phase) were observed near the TiO_2 (darkest material) surface. **Figure 57b** is a HRTEM lattice fringe image marked with the identities of the reactant and product phases next to the indicated interplanar spacings of (110) $BaTiO_3$, and (110) rutile TiO_2. **Figure 57b** also revealed a $BaTiO_3/TiO_2$ interface formed upon MWHT reaction of (110) oriented TiO_2; that is, $BaO\text{-}TiO_2$ compounds other than $BaTiO_3$ were not detected. Top view SE

micrographs and TEM bright field micrographs of cross-sections from (110) oriented single crystal titania specimens after 10 hr and 100 hr reaction times are shown in **Figure 58**. The particle size of $BaTiO_3$ increased with increased reaction time. As with the (100) oriented single crystal specimens, the (110) oriented specimens appear to have the Au particles retained at the $TiO_2/BaTiO_3$ interface.

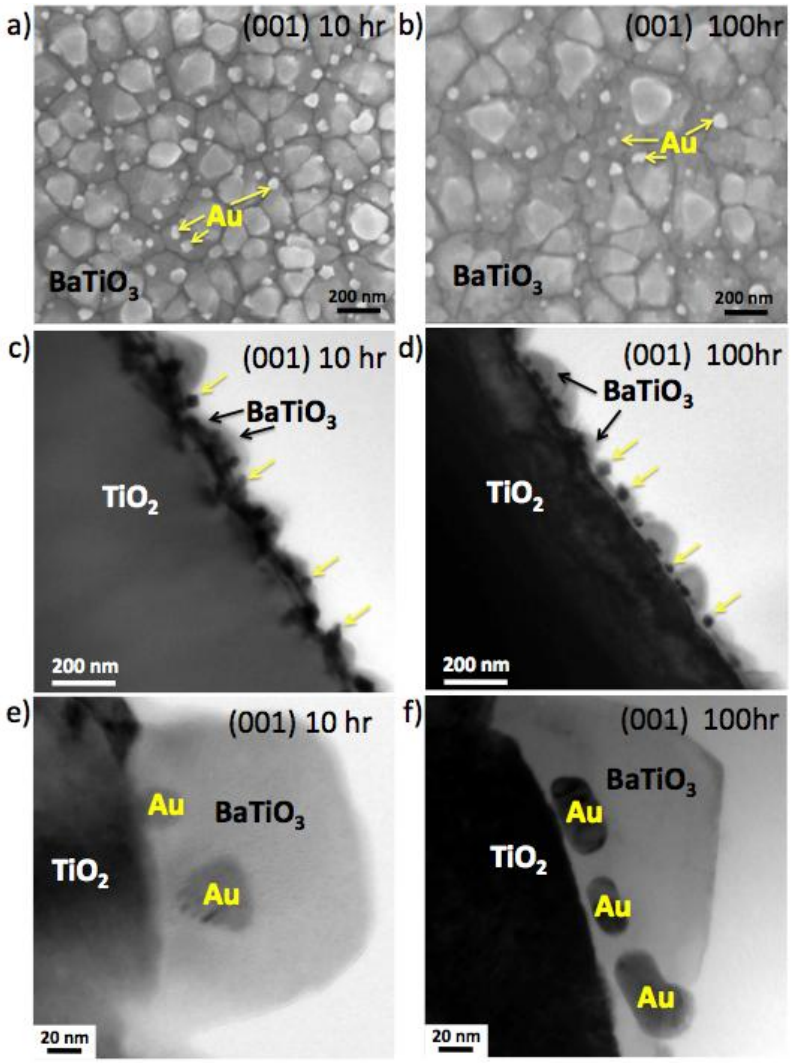

Figure 55: SE top view image of surface of (001) single crystal titania with Au inert markers after MWHT reaction for (a) 10 hrs and (b) 100 hrs at 220°C with 0.125 M barium acetate and 1 M NaOH solution. Corresponding bright field TEM images of Au-marked surface cross-section showing location of Au markers at $TiO_2/BaTiO_3$ interface both after (c,e) 10 hr and (d,f) 100 hr.

Low and moderate magnification images of the (001) and (110) specimens after 100 hr of MWHT treatment are shown in **Figure 59**. The $BaTiO_3/TiO_2$ interfaces (coincide with the Au/TiO_2 interfaces) are marked with a dashed yellow line. The formation of $BaTiO_3$ outside of this line indicated a reaction mechanism involving either titanium cation diffusion outward (**case 1**) through a barium titanate product layer or dissolution of titania followed by heterogeneous precipitation of $BaTiO_3$ (**case 4a**). The presence of an uneven titanium interface showing hillocks (**Figure 57a**) and valleys (**Figure 57a, Figure 59b,** and **Figure 52**), not seen in bright field TEM micrographs of single crystal templates that were decorated with Au nanoparticles (**Figure 52**), also indicated dissolution of the TiO_2 or diffusion of Ti/O from TiO_2 through $BaTiO_3$ product layer. However, a discontinuous product layer (discrete particles) formed on (110) oriented single crystal titania specimens after MWHT reaction for less than 100 hr (**Figure 56, Figure 57a, Figure 58a,c**). Such product particles grew larger with increased MWHT treatment time. The fact that a continuous $BaTiO_3$ layer appeared to form on (100) and (001) crystallographic planes after only 10 hr of MWHT treatment (**Figure 50c**) and the product layer of $BaTiO_3$ did not appear to increase with reaction time (**Figure 50d**) indicated the product $BaTiO_3$ layer may essentially passivate these surfaces against further dissolution.

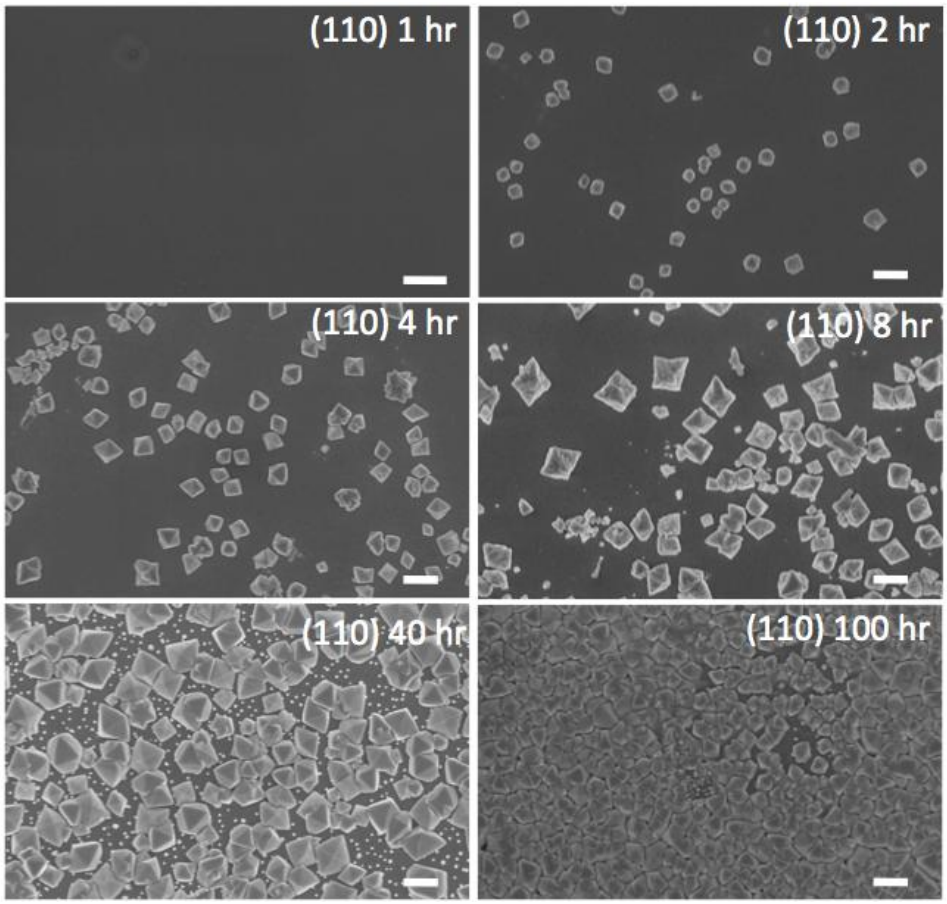

Figure 56: Nucleation and growth of $BaTiO_3$ particles on single crystal (110) oriented TiO_2 specimens as a function of MWHT reaction time. All experiments were conducted at 220°C with 1 M NaOH and 0.125 M barium acetate. All scale bars represent 1 µm.

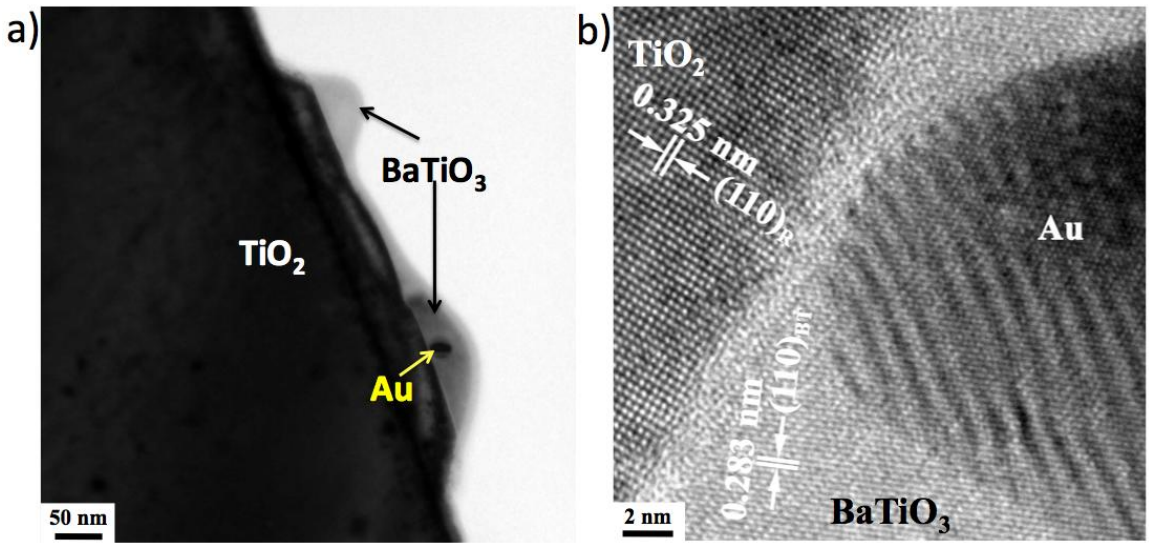

Figure 57: (a) A bright field TEM micrograph and (b) a HRTEM lattice fringe image obtained from cross-sections of (110) oriented single crystal rutile titania specimens with Au inert markers after MWHT reaction for 10 hrs at 220°C with 0.125 M barium acetate and 1 M NaOH solution.

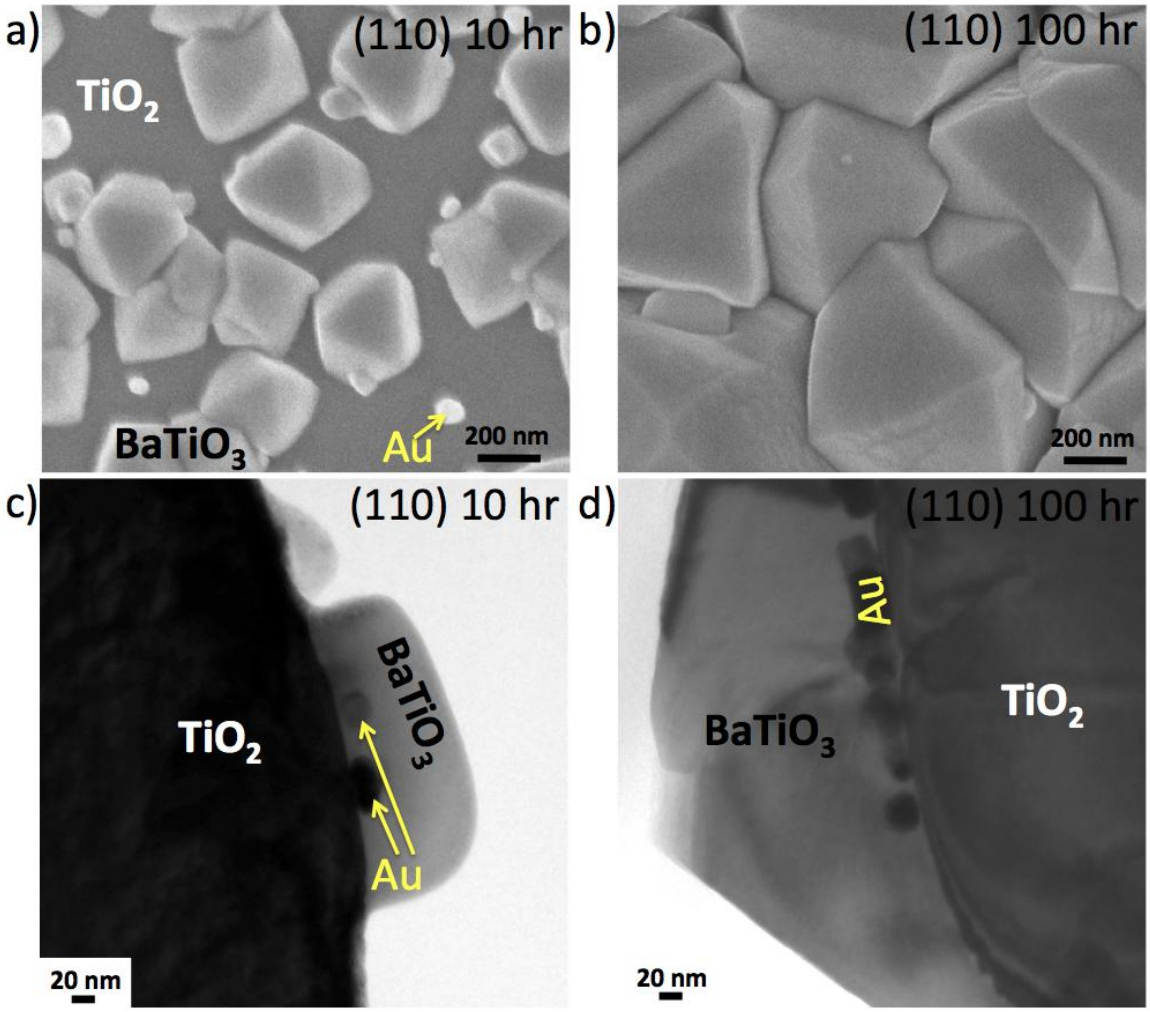

Figure 58: SE top view images of surfaces of (110) oriented single crystal titania specimens with Au inert markers after MWHT reaction for (a) 10 hr and (b) 100 hr at 220°C with 0.125 M barium acetate and 1 M NaOH solution. Corresponding bright field TEM images of cross-sections of surfaces showing the location of Au markers at TiO_2/$BaTiO_3$ interfaces both after c) 10 hr and d) 100 hr.

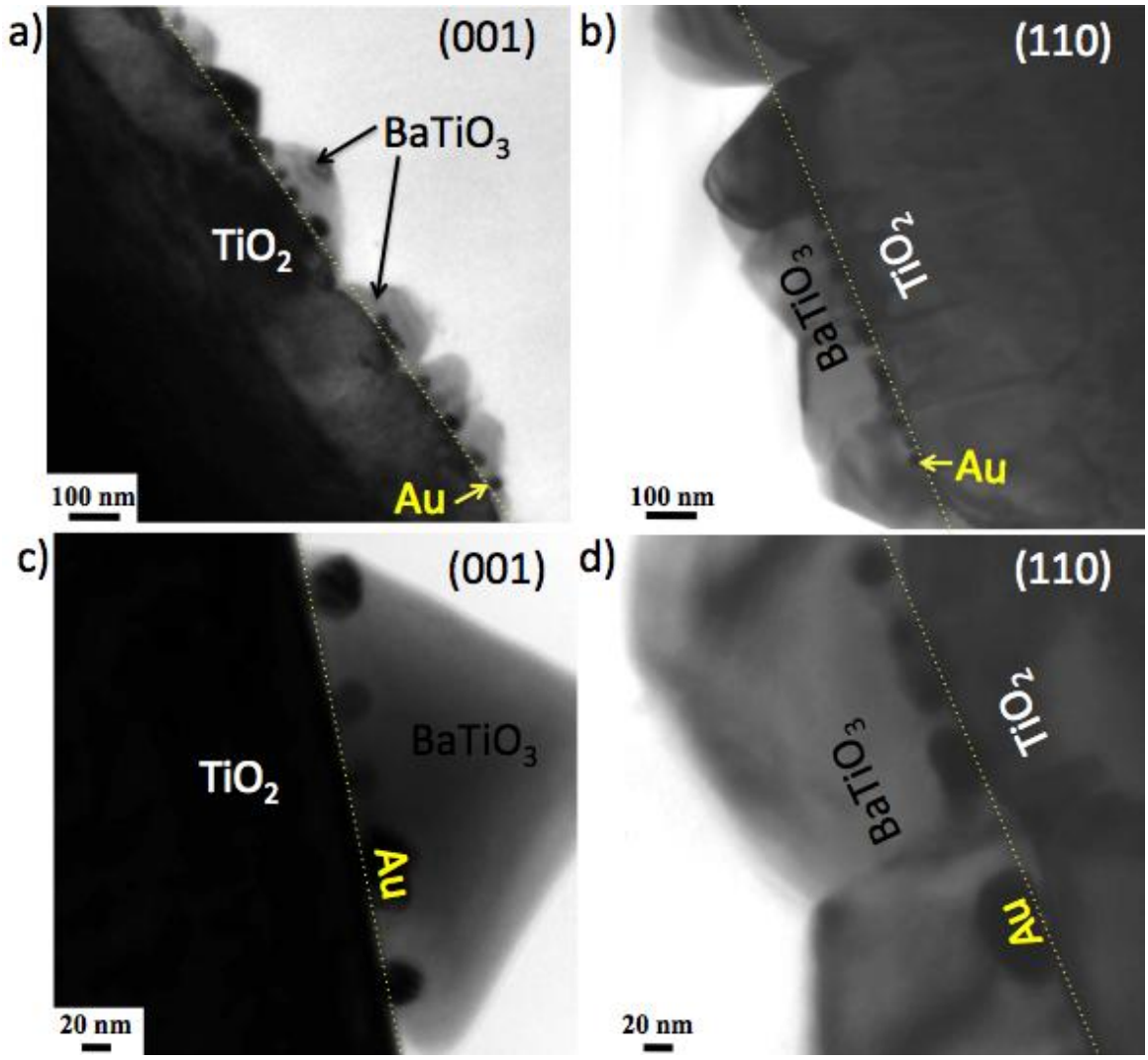

Figure 59: Bright field TEM micrographs of (a, c) (001) oriented and (b, d) (110) oriented single crystal rutile titania specimens after 100 hr MWHT reaction at 220°C with 20 mL of 0.125 M barium acetate and 1 M NaOH solution.

Single crystal titania specimens, with and without the presence of Au markers, were treated with NaOH only. **Figure 60** shows that only the (001) plane revealed a significant change in surface morphology with MWHT treatment for 10 hr in a 1 M NaOH solution. The presence of the Au markers also did not seem to significantly affect the surface morphology of the single crystal titania specimens after treatment with NaOH alone (**Figure 60a vs. b, c vs. d and e vs. f**). As seen after MWHT treatment in the barium-containing solutions the Au particles remained on the surface if the underlying

titania had not been dissolved away. Weight measurements obtained before and after MWHT treatment provided average (total weight loss after 10 hr of reaction) corrosion rate data for the single crystal rutile titania specimens without Au markers in **Table 2**. The average corrosion rate (i.e., after 10 hr of MWHT treatment at 220°C with 1 M NaOH) for (001) rutile titania was the fastest ($0.0041 \pm .0016$ $g \cdot cm^{-2} \cdot s^{-1}$), followed by (100) rutile titania ($0.0032 \pm .0015$ $g \cdot cm^{-2} \cdot s^{-1}$), and (110) rutile titania was the slowest (0.0022 ± 0.0011 $g \cdot cm^{-2} \cdot s^{-1}$). The rates are commensurate with the calculated relative surface energies of the individual planes of rutile titania in the presence of vacuum and water[77,78]. In fact, the relative surface energies of partially and fully hydrogenated rutile TiO_2 crystallographic planes[78] have been reported to be consistent with clean (i.e., in vacuum) surface energies ($\gamma_{(110)} = 0.89$ $J/m^2 < \gamma_{(100)} = 1.12$ $J/m^2 < \gamma_{(001)} = 1.65$ J/m^2)[77]. Based upon average corrosion rate measurements and reported rutile crystallographic plane surface energies, this work has used crystallographic planes of titania spanning the slowest to fastest dissolution rates (lowest to highest surface energies) of single crystal titania. The faster dissolution rates of the (001) and (100) planes may be the reason such planes present similar $BaTiO_3$ product surface morphology in top view SE images taken after 1 hr, 10 hr and 100 hr of MWHT reaction (**Figure 50**).

Although there was a molar excess of NaOH in the MWHT solution with respect to TiO_2, it was hypothesized that further increasing the NaOH concentration would result in faster dissolution rates (Note: TiO_2 is an acidic oxide). This hypothesis was confirmed with (110) rutile titania sections. The (110) specimens demonstrated very little morphology change after 10 hr MWHT treatment at 220°C in 1 M NaOH (**Figure 60e**). After 10 hr MWHT treatment at 220°C in 5 M NaOH, however, the (110) surface

appeared heavily pitted in SE images (**Figure 61**). The apparent enhancement of dissolution was quantified (**Table 2**) by determining average corrosion rate through weight loss after 10 hr MWHT treatment at 220°C for 10 hr in 5 M NaOH. With a quintupling of the NaOH concentration, the corrosion rate of (110) single crystal rutile titania was enhanced ~25 fold (0.057 ± 0.00065 $g \cdot cm^{-2} \cdot s^{-1}$).

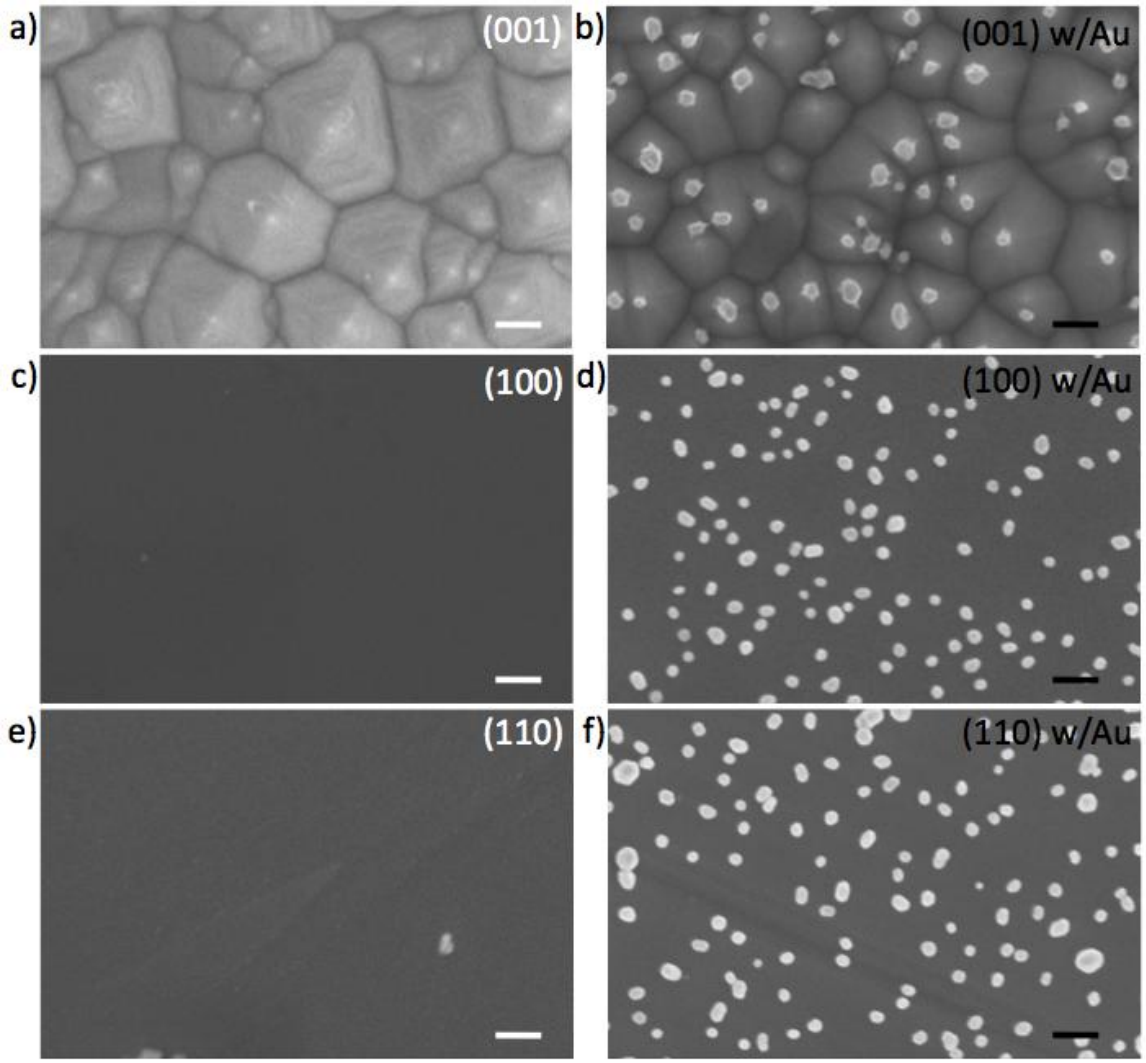

Figure 60: (001) oriented (top row), (100) oriented (middle row), and (110) oriented (bottom row) rutile titania single crystals with (right column) and without (left column) Au markers after MWHT treatment with 1 M NaOH solution for 10 hr at 220°C. All scale bars represent 200 nm.

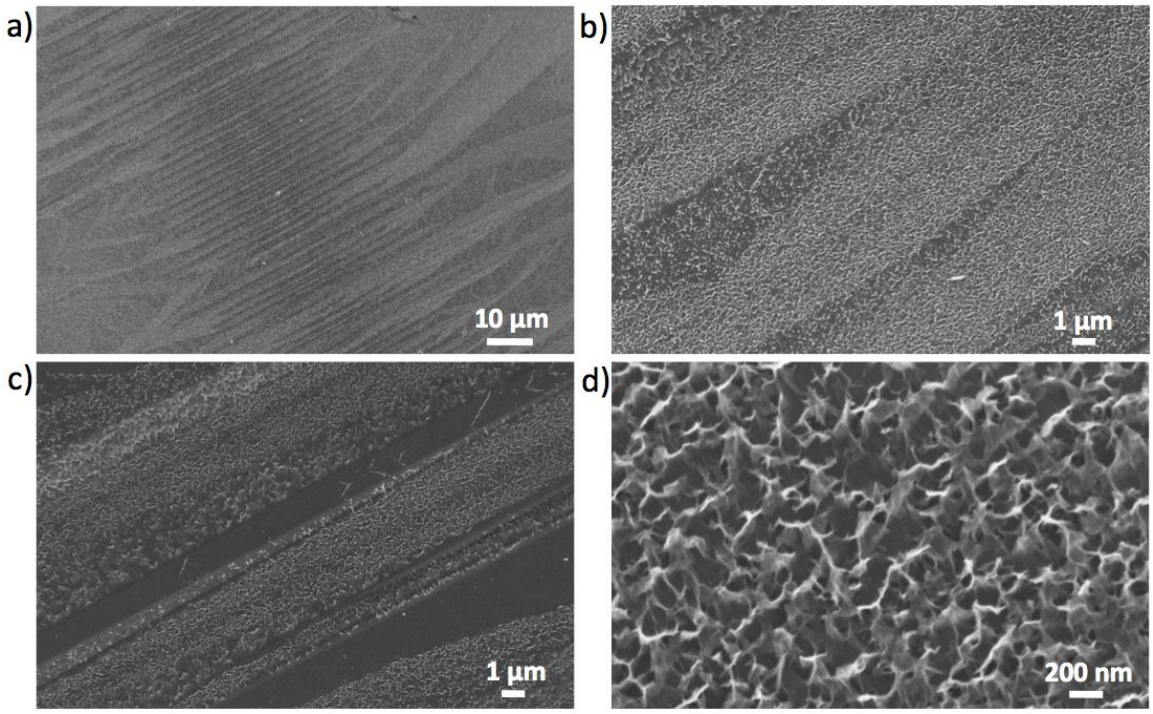

Figure 61: Top view SE images taken with increasing magnification (a→d) of (110) single crystal titania after MWHT treatment in 20 mL of 5 M NaOH at 220°C for 10 hr.

Table 2: Average Corrosion Rates of Rutile Titania Single Crystals at 220°C in NaOH Solutions

Rutile Single Crystal Orientation	MWHT Condition	Average Corrosion Rate ($g / cm^2 * sec$)
(0 0 1)	1M NaOH, 10 hr	$4.1 \times 10^{-3} \pm 1.6 \times 10^{-3}$
(1 0 0)	1M NaOH, 10 hr	$3.2 \times 10^{-3} \pm 1.5 \times 10^{-3}$
(1 1 0)	1M NaOH, 10 hr	$2.2 \times 10^{-3} \pm 1.1 \times 10^{-3}$
(1 1 0)	5 M NaOH, 10 hr	$5.7 \times 10^{-2} \pm 6.5 \times 10^{-4}$

An increase in the sodium hydroxide concentration increased the dissolution rate of the (110) oriented rutile titania single crystals, and because there was already an excess of Ba (with respect to mol TiO_2) in the MWHT solutions, it was hypothesized that the $BaTiO_3$ formation rate would increase with increased NaOH concentration. Similarly, it was hypothesized increased barium concentration would result in little or no change in the $BaTiO_3$ formation rate. The effect of four different MWHT reaction solutions on

$BaTiO_3$ formation rate were compared (all reactions were conducted at 220°C for 4 hr) with top view SE images in **Figure 62**. **Figure 62d** qualitatively shows the dramatic increase in $BaTiO_3$ product phase exhibited by increasing concentration of sodium hydroxide from 1 M to 5 M. The modest effect on formation of product $BaTiO_3$ resulting from an increase in barium acetate concentration over that of the typical MWHT solutions used can be seen qualitatively by comparing **Figure 62b and Figure 62c**. The surface area fraction of (110) oriented rutile titania transformed into $BaTiO_3$ after different reaction times/solution concentrations was measured by overlaying a grid on 5 independent micrographs for each reaction time /conditions and counting the fraction of intersections lying upon $BaTiO_3$ and TiO_2 (see **Section 3.3.4** and **Figure 47** for more details). The resulting $BaTiO_3$ surface area fractions (X_{SA}) transformed for each time/condition are shown in **Figure 63** and tabulated in **Table 3**. The effect of quintupling sodium hydroxide concentration clearly enhanced the product surface area coverage (~94% $BaTiO_3$) over both normal reaction conditions (~16% $BaTiO_3$) and MWHT reaction solution with quintupled barium acetate concentration (~17% $BaTiO_3$). However, the faster reaction rate of (110) oriented rutile TiO_2 with quintupled sodium hydroxide concentration did not result in a $BaTiO_3$ surface morphology similar to that seen with the faster dissolving (100) and (001) oriented rutile TiO_2 specimens (**Figure 50**). Such differences in surface morphology indicated the effect of orientation was more significant than the effect of dissolution rate on $BaTiO_3$ product morphology ((**Figure 50** vs**. Figure 62**).

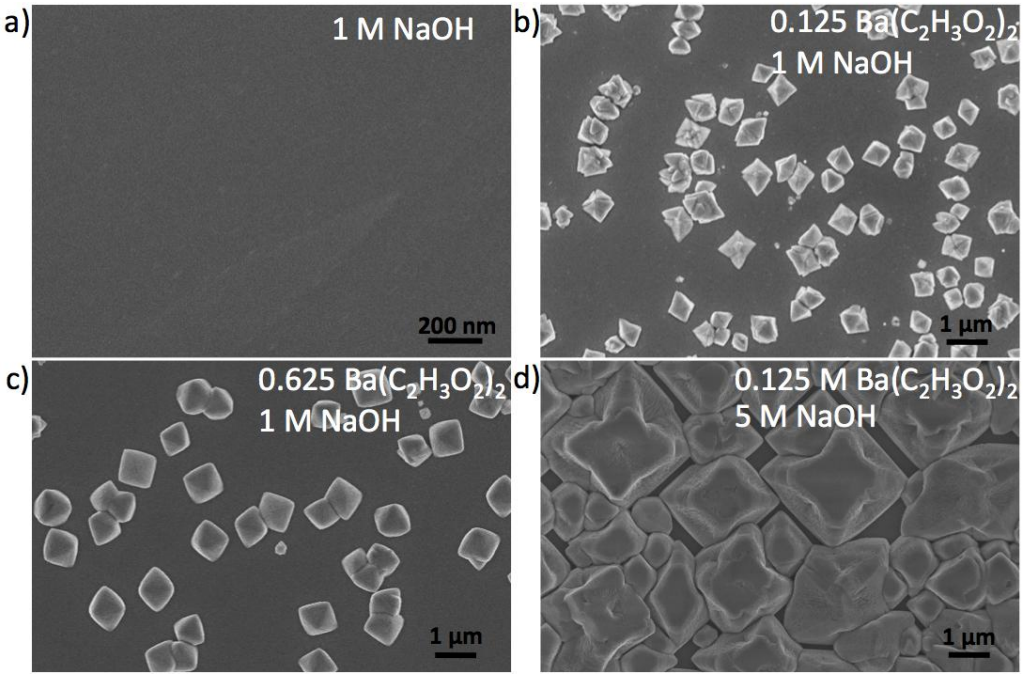

Figure 62: Top view SE images of (110) oriented single crystal titania after 4 hr MWHT treatment at 220°C in (a) 1 M NaOH solution, (b) 1 M NaOH, 0.125 M barium acetate solution, (c) 1 M NaOH, 0.625 M barium acetate solution, and (d) 5 M NaOH, 0.125 M barium acetate solution.

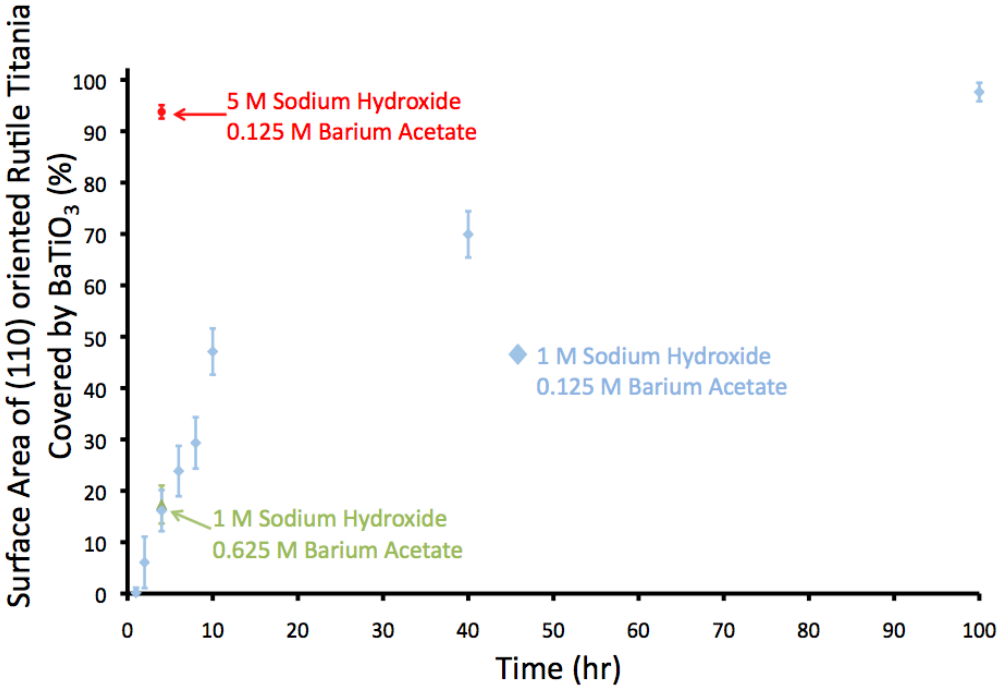

Figure 63: Surface area of (110) oriented rutile titania covered by $BaTiO_3$ product as a function of MWHT reaction time (220°C, 0.125 M barium acetate, 1 M sodium hydroxide). MWHT reactions were also examined after 4 hr reaction time with quintuple the sodium hydroxide concentration and with quintuple the barium acetate concentration.

Table 3: Surface Area of (110) oriented Rutile TiO_2 Covered by $BaTiO_3$ as a Function of Reaction Time

Time (hr)	Surface Area $BaTiO_3$ (%)*
0	0.0 ± 0.0
1	0.15 ± 0.3
2	6.1 ± 1.9
4	16.1 ± 1.4
6	23.9 ± 4.9
8	29.3 ± 3.2
10	47.1 ± 4.5
40	69.9 ± 4.5
100	97.6 ± 4.5
4 –Sodium Hydroxide Quintupled	93.8 ± 3.7
4 - Barium Acetate Quintupled	17.3 ± 1.3

* % Represented by calculated mean and variance represented by ± 1 calculated standard deviation

By counting the number of particles after 1, 2, 4, 6, and 8 hr of reaction time under identical MWHT reaction conditions, it was determined there is approximately a 1 hour incubation (or induction) time for stable nucleation to occur and the number of particles (observable nuclei) appeared to increase linearly with time (**Figure 64**). Such an increase in number of particles with time was inconsistent with rapid, site-saturated (burst) nucleation[79]. Avrami developed the concept of extended volume to factor out nucleation events which otherwise would be thought to occur in volumes (or areas in this case) in which product nuclei have already formed or grown[79]. The Johnson-Mehl-Avrami-Kolmogorov (JMAK) equation for nucleation and growth phase transformations can be generally given as **Equation 1** where $\mathbf{X_{SA}}$ is surface area transformed (typically volume fraction transformed), ***t*** is time, ***m*** is the Avrami exponent for the time dependence of geometry, growth, and nucleation, and ***k*** is a constant affected by the nucleation rate, geometry, and particle growth rate[80].

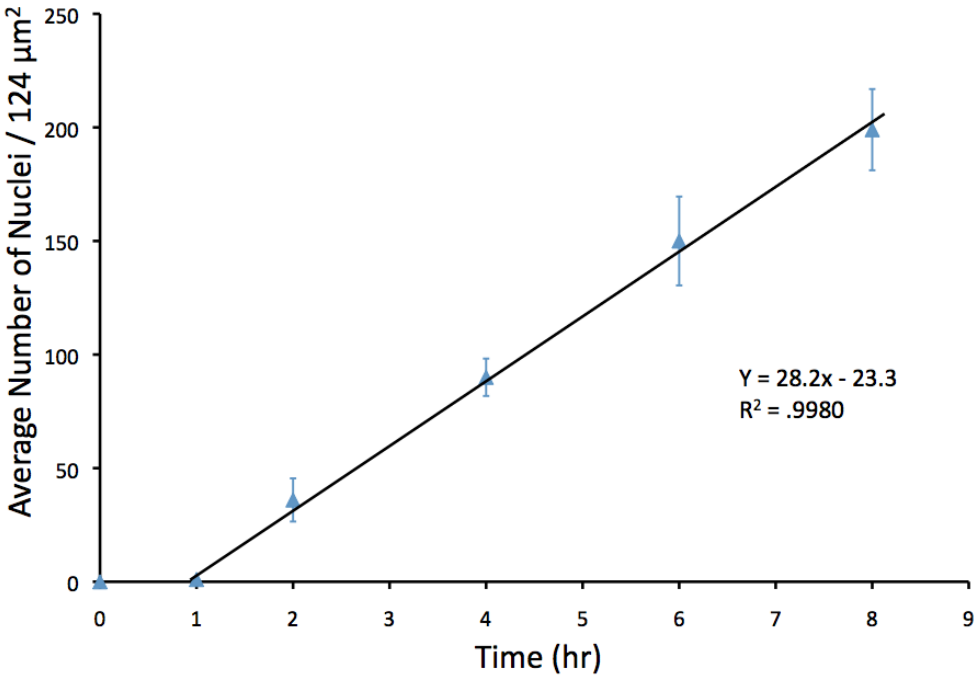

Figure 64: Average number of nuclei present in a 124 square micrometer area of SE micrographs taken of (110) oriented rutile titania after 1, 2, 4, 6, and 8 hr of MWHT reaction with 0.125 M barium acetate and 1 M sodium hydroxide.

Equation 1: $X_{SA} = 1 - \exp(-kt^m)$

The Avrami time exponent (***m***) can be broken up into two components **a** and **b** (**Equation 2**) in which **a** is a nucleation rate-based constant (**a** = 1 for constant nucleation, **a** = 0 for site saturated nucleation), **b** describes the time dependence of particle growth (**b** = 1 for interfacial reaction control of growth and **b** = 0.5 for diffusion control of growth), and **D** represents the dimensionality of growth/transport[81]. When $-\ln(1-X_{SA})$ is plotted against $\mathbf{t}^{\mathbf{m}}$ with fixed values of ***m***, one can evaluate the quality of the fit for such ***m*** exponents via linear regression.

Equation 2: $m = a + Db$

Equation 3: $-\ln(1-X_{SA})] = kt^m$

Data points for evaluating ***m*** were chosen to avoid the incubation period (very low extent of transformation) and impingement (higher extent of reaction) effects[80]. The

measured surface area fraction transformed data (2, 4, 6, 8,and 10 hr data points) were used for generating plots in the form of -ln(1-X_{SA}) vs. t^2 (**Figure 65a**) and t^3 (**Figure 65b**). The quality of fit for JMAK equations with these Avrami exponent values were then evaluated via linear regression. For constant nucleation with diffusion controlled growth in two dimensions (***m*** = 2), the linear regression fit was considerably better (R^2=0.93) than for constant nucleation with two dimensional interfacial reaction control (***m*** = 3, R^2=0.80). Constant nucleation with 2D diffusion controlled growth is consistent with an increase in product formation after increasing sodium hydroxide concentration as the solubility of the titania reactant species was apparently enhanced (as demonstrated by increased average corrosion rate data in **Table 2**). Such an increase in concentration of soluble Ti species at the titania/solution interface may create a larger activity gradient from the titania/solution interface to $BaTiO_3$/solution interface because formation of $BaTiO_3$ is expected to locally decrease the concentration soluble Ti species.

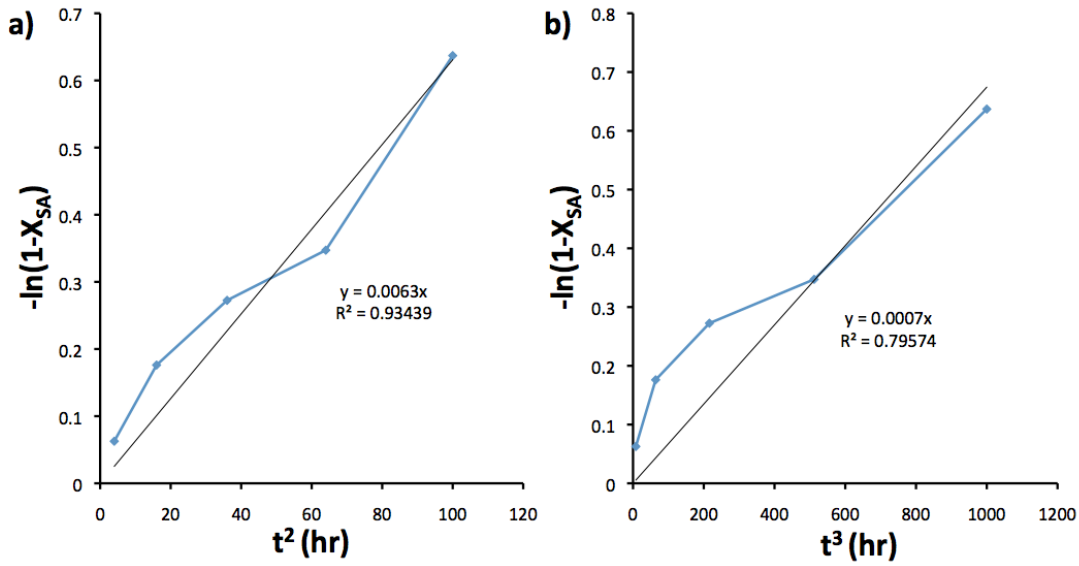

Figure 65: Avrami equation plotted with -ln(1-x) vs. (a) t^2 and (b) t^3 with X_{SA} values corresponding to 2, 4, 6, 8, and 10 hr MWHT reaction times. Each set of data points has a linear fit whose R^2 value and equation are displayed on the chart.

In short, inert marker experiments reveal that the $BaTiO_3$ formed on the (110) oriented TiO_2, under known morphology-preserving reaction processing conditions, via a dissolution heterogeneous reaction (**case 4a**) or an In-Situ transformation mechanism (**case 1**). The presence of Au at the newly- formed (110) TiO_2/$BaTiO_3$ interface (**Figure 52**a, **Figure 58c,d, Figure 59b,d**) indicated the $BaTiO_3$ formed either via titanium cation diffusion outward (with new $BaTiO_3$ formation occurring at $BaTiO_3$/solution interface) or through dissolution of the titania followed by heterogeneous nucleation and growth of $BaTiO_3$. With an order of magnitude increase in reaction time, the $BaTiO_3$ product layer formed on the (001) single crystal titania did not appear to increase in thickness (**Figure 55c,d**). The morphology of the (110) single crystal rutile titania changed from a relatively smooth surface before MWHT treatment (**Figure 53**) to a rough surface after MWHT treatment (**Figure 52**), which indicated dissolution (i.e. removal) of titania from the surface or surface diffusion/rearrangement. An increased NaOH concentration has been shown to increase the average dissolution rate of rutile titania (**Figure 60e,f vs. Figure 61**, **Table 2**). Also, the $BaTiO_3$ formation rate was increased with increased NaOH concentration (**Figure 62**, **Figure 63**). The combined evidence supports that, under morphology-preserving MWHT reaction conditions, the mechanism of (110) oriented single crystal rutile TiO_2 into $BaTiO_3$ was consistent with dissolution-heterogeneous precipitation (i.e., **case 4a**). Analysis of JMAK equations with measured surface area fraction transformed values and fixed values of the Avrami exponent revealed a significantly better fit for $\boldsymbol{m} = 2$ than for $\boldsymbol{m} = 3$. An Avrami exponent of $\boldsymbol{m} = 2$ indicated the surface transformation rate was consistent with constant nucleation with 2D diffusion controlled growth.

3.5. *Concluding Remarks*

For the first time, inert markers have been used in hydrothermal reaction processing to evaluate reaction interfaces. The identification of the marker location at the $TiO_2/BaTiO_3$ interface helped identify the reaction mechanism for morphology-preserving reaction of titania into barium titanate at 220°C with 1M sodium hydroxide and 0.125 M barium acetate. The combined evidence was consistent with a dissolution-heterogeneous reaction mechanism that exhibited a transformation rate controlled by constant nucleation and 2D diffusion until effectively stopped upon the formation of a dense continuous product layer of $BaTiO_3$. Although other authors have shown that the morphology preservation of such reactions can be changed by varying the concentration of reaction solutions and the temperature of reaction[62], the conditions studied in this work have yielded tetragonal $BaTiO_3$ replicas of anatase titania-bearing 3D hierarchical structures[56].

Future experiments are suggested to interrogate the onset of a solid-state diffusion-limited reaction process through conventional hydrothermal reaction at higher temperatures. Upon the onset of a solid-state diffusion-limited process the $BaTiO_3$ product layer thickness should increase with time (at a parabolic rate for planar specimens). The kinetics of $BaTiO_3$ formation could be determined at various temperatures to provide an activation energy and the diffusing species could be identified with similar inert marker experiments. Further understanding for the nucleation differences between (100)/(001) and (110) could be elucidated.

Morphology-preserving hydrothermal reaction processing, and the use of inert markers for identification of reaction mechanisms, are applicable to a vast number of

possible combinations of monolithic or multicomponent templates undergoing conversion into new multicomponent ceramic compounds. Morphology-preserving hydrothermal reaction processing of macro-to-micro-to-nanoscale 3D ceramics or inorganic/organic composites could be attractive in a variety of potential applications that would benefit from low-temperature processing of 3D microstructures.

3.6. *References*

[56] J. Vernon, Y. Fang, Y. Cai, K.H. Sandhage, "Morphology-Preserving Conversion of a 3D Bioorganic Template into a Nanocrystalline Multicomponent Oxide Compound," *Angewandte Chemie International Ed.*, vol. 49, pp. 7765 -7768, 2010.

[57] W. Sun, W. Liu, and J. Li, "Effects of chloride ions on hydrothermal synthesis of tetragonal $BaTiO_3$ by microwave heating and conventional heating," *Powder Technology*, vol. 166, pp. 55-59, 2006.

[58] Y. Ma, E. Vileno, S. Suib, and P. Dutta, "Synthesis of Tetragonal $BaTiO_3$ by Microwave Heating and Conventional Heating," *Chemistry of Materials*, vol. 9, pp. 3023-3031, 1997

[59] B. Gersten, "Growth of multicomponent perovskite oxide crystals: Synthesis conditions for the hydrothermal growth of ferroelectric powders," in *Crystal Growth Technology*: Springer-Verlag, 2003, pp. 299-333.

[60] J. Eckert, C. Hung-Houston, B. Gersten, M. Lencka, and R. Riman, "Kinetics and Mechanisms of Hydrothermal Synthesis of Barium Titanate," *Journal of the American Ceramic Society*, vol. 79, pp. 2929-2939, 1996.

[61] W. Hertl, "Kinetics of Barium Titanate Synthesis," *Journal of the American Ceramic Society*, vol. 71, pp. 879-883, 1988.

[62] X. Wei, A. Vasiliev, and N. Padture, "Nanotubes patterned thin films of barium-strontium titanate," *Journal of Materials Research*, vol. 20, pp. 2140-2147, 2005.

[63] M. McCormick and E. Slamovich, "Microstructure development and dielectric properties of hydrothermal $BaTiO_3$ thin films," *Journal of the European Ceramic Society*, vol. 23, pp. 2143-2152, 2003.

[64] A. Testino, V. Buscaglia, M. Buscaglia, M. Viviani, and P. Nanni, "Kinetic Modeling of Aqueous and Hydrothermal Synthesis of Barium Titanate ($BaTiO_3$)," *Chemistry of Materials,* vol. 17, pp. 5346-5356, 2005.

[65] N. Padture and N. Wei, "Hydrothermal Synthesis of Thin Films of Barium Titanate Ceramic Nano-Tubes at 200°C," *Journal of the American Ceramic Society,* vol. 86, pp. 2215-2217, 2003.

[66] X. Wei, A. Vasiliev, and N. Padture, "Nanotubes patterned thin films of barium-strontium titanate," *Journal of Materials Research,* vol. 20, pp. 2140-2147, 2005.

[67] M. McCormick and E. Slamovich, "Microstructure development and dielectric properties of hydrothermal $BaTiO_3$ thin films," *Journal of the European Ceramic Society,* vol. 23, pp. 2143-2152, 2003.

[68] M. Ryu, T. Suzuki, K. Kobayashi, T. Sakashita, Y. Mizuno, Effects of Titania Surface Orientation on the Heterogeneous Formation of Barium Titanate by hydrothermal Synthesis," *Japanese Journal of Applied Physics,* vol. 49, pp.061101-1 – 061101-8, 2010.

[69] J.G. Lisoni, C.H. Lei, T. Hoffmann, V.M. Fuenzalida, "Hydrothermal growth of $BaTiO_3$ on TiO_2 single crystals," *Surface Science,* vol. 515, pp. 431-440, 2002.

[70] V.M. Fuenzalida, J.G. Lisoni, N.I. Morimoto, J.C. Acquadro, " Tetragonal BaTiO3 thin films hydrothermally grown on TiO2 single crystals," *Applied Surface Science*, vol. 108, pp. 385-389, 1997.

[71] A.D. Smigelskas, E.O. Kirkendall, "Zinc Diffusion in Alpha Brass," *AIME Transactions,* vol. 171, pp. 130-142, 1947.

[72] A. Graff, S. Senz, D. Voltzke, H-P. Abict, D. Hesse, "Microstructure evolution during $BaTiO_3$ formation by solid state reaction on rutile single crystal surfaces," *Journal of the European Ceramic Society,* vol. 25, pp. 2201-2206, 2005.

[73] K. Kajiyosi, K. Tomono, Y. Hamaji, T. Kasanami, M. Yoshimura, "Short-circuit Diffusion of Ba, Sr, and 0 during ATiO, (A = Ba, Sr) Thin-Film Growth by the Hydrothermal-Electrochemical Method," *Journal of the American Ceramic Society*, vol. 78, pp. 1521-1531, 1995.

[74] S.R. Swamy, "An X-Ray Study of the Effect of Heat on the Stucture of Sputtered Films of Gold," *The Proceedings of the Physical Society,* vol. 46, pp. 739-744, 1934.

[75] Y. Xiu, L. Zhu, D.W. Hess, C.P. Wong, Biomimetic Creation of Hierarchical Surface Structures by Combining Colloidal Self-Assembly and Au Sputter Deposition," *Langmuir,* vol. 22, pp. 9676-9681, 2006.

[76] B.N. Taylor and C.E. Kuyatt, "Guidelines for Evaluating and Expressing the Uncertainty of NIST Measurement Results: NIST Technical Note 1297," U.S. Government Printing Office, Washington D.C., USA,1994.

[77] M. Ramamoorthy, D. Vanderbilt, R.D. King-Smith, "First-principles calculations of the energetic of stoichiometric TiO_2 surfaces," *Physical Review B*, vol. 49, pp. 721-727, 1994.

[78] A.S. Barnard, P. Zapol, "Effects of particle morphology and surface hydrogenation on the phase stability of TiO_2," *Physical Review B*, vol. 70, pp. 254303-1 – 254303-13, 2004.

[79] M. Avrami, "Kinetics of Phase Change. II: Transformation-Time Relations for Random Distribution of Nuclei," Journal of Chemical Physics, vol. 8, pp. 212 – 224, 1940.

[80] J.D. Hancock and J.H. Sharp, "Method of Comparing Solid-State Kinetic Data and Its Application to the Decomposition of Kaolinite, Brucite, and $BaCO_3$," *Journal of the American Ceramic Society*, vol. 55, pp. 74-77, 1972.

[81] S.-Y. Jung, S.-J. Hwang, and Y.-M. Sung, "Enhanced Aurivillius phase formation kinetics in seeded SBT thin films," Journal of Crystal Growth, vol. 254, pp. 92-99, 2003.

CHAPTER 4: Layer-by-Layer Conformal Coating and Replication of Structurally Colored Hierarchical Biological Structures with and into Higher Index Materials

4.1. *Summary*

In this Chapter, SSG LbL deposition was used to apply metal oxide coatings of varied thickness onto *Parides sesostris* butterfly scales to understand (i) how conformal coatings of high-index inorganic materials affect the reflected color of both the overall scales and of individual constituent scale structures, and (ii) how both materials chemistry (i.e., doping the Ti-O-bearing coating with Sn) and processing conditions (i.e., heat treatment and/or hydroxyl amplification) affect the reflected color of coated and replicated structures. Quantitative mapping of the reflection spectra from various regions of a single *P. sesostris* wing section were conducted to eliminate spectral differences due to inter- and intra- butterfly color variations. Wing sections were optically interrogated after incremental application of 25 SSG deposition cycles (i.e., 25, 50, 75,100, 125, and 150 total deposition cycles) within identical regions. The reflection spectra of coated specimens became redshifted with an increase in the deposited layer thickness. Hollow inorganic replicas exhibiting structural color were obtained after organic pyrolysis (450°C, 4 hr, in air) of the coated bioorganic template. Focused Ion Beam (FIB) milling was used to isolate the polycrystalline photonic crystal (PPC) component within inorganic scale replicas for quantitative microspectrophotometric (MSP) investigation, which confirmed qualitative observations made via bright field optical microscopy. Dimensional changes within the chemical conversion process were evaluated as a function of coating thickness (i.e., number of SSG cycles) and coating composition. The

PPC (also referred to as a gyroid structure) lattice dimensions were hypothesized to be the determining factor in both the ability to achieve structural color in the inorganic replicas and in the resultant reflection peak position. Such dimensions were controlled by the thickness of the coating applied. This work shows the first characterization of the following: (i) the effect of wet-chemical LbL constructive modification on bioorganic templates exhibiting structural color, while taking into account the natural variation of the template, (ii) the use of a multicomponent oxide coating to tune structural color, and (iii) the interrogation of intrascale features with MSP after FIB micro/nano milling.

4.2. *Introduction*

Researching biological structures that manipulate the visible portion of the electromagnetic spectrum has led a number of applications including: surface enhanced Raman scattering (SERS) templates, highly selective & sensitive chemical sensors, low energy display technology, and iridescent paint / cosmetics[82,83,84,85]. Coating and/or replication of butterfly scales so as to modify the scale chemistry and/or structure has been attempted with impression molding, soaking/sonication in metal salts, hydrothermal reactions, chemical vapor deposition, atomic layer deposition, and SSG[86,87,88,89,90,91]. However, only LbL techniques such as SSG and ALD have provided the ability to precisely adjust (i.e., with sub-nanometer control of layer thickness) the coating thickness[90,91]. To date, there are no reports describing either the tuning of optical response through low-cost, chemically versatile, and readily scalable wet-chemical LbL constructive modification (i.e., through the application of coatings) of organic templates or interrogation of constructive modification in which the natural variation of templates has been taken into account, or eliminated. Furthermore, only monolithic coatings have

been applied when structural color has been reported from inorganic replicas of wing sections[90]. However, the report utilized ALD, a gas-phase reaction methodology requiring expensive specialized equipment, to apply a monolithic coating material. Moreover, interrogation of such replicas involved an entire wing section, thereby providing no information with respect to the effect of the natural variation within a single butterfly or between butterflies. Such prior characterization was unable to deconvolute the effects of tiling of scales or thin film effects from the wing membrane to which the scales are attached. To address the aforementioned deficiencies, the effects of metal oxide coating composition, applied via SSG (e.g., Ti-O- and Sn-doped Ti-O- bearing coatings), and coating thickness on the reflection spectra from both the native *P. sesostris* wing, which consists of multiple scales tiled on the wing surface, and single scales removed from the wing itself were studied. Also, single scale, or subscale, optical spectroscopy was performed in combination with FIB milling. Precision ion-milling of the scales allows for interrogation of the optical response of individual structural components within a single scale.

The complex structure of *P. sesostris* is revealed in **Figure 66**. The green dorsal section of the butterfly forewings are tiled with ovular scales (approximately 40 μm in width and 120 μm in length). Within each scale is a complex ridge structure composed of tubes and fins, a 3D photonic polycrystal (PPC), and a thin membrane. These intrascale components can be removed through the use of FIB milling to evaluate the spectral contribution of each component within a single scale. Detailed methodology for FIB milling of individual butterfly scales and interrogation of *P. sesostris* native intrascale structures through FIB milling will be reported by Craig Cameron.

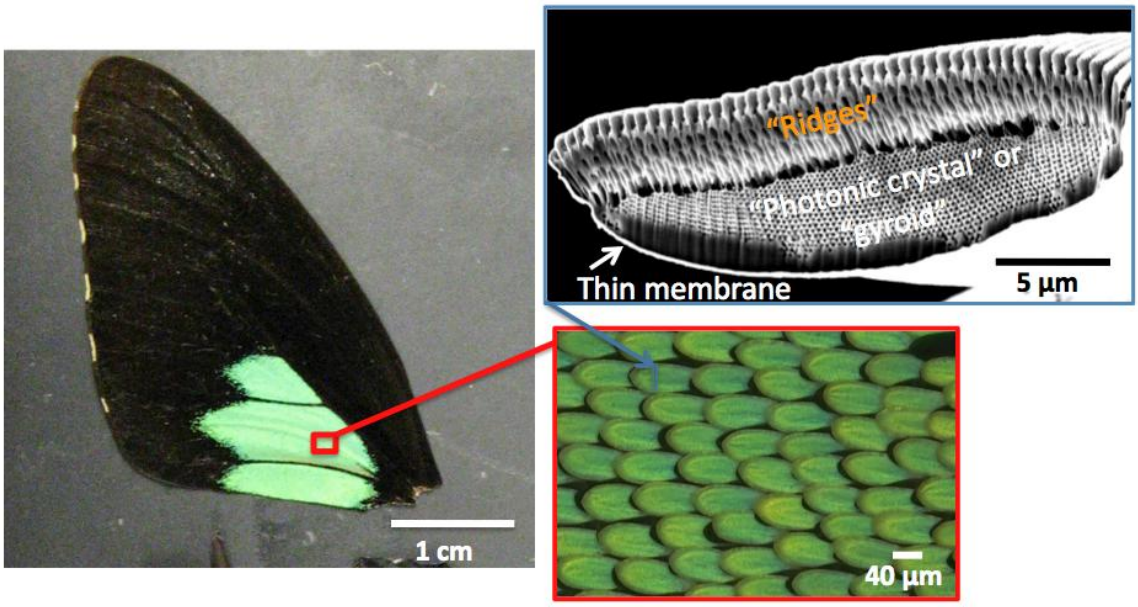

Figure 66: Photograph (left) of the dorsal side of a native *Parides sesostris* butterfly forewing. The green wing sections are imbricated with oval-shaped scales, as shown in the bright field optical micrograph (bottom right). A secondary electron image (top right) of a FIB-milled cross-section of an individual *P. sesostris* green scale reveals intrascale structures: ridges (composed of tubular section covered with fins), PPC, and thin scale membrane. Note: the ridge structure is oriented facing up in the native wing.

Because the chitinous butterfly cuticle provides a richly hydroxylated surface, dendritic amplification[92] of the surface hydroxy groups had not previously been evaluated with respect to the native surface. In the present work, Ti-O and Sn-doped Ti-O coatings were applied to *P. sesostris* wing sections both with and without dendritic amplification in order to: (i) evaluate the effect of dendritic amplification of hydroxy groups on the coating thickness and on the resulting reflection spectra, and (ii) to show the capability for applying multicomponent coatings through the SSG coating methodology. Specifically, the Sn dopant was introduced to reduce the grain size upon crystallization in the replicas[93] and form the rutile polymorph after low temperature (<500°C) heat treatment[91]. Such studies provided evidence as to how the 3D PPC structure within *P. sesostris* butterfly scales can be modified by SSG coating to effect changes in the reflection spectra. This work demonstrates that the 3D structure can indeed be replicated

to provide structural color, despite the tortuous path for solutions through sub- 300 nm diameter pores[94].

4.3. *Experimental Procedures*

4.3.1. Dendritic Amplification of Surface Hydroxy Groups

Dorsal green sections of *P. sesostris* butterfly wings (insect-sale.com, Chia-yi City, Taiwan) were rinsed twice with IPA and then incubated (all incubation solutions within 50 mL graduated centrifuge tubes (Corning, MA, USA)) with a 10 wt% aminosilane (N^1-(3-trimethoxysilylpropyl)diethylenetriamine, Tech. grade, Aldrich, MO, USA) / IPA (Anhydrous Isopropyl Alcohol, ACROS Organics, Geel, Belgium) solution for 18 hr in an incubation shaker (MaxQ5000 heated digital shaker, Barnstead Lab-line, PA, USA) (37°C, 50 rpm) to introduce amine groups to the surface. After three rinses with 15 mL of IPA, each wing section was incubated with 10 wt% dipentaerythritol penta-/hexa-acrylate (DPEPHA, Aldrich, MO, USA) / IPA solution for 1 hr in an incubation shaker (37°C, 50 rpm). After polyacrylate incubation each wing section was rinsed 3x in 15 mL of IPA and then incubated with 15 mL of 10 wt% of Tris(2-aminoethyl)amine (TAEA, 96%, Aldrich, MO, USA) for 1 hr in an incubation shaker (37°C, 50 rpm) followed by three rinses with 15 mL IPA. The combination of one polyacrylate and one polyamine step constituted one dendritic amplification cycle. After 5 such cycles a final exposure of the sample to 10 wt% DPEPHA in IPA for 1 hr was conducted followed by 3 rinses with IPA. The sample was then incubated for 18 hr with 0.05 M Tris(hydroxymethyl)aminomethane (99%, Alfa Aesar, Lanc., UK) in IPA (previously dissolved overnight at 50°C) in an incubation shaker (50°C, 50 rpm) for 1 hr

to introduce surface hydroxy groups. Samples were rinsed 3x with IPA and then stored in an IPA solution prior to SSG processing. Further description and characterization of the dendritic amplification, as well as discussion of the reaction chemistry, are presented in a paper by Wang, *et al.*[92]. The same surface group amplification process was also applied to Si wafers and polished (2.54 x 2.54 x 0.159 cm) fused quartz plates (Technical Glass Products, OH, USA) after oxygen plasma etching for 15 min, soaking in 1 M NaOH (diluted from 50% w/w aq. soln., Alfa Aesar, MA, USA) for 30 min and rinsing with 200 proof ethanol. All planar substrates were stored in high purity (200 proof) ethanol (Ultra Pure LLC, MD, USA) until needed for SSG coating.

4.3.2. Determination of Tin Dopant Concentration

In a nitrogen atmosphere glovebox, known quantities of alkoxide precursors were hydrolyzed for thermal assays in triplicate to determine the actual number of moles of titanium added for a known volume of commercial precursor. One milliliter of IPA was added to a pre-fired (850°C, 2hr, air, removed from the furnace at 200°C and cooled to room temperature in a Pyrex® #3140 glass desiccator (Corning Incorporated, NY, USA) containing 200 g of 80 wt% DRIERITE / 20 wt% indicating DRIERITE (i.e., impregnated with cobalt chloride) (W.A. Hammond DRIERITE Co. LTD, OH, USA) and pre-weighed (AE240 analytical balance, Mettler-Toledo Inc., OH, USA) MgO crucible followed by the addition of 0.5 mL Ti(IV) isopropoxide (99.995%, LOT#H19W013, Alfa Aesar, MA, USA) and then 3 mL DI H_2O. For Sn thermal assays two milliliters of Sn(IV) isopropoxide solution (10%w/v in Toluene and IPA solution, LOT# C29W021, Alfa Aesar, MA, USA) were added to 3 mL of DI H_2O. The hydrolyzed alkoxide solutions were dried on a hot plate in a fume hood (i.e., outside of

N_2 atmosphere glovebox) at 95°C for 1 hr. All three crucibles containing a particular alkoxide were covered with a MgO boat.

Covered crucibles were fired in a tube furnace (Lindberg / Blue M, NC, USA,) using the following thermal treatment (controlled by AutoFire® Controller, Orton Ceramic Foundation, OH, USA outfitted with a k-type thermocouple, OMEGA Engineering, Inc., CT, USA): 120°C/hr ramp to 850°C, 4 hr hold in air, and cooled at 3°C/min to less than 100°C in air before removal from the furnace. After thermal treatment the oxide powders within pre-weighed crucibles were weighed again to determine the remaining oxide mass and the corresponding number of moles of TiO_2 or SnO_2 generated from a known volume (and corresponding moles) of Ti or Sn precursor added to the crucible. The experiment was designed to produce 0.136 g and 0.132 g of TiO_2 and SnO_2, respectively. Such quantities required less than a 5 mL volume of precursor and provided a reasonable (i.e. > 100 mg) product weight for weighing with analytical balance. The precursors utilized for thermal assays were the only bottles utilized for all experimentation in this chapter and were sealed with electrical tape and stored in N_2 atmosphere glovebox for the duration of the research. There was no indication of hydrolysis within the stock precursor solutions throughout the experimentation, which would indicate a change in the concentrations from those determined via thermal assays.

Stoichiometric mixtures of Sn/Ti alkoxide precursor solutions of 0, 5, 10, 12.5, 15, 17.5, 20, and 100 mol % Tin(IV) isopropoxide were hydrolyzed overnight in a 50 mL centrifuge tube. After overnight hydrolysis precipitates were centrifuged down in an centrifuge equipped with a swinging bucket rotor (5408R centrifuge with #A-4-44 rotor,

Eppendorf, Hamburg, Germany) at 4,500 rpm for 10 min and then 2 mL of DI water were added to the supernatant to ensure complete hydrolysis (i.e., no addition precipitation was observed in supernatant after 30 min). After hydrolysis, precipitated powders were rinsed 3x with DI water and 3x with IPA. Each rinse required 25 mL of DI water, or IPA, followed by centrifugation (4500 rpm, 10 min) and removal of the rinse supernatant before adding subsequent solution or drying. After rinsing, powders were dried for 1 hr at 70°C in air. Each type of powder was then heated in air in a tube furnace at 30°C/hr to 450°C in a MgO crucible, held at 450°C for 4 hr, and then furnace-cooled (~ 0.75°C/min) to below 100°C before removal from the furnace.

After firing, samples were ground by mortar and pestle between two sheets of weighing paper, distributed to 1 mL Eppendorf centrifuge tubes, and suspended in 0.5 mL of high purity ethanol. Powder diffraction samples were dispersed on a low background quartz (cut 6° from the (0001)) specimen support (GEM dugout, PA, USA) via pipetting 0.1 mL of ethanol/powder slurry onto the holder and allowing the ethanol to evaporate. XRD analyses were conducted on an X'Pert Pro Alpha-1 diffractometer (PANalytical B.V., ALMELO, Netherlands) with monochromatic $Cu_{K\alpha 1}$(1.5405980 Å) radiation emanating from a 1.8 kW Ceramic X-ray tube with copper anode (45 kV, 40 mA) through a symmetrical Johannson monochromator. The incident beam optics were outfitted with 0.04 rad soller slits, a 1° fixed anti-scatter slit, a ½° programmable divergence slit, and a 20 mm mask. The diffracted beam optics were outfitted with a 5.5 mm anti-scatter slit and 0.04 rad soller slits before the X'Celerator detector. Each pattern was produced with a summation of 4 identical 30 minute scans conducted with Bragg-Brentano geometry and a step size of 0.0166° 2θ over the range of 20° to 65° 2θ. A LaB_6

standard (SRM 660, NIST, MD, USA) was run alone and with 17.5 mol% Sn powder to generate both an internal peak position calibration and an external calibration curve for instrumental broadening.

4.3.3. SSG Coating of Butterfly Scales

Each cycle of the SSG process involved immersion of wing sections clipped to a 1.5 x 1.5 cm silicon wafer substrate in either a pure 0.025M Ti(IV) isopropoxide, or 0.025 M 80 mol% titanium(IV) isopropoxide / 20 mol% Tin(IV) isopropoxide solution in anhydrous isopropanol (IPA) for 2 min, washing three times with 4 mL of IPA, hydrolyzing in 4 mL of 40 vol% IPA in DI water for 2 min, washing again three times with approximately 4 mL of IPA, and then drying with a stream of warm flowing air for 5 min. This process was repeated to reach the desired number of SSG cycles. (Note: the solution molarity was based upon the vendor's reported values that had not yet been corrected by thermal assays of each precursor.) P. sesostris dorsal green wing sections were sent to the A. Lethbridge and P. Vukusic at the University of Exeter for initial reflection spectra (mapping of reflection spectra within a particular wing section) and were then returned to the Georgia Institute of Technology for 25 layers of SSG deposition After SSG deposition of coatings, mapped wing sections were returned to Exeter for optical interrogation of coated wing sections. Such iterative optical interrogation and 25 SSG deposition cycles were continued through 125 layers of Sn-Ti-O or Ti-O only coatings. After 150 layers, optical probe measurements were not continued as shipping the scales a distance equivalent to twice the equatorial distance around the globe had resulted in damage to the surface of the wings. However, individual scales were analyzed via MSP.

4.3.4. Organic Pyrolysis

To create inorganic scales, coated individual scales and coated butterfly wing section samples were clipped (Staples® black metal mini binder clips, MA, USA) between two polished (2.54 x 2.54 x 0.159 cm) fused quartz plates (Technical Glass Products, OH, USA) and then heated in an MgO crucible in a tube furnace at 30°C/hr to 450°C and held at temperature for 4 hr in air to allow for pyrolysis of the chitin and crystallization of the titania. The specimens were then furnace-cooled (~ 0.75°C/min) to below 100°C before removal from the furnace. Fired specimens could then be imaged with a scanning electron microscope and/or an optical microscope and/or mounted onto micromanipulator needles for FIB milling.

4.3.5. Qualitative Optical Interrogation

Photographs of native and coated butterfly wing sections (dead insect specimen) were taken with a 7.1 mega pixel PowerShot A710 IS digital camera (Canon U.S.A., Inc., NY, USA) with the macro feature enabled and using the image stabilizer function with no flash. Typically, individual scales were imaged with a Keyence VHX-600 digital microscope (Keyence Corporation, Osaka, Japan) outfitted with a 250x - 2,500x objective. The Keyence digital microscope was also used to generate wing area images, as well as images of single scales that were dispersed on pre-cleaned (2.54 x 7.62 x 0.1 cm) Gold Seal ® micro slides (Gold Seal® Products, N.H, USA). Before taking images the white balance was set using a Teflon^{TM} block in bright field mode at 1000x magnification. Some images were generated with fine depth composition of at least 5 frames taken at increasing z-heights (i.e., the bottom focal plane to top focal plane of an object were sequentially imaged and then stacked to generate an entire image in focus).

4.3.6. Quantitative Optical Interrogation

All quantitative optical interrogation was performed by A. Lethbridge under the guidance of P. Vukusic, both of University of Exeter. The macroscopic reflection spectra measurements (e.g., mapped wing section measurements) were taken using a QR600-7-SR-125F standard reflection probe (Ocean Optics, FL, USA). The illumination was provided by an HPX high-powered continuous wave Xenon light source (Ocean Optics, FL, USA). The spectral analysis was performed using an HR 2000+ USB spectrophotometer. The spectrophotometer was used in conjunction with Spectra Suite Software Ocean Optics (Ocean Optics, FL, USA). The probe was held normally incident to the sample ~ 2 mm away with a 1 mm spot size. Five measurements for each of three mapped spots per sample type were taken. The position of each reflection peak maximum for each spectrum was determined through a Gaussian fit (i.e., peak of Gaussian fit indicated wavelength of reflection peak position) (utilizing IGOR pro 6.12A data analysis software, WaveMetrics Inc., OR, USA) as demonstrated in **Figure 67**. The average reflection peak wavelength from these 15 measurements were normalized to the uncoated mean reflection peak maximum position to report the relative shift in reflectance peak position.

The imaging and the microspectroscopic spatial reflectivity mapping of single, needle-mounted scales were conducted within a Leica DMRX optical microscope (Leica Microsystems Inc., IL, USA) using a 50x (or 100x) objective lens and the microscope halogen lamp as illumination source. Through an additional microscope port, a fraction of the reflected light was collected and guided by a fiber (50 µm and 550 µm fibers from Thorlabs, Inc., NJ, USA) to the spectrometer (Maya 2000 Pro spectrometer, Ocean

Optics, FL, USA). The detection spot size depends on the diameter of the fiber and the magnification of the objective lens. The combination of a 50x objective and 50 µm core diameter fiber resulted in a detection area of approximately 1.2 μm^2. In order to acquire spatially and spectrally resolved intensity distributions of a single scale the sample was translated in the focal plane of the microscope in steps of 1 µm, scanning an area of typically 60 µm x 60 µm using an automated, remote-controlled stage (ES110 stage with OPTISCAN controller, Prior Scientific, NY, USA). A spectrum was taken after each step resulting in a complete map of the spectrally resolved intensity distribution of the whole scale (typical integration times for each spectrum depend on the reflectivity of the individual sample but were generally of the order of 100-300 ms, each of the acquired spectra results from an average of 3-5 spectra to minimize noise in the data). Using appropriate evaluation algorithms the spatial distribution of peak reflectance intensity and wavelength could be extracted from this data. Equipment driven and analysis of data was processed utilizing code written in Igor Pro 6.12A by Mathias Kolle, Harvard University (advised by Joanna Aizenberg). To obtain an average reflectivity of single surface-modified butterfly scales that were coated with Ti-O and Sn-Ti-O in a layer-by-layer surface sol-gel process, spectra were acquired from at least 8 different scales mounted on a glass slide. For the collection of the spectra a 550 µm core diameter fiber and a 20x objective were used in the Leica microscope (i.e., set-up used for needle mounted scales) to allow for the collection of data from a sufficiently large, representative area (i.e., ~30 µm in diameter) on each scale. As with the mapped reflectance spectra from wing sections, the reflection peak maximum for each single scale measurement was determined through a Gaussian fit of the reflectance peak. The position of the peak of the Gaussian

fit was reported as the reflection peak wavelength position for each spectrum. The Gaussian fit was conducted in wavelength space rather than frequency space which may artificially compress the left tail of the curve away from a truly normal distribution. However such errors resulting from the reciprocal relationship between frequency and wavelength were present in all Gaussian fits and it should be noted similar trends were observed in plotting peak positions identified with wavelength of maximum peak reflectance value. The position and uncertainty of the peak reflectance wavelength for a given sample was represented by sample mean ± calculated standard uncertainty (i.e., represented by estimated standard deviation from at least 8 independent measurements). It was assumed that the estimated mean values of the peak position wavelength are approximately normally distributed. For this reason the mean peak wavelength ($\lambda_{measured}$) ± uncertainties ($u_{measured}$) indicates that the unknown true peak position values should lie in the interval $\lambda_{measured} \pm u_{measured}$ with a 68% confidence level[95].

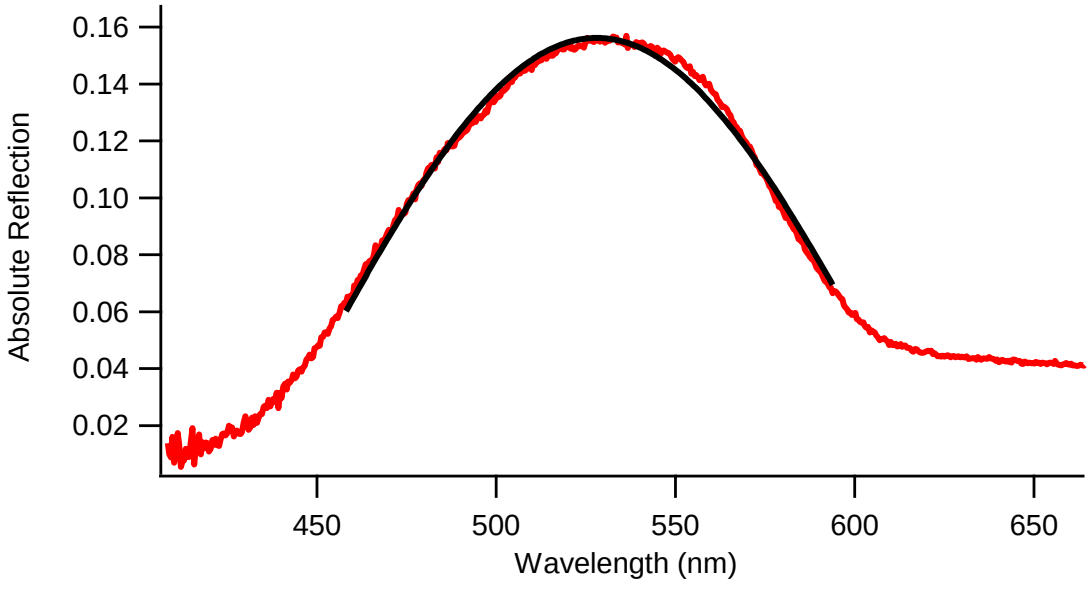

Figure 67: A single reflection spectrum from a native *P. sesostris* wing section (red line) with Gaussian fit (black line) used to determine the reflectance peak position. For mapped specimens 3 areas had 5 such spectra taken and the average reflectance peak wavelength of the 15 values was

reported in relative peak shift data. Representative spectrum and Gaussian fit courtesy of A. Lethbridge and P. Vukusic, University of Exeter.

4.3.7. Characterization of the Morphology, Chemistry, and Phase Content

The morphologies of the starting *Parides sesostris* wing scales, the SSG-coated scales, and the coated and pyrolyzed scales were evaluated with a field emission scanning electron microscope (1530 SEM, LEO/Zeiss Electron Microscopy NY, USA) after mounting directly on aluminum stubs (Ted Pella, CA, USA) with double-sided carbon tape (Ted Pella, CA, USA). EDS spectra were collected on the LEO 1530 outfitted with an INCA EDS system (Model 7426, Oxford Instruments, Bucks, UK). Microsurgeries of individual *P. sesostris* butterfly scales, and subsequent secondary electron imaging were performed by Craig G. Cameron, Georgia Institute of Technology, via use of a dual beam focused ion beam (FIB) instrument (Nova Nanolab 200 FIB/SEM, FEI, Hillsboro, OR, USA). For FIB milling, single scales were mounted onto a micromanipulator needle with epoxy. Typically, mounted scales were imaged with a Keyence VHX-600 digital microscope before and after FIB milling to correlate optical and SE images. FIB-milled specimens were then shipped to the University of Exeter for MSP analyses by Alfie Lethbridge and Prof. Pete Vukusic.

High magnification (150,000 kx) SE images were taken of a carefully chosen orientation (i.e., normal to hexagonal pore array) within gyroid structure of native and inorganic replica *P. sesostris* green scales. Eight individual measurements were taken on a minimum of 5 different scales for a total of 40 measurements of the hexagonal pore spacing within a single type of specimen. The measurements were taken of center-to-center distances of the solid (i.e., cuticle or hollow inorganic material) surrounding each hexagonal pore as shown in **Figure 68a**. The center of the solid was more readily

determined and such measurements were equivalent to the center-to-center distance between pores. Alfie Lethbridge of the University of Exeter, scaled the hexagonal array dimensions of a SolidWorks 3D CAD (SolidWorks Corporation, MA, USA) gyroid model to those measured via SE images of native scales (Average pore spacing = 235 nm). The 3D model was then reoriented in three dimensional space without changing the zoom to measure the lattice parameter (a = 264 nm) and compared with previously reported values (a = 261 nm)[94]. Additionally, the reported variation of the hexagonal pore spacings for all specimens was calculated from the average lattice spacing from each micrograph (5 mean values each calculated with8 independent measurements, utilizing a sample size of 5 rather than a sample size of 40 ensured the deviation was not artificially reduced by large number of measurements.

High magnification SE images (taken at 260,000x magnification) of coated/pyrolyzed inorganic shell cross-sections were utilized to measure the shell wall thickness as shown in **Figure 68b**. Reported average wall thickness and standard deviation values were calculated from 40 independent measurements. All measurements taken were on samples without any sputter coatings to ensure the dimensions were only a function of the inorganic replica. The uncertainty of the hexagonal pore spacing and inorganic shell thickness measurements was represented by sample mean ± calculated standard uncertainty (i.e., represented by estimated standard deviation from 40 independent measurements). It was assumed that the estimated mean values of the dimensional measurements are approximately normally distributed. For this reason the mean hexagonal spacing / inorganic shell thickness ($m_{measured}$) ± uncertainties ($u_{measured}$)

indicates that the unknown true spacing/thickness values should lie in the interval $m_{measured} \pm u_{measured}$ with a 68% confidence level[95].

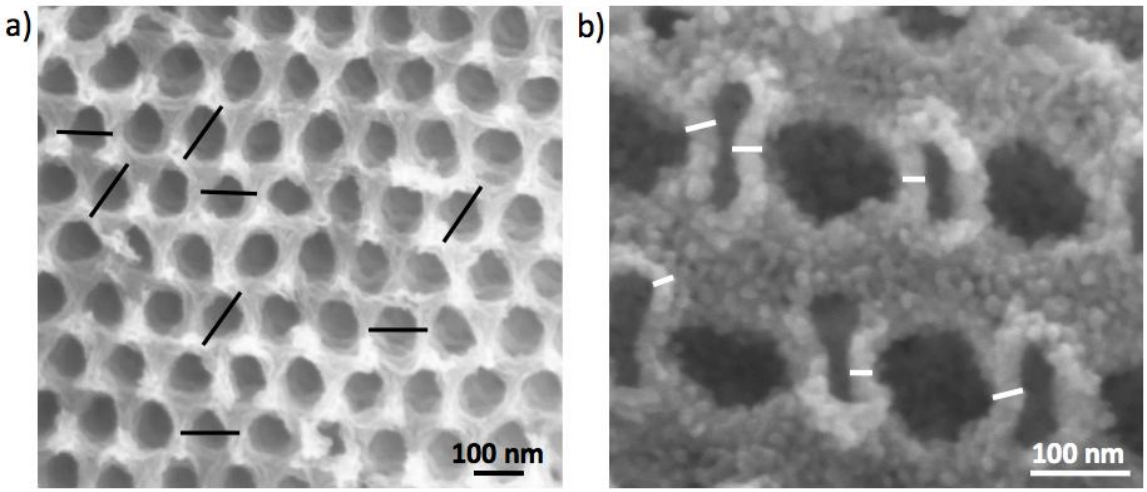

Figure 68: SE images of representative fracture cross-sections imaged for determining (a) hexagonal pore spacing (10 Ti-O SSG deposition cycles after organic pyrolysis) and (b) inorganic shell thickness (75 Sn-Ti-O SSG deposition cycles after organic pyrolysis).

4.4. *Results & Discussion*

Prior to the application of Sn-doped Ti-O-bearing coatings, it was necessary to interrogate the relationship between tin dopant concentration in the precursor solution and the formation of rutile titania at 450°C for 4 hr in air, so an appropriate precursor composition could be chosen for SSG deposition. In this experiment, stoichiometric mixtures of tin(IV) and titanium(IV) isopropoxides were hydrolyzed and pyrolyzed (450°C, 4 hr, in air). The resulting XRD patterns from hydrolyzed and heat treated 0, 10, 12.5, 15, 17.5, 20 and 100 mol% Sn-doped precursor solutions are shown in **Figure 69**. Peak positions and intensities were matched to Powder Diffraction File Card Numbers 98-000-0081, 98-000-0128, 98-000-0375, and 98-000-0151 in the International Center for Diffraction Data database for anatase TiO_2, brookite TiO_2, rutile TiO_2, and SnO_2 (cassiterite) respectively. After hydrolysis and pyrolysis of pure tin(IV) isopropoxide,

nanocrystalline cassiterite (SnO_2) was formed. Hydrolysis and pyrolysis of titanium(IV) isopropoxide resulted in primarily anatase titania with a minority brookite phase. It should be noted the 20 mol% Sn solution led to nearly pure rutile titania after hydrolysis and organic pyrolysis. The crystallite size was determined via Scherrer analysis from five peaks and revealed sub-10 nm crystallite sizes (i.e., ~5-8 nm) for all powder specimens. Such crystallite sizes were consistent with particle sizes observed in high magnification SE images and are well below dimensions thought to contribute considerable elastic scattering. The true composition of the Sn and Ti precursors was determined by thermal assays completed in triplicate as described in **Section 4.3.2**. Thermal assays revealed the Sn precursor was actually ~10.5% less concentrated than reported by the manufacturer and Ti precursor concentration was ~1.04% less concentrated than reported by the manufacturer. Hence, the 20 mol% Sn / 80 mol% TiO_2 mixture was determined to have 18.4 mol% Sn. **Table 4** reveals the expected values from the manufacturer's reported concentration and the corresponding calculated solution concentrations obtained using data from thermal assays of precursors. Reported variance is ± one standard deviation calculated from thermal analysis measurements each done in triplicate. For quick reference, this particular lot of Ti(IV) isopropoxide produced 0.265 g TiO_2, or 3.32×10^{-3} mol TiO_2, per milliliter of solution. This particular lot of Sn(IV) isopropoxide solution produced 0.0383 g SnO_2, or 2.54×10^{-4} mol SnO_2, per milliliter of solution.

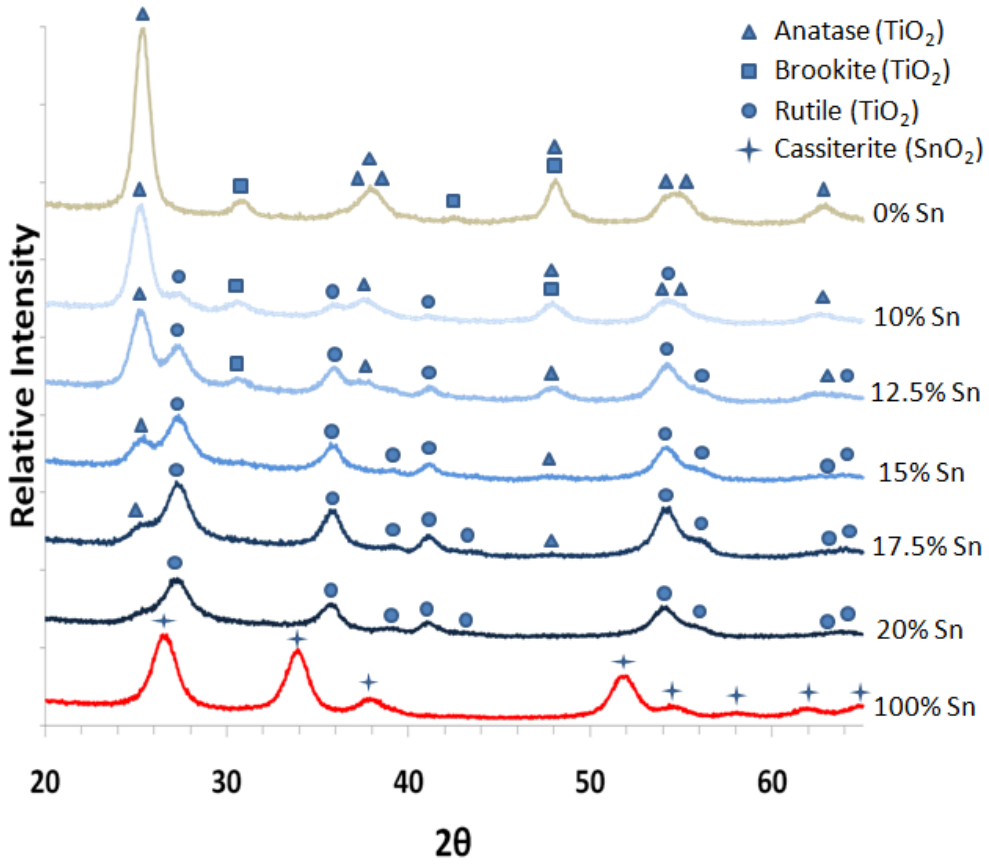

Figure 69: XRD patterns of both pure TiO_2 and various SnO_2/TiO_2 stoichiometric mixtures (concentrations marked as expected concentrations based upon manufacturer reported values) after pyrolysis (450°C, 4 hr, air) of hydrolyzed precursors showing the increase in rutile phase content with increasing Sn content, the presence of anatase/brookite TiO_2 without Sn-doping, and cassiterite SnO_2 without presence of TiO_2.

Table 4: Expected Concentration vs. Actual Concentration of Sn-doped TiO_2 solutions

Expected Sn Mol%	Actual Sn Mol%
7.5	6.82 ± 0.07
10	9.12 ± 0.09
12.5	11.4 ± 0.11
15	13.7 ± 0.14
17.5	16.1 ± 0.16
20	18.4 ± 0.18

Based upon X-ray analysis and thermal assay results, a minimum of 18.4 mol% Sn dopant was required to produce nearly phase-pure rutile polymorph after pyrolysis at 450°C for 4 hr in air. Butterfly wings were coated with either Ti(IV) isopropoxide or 18.4 mol% Sn(IV) isopropoxide/ 81.6 mol% Ti(IV) isopropoxide to form anatase and

rutile polymorphs replicas after organic pyrolysis. SSG coatings were applied to both native *P. sesostris* surfaces and to wing surfaces that had undergone dendritic amplification of hydroxy groups. The SSG process for forming constructively modified (i.e., SSG-coated) templates, as well as anatase and rutile inorganic replicas, are shown schematically in **Figure 70** and **Figure 71**, respectively. The inorganic scales are referred to as hollow replicas as the SSG coating does not penetrate deeply into the template and forms a shell around space chitin once occupied as demonstrated by SE images of coated and pyrolyzed specimens in **Figure 72**.

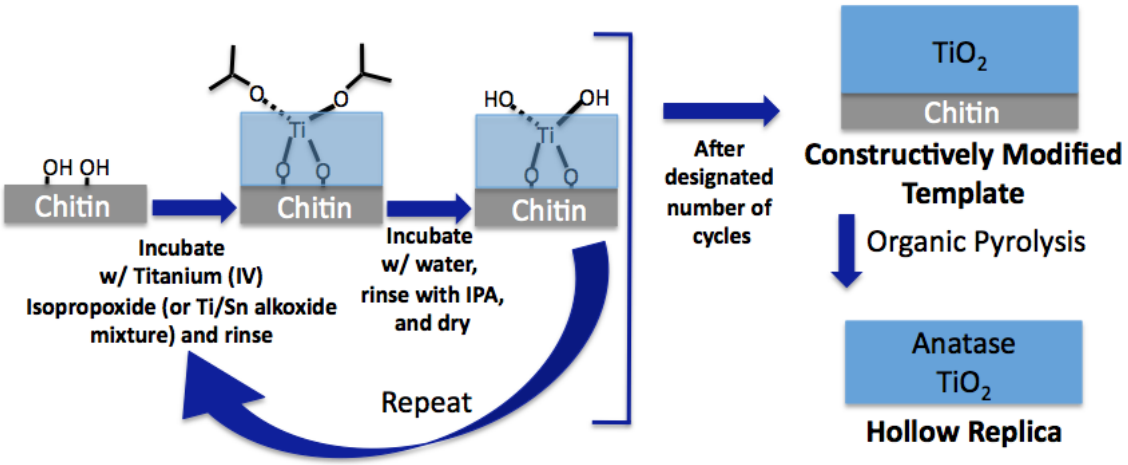

Figure 70: A schematic of the SSG deposition of Ti-O- bearing SSG coatings and subsequent heat treatment resulting in hollow anatase titania replicas.

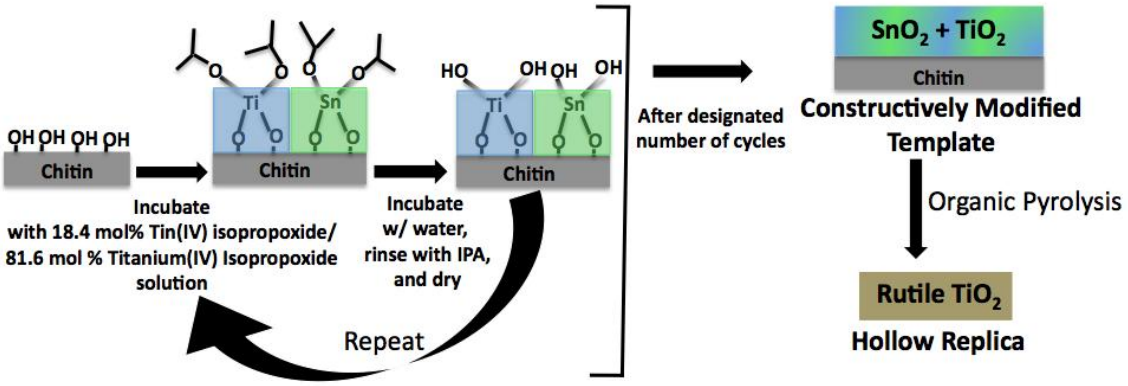

Figure 71: A schematic of the SSG deposition of Sn-Ti-O- bearing SSG coatings and subsequent heat treatment resulting in hollow rutile titania replicas.

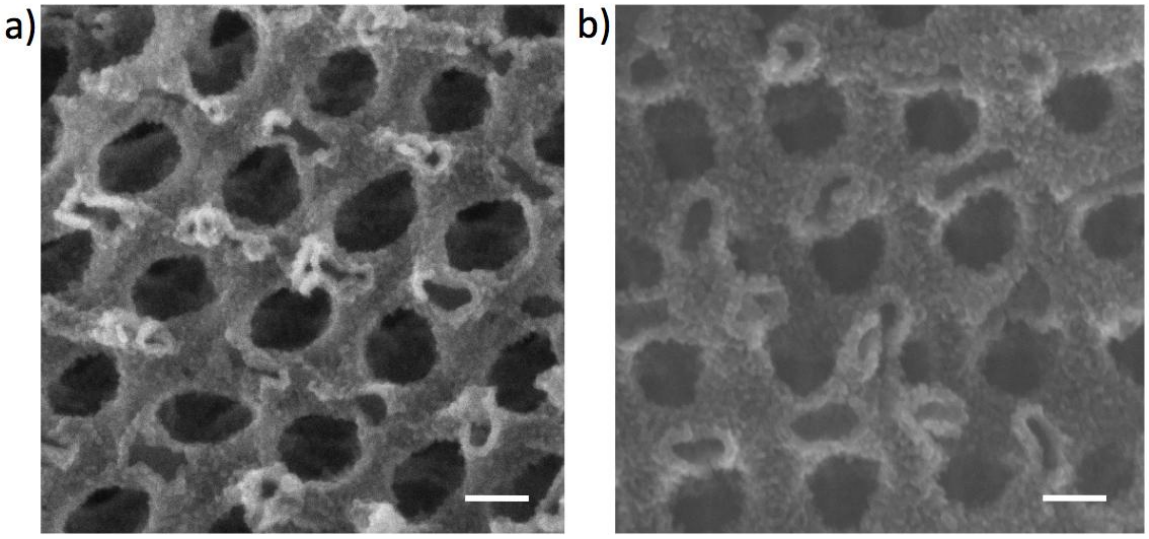

Figure 72: SE images off PPC structure within *P. sesostris* green scales showing hollow nature of (a) 150 SSG deposition cycles of Ti-O and (b) 100 SSG deposition cycles of Sn-Ti-O coatings after organic pyrolysis (450°C, 4 hr, in air) of chitinous template. Both scale bars represent 100 nm.

To isolate the effect of SSG coatings, reflection spectra from individual wing sections were mapped. Such mapping reduced the role of intrabutterfly variations. Utilizing sections from an individual butterfly eliminated interbutterfly variations. Tabulating the wavelength maxima as a function of location within a single green dorsal region of *P. sesostris* wing (shown in **Figure 73**) indicated intrascale reflection peak variations. Bright field optical micrographs of two different *P. sesostris* butterflies (note: images taken on the same day with identical white balance, shutter speed, gain, and magnification) shown in **Figure 73** revealed considerable interbutterfly variations. Mapped specimens were coated in increments of 25 SSG cycles (i.e., 25 cycles followed by optical interrogation, then 25 more cycles followed by optical interrogation, etc.). Bright field microscopy revealed the color change of representative areas from mapped *P. sesostris* wing sections with and without dendritic amplification after 25, 50, 75, 100, and 125 SSG layers of Ti-O- or Sn-doped Ti-O- coatings (**Figure 74**). Both optical microscopy (**Figure 74**) and quantitative optical spectroscopy (**Figure 75**) revealed no

consistent enhancement in the redshift through the dendritic surface hydroxy group amplification process before coating via SSG deposition. Thus, further interrogation of coated and inorganic replica scales focused upon native scales with no amplification of surface hydroxy groups.

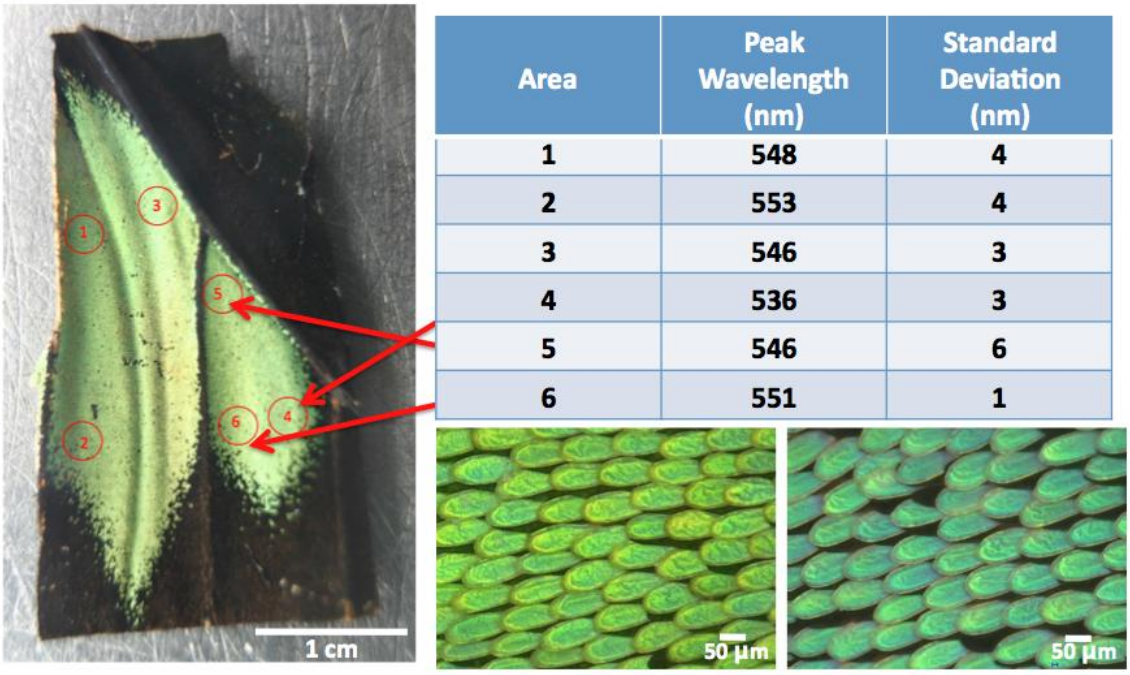

Area	Peak Wavelength (nm)	Standard Deviation (nm)
1	548	4
2	553	4
3	546	3
4	536	3
5	546	6
6	551	1

Figure 73: Photograph of a *P. sesostris* wing section (left) with numbered mapped regions showing intrabutterfly variations in reflectance spectra peak wavelength (standard deviation calculated from five 1mm spot size measurements within indicated mapped region). Bright field micrographs taken with identical conditions (lower right) of green scales from two different *P. sesostris* butterflies demonstrating interbutterfly color variation.

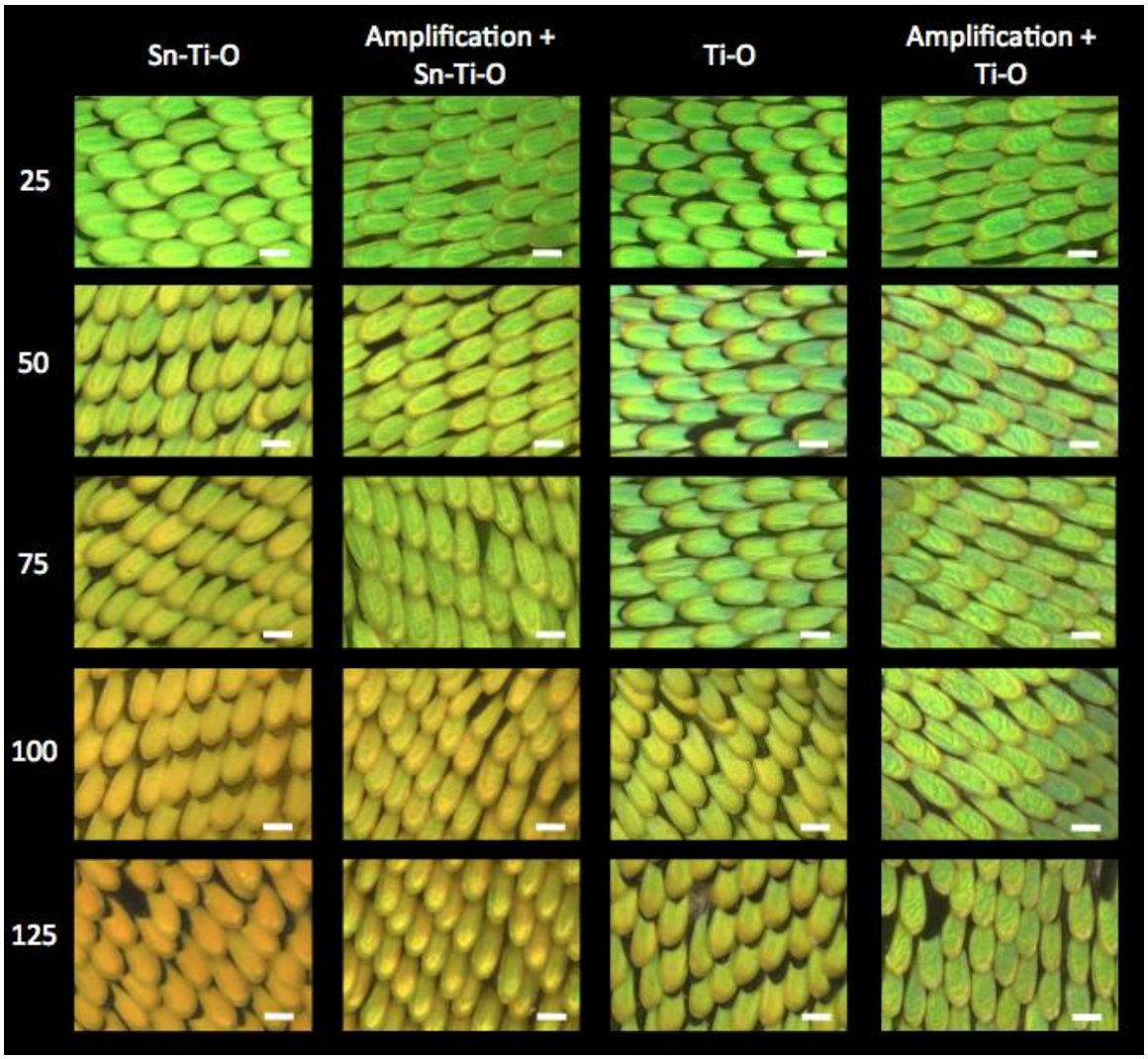

Figure 74: Bright field optical images of *P. sesostris* green dorsal wing sections with and without amplification of surface hydroxy groups, with 25, 50, 75, 100, and 125 layers of SSG deposition of both Ti-O- or Sn-Ti-O- bearing precursor solutions. All images taken with identical white balance and conditions but not on same day (lamp brightness may be different). All scale bars indicate 50 µm.

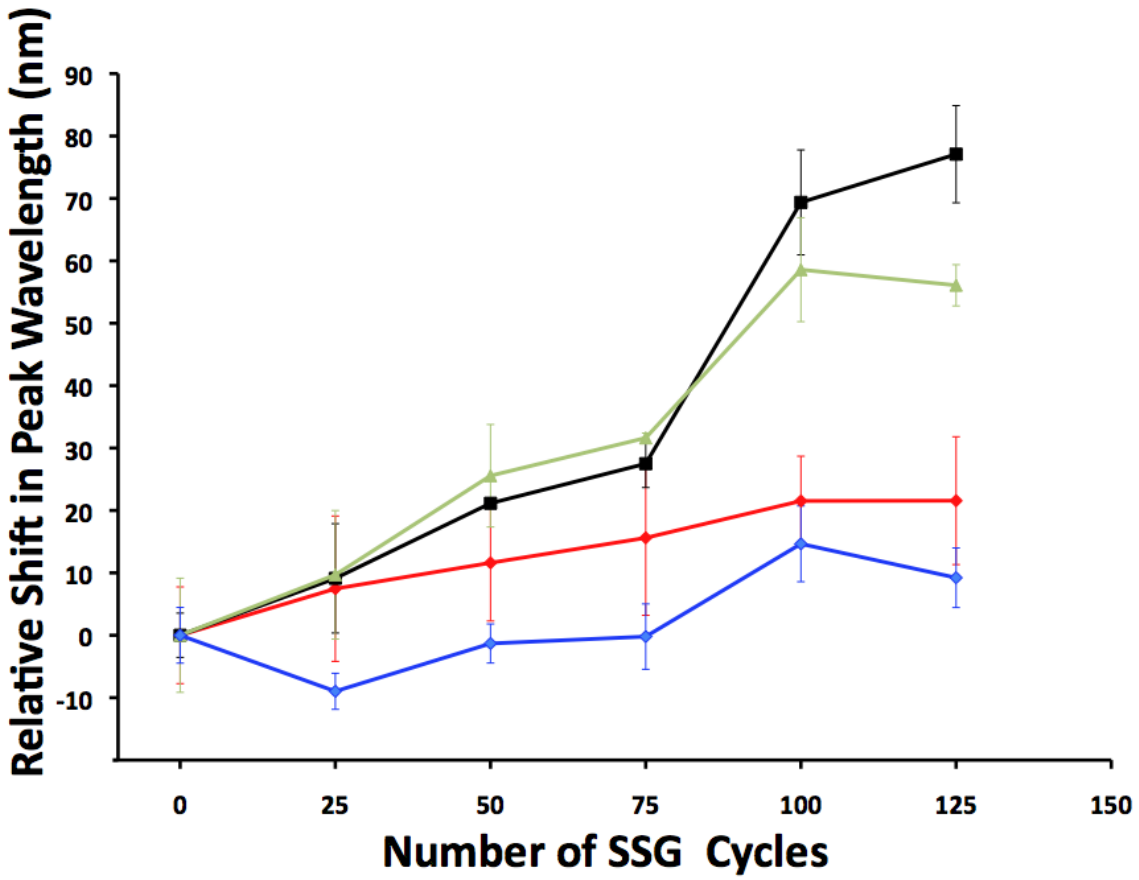

Figure 75: Bifurcated probe spectrophotometer data from average of five measurements from each of three mapped spots within a wing section (each data point represents an average of 15 reflectance peak values and variance is shown with error bars representing calculated standard deviations from 15 peak wavelength values) as a function of number of SSG deposition cycles. Specimens were evaluated with and without hydroxy group amplification and coated either with Sn-Ti-O- or Ti-O-bearing SSG deposition. All data was normalized to initial reflectance spectra of corresponding native or dendritically amplified wing sections mapped before application of SSG coatings. Spectra and data analysis provided by A. Lethbridge and P. Vukusic, University of Exeter. Solid lines meant to guide the eye.

Native wing sections with Ti-O and Sn-Ti-O coatings both exhibited a redshift in the peak reflectance. Linear fits of the peak reflectance shift (mapped area measurements) from normalized native scales revealed an average 0.6 nm/layer shift for Sn-Ti-O coatings and a 0.2 nm/layer shift for Ti-O coatings. Coatings on quartz plates and silicon wafers revealed no color imparted by either Ti-O or Sn-Ti-O SSG coatings. Although using a section from a single butterfly reduced variation from the native template, and the section was mapped and iteratively coated and characterized;

handing/shipment of the scales could result in changing the orientation of the scales with respect to the wing membrane and/or loss of scales. However, this variation was accounted for within the standard deviation of the 15 measurements (5 measurements within 3 different mapped regions) within each type of mapped specimen. Additionally, single scale MSP measurements were taken on Sn-Ti-O and Ti-O coated scales removed from areas outside of the mapped regions for optical analyses at each 25 layer step in the coating process.

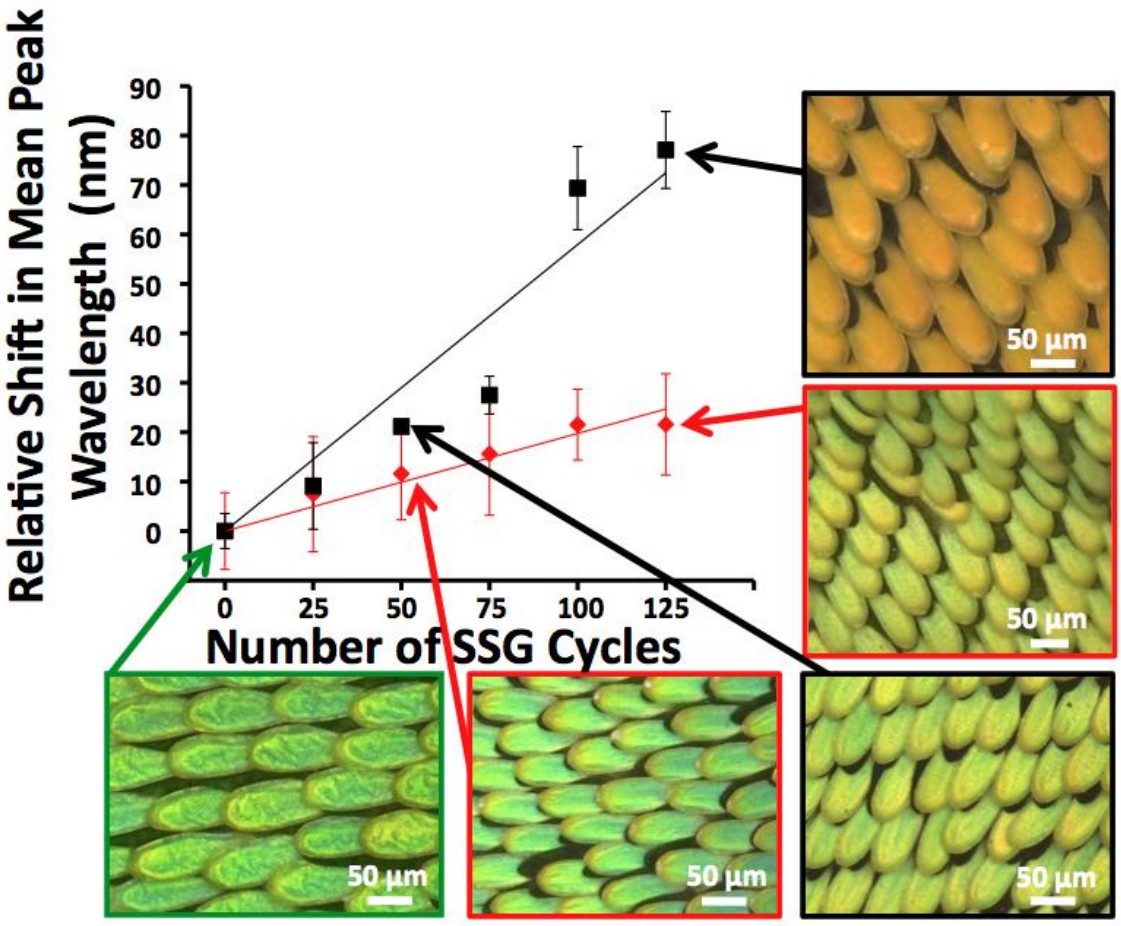

Figure 76: Plot of the relative shift in the wavelength of the mean reflectance peak maximum with increasing number of Ti-O or Sn-Ti-O SSG deposition cycles applied to native green *P. sesostris* butterfly wing sections. Bright field micrographs of corresponding native scales, and scales coated with 50 or 125 layers of Ti-O and Sn-Ti-O, are also shown. The data points represent mean reflectance peak wavelength with ± 1 standard deviation error bars (calculated from 15 individual measurements). Spectra and data analysis provided by A. Lethbridge and P. Vukusic, University of Exeter.

Single scale imaging (**Figure 77**) and microspectrophotometry (MSP) measurements (**Figure 78**) corroborated the larger redshift of the reflectance peak in Sn-containing coatings, and revealed a much larger absolute overall redshift in both types of coatings (Sn-Ti-O and Ti-O) with respect to larger area interrogation on mapped wing sections. MSP measurements were taken on at least 8 (i.e., 10 measurements per sample type except for 25 and 125 layer samples) individual scales with the native orientation (ridge side up) as well as with the PPC side of the scale facing up. The redshift for Sn-Ti-O coatings on single scales approached nearly 1 nm/SSG deposition cycle (~160 nm shift after 150 layers). The redshift for Ti-O coatings was ~0.5 nm/SSG deposition cycle (80 nm shift after 150 SSG deposition cycles). Linear fits to the single scale MSP data (**Figure 78**) yielded slopes of 0.961 (Sn-Ti-O ridge side up), 1.06 (Sn-Ti-O PPC side up), 0.489 (Ti-O ridge side up), and 0.503 (TiO PPC side up).

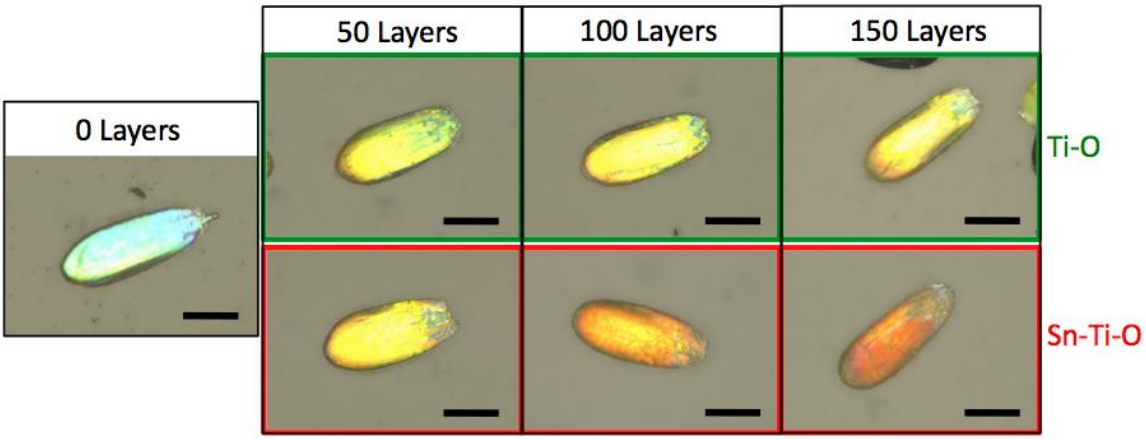

Figure 77: Single scales PPC side up imaged under identical conditions (i.e., on the same day, with the same gain, the same shutter speed and with the same white balance) showing the color change with increasing number of layers of Ti-O and Sn-Ti-O SSG coatings. All scale bars indicate 50 µm.

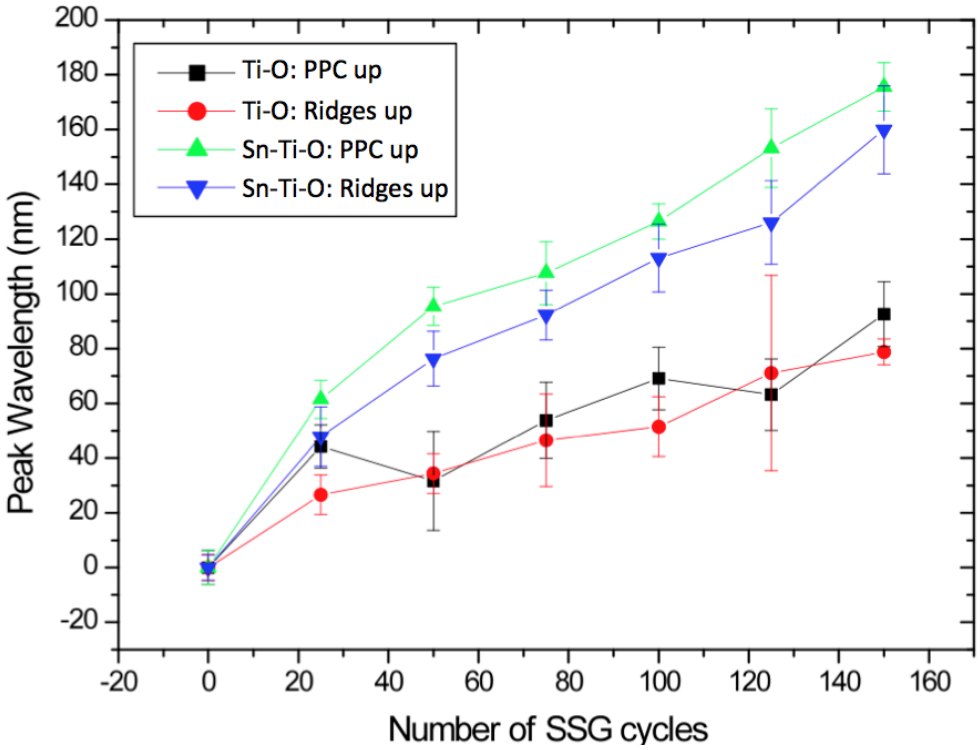

Figure 78: The MSP relative peak reflectance wavelength shift as a function of number of SSG cycles of Ti-O, and Sn-Ti-O- bearing SSG coatings. Spectra taken from individual scales oriented with PPC side up or ridge side up. The data points represent mean reflectance peak wavelength with ± 1 standard deviation error bars (calculated from a minimum of 8 individual measurements). Spectra and data analysis provided by A. Lethbridge and P. Vukusic, University of Exeter.

Both Ti-O- and Sn-Ti-O- coated wing sections shrank after organic pyrolysis as demonstrated with Ti-O coated wing sections in **Figure 80** and **Figure 81**. The degree of macroscopic shrinkage appeared to be reduced with an increase in the number of SSG cycles (10 Ti-O cycles (**Figure 79b**) vs. 30 Ti-O cycles (**Figure 80b**)). However, wing sections appeared white after organic pyrolysis. Factors that could have caused such firing-induced whiteness include: (i) lack of structural retention, (ii) shrinkage of the PPC lattice causing a reflection peak shift into the UV, (iii) scattering due to crystallization, (iv) the generation of a hollow replica, and/or (v) loss of absorbing/emitting bioorganic material.

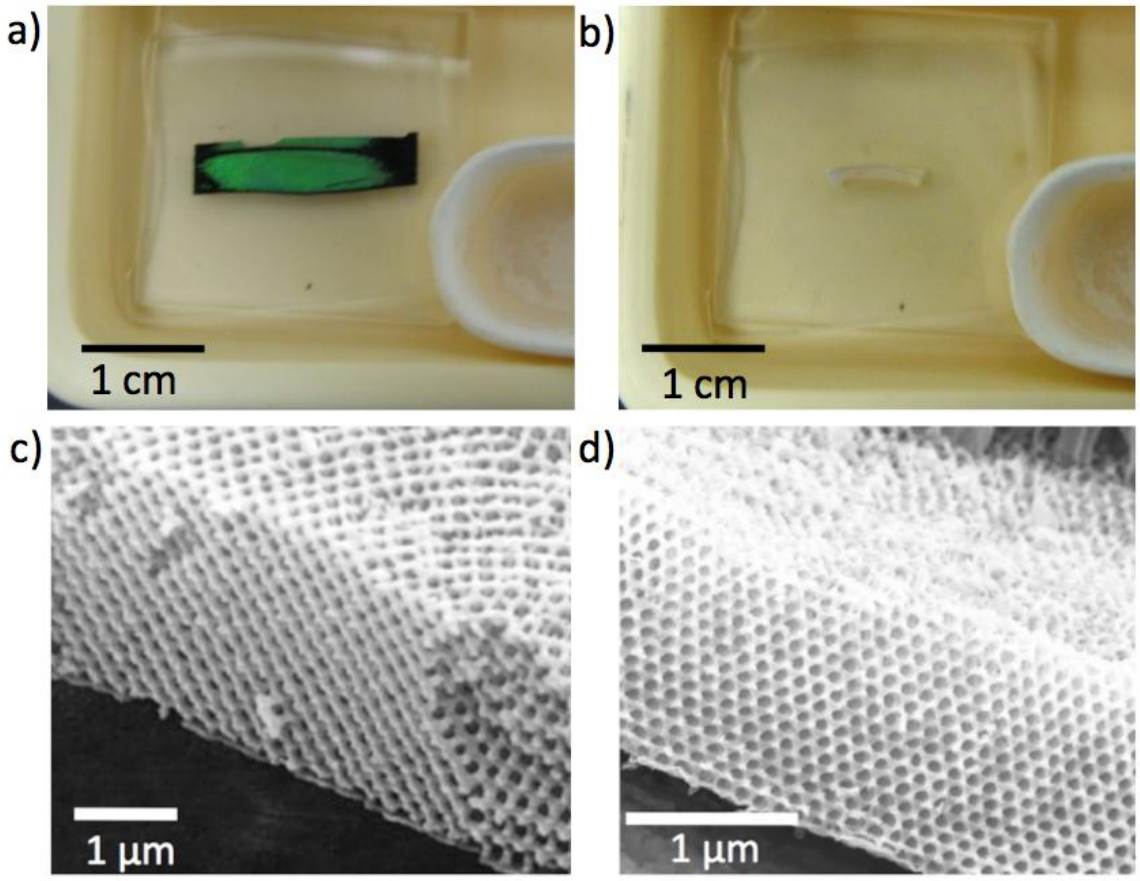

Figure 79: A coated *P. sesostris* wing section with 10 layers of Ti-O- bearing SSG deposition (a) before and (b) after organic pyrolysis (450°C, 4 hr, in air) along with SE images of (c) native PPC (courtesy P. Vukusic, University of Exeter) and (d) PPC of inorganic replica after 10 layers of SSG deposition and organic pyrolysis.

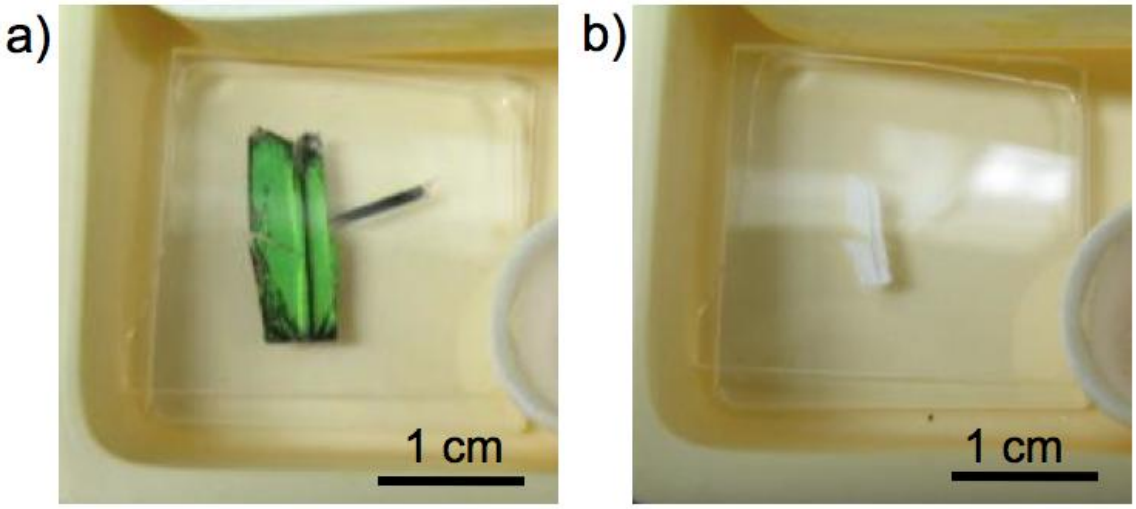

Figure 80: Photograph of (a) a coated *P. sesostris* wing section with 30 layers of Ti-O-bearing SSG and (b) the same coated wing section after organic pyrolysis (450°C, 4 hr, in air).

Despite considerable macroscopic and microscopic shrinkage the periodic microstructure of the PPC was retained with only 10 layers of SSG coating (**Figure 81a**). Interestingly, the lattice pore spacing of the inorganic PPC gyroid structure increased with an increasing number of SSG cycles (**Figure 81**, **Figure 82**, **Figure 83**). Quantification of shrinkage (**Figure 83**) was evaluated by measuring (see **Section 4.3.7** for method) the average hexagonal pore spacing in inorganic replicas as a function of the number of SSG deposition cycles. After organic pyrolysis of SSG-coated wing sections, there appeared to be an increased hexagonal pore spacing with increased number of SSG cycles, and apparent increased fill fraction with increased number of SSG cycles (see thickness of inorganic shell values in **Table 5**). A solid works model of the gyroid structure and prior reports in the literature were used to correlate the values determined via SE image measurements of the hexagonal pore spacing to the reported lattice spacing of the gyroid ($Ia\bar{3}d$) structure (i.e., 260 ± 63 nm)[94]. Rotation of the 3D gyroid model (with dimensions defined by SE image revealing a 235 ± 19 nm hexagonal pore spacing) in fact represented a native gyroid ($Ia\bar{3}d$) lattice parameter of ~264 nm.

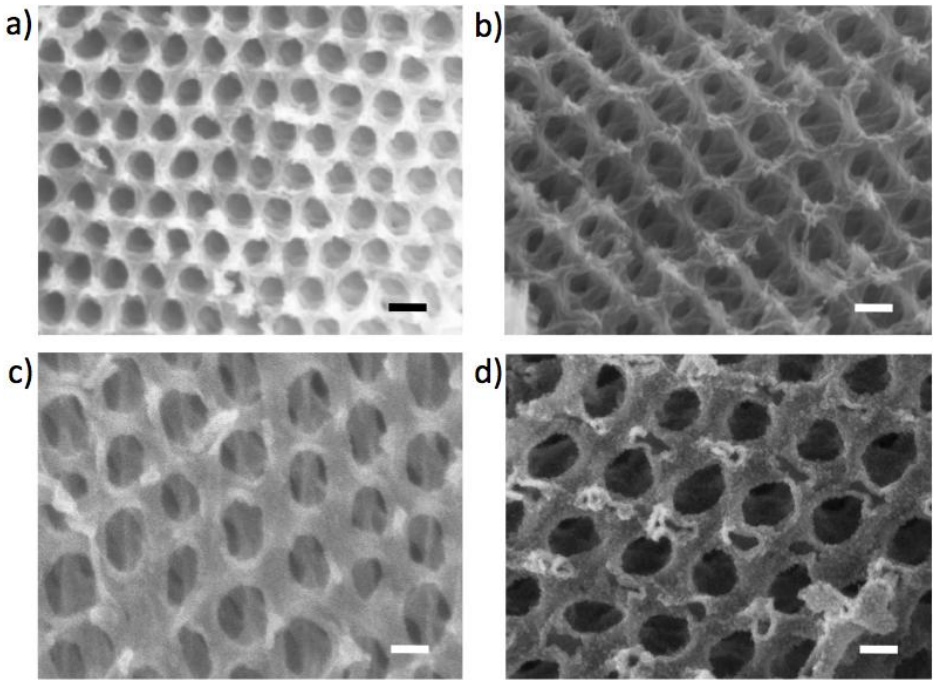

Figure 81: Secondary electron images of the Ti-O-coated PPCs with (a) 10 layers, (b) 25 layers, (c) 100 layers and (d) 150 layers of SSG deposition after organic pyrolysis (450°C, 4 hr, air) showing the retention of the periodic nanostructure. All scale bars indicate 100 nm.

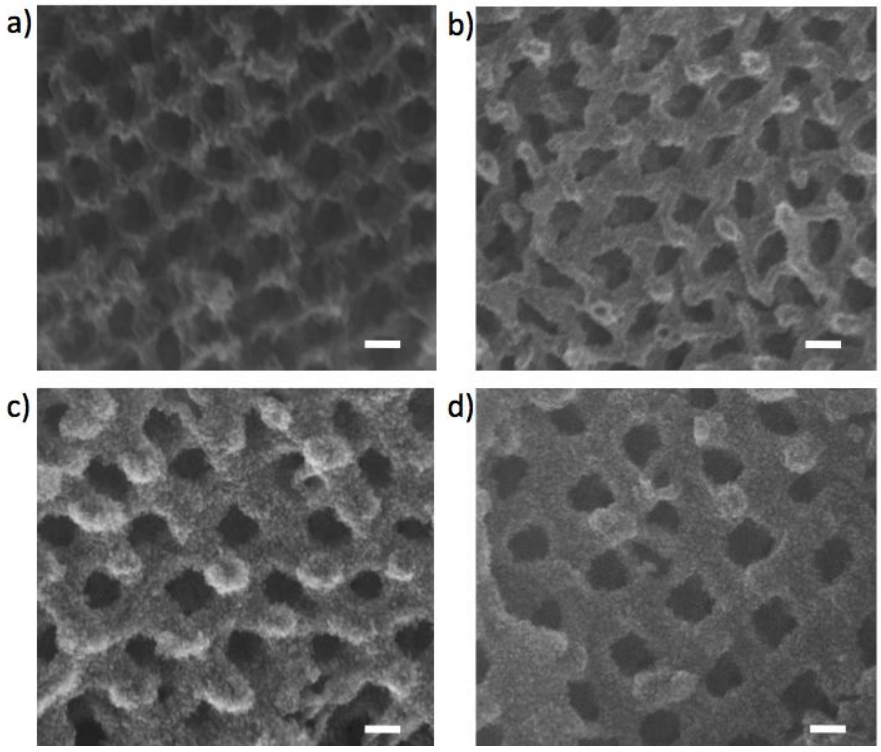

Figure 82: Secondary electron images of Sn-Ti-O-coated PPC with (a) 25 layers, (b) 50 layers, (c) 75 layers, and (d) 100 layers of SSG deposition after organic pyrolysis (450°C, 4 hr, in air) showing the retention of the periodic nanostructure. All scale bars indicate 100 nm.

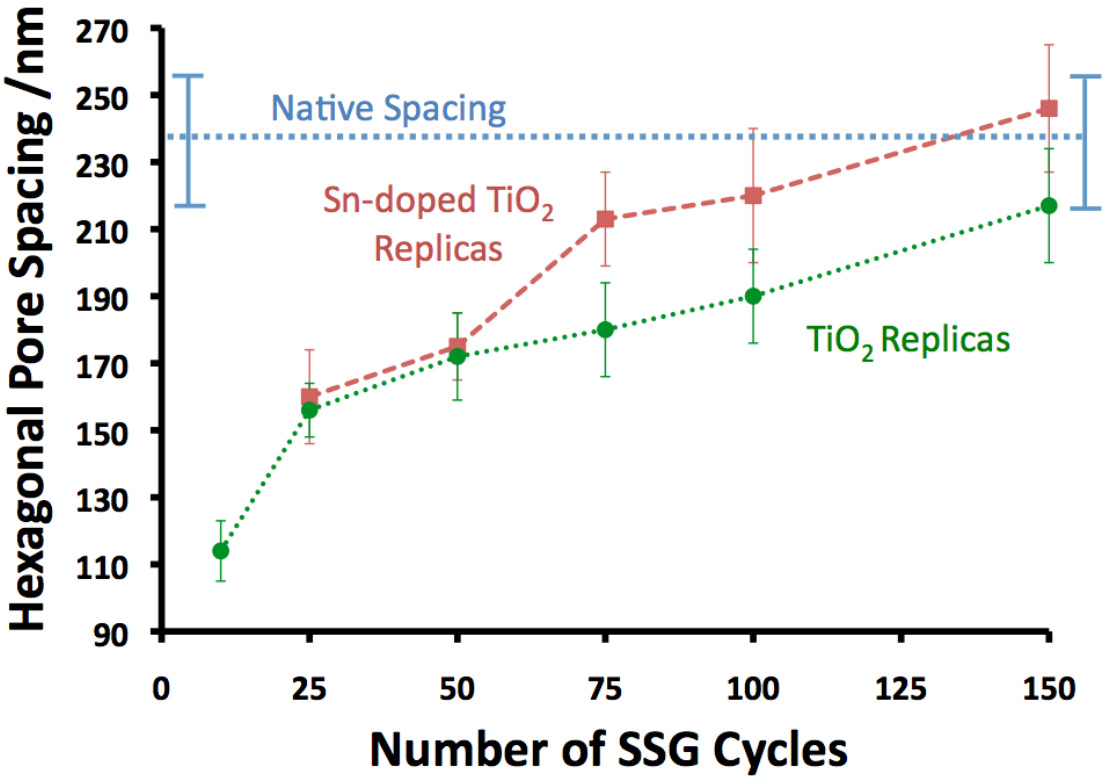

Figure 83: The average hexagonal pore spacing of native *P. sesostris* PPC vs. inorganic replica pore spacings measured after organic pyrolysis (450°C, 4 hr, air) of *P. sesostris* PPC coated with 10, 25, 50, 75, 100, and 150 Ti-O SSG deposition cycles(TiO_2 Replicas), and replica pore spacings measured after organic pyrolysis (450°C, 4 hr, air) of *P. sesostris* PPC coated with 25, 50, 75, 100, and 150 Sn-Ti-O SSG deposition cycles (Sn-doped TiO_2 Replicas). The data points represent mean hexagonal pore spacing ± 1 standard deviation error bars (calculated from at least 40 individual measurements). Dashed lines provided simply to guide the eye.

As expected, replicas from SSG coatings with Sn-doping were comprised of rutile and those without Sn-doping were comprised of anatase titania. Polymorphs of the inorganic replica scales were determined with Raman spectroscopy (spectra shown in **Figure 84**). Peaks at 398 cm^{-1}, 517 cm^{-1}, and 639 cm^{-1} were consistent with reported Stokes shifts for anatase titania[96]. Peaks at 431 cm^{-1}, and 615 cm^{-1}, were consistent with reported Stokes shifts for nanophase rutile titania[97]. SAED pattern of as-coated Sn-Ti-O scales (**Figure 85**) indicated that the SSG coatings were amorphous. SSG deposited Ti-O coatings on butterfly templates have been repeatedly been shown to be amorphous[91,98]. The elemental composition of the coatings was indeed similar to the composition of the

alkoxide stoichiometric mixture. Semiquantitative (standardless) EDS analyses revealed the presence of Sn, Ti, and O in the inorganic replicas coated with SSG deposition of Sn-doped titania alkoxide solutions as shown in **Figure 86**. EDS analyses performed on four different areas within pyrolyzed scales after 150 cycles of Sn-Ti-O- bearing SSG deposition indicated the Sn dopant concentration in the coating to be between 20.5 and 21.6 mol% Sn (calculated by (atomic% Sn) divide by (atomic% Ti + atomic %Sn)). Similarly, EDS of the Ti-O coatings revealed the presence of Ti, O, and C. The small (< 1 at%) carbon peak is most likely attributed to the carbon tape used for mounting. Due to the larger redshift in coated specimens and for demonstration of the facile application of multicomponent coatings, the optical response of Sn-doped rutile titania replicas were studied in detail.

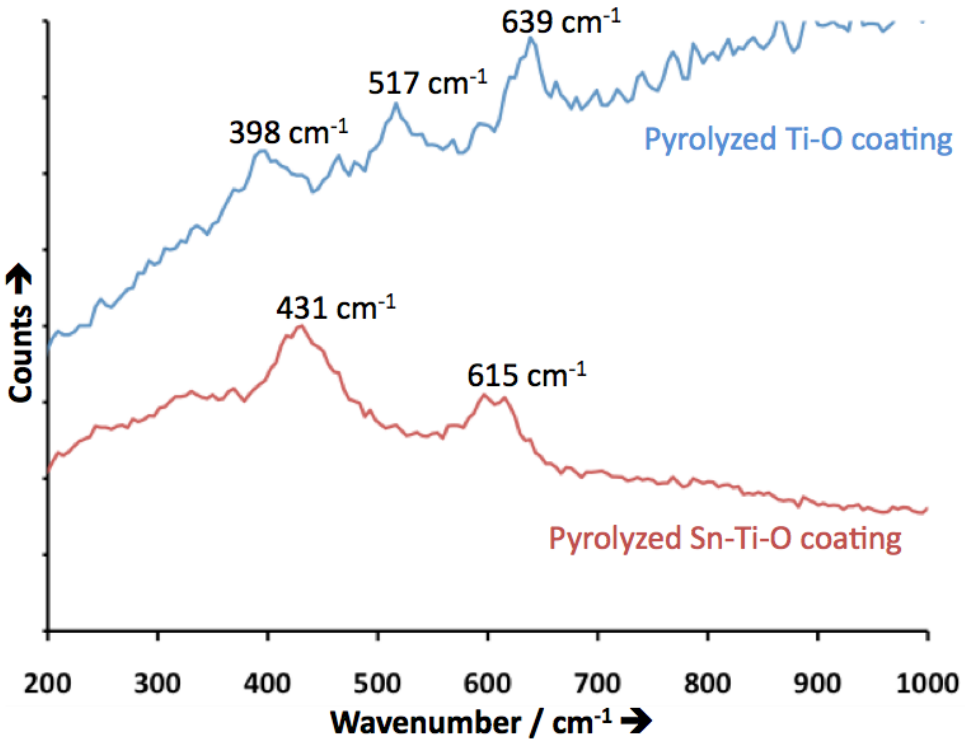

Figure 84: Raman spectra showing the rutile polymorph formed upon organic pyrolysis (450°C, 4 hr, air) of the Sn-Ti-O SSG coating, and the anatase polymorph of TiO_2 formed after organic pyrolysis (450°C, 4 hr, air) of the Ti-O SSG coating.

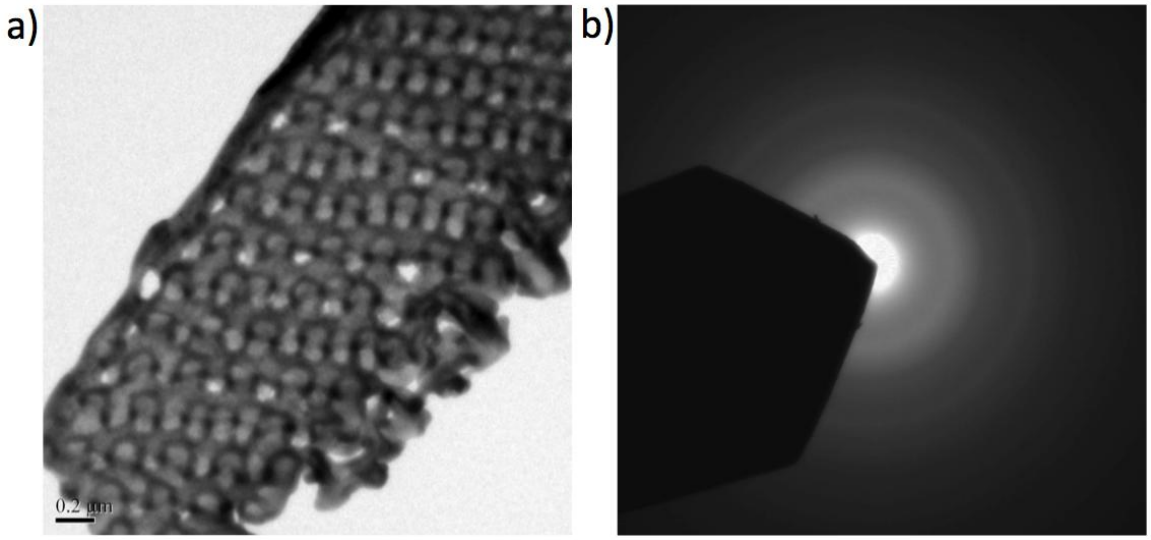

Figure 85: (a) A bright field TEM micrograph and (b) corresponding SAED pattern of FIB-milled cross-section of PPC portion of *P. sesostris* green scale after 150 Sn-Ti-O SSG deposition cycles.

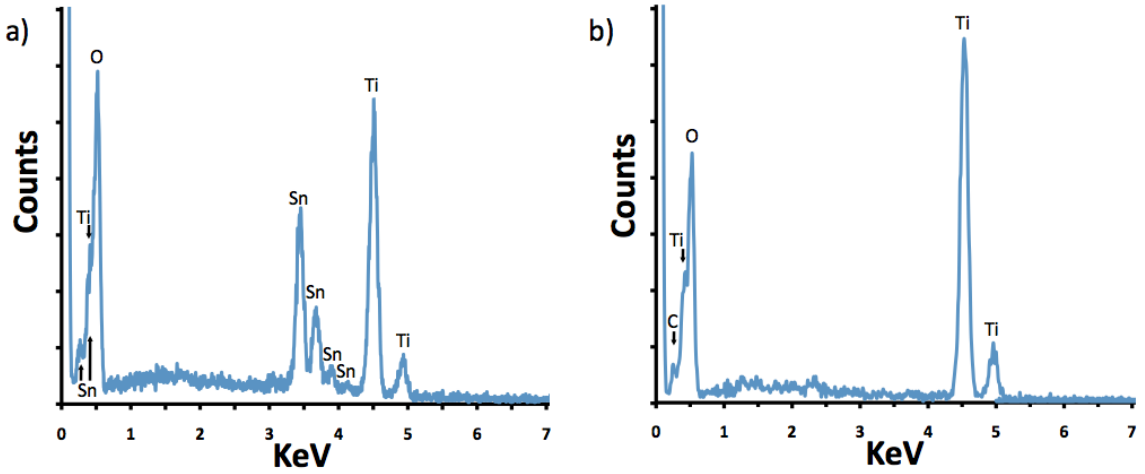

Figure 86: EDS spectra of (a) Sn-Ti-O coated and (b) Ti-O coated *P sesostris* wing scales after organic pyrolysis (450°C, 4 hr, in air).

It was hypothesized that structural color may be recovered if the lattice spacing of the inorganic hollow replicas approached that of the native lattice spacing. Unfortunately, inorganic wing sections macroscopically appeared white even after organic pyrolysis of samples with 150 cycles of SSG deposition. However, microscopic interrogation indicated that single inorganic replica scales facing PPC side up exhibited significant color. Bright field images of Sn-doped rutile titania replicas, which were fired

after 100 SSG deposition cycles of Sn-Ti-O, with both PPC and ridge side up are shown in **Figure 87**. The ridge structure deformed during organic pyrolysis and appeared to act as a scattering layer inhibiting the macroscopic observation of color. The gap in the ridge structure (**Figure 87a**) after organic pyrolysis provided direct proof of the deleterious effect of the coated/fired ridges on observed structural color (i.e. color was observed from exposed PPC within gap of ridges). Also, the color appeared roughly the same from the PPC side up and the ridge side up (**Figure 87b vs. a**). To interrogate structural components of inorganic scales, and to understand the detailed effects of replicating bioorganic cuticle with higher index materials, FIB removal of deformed ridge structure was necessary.

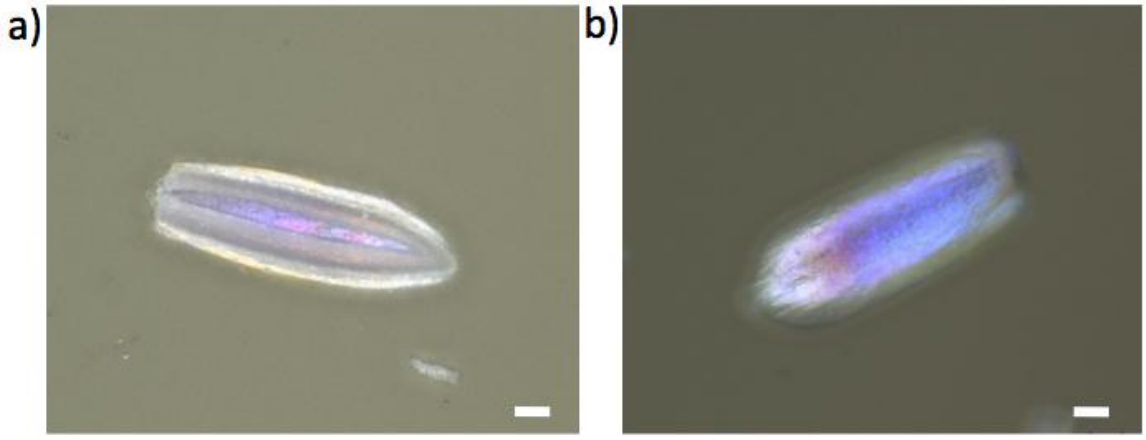

Figure 87: Bright field optical micrographs of inorganic replicas formed after organic pyrolysis of scales with 100 SSG layers of Sn-doped TiO_2 showing color emanating through gap in ridges (a) and from PPC side up (b). Scale bars indicate 10 µm.

It is important to note the shrinkage/deformation of the coated/fired ridges rendered large area spectroscopy of wing sections ineffective, as well as causing the white macroscopic appearance. Single scales mounted to a micromanipulator needle tip for FIB milling allowed for single scale optical interrogation with one or more intrascale components removed. **Figure 88** shows bright field optical images of FIB-milled inorganic scale replicas exhibiting tunable reflectance spectra as a function of the number

of applied SSG layers. SE images in **Figure 88** clearly show the FIB-milled and unmilled regions of the scale Considerable whole scale shrinkage was evident when comparing the 50 layer sample (**Figure 88:** left column) with the 100 layer (**Figure 88:** middle column) and 150 layer (**Figure 88:** right column) samples. This demonstration suggests that the optical response is strongly governed by the lattice/pore spacing of the replicas, which in turn is controlled by the coating and firing conditions. It has been reported that changing the fill fraction of the gyroid material should also redshift the reflectance spectra[94]. The increased fill fraction with increased coatings not only may be responsible for the color shift in the coated scales, but may also aid in the reproduction and redshifting of structural color in inorganic replicas. The enhanced fill fraction is qualitatively demonstrated in **Figure 82**. Deconvoluting refractive index, fill fraction, and lattice spacing effects may be investigated computationally. The mean (from 40 independent measurements on SE images of fracture sections taken at 260,000x magnification) inorganic shell wall thicknesses of the anatase TiO_2 and Sn-doped rutile TiO_2 replicas after 75, 100, and 150 layers are shown in **Table 5**. For modeling purposes, the wall thickness of Sn-doped TiO_2 coatings appears to increase by 0.32 nm per SSG cycle and the wall thickness of TiO_2 coating appears to increase by 0.16 nm per SSG cycle. These thicknesses were reasonable considering shrinkage due to crystallization and sintering of 0.6 nm per cycle thicknesses of the applied Ti-O coatings reported in **Chapter 1**[98]. Interestingly, the relative reflectance peak shift of the Sn-Ti-O- coated individual scales were nearly double that of the Ti-O coated scales (**Figure 78**).

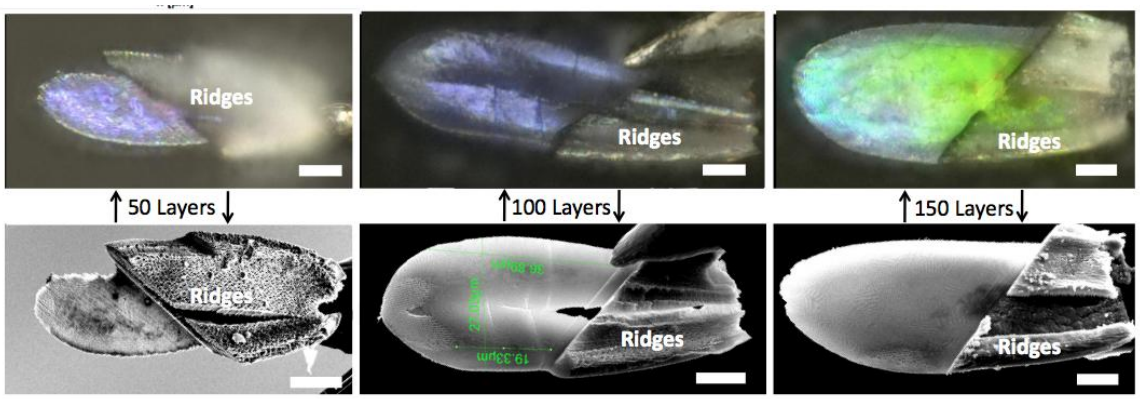

Figure 88: Bright field optical micrographs (top row) and SE images (bottom row) of a (left column) FIB-exposed photonic solid region (violet) from a 50 SSG cycle Sn-Ti-O coated and pyrolyzed inorganic replica scale, (middle column) a FIB-exposed photonic solid region (blue/violet) from a 100 SSG cycle Sn-Ti-O coated and pyrolyzed inorganic replica, and (right column) a FIB-exposed photonic solid region (largely green) of a 150 SSG cycle Sn-Ti-O coated and pyrolyzed inorganic replica. All unmarked scale bars indicate 10 µm. All images provided by C.G. Cameron, Georgia Institute of technology.

Table 5: Inorganic Shell Wall Thickness as a Function of Number of SSG Cycles Applied

# SSG Layers	Sn-doped TiO_2 Inorganic Shell Thickness (nm)	TiO_2 Inorganic Shell Thickness (nm)
75	27 ± 4	14 ± 3
100	30 ± 5	15 ± 2
150	46 ± 7	24 ± 5

It is still not fully understood why the SSG deposition thickness of Ti-O would be half that of Sn-Ti-O. Kunitake has shown significantly different layer thicknesses for Ti-O and Zr-O bearing precursors[99]. The two most likely causes of such a considerable increase in Sn-doped Ti-O coating thickness after organic pyrolysis are as follows: i) the incubation times are not adequate to completely coat the intricate surface with Ti-O bearing SSG and/or ii) the Sn-Ti-O precursor solution forms oligomers in solution that do not disaggregate upon chemisorption to chitinous template or subsequent anhydrous IPA rinsing / hydrolysis in DI water/IPA solution. Both causes would indicate the Sn-containing precursor was less stable than the Ti precursor. The time for hydrolysis of

precursor solutions in air to produce noticeable precipitates in solution were considerably less for Sn-Ti-O precursor (~ 1 hr) solution than the Ti-O solution (~ 1.5 hr) .

Intrascale MSP measurements were performed by A. Lethbridge, University of Exeter and Mathias Kolle, Harvard University. All data analyses were performed by A. Lethbridge. A representative reflection spectrum from a native *P. sesostris* butterfly scale with the ridges removed via FIB milling is shown in **Figure 89b**. The reflection peak centered at about 480 nm is consistent with the blue color seen in the bright field micrograph shown in **Figure 89a.** The intensity of the 480 nm light is mapped in **Figure 89c** showing the greatest intensity of 480 nm light near the tip of the revealed PPC structure. The color of each pixel in the color map of a native scale with ridges removed (shown in **Figure 89d)** represent the peak wavelength of each spectrum (peak wavelength color range indicated to the right of each map) from each 1.0 μm x 1.0 μm pixel.

The green color of the 150 layer PPC replica (**Figure 88**) is of particular interest for modeling as there appears to be no decrease in hexagonal pore spacing (**Figure 83**) and, thus, only the fill fraction is directly affected by the coating thickness (i.e., there is no indication of collapse of the coating into the space previously occupied by the cuticle). In this case the cuticle gyroid was replaced with a 46 nm thick Sn-doped titania rutile titania shell (see APPENDIX A for discussion of refractive index) with a hollow (air) core. The redshift of inorganic replicas with greater number of SSG deposition cycles seen qualitatively in **Figure 88** is also observed quantitatively via MSP (**Figure 91**). The reflection spectra from 50 layer (ridge side up – left column) and 150 layer Sn-Ti-O (ridge – middle column) and PPC side up – right column) inorganic replicas after FIB removal of ridges are shown in **Figure 90**. The corresponding bright field optical images

and intensity maps (chosen wavelength indicated) of the specimens from which the spectra were taken are also shown in **Figure 90.** Each spectrum is representative of one pixel on the corresponding color maps shown in **Figure 91**. The color of each pixel in color maps of inorganic replicas represents the peak wavelength of the spectrum (peak wavelength color range indicated to the right of each map) from each 1.0 μm^2 pixel. The redshift of inorganic replicas with greater number of SSG deposition cycles seen qualitatively in **Figure 88** is also observed quantitatively via MSP (**Figure 91**). The left edge of the 150 SSG deposition cycle inorganic replica is blue-shifted with respect to the center of the scale (**Figure 88**) and the blue edge is indicated in the MSP color map of that same portion of the scale (**Figure 91c**).

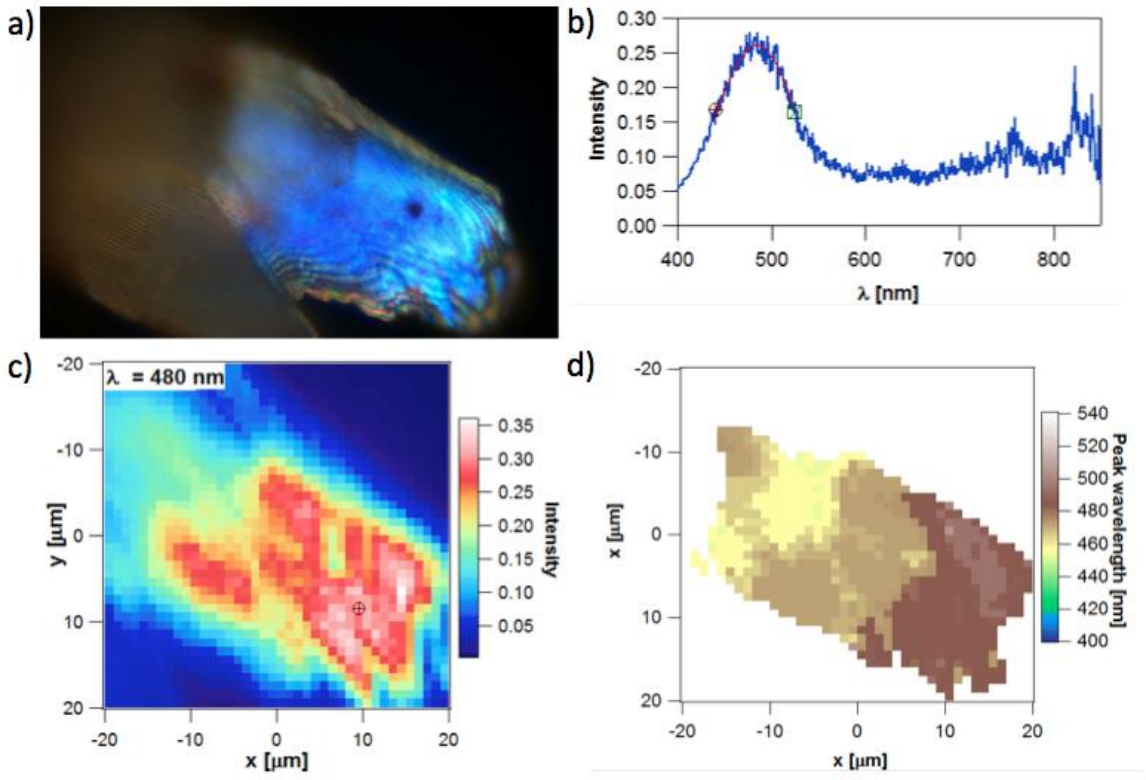

Figure 89: (a) A Bright field image of a native *P. sesostris* scale after FIB milling removal of the ridge structure along with (b) a representative MSP spectrum from the sample, (c) an intensity map of 480 nm light, and (d) a color map of the specimen with each 1.0 x 1.0 µm pixel color-coded to its peak reflection wavelength. All data courtesy A. Lethbridge and P. Vukusic, University of Exeter and M. Kolle, Harvard University.

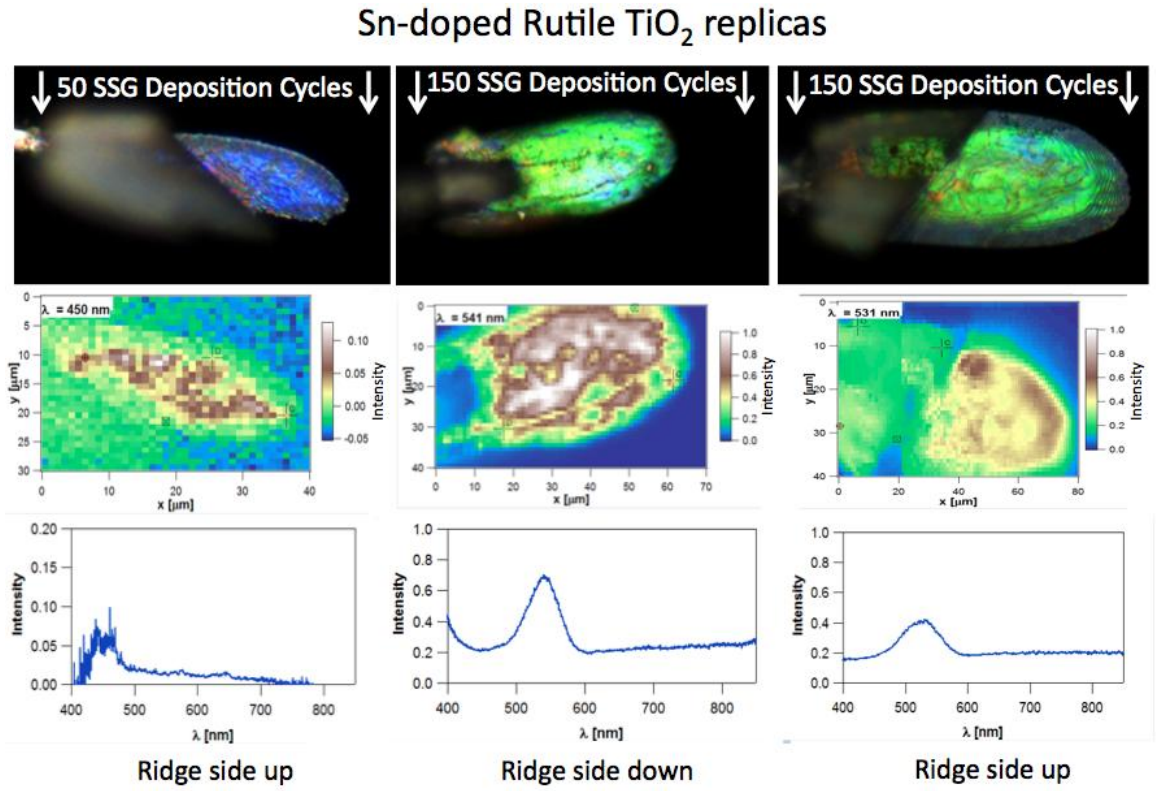

Figure 90: (Top row) Bright field images of *P. sesostris* Sn-doped TiO_2 inorganic scale replicas after FIB milling removal of the ridge structure along with (bottom row) a representative MSP spectrum from a single 1 µm^2 pixel area within the sample, and (middle row) an intensity map of the peak reflectance wavelength from the representative spectrum for each specimen. All data courtesy A. Lethbridge and P. Vukusic, University of Exeter and M. Kolle, Harvard University.

Initial characterization of native *P. sesostris* scales indicated the scale membrane underneath the PPC may be contributing to the coloration of the scale. In order to ensure the color emanating from the PPC was only resulting from the PPC structure, an inorganic replica was interrogated after the removal of both the ridges and scale membrane. The inorganic replica evaluated was formed after organic pyrolysis of a scale coated with 150 Sn-Ti-O SSG deposition cycles. SE images of the FIB milled inorganic scales and the corresponding bright field optical micrographs are shown in **Figure 92**. Indeed the PPC-only region exhibited the green coloration seen with the membrane intact (**Figure 88:** right column), **Figure 90**: right column)). An edge on view of the PPC also revealed green coloration (**Figure 92e**). It should be noted the coloration of the inorganic

replicas from the membrane side up are highly dependent on orientation and the membrane may provide coloration due to thin film effects. Hence all of the color maps were generated with PPC exposed specimens oriented with ridge side up (**Figure 91**).

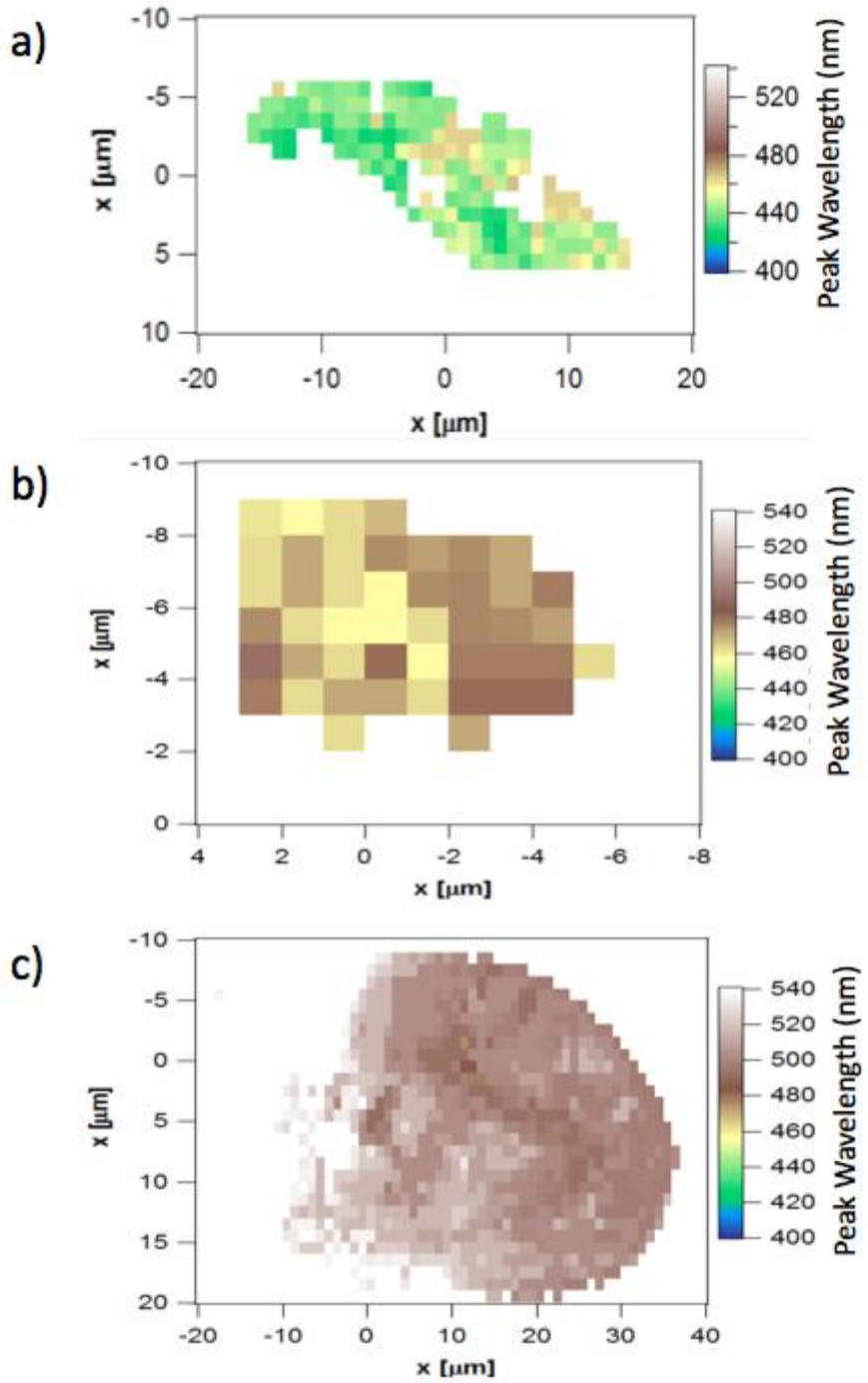

Figure 91: : MSP color maps from (a) a FIB-exposed photonic solid region (violet) from a 50 SSG cycle Sn-Ti-O coated and pyrolyzed inorganic replica scale, (b) a FIB-exposed photonic solid region

(blue/violet) from a 100 SSG cycle Sn-Ti-O coated and pyrolyzed inorganic replica scale, and (c) a FIB-exposed photonic solid region (largely green) of a 150 SSG cycle Sn-Ti-O coated and pyrolyzed inorganic replica scale. Color maps courtesy A. Lethbridge and P. Vukusic, University of Exeter and M. Kolle, Harvard University.

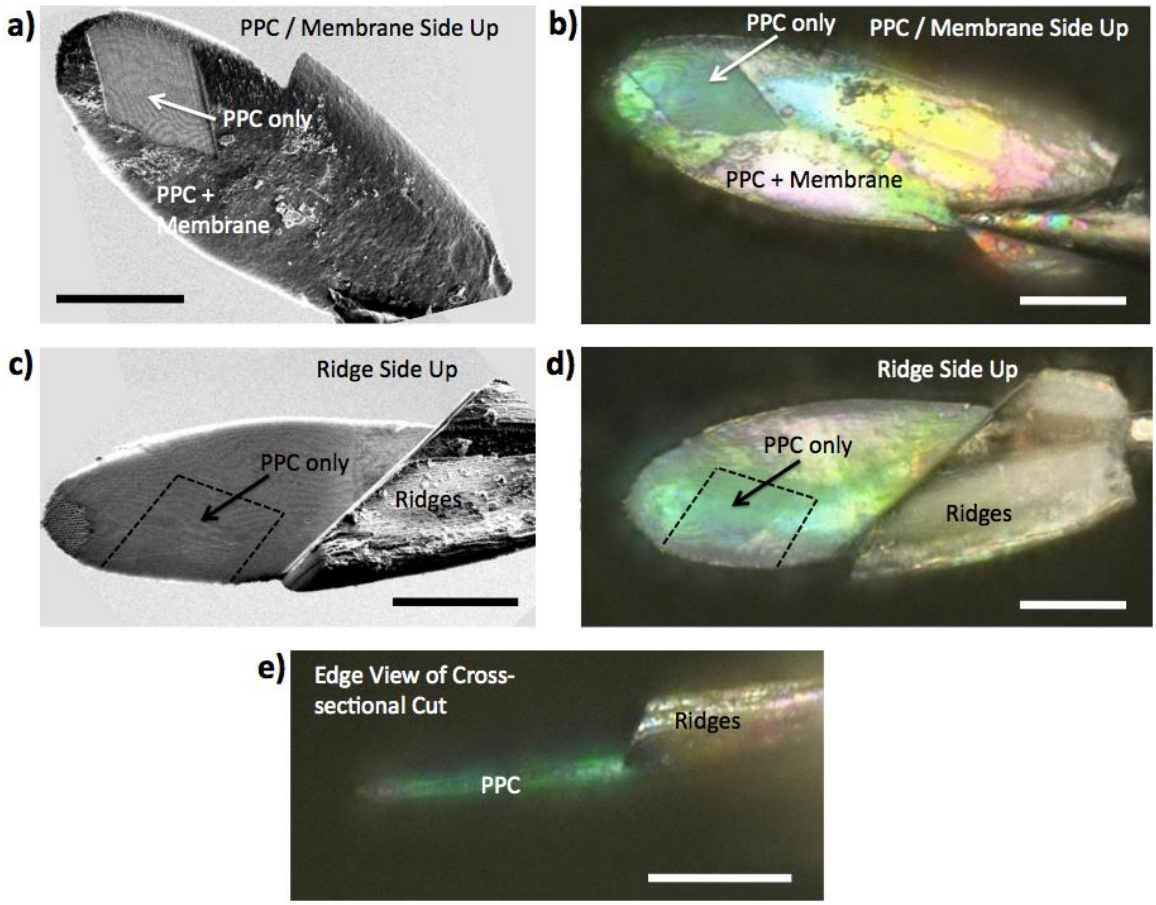

Figure 92: (a,c) SE images and (b,d,e) bright field optical images of FIB-milled inorganic replica of *P. sesostris* scale formed via 150 deposition cycles of Sn-Ti-O coating after organic pyrolysis at 450°C for 4 hr. Both the PPC (i.e. membrane) side up (a,b) and ridge side up (c,d) orientations are shown in addition to an edge on view of the PPC. All scale bars represent 20 µm. All images courtesy C. G. Cameron, Georgia Institute of Technology.

4.5. *Concluding Remarks*

The capability for fine-scale tuning of the reflection spectra obtained from structurally-colored natural bioorganic templates via the well-controlled, layer-by-layer, wet-chemical SSG deposition of higher-index materials has been demonstrated for the first time. This work has also resulted in the first demonstration of fine-scale tailoring of structural color in freestanding, all-inorganic three-dimensional replicas of natural

bioorganic templates. The importance of careful interrogation to isolate the effects of constructive modification from that of inter- and intra-butterfly color variations has also been revealed. A highlight of this research was the use of FIB microsurgery to interrogate the function of intrascale structures. Lattice spacing and fill fraction are crucial components for replicating and tuning structural color in inorganic *P. sesostris* butterfly scales. In fact, **Figure 88**, **Figure 90,** and **Figure 91** revealed the first qualitative and quantitative demonstration of wet-chemical-based replication and tuning of structural color from individual butterfly scales. However, the effect of higher index hollow inorganic replicas is not fully understood, and the chemistry within native scales cannot be ignored. FIB deconstruction techniques are currently underway at the Georgia Institute of Technology by Craig G. Cameron and Prof. Kenneth H. Sandhage in collaboration with Alfie Lethbridge and Peter Vukusic at Exeter University to understand the role of each intrascale structure within native *P. sesostris* scales. In addition to fundamental understanding of structural color, such microsurgical techniques were critical to reveal and interrogate the structural color exhibited by the PPC of inorganic replicas.

Future work should include: (i) modeling the optical functions of inorganic coated bioorganic templates and of hollow inorganic replicas, (ii) further interrogation into the role of intrascale chemistry and structure within native *P. sesostris* scales, (iii) continued MSP characterization of native, coated, and inorganic single scales, and (iv) evaluating the effects of additional inorganic material coating chemistries on the reflection peak shift of templates exhibiting structural color.

4.6.*References*

[82] R.A. Potyrailo, H. Ghiradella, A. Vertiatchikh, K. Dovidenko, J.R. Cournoyer, E. Olsen, "Morpho butterfly wing scales demonstrate highly selective vapour response," *Nature Photonics*, vol. 1, pp. 123-128, 2007.

[83] N.L. Garrett, P. Vukusic, F. Ogrin, E. Sirotkin, C.P. Winlove, J. Moger, "Spectroscopy on the wing: Naturally inspired SERS substrates for biochemical analysis," *Journal of Biophotonics*, vol. 2, pp. 157-166, 2009.

[84] L. Collins, "You ain't seen nothin' yet." *Engineering and Technology*, vol. 5, pp.64-65, 2010.

[85] P. Vukusic, "An Introduction to Bio-Inspired Design," *Contact Lens Spectrum, Special Edition*, pp. 6-13, 2010.

[86] B. Li, J. Zhou, R. Zong, M. Fu, Y. Bai, L. Li, Q. Li, "Ordered Ceramic Microstructures from Butterfly Bio-template," *Journal of the American Ceramic Society*, vol. 89, pp. 2298-2300, 2006.

[87] W. Zhang, D. Zhang, T. Fan, J. Ding, Q. Guo, H. Ogawa, "Morphosynthesis of Hierarchical ZnO replica using butterfly wing scales as templates," *Microporous and Mesoporous Materials*, vol. 92, pp. 227-233, 2006.

[88] W. Peng, X. Hu, D. Zhang, "Bioinspired fabrication of magneto-optic hierarchical architecture by hydrothermal process from butterfly wing," *Journal of Magnetism and Magnetic Materials*, vol. 323, pp. 2064-2069, 2011.

[89] G. Cook, P.L. Timms, C. Goltner-spickermann, " Exact Replication of Biological Structures by Chemical Vapor Deposition of Silica," *Angewandte Chemie International Edition*, vol. 42, pp. 557-559, 2003.

[90] J. Huang, X. Wang, Z.L. Wang, "Controlled Replication of Butterfly Wings for Achieving Tunable Photonic Properties," *Nanoletters*, vol. 6, pp. 2325-2331, 2006.

[91] Michael R. Weatherspoon, Y. Cai, M. Crne, M. Srinivasarao, and K. Sandhage, "3D Rutile Titania-Based Structures with Morpho Butterfly Wing Scale Morphologies," *Angewandte Chemie*, vol. 120, pp. 8039-8041, 2008.

[92] G. Wang, Y. Fang, P. Kim, A. Hayek, M.R. Weatherspoon, J. W. Perry, K.H. Sandhage, S.R. Marder, S.C. Jones, "Layer-By-Layer Dendritic Growth of Hyperbranched Thin Films for Surface Sol-Gel Syntheses of Conformal, Functional, Nanocrystalline Oxide Coatings on Complex 3D (Bio)silica Templates," *Advanced Functional Materials*, vol. 19, pp. 2768-2776, 2009.

[93] X.-Z. Ding, Z.-A. Qi, and Y.-Z. He, "Effect of Tin Dioxide Doping on Rutile Phase Formation in Sol-Gel-Derived Nanocrystalline Titania Powders," *Nanostructured Materials*, vol. 4, pp. 663-668, 1994.

[94] K. Michielsen, D.G. Stavenga, "Gyroid cuticular structures in butterfly wing scales: biological photonic crystals," *Journal of the Royal Society Interface*, vol. 5, pp. 85-94, 2008.

[95] B.N. Taylor and C.E. Kuyatt, "Guidelines for Evaluating and Expressing the Uncertainty of NIST Measurement Results: NIST Technical Note 1297," U.S. Government Printing Office, Washington D.C., USA,1994.

[96] U. Balachandran, E.G. Error, "Raman spectra of titanium dioxide," *Journal of Solid State Chemistry*, vol. 42, pp. 276-282, 1982.

[97] J.C. Parker and R.W. Siegel, "Raman microprobe study of nanophase TiO_2 and oxidation-induced spectral changes," *Journal of Materials Research*, vol. 5, pp. 1246-1253, 1990.

[98] J. Vernon, Y. Fang, Y. Cai, K.H. Sandhage, "Morphology-Preserving Conversion of a 3D Bioorganic Template into a Nanocrystalline Multicomponent Oxide Compound," *Angewandte Chemie International Ed*., vol. 49, pp. 7765 -7768, 2010.

[99] I. Ichinose, H. Senzu, and T. Kunitake, "Stepwise Adsorption of Metal Alkoxides on Hydrolyzed Surfaces: A Surface Sol-Gel Process," *Chemistry Letters*, pp. 831-832, 1996.

APPENDIX A: Sn-doped Titania Index of Refraction

Although many factors can affect the optical properties calculated/measured from materials, a simple weight averaging of mol% SnO_2 and mol% TiO_2 was used to estimate the effective refractive index of Sn-doped TiO_2. It is assumed both pure and doped materials are fully crystallized. Rutile TiO_2 is assumed to have an index of refraction of 2.616[100]. SnO_2 is assumed to have a refractive index of 2.010[100]. Anatase TiO_2 is assumed to have a refractive index of 2.561[100]. All refractive indices represent ordinary ray refractive indices determined through immersion method commonly used in optical mineralology[100]. The extraordinary ray index of refraction for anatase TiO_2 is assumed to be 2.488[100]. It is hypothesized that in order to form Sn-doped TiO_2 with an effective refractive index greater than or equal to anatase titania, the SnO_2 content cannot exceed 9 (ordinary ray refractive index) – 21 (extraordinary ray refractive index) mol% (**Text in red in Table 6**). The calculated effective indices are shown in **Table 6**. Such hypothesized values were only used as a guideline for precursor doping concentrations (see **Section 4.3.2**). Potentially some of these values could be used as a starting estimate for the refractive index of Sn-doped TiO_2 coatings (**18.4 mol% Sn doping highlighted in green in Table 6**) after organic pyrolysis.

Table 6: Estimated Effective Refractive Index From Weight Averaging of Pure Rutile TiO_2 and Pure SnO_2

TiO_2	SnO_2	Effective n_ω
0.990	0.010	2.610
0.980	0.020	2.604
0.970	0.030	2.598
0.960	0.040	2.592
0.950	0.050	2.586
0.940	0.060	2.580
0.930	0.070	2.574
0.920	0.080	2.568
0.910	0.090	2.561
0.900	0.100	2.555
0.890	0.110	2.549
0.880	0.120	2.543
0.870	0.130	2.537
0.860	0.140	2.531
0.850	0.150	2.525
0.840	0.160	2.519
0.830	0.170	2.513
0.820	0.180	2.507
0.816	0.184	2.504
0.810	0.190	2.501
0.800	0.200	2.495
0.790	0.210	2.489
0.780	0.220	2.483

A.1. *References*

[100] W.R. Phillips and D.T. Griffen, *Optical mineralogy: the nonopaque minerals*, W.H. Freeman, San Francisco, 1981.

Vita

Jonathan Paul Vernon was born to George and Donna Vernon January 19th, 1984 in Cincinnati, OH. He grew up with his older sister Andrea Vernon in Hamilton, Ohio until age 11 when his family moved to Franklin County, Indiana. He graduated from Franklin County High School as salutatorian of the Class of 2002. In May of 2007 Jonathan graduated from Purdue University where he earned a Bachelors of Science degree in Materials Science and Engineering and an engineering co-op certificate by working full-time at Raybestos Powertrain, LLC in Crawfordsville, IN for five academic terms. In the summer of 2007 he joined Kenneth H. Sandhage's research group and began the Materials Science and Engineering Ph.D. program of study at Georgia Institute of Technology. Upon completion of all graduation requirements, in January 2012, Jonathan will begin work in a postdoctoral research position within Dr. Timothy Bunning's group at Wright Patterson Air Force Base in Dayton, OH.